

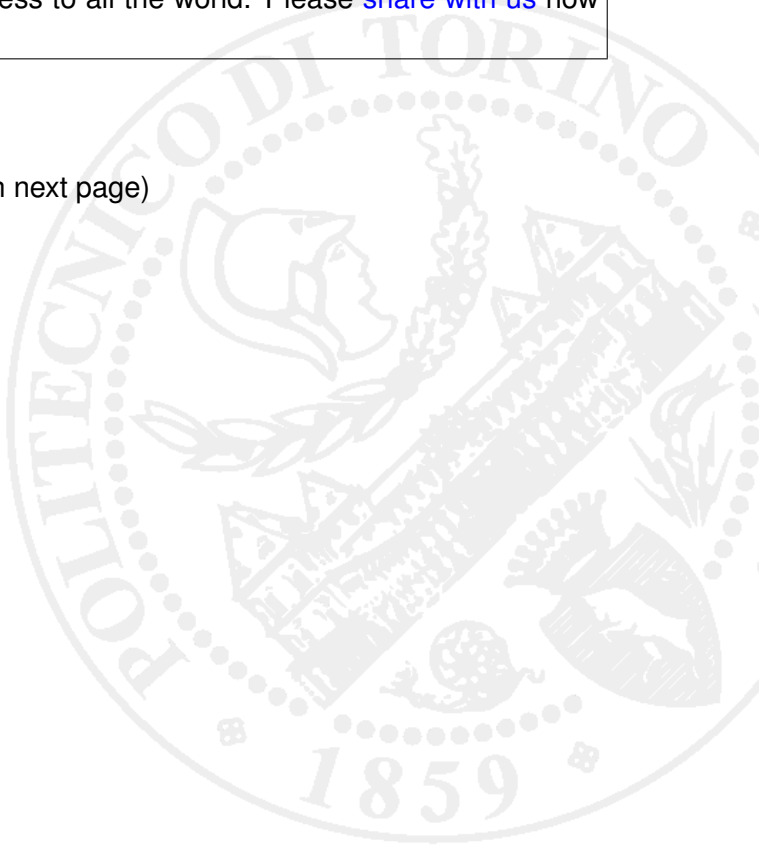


Politecnico di Torino

Department of Mechanical and Aerospace Engineering

Doctoral Program in Biomedical Engineering

Final Dissertation

# Exploring the mechanical properties of ex vivo human dermis in vitro and in silico

Candidate:
Mara Terzini

Tutor:
Prof. Alberto L. Audenino

Coordinator of the Research Doctorate Course:
Prof. Cristina Bignardi

2013-2016

*Table of Contents*

## Short Curriculum Vitae

Mara Terzini was born in 1985 in Moncalieri (TO), Italy. She received a BS degree (October 2009) and a MS degree (December 2012) in Biomedical Engineering from Politecnico di Torino. During her MS thesis, she focused on the soft tissues mechanical characterization, within a collaboration with the Turin Skin Bank (AOU Città della Salute e della Scienza). In 2013 she was qualified to practice the profession of Industrial Engineering.

From March 2013 to March 2016 she was a PhD student in Biomedical Engineering at the Department of Mechanical and Aerospace Engineering, Politecnico di Torino, where she worked on the engineering and characterization of a human acellular allograft for applications in reconstructive surgery. Her reaserch activity is part of a collaboration with the Turin Skin Bank (AOU Città della Salute e della Scienza), which aim at the development of an acellular allograft for load bearing clinical applications.

As a PhD student of Industrial Bioengineering group, she has been involved in the research activites included in the BBS ("Bioactive Bone Substitutes") project and in the E.F.I.N. (Expandable Femoral Endomedullary Nail) starting project. Moreover, she has been involved in several industrial collaborations, aimed at the characterization of medical devices in vitro and in silico.

From 2013 she works as a teaching assistant at Politecnico di Torino, in courses related to the biomechanics field: "Bioingegneria Meccanica" (AY 2013/2014), "Progettazione di Protesi e Organi Artificiali" (AY 2013/2014, AY 2014/2015, AY 2015/2016), "Biomeccanica dei Solidi" (AY 2014/2015, AY 2015/2016).

Up today, as a results of her research work, she is the author of 3 published articles and 9 abstracts in national/international conferences.

## List of Publications

### International Journals with referee

1. **Mara Terzini**, Cristina Bignardi, Carlotta Castagnoli, Irene Cambieri, Elisabetta M. Zanetti, Alberto L. Audenino, (2016) Dermis Mechanical Behaviour after Different Cell Removal Treatments. Medical Engineering & Physics, doi:10.1016/j.medengphy.2016.02.012.
2. **Mara Terzini**, Cristina Bignardi, Carlotta Castagnoli, Irene Cambieri, Elisabetta M. Zanetti, Alberto L. Audenino, (2016) Ex-Vivo Dermis Mechanical Behavior in Relation to Decellularization Treatment Length. The Open Biomedical Engineering Journal, doi: 10.2174/1874120701610010034.
3. Giuseppe Falvo D'Urso Labate, Francesco Baino, **Mara Terzini**, Alberto L. Audenino, Chiara Vitale-Brovarone, Patrick Segers, Rodolfo Quarto, Gerardo Catapano (2016) Bone structural similarity score: a multiparametric tool to match properties of biomimetic bone substitutes with their target tissues. Journal of Applied Biomaterials and Functional Materials, doi: 10.5301/jabfm.5000283.

### Communications in National/International Conferences

1. Giuseppe Falvo D'Urso Labate, Francesco Baino, **Mara Terzini**, Alberto Audenino, Chiara Vitale-Brovarone, Patrick Segers, Rodolfo Quarto, Gerardo Catapano (2015) Bone Substitute Score (BoSS): an Index to Assess Scaffold Performance for Bone Tissue Engineering, Congress SIB 2015, Ancona.
2. Giuseppe Falvo D'Urso Labate, Francesco Baino, **Mara Terzini**, Chiara Vitale-Brovarone, Patrick Segers, Alberto Audenino, Rodolfo Quarto, Gerardo Catapano (2015) Biomimetic evaluation of scaffold performance for bone tissue engineering, In: INTERNATIONAL JOURNAL OF ARTIFICIAL ORGANS, 38(7), pp 360-392, ISSN: 0391-3988, DOI: 10.5301/ijao.5000417.

3. Cristina Bignardi, Elisabetta M. Zanetti, **Mara Terzini**, Giuseppe Pisani, Alberto L. Audenino (2014) Cranial Cruciate Ligament Rupture: A Multi-Body Analysis Comparing Corrective Tibial Osteotomies, In: INTERNATIONAL JOURNAL OF ARTIFICIAL ORGANS, 37(8), pp 592-592, ISSN: 0391-3988, DOI: 10.5301/ijao.5000346.
4. **Mara Terzini**, Cristina Bignardi, Carlotta Castagnoli, Elisabetta M. Zanetti, Gerardo Catapano, Alberto L. Audenino (2014) Influence of cell removal treatment on dermis mechanical behaviour, In: INTERNATIONAL JOURNAL OF ARTIFICIAL ORGANS, 37(8), pp 640-640, ISSN: 0391-3988, DOI: 10.5301/ijao.5000347.
5. **M. Terzini**, A. R. Ciccola, G. Menicucci, C. Manzella, S. Carossa, E.M. Zanetti, C. Bignardi, A.L. Audenino (2014) Experimental set-up for the study of dental implant retrieval, IV Meeting of European Society of Biomechanics - Italian Chapter, Pavia.
6. **M. Terzini**, C. Bignardi, C. Castagnoli, E.M. Zanetti, L. Audenino (2014) Influence of cell removal treatment on dermis mechanical behaviour, In: IV GNB National Congress, Pavia, 25-27 June.
7. **M. Terzini**, A. R. Ciccola, G. Menicucci, C. Manzella, S. Carossa, E.M. Zanetti, C. Bignardi, A.L. Audenino (2014) Experimental set-up for the study of dental implant retrieval, In: IV GNB National Congress, Pavia, 25-27 June.
8. **M. Terzini**, A.L. Audenino, C. Bignardi, E. Businaro, C. Castagnoli, E.M. Zanetti (2013) Dermis mechanical behaviour: influence of cell removal treatment. Summer-Workshop on Mechanics in Biology, Berlin, 16-17th September.
9. Audenino A.L., Bignardi C., Businaro E., Castagnoli C., **Terzini M.**, Zanetti E.M. (2013) Dermis mechanical behaviour: influence of cells removal treatment. In: Modelling in Medicine and Biology X / R.Kiss & C.A. Brebbia. WIT Press, ASHURST SOUTHAMPTON, pp. 183-192. ISBN 9781845647063

## Abstract

Human acellular dermal matrices (HADMs) are used in reconstructive surgery as scaffolds promoting autologous tissue regeneration. Despite their primary usage was in burn surgery, HADMs have recently been employed in reconstructive surgeries, which involve the high mechanical resistance prerequisite (e.g. rotator cuff tears repair, Achilles tendon augmentation, breast reconstruction procedure, hernia repair). Critical to the HADM ability to remodel and integrate into the host tissue is the removal of cells while maintaining an intact extracellular architecture. First objective of this research is to develop a methodology to analyze the mechanical properties of HADMs after decellularization to identify its ideal form of treatment and its duration. Two different decellularization techniques were used as a benchmark: the first is a well-established technique (incubation in NaOH for 1 to 7 weeks), and the second is an innovative technique developed by the Turin Skin Bank (AOU Città della Salute e della Scienza) research group (incubation in DMEM (Dulbecco's modified Eagle medium) for 1 to 7 weeks). After decellularization, the specimens underwent uniaxial tensile tests, and experimental data were represented with stress strain curves, calculating both engineering and true values. Mechanical tests, coupled to the immunohistochemical evaluation and the surgeons' macroscopic analysis, have led to the identification of the optimal method (DMEM) and duration (5 weeks) for the decellularization treatment. Moreover, despite differences have been found between engineering and true values, which can reach 84%, the engineering values remain useful to make comparisons, providing reliable indications with a simpler experimental set up and data processing.

Once identified the most suitable decellularization treatment, the preservation process has been inquired analysing its effects on the ECM mechanical properties. The standardized glycerolization procedure for the preservation of skin allograft is considered a simple and cost-effective method resulting in non-viable but intact skin that can be used as biological dressing on scalds, temporary coverage on excised burns and as a

means of wound bed preparation. This same procedure can be used for the conservation of the decellularized dermis, whose application is in the reconstruction of tissues subjected to high mechanical in vivo solicitations. The preservation of the ECM's integrity during the storage period is mandatory. Therefore, dermis tissue harvested from four donors was subjected to glycerolization and uniaxial mechanical tests were carried out on paired samples composed by de-glycerolized allograft and freshly excised human dermis collected from the same donor. Mechanical tests have led to the identification of the treatment influence, showing post-treatment increases in ultimate stress and elastic modulus of up to 191% and 212% respectively. In addition, donor and orientation factors were investigated, confirming the higher anisotropy of skin in older donors.

Fundamental in the clinical uses of HADM is its suturability during the surgery procedure and the sutured allograft behavior when physiologically solicited. The first feature can be evaluated through a macroscopic analysis carried out by an experienced clinical examination. For the second one a mechanical characterization is mandatory, and it was here performed investigating the sutured HADM in various condition (one single suture at one end of the specimen (I), one or two stitches between two pieces of dermis in quasi-static (II) and dynamic conditions (III)). Standard uniaxial tensile tests were performed, coupling tensile machine sensor outputs to image analysis, with the aim of providing additional information other than just the "suture retention strength" value. Characteristic curves of the sutured dermis behaviour were obtained and were compared with control intact specimens. This analysis showed an increase in the elasticity of the sutured specimens, which appears to have beneficial effects in the immediate post-operative period, when the dermis allograft has not yet been incorporated and colonized by the host tissue.

Uniaxial engineering stress-strain curves obtained in the first phase of this work were then exploited for the implementation of four different computational model (both linear and non-linear), and an evaluation procedure was carried out based on a quantitative comparison of the simulation results with parameters extracted from the true stress-strain

curves. It was found that the results obtained from the hyperelastic models well represent the experimental situation, and in particular, the incompressible Odgen model shows less than 7% percentage variations for all the considered parameters. It was then confirmed the inadequacy of the linear models to describe the behaviour of a biological material like dermis.

The last aspect investigated in this research was the biaxial characterization of the engineered HADMs. In fact, planar biaxial testing allows for a two-dimensional stress-state that can be used to fully characterize the dermis properties. The high cost related to this type of analysis has lead to the development of a new low cost biaxial conversion mechanism for a uniaxial testing machine. This mechanism was realized through rapid prototyping considerably reducing the implementation costs and facilitating the design phase, assisted by the immediate printing and testing of the components. Before use, the device was validated through both experimental and computational tests which involved the response of the mechanism when subjected to unbalanced loads and the evaluation of the uniformity of the strain distributions in a small central region of the specimen. This latter was performed through different procedures (the finite element method, the DIC method and the rosette gage theory) all employing the optical measure of strains. The biaxial mechanical behaviour of untreated and decellularized dermis was measured exploiting the purpose-made biaxial fixture. Stress-strain curves were evaluated from loads acquired by two load cells positioned along two orthogonal axis and the optical measure of the deformations of four markers located in the central area of the specimen. The specimens resulted on average less extensible in the medio-lateral direction (namely, along the Langer lines) then in the cranio-caudal direction, confirming the correlation of dermis mechanical response with collagen fibres disposition with respect to the loading direction.

# Chapter 1

# Introduction

## 1.1 Motivation

The aim of the research here presented is the engineering of an acellular matrix produced from dermal tissue aimed at clinical applications which implicate demanding mechanical properties. In fact, despite the ADM (acellular dermal matrix) primary usage was in burn surgery as biological dressing on scalds, temporary coverage on excised burns and in wound bed preparation, ADMs have recently been employed in reconstructive surgeries which involve the high mechanical resistance prerequisite (e.g. rotator cuff tears repair, Achilles tendon augmentation, breast reconstruction procedure, hernia repair). A thorough mechanical characterization aimed at optimizing the chemical treatments required for the acellular matrix engineering is therefore mandatory, and it is functional to the obtaining of the optimal mechanical performance for the resulting ADM. Subsequent characterizations aimed at the investigation of the engineered tissue response when subjected to stresses similar to those in vivo are needed in order to provide additional guidance to surgeons.

A secondary purpose of this research is widening the existing knowledge of the mechanical properties of dermis tissue. Accurate measurements of the mechanical properties of soft biological tissues, like dermis, allows improving the safety and the efficacy of medical implants in soft tissues through the development of more faithful computer simulation tools.

## 1.2 Approach

Uniaxial Tensile Tests will be employed in order to optimize the engineered allograft in terms of decellularization medium and treatment duration with respect to the chemical treatment effects on the mechanical behavior of the tissue. Together with the experimental analysis, efforts will be made to identify the more correct stress-strain formulation for the reliable identification of faithful mechanical parameters, while maintaining a simple experimental set-up. The stress-strain curves obtained by this first investigation will be used for the implementation and validation of linear and nonlinear computational models. The set-up will be then employed in the study of the impact of a standard preservation method on the mechanical properties of dermis comparing results with the native dermis ones.

Next, the optimized acellular allograft will be subjected to loads which mimics the surgical procedure and the immediate post-operative period, performing suture retention strength tests and equibiaxial testing. The latter will be made possible by the design and realization of a low-cost biaxial conversion device for a uniaxial testing machine. The effectiveness of the device design will be pre-emptively validated by means of experimental tests and computational analysis.

## 1.3 Background

Acellular dermal matrices (ADMs) are a class of scaffold which is employed in the augmentation and replacement of deficient or missing soft tissues. They are divided into three families: **biological**, which are derived from human, animal or plant origin; **synthetic**, which are derived

from manmade materials; **composite**, which are derived from a mix of biological and manmade materials (Harding, et al., 2010). Historically, most ADMs have been harvested from the superficial (papillary) dermis just beneath the epidermis. The papillary dermis has a denser and more organized collagen arrangement when compared with the deeper reticular dermis. However, several newer ADMs are specifically harvested from this deeper layer, because of its higher flexibility. Moreover this skin layer is potentially more conducive to ingrowth.

The acellular dermal matrix engineered in this study has the human reticular dermis as a starting biological material.

Dermis strips unfit for transplantation were used for these research after the approval of the Institutional Ethical Board of A*zienda Ospedaliera Universitaria Città della Salute e della Scienza* of Turin, Italy, (approved on January 23rd, 2012 with protocol number 0006730), and written informed consent was obtained from all study participants.

### 1.3.1 Dermis structure

The skin is the largest organ of the body and it works as a physical barrier to loss of water and electrolytes, as a mechanical barrier to external agents and as a thermoregulator. Moreover, its functions include the transduction of signals from the environment such as touch, pressure and temperature (Ambrosio, et al., 2002).

The skin is a multilayered and highly organized thin membrane, organized in four principal types of tissues: the epidermis, the **dermis**, the basement membrane, and the sub cutis (Figure 1.1). The outermost layer, the epidermis, is a 0.1-mm-thick continuous sheet, perforated only at the pores of sweat glands and by the hair follicles. It consists of epithelial tissue in which the cells are tightly packed together providing a barrier between the inside of the body and the outside world.

The dermis is the structure beneath the epidermis, and the two are separated by the basal membrane. The latter is an approximately 20-nm-thick multilayered membrane, which is responsible for adherence between the epidermis and the dermis and for the mechanical support of the epidermis.

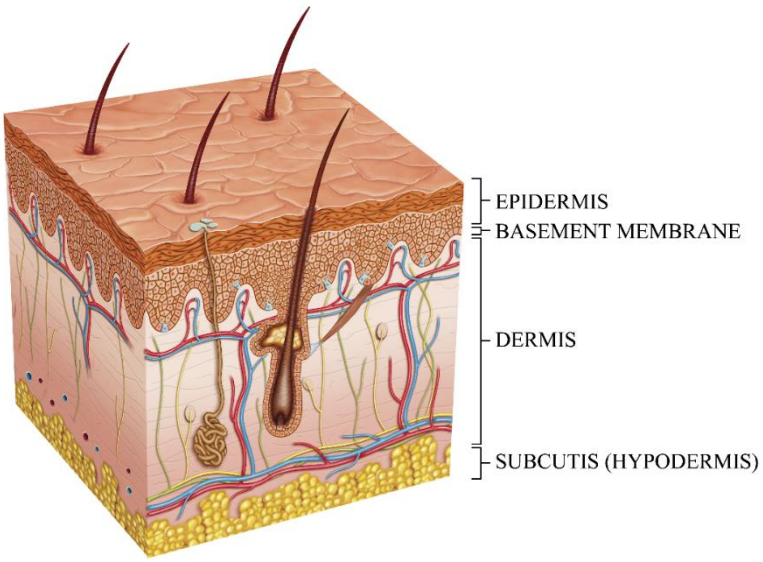


*Figure 1.1 Structure of skin*

The dermis is a 2-5-mm-thick layer of vascularized and innervated connective tissue with few cells, mainly fibroblasts. It consists of three layers (Figure 1.2):

**Papillary layer:** The dermal area that project into the intervals between the epidermal ridges.

**Sub papillary layer:** The area underlying the epidermis, containing the same components as the papillary layer.

**Reticular layer:** The largest part of the dermis with a dense connective tissue comprising fiber components. (Shimizu, 2007)

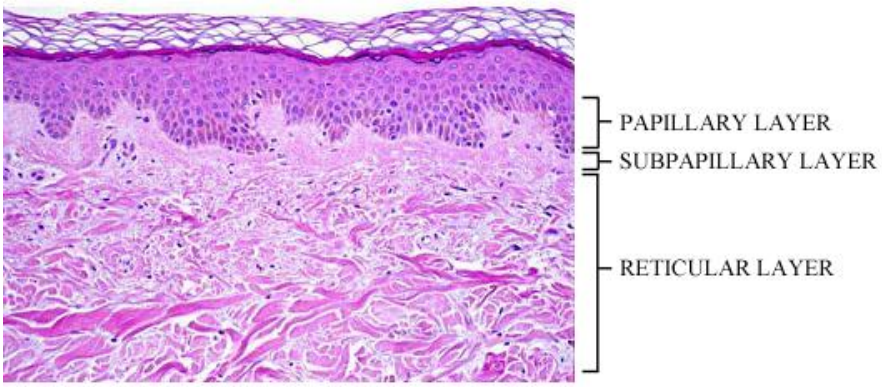


*Figure 1.2 Structure of dermis*

The lower part comes into contact with the sub cutis, which is 0.4-4 mm in thickness and comprises loose areolar connective tissue and fat. The dermis in most responsible for the mechanical performance of the skin. As a consequence particular attention should be paid to its structure.

The major components mainly consist of collagen fibers (Type I and Type III), with smaller amounts of elastic fibers, reticular fibers and matrix. This matrix generally comprises the extra-cellular matrix and ground substance made up of proteoglycans and gelatin. Fibroblasts, macrophages, mast cells, plasma cells, vascular channels and nerves are common cellular components.

**Collagen** makes up over 75% of dry fat weight of the skin. Collagen bundles (2-15 μm in diameter) are densely interwoven in the reticular dermis upper layers, with a meshwork of thicker elastin fibers, and a lesser content of interfibrillar ground substance components. The collagen fibrous components is poorly extensible; however, it is extremely tough and resistant to tension parallel to the fibers.

The **elastic fiber** (1-3 μm in diameter) is not as tough as the collagen fiber; however it is extremely elastic. In the reticular layers, elastic fibers are scattered among collagen bundles running parallel to the skin surface.

### 1.3.2 Dermal substitutes

Dermal substitutes, taken from multi-organ donors, are the most suitable replacement integumentary for reconstructive surgery and the utility of ADMs continues to evolve. While originally developed as a dermal replacement scaffold, minimizing the morbidity of skin harvests, new generations of ADMs are now used to replace and augment missing and deficient soft tissue in the reconstruction of the head and neck, breast and abdominal wall (Carlsson, et al., 2016).

They are typically derived by processes that involve **decellularization** of tissues (Crapo, et al., 2011). The goal of a decellularization protocol is to efficiently remove all cellular and nuclear material while minimizing

any adverse effect on the composition, biological activity, and mechanical integrity of the remaining ECM. The most commonly utilized methods for the tissues decellularization involve a combination of physical and chemical treatments. These methods disrupt the cell membrane, release cell contents, and facilitate subsequent rinsing and removal of the cell contents from the ECM. These physical treatments are generally insufficient to achieve complete decellularization and must be combined with a chemical treatment. The intent of most decellularization processes is to minimize the ECM disruption and thus retain native mechanical properties of the tissue.

The effectiveness of decellularization and the alterations to the ECM vary depending on the source, composition and density of the tissue. However, it is unlikely that any combination of methods will remove 100% of all cell components, but it seems apparent that methods which remove most of the visible cellular material result in biologic scaffold materials that are safe for implantation (Gilbert, et al., 2006).

Dermal substitutes can be derived from human skin, removing all cells and hairs, so that the structure of the collagen and elastin fibers is preserved. ADMs manufacturing methods need therefore to preserve the mechanical characteristics of the tissue, in order to maintain a structurally intact natural three-dimensional extracellular matrix able to integrate into the host tissue, but also need to produce a tissue as free as possible of potentially immunogenic antigens.

The **preservation** treatment is the other process involved in the production of substitutes. The most common preservation methods used for skin dermo-epidermal allografts are cryopreservation and glycerolisation. The latter is a simple and cost-effective method to produce non-viable but intact skin grafts that can be used as biological dressing or as temporary coverage on excised burns. Human skin allografts preserved in 85% glycerol have been produced by the Euro Skin Bank (formerly the Dutch National Skin Bank) since the early 1980s. Allografts preserved in glycerol have a number of advantages: storage at 4°C provides a long shelf-life; microscopic morphology is well-preserved; GPA appear to be less antigenic than the cryopreserved equivalent; there is evidence that

viruses and bacteria present in allografts preserved in 85% glycerol will be eliminated. On the other hand, GPAs are non-viable and there is a perception that these allografts take less readily to the freshly excised wound bed than viable equivalents (Mackie, 2002).

Commercially available HADMs are structurally composed by the entire dermal layer. In the present research only reticular dermis has been use, preserved by means of glycerol in order to obtain dermal grafts suitable for clinical use. In fact, reticular dermis is relatively poor in cellularity and shows a strong mechanical resistance, if compared with sub-papillary dermis. However, decellularization remains a mandatory step for ADMs production, in order to obtain a non-immunogenic matrix.

### 1.3.3 Clinical applications

As the understating of the biological characteristics of dermis increases, the indications for its use evolve and expand. Initially ADMs were utilized in skin replacement therapies for burn patients. Soon after, the usage of ADMs evolved into other applications, but it must remembered that the acellular dermal grafts were originally developed for use in the treatment of full-thickness burns, because of their not immunogenic response, handling, long shelf-life and expedite healing.

Recently it found application in the repair of oral mucosal presenting very high success rates and avoiding any immunologic reactions and infections (Shi, et al., 2012). The ADM use in this application, similar to the skin coverage, requires the same mechanism of incorporation and the same uncritical requisites in terms of mechanical response.

The high strength applications are born and raised in the last two decades. For instance, the use of ADMs in breast surgery began in 2001 (Duncan, 2001) and the first published application of ADM use in breast reconstruction came in 2005 (Breuing & Warren, 2005). This initial publications started the ADM use in breast surgery, making it one of the most popular applications. Uses in the hernia repair are reported, in substitution of the mesh materials which results in high incidence of

mesh infections and adhesion formation. ADMs have therefore been proposed as an alternative because of its lower rates of infection and breakdown (Garvey, et al., 2014). In this case, the strength of the hernia repair is mandatory to a successful outcome, and similar requisite is desired in applications such as the repair of rotator cuff tears (Barber, et al., 2008; Burkhead , et al., 2007; Snyder & Bond, 2007; Wong, et al., 2010), during which the dermal matrix is typically used to provide biomechanical strength as well as to support directed healing, and the Achilles tendon augmentation (Lee, 2007; Barber, et al., 2006), where ADM is used as an augmentation graft which facilitate the end-to-end anastomosis. Hence, dependent on the intended use, the biomechanical response of ADMs may be of clinical significance, especially in potentially load bearing applications (Moore, et al., 2015).

### 1.3.4 Mechanical properties

The mechanical properties of the dermis are dependent on the relative composition on the ECM components and the organization of the collagen and elastin.

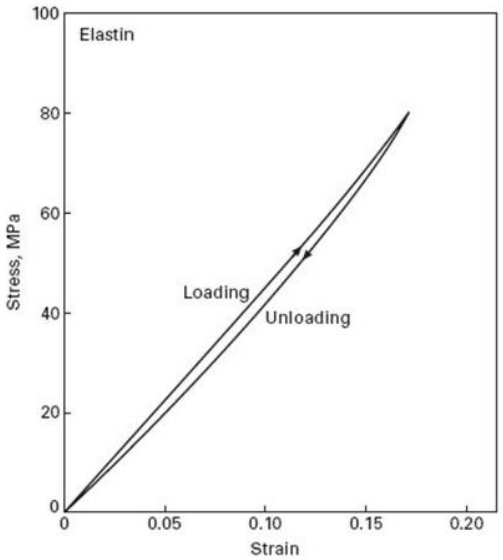


*Figure 1.3 Stress-strain response for elastin (Fung, 1993)*

Elastin is the most "linearly" elastic biosolid material known. Considering the stress-strain relationship, the loading curve is almost a straight line (Figure 1.3). Loading and unloading do lead to two different curves, showing the existence of an energy dissipation mechanism in the material, but the difference is small (Fung, 1993).

Collagen is the main load carrying element in dermis. The mechanical properties of collagen are therefore very important to biomechanics. Type I collagen is virtually ubiquitous in distribution, and with type III collagen is a major constituent of dermis. Depending on how the fibers, cells, and ground substance are organized into a structure, the mechanical properties of tissue vary. The structure of collagen fibers in the dermis must be considered as a three-dimensional network of fibrils, although the predominant fiber direction is parallel to the surface. However, in order to prevent out-of-plane shearing, some fiber orientations also have components out-of-plane (Holzapfel, 2001). These fibers are woven into a more or less rhombic parallelogram pattern, which allows considerable deformation without requiring elongation of the individual fibers.

When considering the skin as a whole, incorporating the three layers, it can be described as anisotropic, viscoelastic, nonlinear (Fung, 1993), and non-homogenous, resulting in an ability to endure large deformations. Due to the viscoelastic properties, under cyclic loads the stress-strain relationship continuously alters until a steady state is reached. This phenomenon is known as preconditioning (Liu & Yeung, 2008). Moreover, the skin in vivo is forced by a pre-stress of different degrees all over the body (Jacquet, et al., 2008; Alexander & Cook, 1977).

The overall mechanical response of skin tissue under applied tension can be divided into three main phases, shown in Figure 1.4.

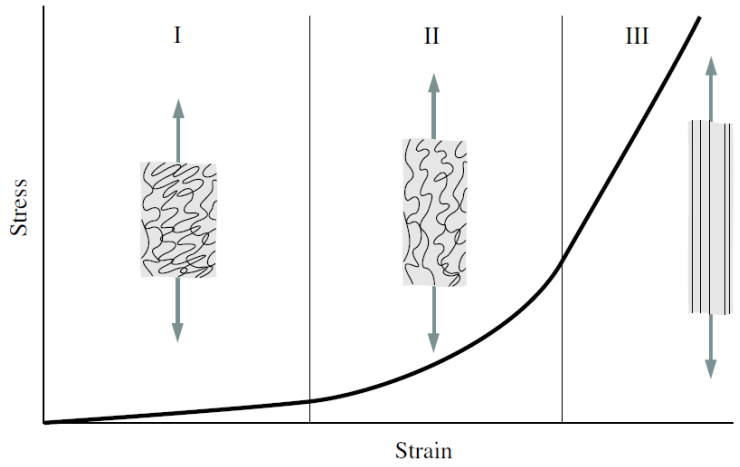


*Figure 1.4 Schematic diagram of a typical (tensile) stress-strain curve for skin showing the associated collagen fibre morphology (Holzapfel, 2001).*

Phase I illustrates great extension at low load and modulus as the dermal fibrils re-orientate towards the load axis. Unstretched skin behaves approximately isotropically. Phase II shows a gradual increase of the module. The collagen fibers tend to line up with the load direction and bear loads. The crimped collagen fibers gradually elongate and they interact with the hydrated matrix. Phase III is characterized by high tensile stresses. The crimp patterns disappear and the collagen fibers become straighter. The straightened collagen fibers resist the load strongly and the tissue becomes stiff at higher stresses, while the stress-strain relation becomes linear again. Beyond the third phase the ultimate tensile strength is reached, culminating in the complete failure of the fibrils (Holzapfel, 2001).

The influence of the collagen fibrils on the biomechanical properties of dermal tissue have been examined by altering fibril diameter and density (Sanders & Goldstein, 2001), together with the properties of the individual collagen fibrils themselves (Parkinson, et al., 1997; Wenger, et al., 2007). Instead, dermal elastin fibrils contribute to the mechanical response only at low loads and during tissue recoil.

The stress-strain curve depicted in Figure 1.4 is the output of a typical uniaxial tensile test. This test however is not sufficient alone to

determine multi-dimensional material models. Ideally, testing of dermis should involve planar biaxial tests with an in-plane shear, and separate through-thickness shear tests (Nì Annaidh, et al., 2012a).

### 1.3.5 Langer's lines

Langer's lines, sometimes called cleavage lines, are topological lines drawn on a map of the human body which correspond to the natural orientation of collagen fibres in the dermis (Physiology, 2015). These lines were first described in 1861 by Karl Langer, who punctured numerous holes at short distances into the skin of a cadaver with a circular-shaped tip noticing that the resultant holes in the skin had ellipsoidal shapes (Langer, 1978). Skin mechanical behaviour analysed through tensile tests suggested in the following years that the skin deformation response is dependent upon specimen orientation with respect to the Langer's Lines.

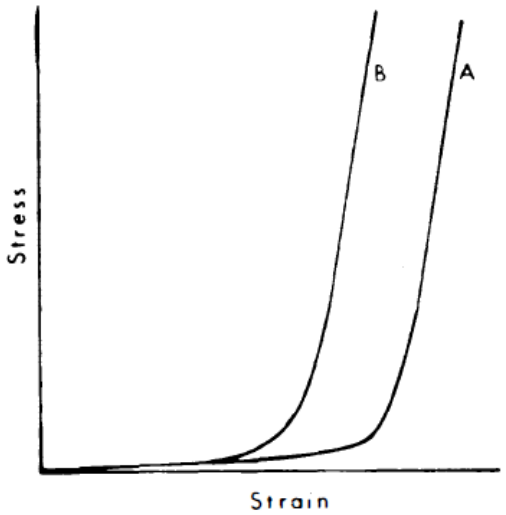


*Figure 1.5 Effect of specimen orientation. A=specimen taken parallel to cranio-caudal axis; B=specimen taken perpendicular to the cranio-caudal axis (Daly, 1982).*

In 1966 Ridge & Wright performed tensile tests on cadavers to investigate the directional properties of skin (Ridge & Wright, 1966). They stated that, on extension, the specimen taken along Langer's lines ex-

tended only a small amount before all fibres become orientated and parallel to each other, while the specimen taken across Langer's lines extended considerably before the fibres become oriented. A couple of decades later, Daly presented the characteristic stress-strain curves for the abdomen skin describing the effects of specimen orientation (Figure 1.5). He confirmed the lower deformation of specimens taken perpendicular to the cranio-caudal direction, which in the abdomen region corresponds to the Langer's line direction (Langer, 1978).

The anisotropic mechanical properties of skin in vitro was recently thoroughly analyzed by Nì Annaidh, who investigated the influence of location and orientation on the deformation characteristic of excised human skin. He found a significant effect of the orientation of the Langer's lines on the ultimate tensile stress (UTS) and the elastic modulus of skin subjected to uniaxial tensile test. In particular, the UTS and the elastic modulus were found to be higher in specimens taken parallel to the Langer's lines (Nì Annaidh, et al., 2012a).

## 1.4 Purpose

The work presented in this dissertation shows the efforts to explore the mechanical properties of ex vivo human dermis in vitro and in silico developing protocols for easy-to-implement but effective uniaxial and biaxial experimental tests. Uniaxial methods are exploited for the engineering of an acellular dermal allograft, identifying decellularization parameters including the effects due to medium type and treatment duration. This tests are performed on native and treated human dermis, decellularized for 1 to 7 weeks with two different decellularization mediums. The obtained allograft is then characterized using both experimental and computational method to investigate the mechanical response of the ADM to diverse stimuli mimicking the in vivo deformation state.

This study represents an advancement of biomaterial science in the field of mechanical characterization of soft materials with specific applications towards medical science.

## 1.5 References


Alexander, H. & Cook, T., 1977. Accounting for natural tension in the mechanical testing of human skin. *The Journal Of Investigative Dermatology,* 69(3), pp. 310-314.

Ambrosio, L., Netti, P. & Nicolais, L., 2002. Soft Tissue. In: *Integrated Biomaterials Science.* New York: Springer US, pp. 347-365.

Barber, F., Herbert, M. & Boothby, . M., 2008. Ultimate tensile failure loads of a human dermal allograft rotator cuff augmentation. *Arthroscopy: The Journal of Arthroscopic and Related Surgery,* 24(1), pp. 20-24.

Barber, F., Herbert, M. & Coons, D., 2006. Tendon Augmentation Grafts: Biomechanical Failure Loads and Failure Patterns. *Arthroscopy: The Journal of Arthroscopic and Related Surgery,* 22(5), pp. 534-8.

Breuing, K. & Warren, S., 2005. Immediate bilateral breast reconstruction with implants and inferolateral AlloDerm slings. *Annals of Plastic Surgery,* 55(3), pp. 232-239.

Burkhead , W., Schiffern, S. & Krishnan, S., 2007. Use of Graft Jacket as an Augmentation for Massive Rotator Cuff Tears. *Seminars in Arthroplasty,* 18(1), pp. 11-18.

Carlsson, A.H., Gronet, E.M., Rose, L.F. & Chan, R., 2016. Clinical Applications of Acellular Dermal Matrices in Reconstructive Surgery. In: *Skin Tissue Engineering and Regenerative Medicine.* s.l.:Elsevier.

Crapo, P., Gilbert, T. & Badylak, S., 2011. An overview of tissue and whole organ decellularization processes. *Biomaterials,* 32(12), pp. 3233-43.

Daly, C., 1982. Biomechanical Properties of Dermis. *The Journal of Investigative Dermatology,* 79(S1), pp. 17-20.

Duncan, D., 2001. Correction of implant rippling using allograft dermis. *Aesthetic Surgery Journal,* 21(1), pp. 81-84.

Fung, Y.-C., 1993. *Biomechanics: Mechanical properties of living tissues.* New York: Springer-Verlag.

Garvey, P. et al., 2014. Outcomes of Abdominal Wall Reconstruction with Acellular Dermal Matrix Are Not Affected by Wound Contamination. *Journal of the American College of Surgeons,* 219(5), pp. 853-864.

Gilbert, T., Sellaro, T. & Badylak, S., 2006. Decellularization of tissues and organs. *Biomaterials,* Volume 27, pp. 3675-3683.

Harding, K. et al., 2010. *Acellular matrices for the treatment of wounds. An expert working group review.* London: Wounds International.

Holzapfel, G., 2001. Biomechanics of soft tissue. In: *The Handbook of Materials Behavior Models.* Boston: J. Lemaitre.

Jacquet, E., Josse , G., Khatyr, F. & Garcin, C., 2008. A new experimental method for measuring skin's natural tension. *Skin Research and Technology,* 14(1), pp. 1-7.

Langer, K., 1978. On the anatomy and physiology of the skin. I. The cleavability of the cutis. *British Journal of Plastic Surgery,* 31(1), pp. 3-8.

Lee, D., 2007. Achilles Tendon Repair with Acellular Tissue Graft Augmentation in Neglected Ruptures. *The Journal of Foot and Ankle Surgery,* 46(6), pp. 451-455.

Liu, Z. & Yeung, K., 2008. The Preconditioning and Stress Relaxation of Skin Tissue. *Journal of Biomedical & Pharmaceutical Engineering,* 2(1), pp. 22-28.

Mackie, D. P., 2002. Postal survey on the use of glycerol-preserved allografts in clinical practice. *Burns,* 28(1), pp. 40-44.

Moore, M. et al., 2015. Decellularization of human dermis using non-denaturing anionic detergent and endonuclease: a review. *Cell and Tissue Banking,* 16(2), pp. 249-259.

Nì Annaidh, A. et al., 2012. Characterization of the anisotropic mechanical properties of excised human skin. *Journal of the Mechanical Behavior of Biomedical Materials,* Volume 5, pp. 138-48.

Parkinson, J., Brass, A., Canova, G. & Brechet, Y., 1997. The mechanical properties of simulated collagen fibrils. *Journal of Biomechanics,* June, 30(6), pp. 549-554.

Physiology, B. A. a., 2015. *Lines of Cleavage and Surgery.* [Online] Available at: https://www.boundless.com/physiology/textbooks/-boundless-anatomy-and-physiology-textbook/the-integumentary-system-5/skin-diseases-disorders-injury-and-clinical-cases-69/lines-of-cleavage-and-surgery-424-184/ [Accessed 20 March 2016].

Ridge, M. & Wright, V., 1966. The directional effects of skin. *The Journal of Investigative Dermatology,* 46(4), pp. 341-346.

Sanders, J. & Goldstein, B., 2001. Collagen fibril diameters increase and fibril densities decrease in skin subjected to repetitive compressive and shear stresses. *Journal of Biomechanics,* December, 34(12), pp. 1581-1587.

Shi, L., Wang, J., Yang, C. & Jiang, W., 2012. Application of Acellular Dermal Matrix in Reconstruction of Oral Mucosal Defects in 36 Cases. *Journal of Oral and Maxillofacial Surgery,* 70(11), pp. 586-91.

Shimizu, H., 2007. *Shimizu's textbook of dermatology.* Hokkaido: Hokkaido University Press/Nakayama Shoten.

Snyder, S. & Bond, J., 2007. Technique for Arthroscopic Replacement of Severely Damaged Rotator Cuff Using "GraftJacket" Allograft. *Operative Techniques in Sports Medicine,* 15(2), pp. 86-94.

Wenger, M. P., Bozec, L., Horton, M. & Mesquida, P., 2007. Mechanical Properties of Collagen Fibrils. *Biophysical Journal,* 93(4), pp. 1255-1263.

Wong, I., Burns, J. & Snyder, . S., 2010. Arthroscopic GraftJacket repair of rotator cuff tears. *Journal of Shoulder and Elbow Surgery,* 19(2S), pp. 104-9.

# Chapter 2

# Optimization of decellularization parameters through the ex-vivo mechanical characterization of the dermis

## 2.1 Preface

A version of this study was published in the peer-reviewed journal "Medical Engineering and Physics" (available online 17 March 2016) under the title, "Dermis mechanical behaviour after different cell removal treatments" by Terzini M., Bignardi C., Castagnoli C., Cambieri I., Zanetti E.M., Audenino A.L.

## 2.2 Introduction

Engineered skin substitutes have a significant medical practice for patients with extensive burn wounds (Sanders, et al., 2014). Advances in tissue engineering suggest that skin substitutes will be indistinguishable from the normal skin in the near future (Sun, et al., 2014). However, current skin substitutes do not restore the full native skin physiology because they lack some components such as hair follicles, sebaceous glands and sweat glands (Sun, et al., 2014). Additionally, the engineered

tissue cannot faithfully replicate the mechanical properties of the native skin (Sanders, et al., 2014).

Currently, alloplastic material and skin allografts, taken from multi-organ donors, are the most suitable integumentary replacement for reconstructive surgery (Wong & Chang, 2009). The immune response to allograft skin is directed primarily against epidermal, endothelial and fibroblast cells in the dermis, while the non-cellular component of the dermis (extracellular matrix) has been demonstrated to be relatively non-immunogenic (Badylak, et al., 2015). Glycerolised acellular alloplastic human dermis (HADM) is used as a matrix for various reconstructive plastic purposes, where it retains almost all of the healthy dermal properties: it is compact and elastic, can be taken into the bed wound, and it retains the intact tissue morphology (Deeken, et al., 2012).

Different treatments can be used for tissue decellularization (Crapo, et al., 2011). Commonly, a low concentration of NaOH has been used for this aim. The result of this technique is a reliably decellularized matrix. However, surgeons report that this matrix is inferior with reference to handling, ease of use, elasticity and needle penetration resistance. Additionally, decellularization using sodium hydroxide implies the direct contact of the tissue with an aggressive chemical agent, which must necessarily be neutralized by means of incubation in 0.1 N HCl at the end of the decellularization phase. These are the reasons why, in recent times, our research unit has developed an alternative procedure that aims to overcome these limitations. The new methodology consists of keeping the tissue in DMEM (Dulbecco's modified Eagle medium) for a long period of time (several weeks) while being subjected to mechanical action (tilting). From a biological point of view, the efficiency of the different treatments can be verified by means of an immunohistochemistry analysis, but the preservation of the main mechanical properties of the native dermis also needs to be checked (Butler, et al., 2000).

The aim of this work is to evaluate the mechanical properties of tissue subjected to decellularization treatments varying by type and length to establish the best compromise between a reliably complete decellularization and adequate mechanical properties.

The mechanical properties here analysed are the elastic modulus and the ultimate load and strain (Nì Annaidh, et al., 2012a), considering that repaired full-thickness burn wounds may be subject to loss due to dermal substitute deficiencies in tensile strength and elasticity (Sanders, et al., 2014) and the requirements of soft-tissue augmentation procedures like rotator cuff (Moore, et al., 2015)

The dermis provides a major contribution to the overall mechanical characteristics of the skin due to its main constituents, collagen and elastin fibrils, which allow high levels of deformation and flexibility as the fibrils stretch and re-orientate (Sanders, 1973). Collagen fibres are crimped and almost inactive at low strains, while they play a major role at high deformations (where they are stiffer than elastin by approximately three orders of magnitude (Nì Annaidh, et al., 2012a)). The skin is anisotropic due to the variable orientation of collagen fibres, with a prevalence along the orientation of the so-called Langer' s lines (Nì Annaidh, et al., 2012a). The dermis can therefore be described as an anisotropic, viscoelastic, nonlinear (Fung, 1993) and non-homogenous material.

The tensile test is the most widely used mechanical test performed on *ex vivo* skin specimens. Using this method, the anisotropic, non-linear and viscoelastic behaviours of skin have been explored, as well as its failure properties (Pereira, et al., 1997), creep (Del Prete, et al., 2004), fatigue (Muñoz, et al., 2008) and preconditioning behavior (Liu & Yeung, 2006). This test is here being used to assess changes in the biomechanical behavior produced by alterations of the dermis structure, similarly to the approach followed by those authors who studied variations in the collagen content (Del Prete, et al., 2004) or elastin and proteoglycans contents (Eshel & Lanir, 2001).

Due to section narrowing taking place during the specimen loading, different formulations of stress in mechanical tests can produce different results: these are the so called 'nominal' or 'engineering values'; their respective 'true' values can be obtained from engineering values under specific assumptions such as volume constancy (Jacquemoud, et al.,

2007; Khanafer, et al., 2013). As true values provide the most faithful representation of the material properties, their estimation requires a complex and demanding experimental set up. This work is also an attempt to quantify differences among these expressions and their limits, establishing if they can or cannot be used for tissue characterization and/or to make comparisons among decellularization treatments.

## 2.3 Materials and Methods

### 2.3.1 Specimens

Strips of dermis tissue, collected from the backs of human donors, were dissected along the cranio-caudal direction. They were decellularized using two different methods based on incubation in 0.06 N NaOH or DMEM for 1 to 7 weeks (Ferrando, et al., 2016). Immunohistochemistry has been performed for all treatments to verify the decellularization, according to the following procedure. Biopsy samples were washed in physiological solution, fixed in 4% neutral-buffered formalin and embedded in formalin by routine processing (FFPE). FFPE samples were sectioned at a thickness of 2-3 μm for immunohistochemistry reactions, and immunohistochemistry was performed using an automated slide-processing platform (Ventana BenchMarckXT Autostainer, Ventana Medical Systems, Tucson, AZ, USA). HADMs, preserved at 85% glycerol in a 4°C refrigerator were used for these experiments. Before use, the dermis grafts were washed to remove all of the glycerol, dipping them sequentially in three different beakers filled with abundant saline solution 0.9% at +37°C for more than three minutes each, as prescribed by the Euro Skin Bank (Euro Tissue Bank, 2011). The specimens were obtained by cutting out approximately 2x4-mm strips along the cranio-caudal (CC) and medio-lateral (ML) directions using a custom made die cutter; this cutting method avoids generating notches and defects that could bias tests. The resulting specimen sizes were measured by means of photogrammetry before mechanical testing: 4.33±0.57-mm width, 2.21±0.32-mm thickness, 10.10±0.38-mm length (average ± std). On the whole,

there were 3–4 specimens (depending on the original strip size and shape) for each combination of decellularization method (NaOH or DMEM), duration (called 'Tx' in the following, where x represents the number of weeks of incubation) and cut orientation (CC or ML), for a total 96 specimens. Intact human dermis was used as a control (called 'T0' in the following, as it did not undergo any decellularization treatment).

### 2.3.2 Photogrammetry set-up

Two different photographic set-ups have been developed to measure the specimens. The first was finalized to measure the specimens size at rest and was made of a full-frame digital camera (Canon EOS 5D Mark II) with an autofocus lens for macro photography (Canon EF 100 mm f/2.8 Macro USM), a camera stand with two light stands, and a tripod. A second set-up was developed to follow tensile tests; it included the previously described digital camera as well as a second digital single-lens reflex camera (Canon EOS 400D). When the two cameras were triggered, they acquired the frontal and lateral views of the specimen through a remote capture software (DSLR Remote Pro). The width and the thickness of the specimens were measured using the image analysis software ImageJ (National Institutes of Health, Bethesda, Maryland, U.S.) as an average of five different measurements, reaching a 0.01 mm/pixel measurement resolution given a 21.0 MP image (5616x3744 pixels).

### 2.3.3 Mechanical tests

Samples were subjected to uniaxial tensile tests along both the cranio-caudal and medio-lateral directions to quantify the influence of the chemical treatment on the dermis tissue's biomechanical behaviour. Testing parameters have been set according to the physiological loads, the expected tissue behaviour, and the Bose Electroforce® features. For example, the strain rate could reach very high values in reality due to impact forces, but the characteristics of the material are strain rate dependent (Arumugam, et al., 1994), and the test speed had to be limited

to 3.2%/s so as not to exceed the load cell range and risking rupture. The specimen length also had to be chosen considering the physiologic peak strain (over 100%) and the machine stroke (±6 mm), together with the limited sample extension; these considerations led to the selection of a 10 mm specimen length. The specimens were clamped by titanium machine grips that were specifically developed for biomaterials and have knurled-flat faces to prevent slipping. The analysis of the video recordings demonstrates that there were neither anomalous behaviours nor failures near the clamps. Sliding through the testing grips was excluded, too, as no abrupt increase or decrease was detected in the experimental curves. No marks were observed on the specimen ends, and the extension of the grasped ends was found to be unchanged. Up to the instant preceding the tensile test, all specimens were kept hydrated in physiological solution; no additional hydration was carried out during the test due to the absence of a thermostatic bath. This was not judged to be a major shortcoming because the tests lasted less than one minute. Specimens were constrained to the Bose Electroforce® testing machine, clamping their ends along the longitudinal direction.

No preconditioning cycles were performed because the dermal tissue is a bi-phasic structure, like most soft tissues, and preconditioning has been demonstrated to significantly influence the mechanical response of these tissues. Slow viscoelastic phenomena related to fluid flow initiate starting from the very first loading cycles, so the final mechanical properties would depend on the pre-conditioning protocol (Hosseini, et al., 2014).

The testing room temperature was 20°C, while the humidity ranged between 40 and 65%. The displacement was set equal to zero when a 0.05N force was recorded.

Rupture tensile tests were performed for all samples in displacement control at a strain rate of 0.032 $s^{-1}$. The initial gap between the grips was 5 mm.

### 2.3.4 Data Elaboration

The results of rupture tests on soft tissues are often reported in terms of 'engineering' stress and strain in the literature, with a few exceptions where the specimen section is monitored during tests, and the strain distribution is assessed by full-field techniques (Jacquemoud, et al., 2007; Bel-Brunon, et al., 2014). In this work, the engineering and true values have been calculated, as detailed in the following.

The 'engineering curve' is obtained by ignoring the narrowing of the section during the elongation of the sample and referring always to the initial specimen length. The engineering stress $\sigma_e$ is therefore calculated by dividing the force F by the unloaded-cross sectional area $A_0$ of the specimen; the engineering strain $\varepsilon_e$ is expressed as the change in length $\Delta L$ per unit of the original length $L_0$. It should be emphasised that the measurement of the engineering strain would require a dog-bone shaped specimen and a calibrated length whose elongation is monitored, while a rectangular specimen has been here used and its elongation has been evaluated on the basis of the clamp-to-clamp displacement; this was not considered a hard limitation due to the high compliance of the tissue, which 'homogenises' the stress field (see, for example, the work of Taylor et al. on crack propagation (Taylor, et al., 2012)). The engineering elastic modulus ($E_e$) has been calculated from the linear portion of the stress-strain curve (Nì Annaidh, et al., 2012a), which is the so-called 'linear region' where collagen chains are stretched (Fung, 1993; Özkaya, et al., 2012): curve data were locally derived with a moving average linear regression, and the constant trend of the derived curve was considered.

The true stress $\sigma_t$ is the ratio between the force and the minimum section $A_{min}$; it is approximately coincident with the engineering curve, up to the strain where section narrowing becomes conspicuous. The true curve can be obtained by monitoring the neck area during the tensile test: the history of the section variation $A_{min}(t)$ needs to be acquired, monitoring both the specimen width $b_{min}(t)$ and thickness $s_{min}(t)$ at the neck region. In the literature, an alternative expression for the true stress

is often used, which relies on the hypothesis of a null variation of the specimen volume (Silver, et al., 2001): this expression is simpler to be implemented because it requires only the estimation of the real-time specimen length (like for the engineering curve). The respective value $\sigma_{st}$ will be called the 'simplified true' stress, and it can be obtained from the engineering curve by analytical transformations ($\sigma_{st} = \sigma_e(1 + \varepsilon_e)$). The corresponding 'simplified true' elastic modulus $E_{st}$ can be calculated on $\sigma_{st}/\varepsilon_e$ curves.

The evaluation of the true elastic modulus $E_t$ has been performed on the basis of the acquired force and displacement signals and of the specimen shape; given a certain force $F$, the specimen volume can be divided axially into infinitesimal portions $dy$ whose section is $A(y,F)$. Therefore, the whole specimen elongation $\Delta s_{ab}$ in the linear portion of the force/displacement curve (A, B, Figure 2.1) can be expressed as

$$\Delta s_{ab} = \int_{F_a}^{F_b} \int_0^l ds = \int_{F_a}^{F_b} \int_0^l \varepsilon_t \cdot dy = \int_{F_a}^{F_b} \left[ \int_0^l \frac{1}{E_t \cdot A(y,F)} dy \right] dF$$
$$= \frac{1}{E_t} \int_{F_a}^{F_b} \left[ \int_0^l \frac{dy}{A(y,F)} \right] dF$$

*Equation 2.1*

where the elastic modulus has been considered to be linear (independent of the force level) and constant all over the specimen, as it should be in the above-mentioned 'linear elastic region'. This formula could not be used up to the failure region (to obtain the true ultimate strain, for example). The 'true' Young's modulus can be so derived:

$$E_t = \frac{\int_{F_a}^{F_b} \left[ \int_0^l \frac{dy}{A(y,F)} \right] dF}{\Delta s_{ab}}$$

*Equation 2.2*

The numerator requires the knowledge of the section variation for each force step, and at different quotes ($y$), and it can be estimated thanks to the photogrammetry set up.

A number of descriptive parameters can be so obtained: the ultimate tensile strength (UTS, $UTS_t$, $UTS_{st}$), the ultimate deformation ($\varepsilon_{UTS,e}$), and the elastic modulus ($E_e$, $E_{st}$, $E_t$). True values have been calculated only for those decellularization treatments that produced 'engineering' and 'simplified true' mechanical properties similar to those of the native dermis ($p<0.05$, Tukey-Kramer test, as detailed in the following).

### 2.3.5 Statistical analysis

The mechanical properties of the dermis were reported in relation to the testing direction (CC or ML), the type of decellularization treatment (called NaOH or DMEM in the following), and the duration of the treatments (from 0 to 7 weeks at 1 week steps, called T0, T1 …. T7 in the following). The statistical analysis of the experimental results was carried out using a multivariate analysis of variance (Matlab function 'anovan'), followed by a Tukey–Kramer post hoc test, after having tested the normality of the statistical distribution of all parameters by the Lilliefors test function. Significance levels were set to $p < 0.05$ for all tests.

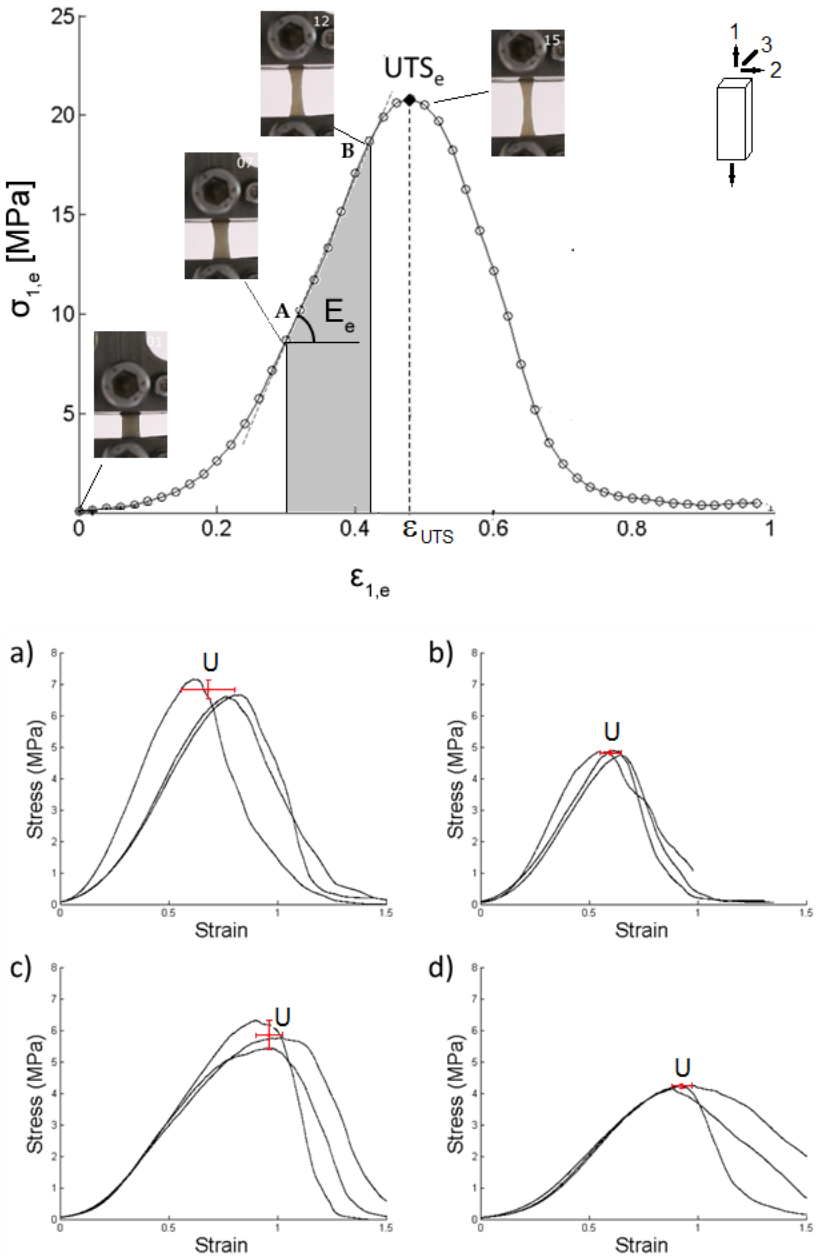


*Figure 2.1 (Up) An interpolated engineering stress-strain curve, its descriptive parameters, and specimen images. (Down) Experimental stress strain curves, where point 'U' represents the average ultimate strain/stress point with its standard deviations; a) DMEM, T6, ML direction; b) DMEM, T6, CC direction; c) NaOH, T6, ML direction; d) NaOH, T6, CC direction.*

## 2.4 Results

The analysis of video recordings demonstrated that there were neither anomalous behaviours nor failures near clamps; therefore, all acquired data have been elaborated.

Figure 2.2 shows typical stress/strain curves for the engineering, simplified true and true formulations. Dealing with the ultimate stress (Figure 2.3-2.4), the engineering stress leads to underestimate the UTS by up to -71% and the elastic modulus by up to -84%. The simplified true stress would underestimate the UTS by up to -44%.

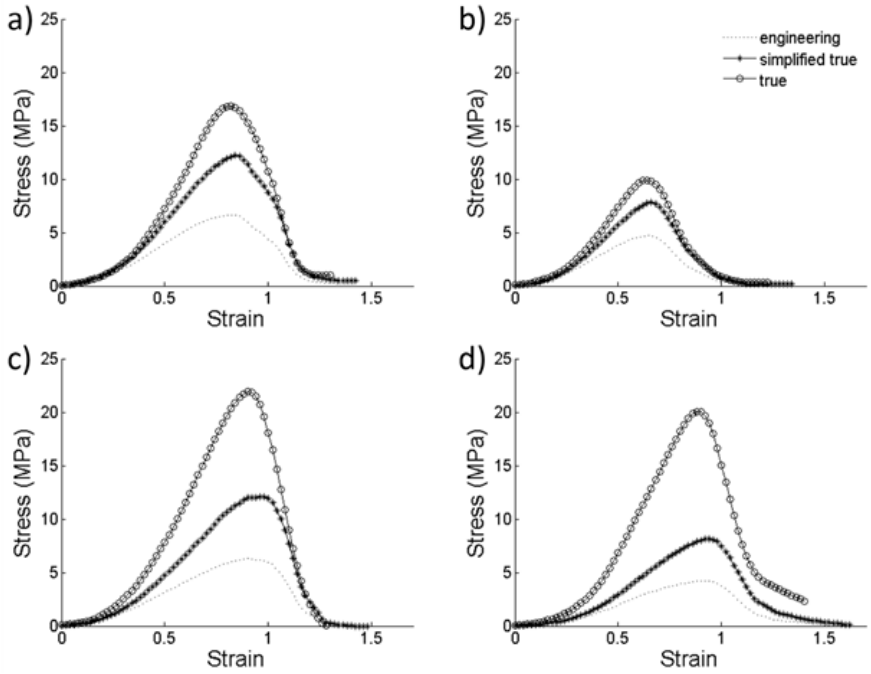


*Figure 2.2 Engineering, simplified true, and true formulation curves; a) DMEM, T6, ML direction; b) DMEM, T6, CC direction; c) NaOH, T6, ML direction; d) NaOH, T6, CC direction.*

The error coming from the simplified true stress evaluation demonstrates how the hypothesis that the section variation is inversely proportional to the longitudinal strain (equivalent to the 'constant volume' hypothesis for small deformations) does not hold: this is not surprising

because in the literature, both analytical and experimental demonstrations of the soft tissue volume variation during tensile tests can be found (Adeeb, et al., 2004; Reese, et al., 2010).

All sample properties are shown to be normally distributed, according to the Lilliefors test ($p<0.05$), so the following variance analysis could be performed.

The results of the analysis of variance are shown in Table 2.1: the type of treatment, its duration, and the specimen orientation are all significant factors, as is their interaction ($p<0.05$), with the only exception of the specimen orientation for the ultimate strain. The T0 mechanical behaviour along the CC direction is significantly stiffer compared to that in the ML direction, and the mechanical strength is higher (+77.1% $E_e$, +46.6% $UTS_e$, -16.1% $\varepsilon_{UTS,e}$, Figure 2.3-2.4). DMEM treatment is generally less aggressive than NaOH treatment (Figure 2.3-2.4), and the mechanical properties do not vary monotonously over the treatment length (Figure 2.3-2.4).

A more detailed statistical analysis has been undertaken to establish which factor levels produced significantly different results compared to reference groups (respectively, T0-CC and T0-ML) by means of Tukey-Kramer tests, aiming to identify the best treatment type and duration as the combination producing the results most similar to those of native tissue. Looking at Figure 2.3-2.5 only minor differences exist between the 'engineering' and 'simplified true' formulation results, and some general conclusions could be drawn. The tissue properties along the CC direction significantly degrade (lower UTS and E) for all treatments and durations, with $\varepsilon_{UTS,e}$ being the only mechanical property that is not affected significantly.

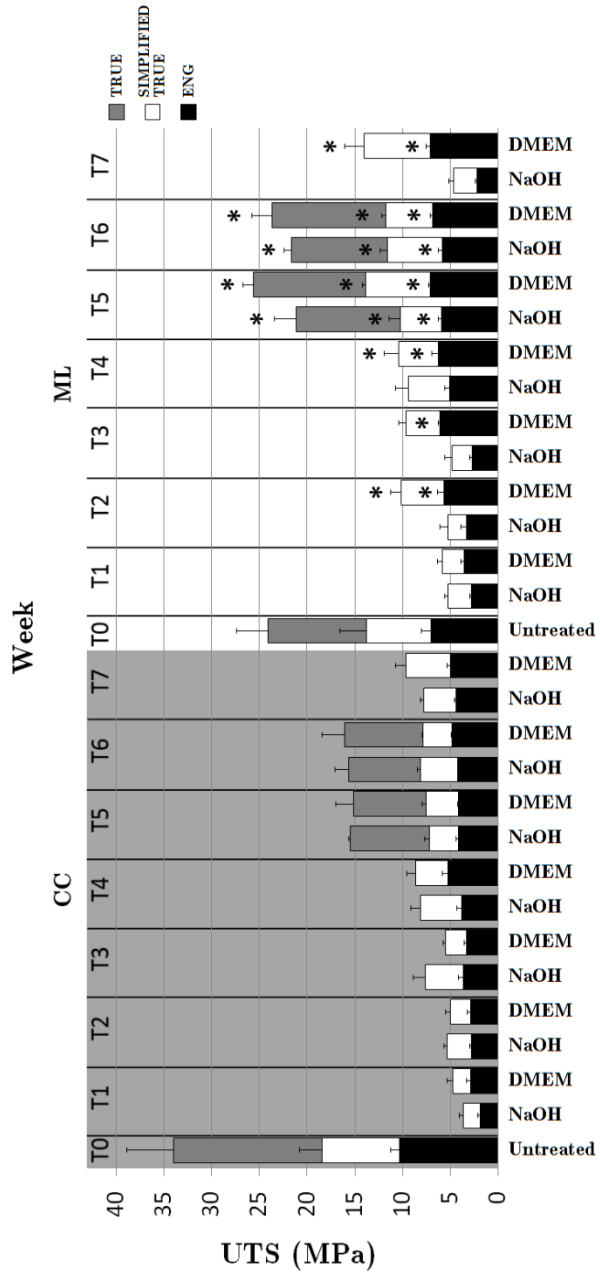


*Figure 2.3 UTS values obtained from engineering, simplified true, and true formulations for different decellularization treatments. Left side (grey background): results obtained along CC direction; right side (white background): results obtained along ML direction*

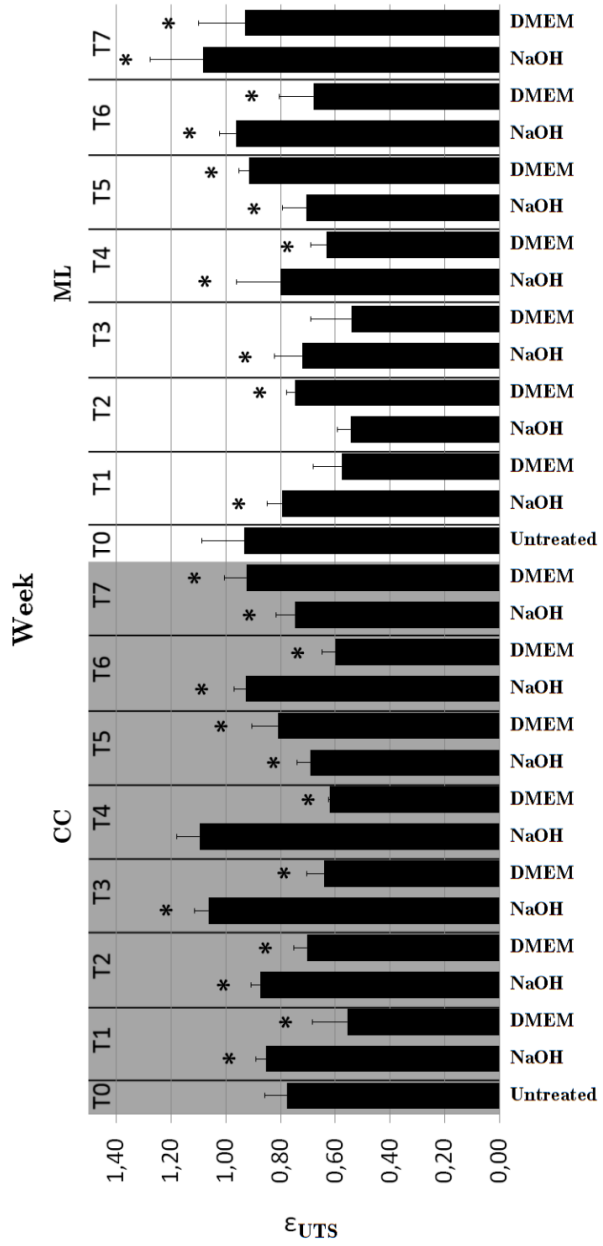


*Figure 2.4 Engineering strain corresponding to the ultimate stress for different decellularization treatments. Left side (grey background): results obtained along CC direction; right side (white background): results obtained along ML direction*

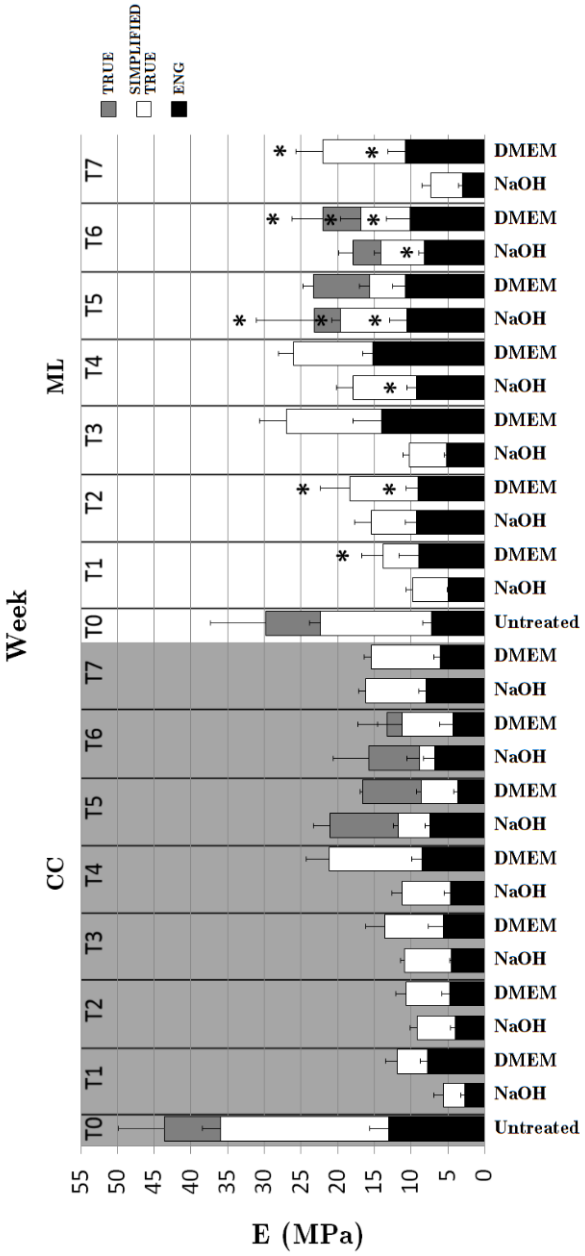


*Figure 2.5 Elastic modulus values for different decellularization treatments. Left side (grey background): results obtained along CC direction; right side (white background): results obtained along ML direction*

*Table 2.1 Anova results for the ultimate stress, ultimate strain and elastic modulus with reference to the engineering formulation. Boldface characters are used to highlight factors that are not significant ($p > 0.05$).*

| **Ultimate Stress** | | | | | |
|---|---|---|---|---|---|
| *Source* | *Sum Sq.* | *DOF* | *Mean Sq.* | *F* | *p* |
| Treatment | 30.90 | 1 | 30.90 | 128.22 | 6.28E-17 |
| Orientation | 11.00 | 1 | 11.00 | 45.67 | 4.94E-09 |
| Duration | 257.24 | 7 | 36.75 | 152.50 | 2.08E-37 |
| Treatment*Orientation | 12.04 | 1 | 12.04 | 49.97 | 1.41E-09 |
| Treatment*Duration | 13.57 | 7 | 1.94 | 8.05 | 5.45E-07 |
| Orientation*Duration | 64.42 | 7 | 9.20 | 38.19 | 1.67E-20 |
| Error | 15.42 | 64 | 0.24 | | |
| Total | 421.99 | 95 | | | |

| **Ultimate Strain** | | | | | |
|---|---|---|---|---|---|
| *Source* | *Sum Sq.* | *DOF* | *Mean Sq.* | *F* | *p* |
| Treatment | 0.37 | 1 | 0.37 | 40.22 | 2.61E-08 |
| Orientation | 0.00 | 1 | 0.00 | 0.27 | **6.05E-01** |
| Duration | 0.45 | 7 | 0.07 | 7.00 | 3.42E-06 |
| Treatment*Orientation | 0.06 | 1 | 0.06 | 6.73 | 1.17E-02 |
| Treatment*Duration | 0.76 | 7 | 0.11 | 11.80 | 1.52E-09 |
| Orientation*Duration | 0.44 | 7 | 0.06 | 6.86 | 4.40E-06 |
| Error | 0.59 | 64 | 0.01 | | |
| Total | 2.94 | 95 | | | |

| **Elastic Modulus** | | | | | |
|---|---|---|---|---|---|
| *Source* | *Sum Sq.* | *DOF* | *Mean Sq.* | *F* | *p* |
| Treatment | 318.03 | 1 | 318.03 | 108.72 | 1.98E-15 |
| Orientation | 98.80 | 1 | 98.80 | 33.77 | 2.13E-07 |
| Duration | 748.22 | 7 | 106.89 | 36.54 | 5.10E-20 |
| Treatment*Orientation | 44.72 | 1 | 44.72 | 15.29 | 2.25E-04 |
| Treatment*Duration | 295.62 | 7 | 42.23 | 14.44 | 4.16E-11 |
| Orientation*Duration | 578.59 | 7 | 82.66 | 28.26 | 2.67E-17 |
| Error | 187.22 | 64 | 2.93 | | |
| Total | 2386.48 | 95 | | | |

In the ML direction, T0, DMEM T5, DMEM T6, DMEM T7, and NaOH T5 produce similar mechanical properties, according to both the engineering and simplified true formulations. These same treatments have been further investigated to assess if the true stress formulation would lead to the same conclusions. DMEM T5, DMEM T5, NaOH T5, and, partly NaOH T6 (assuming p=0.03) still produced mechanical properties close to those of native tissue for samples cut along the ML direction. Native specimens cut along the CC direction continued to show a higher elastic modulus $E_t$ and $UTS_t$; no treatment for any duration could preserve these properties.

## 2.5 Discussion

The native skin from which the HADM scaffold is prepared must be mechanically or physically separated from unwanted tissue and cell structures, and this processing step could alter the integrity and the architecture of the matrix and, in turn, influence the mechanical and material properties of the matrix. The efficiency of cell removal from a tissue is dependent on the origin of the tissue and the specific physical, chemical, and enzymatic methods that are used (Chen, et al., 2004). A similar consideration holds for the mechanical properties of the scaffold, as demonstrated in this work.

Experimental tests were performed at 20°C, so the measured properties cannot be immediately converted to physiological properties at 37°C. The reason for this choice is the simplification of the experimental set up and being able to compare these results with most works in the literature in which mechanical tests have been carried out at 'room temperature' (Nì Annaidh, et al., 2012a; Sanders, 1973; Muñoz, et al., 2008; Jacquemoud, et al., 2007; Khanafer, et al., 2013; Li, et al., 2013; Nì Annaidh, et al., 2012b). The results of the experimental tests were compared, assuming a perfectly uniaxial loading condition and a uniform distribution of collagen fibres. This is a limit in the present experimental set up, as the specimen is rectangular and its contraction is not allowed at the machine clamps, so the uniaxial stress hypothesis is not verified

at the specimen ends. Using dog-bone shaped specimens would not completely solve this issue: in the case of longitudinal samples with most collagen fibres oriented axially, it would make no difference because the interrupted fibres (those placed more laterally) would be inactive. Longer specimens would have minimised the influence of the clamped ends, but they would have limited the maximum strain because the employed loading machine allows 12 mm displacement at the most. Finally, it should be stressed that the notch sensitivity in soft tissues is very low (Taylor, et al., 2012), so a minor area on the specimen is likely to be affected by the clamps. Numerical tests confirmed these hypotheses (nonlinear analysis, with large displacements, see Chapter 5), but the full strain field should be experimentally acquired as a final validation. This is a quite demanding experimental set-up. Some authors are setting up systems based on digital image correlation (Bel-Brunon, et al., 2014); this is certainly a promising technique that deserves to be considered in future tests on biological tissues.

Results have been here expressed through engineering, simplified true and true curves because the results of rupture tests for soft tissues have not always been reported in a standard manner in the literature (Khanafer, et al., 2013). Dealing with comparisons among different treatment types and durations and sample directions, all three representations produced substantially similar results.

A review of decellularization methods (Crapo, et al., 2011) agrees with the results here obtained regarding the NaOH cell removal treatment. In fact, it stated that bases are harsh, so are commonly used to eliminate growth factors from the matrix, even though they decrease ECM mechanical properties more significantly than chemical and enzymatic agents. In this work, the NaOH treatment has been proven to weaken the mechanical properties of the tissue, especially with reference to the cranio-caudal direction. The primary mechanism by which bases such as sodium hydroxide reduce the mechanical properties is the cleavage of collagen fibrils and disruption of collagen crosslinks. Richters *et al.* (Richters, et al., 2008) evaluated a cost-effective method based on low concentrations of NaOH for the decellularization of human donor

skin preserved in 85% glycerol, and they found that a 6 week incubation period was optimal, as stated in the present work, while longer periods caused damage to the collagen fibres, although the elastin fibres appeared to be well preserved, and this could explain the different behaviours observed along the cranio-caudal and medio-lateral directions.

DMEM coupled to mechanical action has been used as a cell removal treatment for the first time in this work, so similar tests cannot be found in the literature. Other decellularization methods include a wide variety of chemicals, but if the chemicals remain within the tissue in high concentrations after treatment, they can potentially invoke an adverse immune response by the host (see, for example, enzymes commonly derived from bovine sources such as DNase, RNase, and trypsin). Herein, one of the most simple decellularization methods was studied (long-term incubation in culture medium), and preliminary immunohistochemical and histological results (Ferrando, et al., 2016) demonstrate the complete decellularization of the tissue. DMEM treatment has also proven to be more conservative with reference to the medio-lateral direction because the mechanical properties of specimens treated with DMEM are generally higher than those measured on specimens treated with NaOH for the same number of weeks.

From a biological point of view, both DMEM and NaOH show, in the immunohistochemical evaluation, a good decellularization of grafts after only 4 weeks of treatment. However, the DMEM-treated samples exhibit better handling, greater flexibility and lower needle penetration resistance, according to surgeons 'evaluations, and are therefore preferable. Additionally, the DMEM treatment avoids the use of chemical agents, as opposed to NaOH, which needs to be neutralized at the end of the decellularization process. Therefore, DMEM is less likely to produce inflammatory responses.

The objective of this work was to set up a procedure to perform biomechanical comparisons among decellularization treatments; the complete quantification of the skin anisotropic behaviour would require a greater number of samples, from different donors, and biaxial testing

(see Chapter 7). This experimental set up can allow only the measurement of the elastic modulus and failure properties along two reference orthogonal directions (parallel and perpendicular to the Langer's lines (Nì Annaidh, et al., 2012a)). Nevertheless, in the following, a comparison with results obtained from other authors (Nì Annaidh, et al., 2012a; Yoder & Elliott, 2010; Edwards & Marks, 1995) is reported to verify the differences that exist and how they can be justified (Table 2.2).

Nì Annaidh *et al.* (Nì Annaidh, et al., 2012a) reported force–displacement curves for each tensile test performed and calculated the engineering stress and strain. Their standard deviations were much larger; the average coefficients of variation (ratios of the standard deviation to the mean) are up to 0.80 for UTS and 0.97 for E, against the values obtained in this work, 0.09 and 0.10, respectively, due to the number of specimens and the specimens having been taken from several donors (Table 2.2). The values calculated in this work are most similar to those obtained on the 'lower back' and are generally lower (up to -43% for UTS, up to -46% for $\varepsilon_{UTS}$, up to -68% for E) compared to those reported in (Nì Annaidh, et al., 2012a). This can be explained by the smaller size of the specimens, which results in more severe striction and consequently lower nominal stresses.

Yoder and Elliott (Yoder & Elliott, 2010) characterized human allografts by considering the engineering stress and calculated two-dimensional Langrangian strains from optical images using Vic2D software. The Young's modulus (Table 2.2) compares favourably to the results here reported for DMEM and NaOH at T5 or T6 for engineering curves with reference to the ML direction. A 20 times higher E along the 'parallel' direction is reported in Yoder & Elliott's work; this result is against the findings of this work and Nì Annaidh (2012), which both report a lower level of anisotropy in tested tissues.

Up to now, the failure properties and the elastic behaviour for static loads has been investigated, as critical aspects of dermal patches include stiffness mismatch (Hopp, et al., 2013) and the eventual failure. Nevertheless, cyclic loading parameters also need to be considered because in

a highly collagenous tissue such as skin, the elastic recoil and hysteresis of the material would be of utmost importance.

*Table 2.2 Mechanical properties of skin in literature and in this work (average±SD).*

| Author | Skin Location (Langer Line Orientation) | UTS (MPa) | Failure Stretch | Elastic Modulus (MPa) | Reference Variables |
|---|---|---|---|---|---|
| (Nì Annaidh, et al., 2012a) | Middle Back (Parallel) | 28.64 ± 9.03 | 1.46 ± 0.07 | 112.47 ± 36 | $\sigma_e$,$\varepsilon_e$ |
| | Bottom Back (Parallel) | 17.60 ± 4.77 | 1.74 ± 0.32 | 73.81 ± 19.41 | |
| | Middle Back (Perpendicular) | 16.53 ± 5.71 | 1.52 ± 0.08 | 63.75 ± 24.59 | |
| | Bottom Back (Perpendicular) | 10.56 ± 8.41 | 1.61 ± 0.14 | 37.66 ± 36.41 | |
| (Edwards & Marks, 1995) | | 5-30 | 35-115% | 15-150 | Various authors |
| (Yoder & Elliott, 2010) | Alloderm (Parallel) | | | 221.48 ± 141.20 | $\sigma_e$, $\varepsilon_{Lagrange}$ |
| | Alloderm (Perpendicular) | | | 11.21 ±3.53 | |
| This work ($T_0$) | Back (cranio-caudal) | 10.28 ± 0.96 | 0.77 ± 0.08 | 13.01 ± 2.61 | $\sigma_e$,$\varepsilon_e$,$E_e$ |
| | | 18.38 ± 2.42 | | | $\sigma_{st}$ |
| | | 33.95 ± 4.93 | | 43.63 ± 6.29 | $\sigma_t$, $E_t$ |
| | Back (medio-lateral) | 7.01 ± 0.10 | 0.93 ± 0.15 | 7.20 ± 1.22 | $\sigma_e$,$\varepsilon_e$,$E_e$ |
| | | 13.81 ± 2.80 | | | $\sigma_{st}$ |
| | | 24.11 ± 3.24 | | 29.77 ± 7.54 | $\sigma_t$, $E_t$ |

According to experimental tests on mice skin (Del Prete, et al., 2004; Muñoz, et al., 2008), the primary loading curve in a cyclic test would closely follow the stress–strain curve for the monotonic test. However the unloading curve slope is likely to be different due both to viscoelastic and inelastic effects: experimental tests have clearly demonstrated the

presence of residual strain when large-displacement cyclic loading and large deformations are performed on mice skin (Del Prete, et al., 2004; Muñoz, et al., 2008), and on human skin undergoing sustained compression (Edsberg, et al., 1999).

## 2.6 Conclusions

This work was focused on the mechanical characterization of a human acellular dermal matrix. The mechanical properties of the decellularized excised human dermis have been quantified and compared to those of native ones in order to develop the most suitable procedure for dermis decellularization. Different types and durations of cell removal treatment have been considered, as well as different cut orientation, due to tissue anisotropy. Hence a systematic analysis heretofore lacking in literature has been carried out.

According to results here reported, the human excised HADM under incubation culture in NaOH and in DMEM respectively for 5-6 weeks and 5-7 weeks, exhibited the mechanical properties most similar to the native tissue ones. However, the DMEM-treated samples exhibit better handling, greater flexibility and lower needle penetration resistance, according to surgeons‘ evaluations, and are therefore preferable.

The comparison among mechanical properties measured from engineering, simplified true or true curves has demonstrated that ultimate tensile strength, deformation and maximum elastic modulus can be heavily underestimated considering engineering and simplified true curves. More realistic values obtained from true curves are therefore recommended when setting up dermis computational models, while engineering and true curves values remain useful for comparative analyses.

## 2.7 References

Adeeb, S. et al., 2004. Modelling the Behaviour of Ligaments: A Technical Note. *Computer Methods in Biomechanics and Biomedical Engineering,* Volume 7, pp. 33-42.

Arumugam, V., Naresh, M. & Sanjeevi, R., 1994. Effect of strain rate on fracture behaviour of skin. *Journal of Biosciences,* Volume 19, pp. 307-13.

Badylak, S., Freytes, D. & Gilbert, T., 2015. Reprint of: Extracellular matrix as a biological scaffold material: Structure and function. *Acta Biomaterialia,* 23(Supplement), pp. S17-S26.

Bel-Brunon, A. et al., 2014. Numerical identification method for the non-linear viscoelastic compressible behaviour of soft tissue using uniaxial tests and image registration - application to rat lung parenchyma. *Journal of the Mechanical Behavior of Biomedical Materials ,* Volume 29, pp. 360-74.

Butler, D., Goldstein, S. & Guilak, F., 2000. Functional tissue engineerign: the role of biomechanics. *Journal of Biomechanical Engineering,* Volume 122, pp. 570-5.

Chen, R., Ho, H., Tsai, Y. & Sheu, M., 2004. Process development of an acellular dermal matrix (ADM) for biomedical applications. *Biomaterials,* 25(13), pp. 2679-86.

Crapo, P., Gilbert, T. & Badylak, S., 2011. An overview of tissue and whole organ decellularization processes. *Biomaterials,* 32(12), pp. 3233-43.

Deeken, C. et al., 2012. Differentiation od biological scaffold materials through physicomechanical, thermal, and enzymatic degradation techniques. *Annals of Surgery,* Volume 255, pp. 595-604.

Del Prete, Z., Antonucci, S., Hoffman, A. & Grigg, P., 2004. Viscoelastic properties of skin in Mov-13 a Tsk mice. *Journal of Biomechanics,* Volume 37, pp. 1491-7.

Edsberg, L., Mates, R., Baier, R. & Mark, L., 1999. Mechanical characteristics of human skin subjected to static versus cyclic normal pressures. *Journal of Rehabilitation Research & Development,* 36(2), pp. 133-41.

Edwards, C. & Marks, R., 1995. Evaluation of biomechanical properties of human skin. *Clinics in Dermatology ,* 13(4), pp. 375-80.

Eshel, H. & Lanir, Y., 2001. Effects of strain level and proteoglycan depletion on preconditioning and viscoelastic response of rat dorsal skin. *Annals of Biomedical Engineering,* Volume 29, pp. 164-72.

Euro Tissue Bank, 2011. *Euro Tissue Bank - Manual.* [Online] Available at: http://www.eurotissuebank.nl/euro-skin-bank-huidbank-esb-en-GB/what-is-donor-skin/manual/ [Accessed 14 October 2015].

Ferrando, P. et al., 2016. Glycerolized Reticular Dermis as a New Human Acellular Dermal Matrix: An Exploratory Study. *PLOS ONE.*

Fung, Y.-C., 1993. *Biomechanics: Mechanical properties of living tissues.* New York: Springer-Verlag.

Hopp, I. et al., 2013. The influence of substrate stiffness gradients on primary human dermal fibroblasts. *Biomaterials,* 34(21), pp. 5070-7.

Hosseini, S., Wilson, W., Ito, K. & van Donkelaar, C., 2014. How preconditioning affects the measurement of poro-viscoelastic mechanical properties in biological tissues. *Biomechanics and Modeling in Mechanobiology,* 13(3), pp. 503-13.

Jacquemoud, C., Bruyere-Garnier, K. & Coret, M., 2007. Methodology to determine failure characteristics of planar soft tissues using a dynamic tensile test. *Journal of Biomechanics,* Volume 40, pp. 468-75.

Khanafer, K., Schlicht, M. & Berguer, R., 2013. How Should We Measure and Report Elasticity in Aortic Tissue? *European Journal of Vascular and Endovascular Surgery,* Volume 45, pp. 332-9.

Li, L. et al., 2013. Power type strain energy function model and prediction of the anisotropic mechanical properties of skin using uniaxial extension data. *Medical & Biological Engineering & Computing,* 51(10), pp. 1147-56.

Liu, Z. & Yeung, K., 2006. *On Preconditioning and Stress Relaxation Behaviour o Fresh Swine Skin in Different Fibre Diraction.* s.l., s.n., pp. 221-6.

Moore, M. et al., 2015. Decellularization of human dermis using non-denaturing anionic detergent and endonuclease: a review. *Cell and Tissue Banking,* 16(2), pp. 249-59.

Muñoz, M. et al., 2008. An experimental study of the mouse skin behaviour: Damage and inelastic aspects. *Journal of Biomechanics,* 41(1), pp. 93-99.

Nì Annaidh, A. et al., 2012b. Automated estimation of collagen fibre dispersion in the dermis and its contribution to the anisotropic behaviour of skin. *Annals of Biomedical Engineering,* 40(8), pp. 1666-78.

Nì Annaidh, A. et al., 2012a. Characterization of the anisotropic mechanical properties of excised human skin. *Journal of the Mechanical Behavior of Biomedical Materials,* Volume 5, pp. 138-48.

Özkaya, N., Nordin, M., Goldsheyder, D. & Leger, D., 2012. *Fundamentals of Biomechanics - Equilibrium, Motion, and Deformation.* New York: Springer-Verlag.

Pereira, B., Lucas, P. & Swee-Hin, T., 1997. Ranking the fracture toughness of thin mammalian soft tissues using the scissors cutting test. *Journal of Biomechanics,* Volume 30, pp. 91-4.

Reese, S., Maas, S. & Weiss, J., 2010. Micromechanical models of helical superstructures in ligament and tendon fibers predict large Poisson's ratios. *Journal of Biomechanics,* Volume 43, pp. 1394-400.

Richters, C. et al., 2008. Development of a dermal matrix from glycerol preserved allogeneic skin. *Cell and Tissue Banking,* 9(4), pp. 309-15.

Sander, E., Lynch, K. & Boyce, S., 2014. Development of the mechanical properties of engineered skin substitutes after grafting to full-thickness wounds. *Journal of Biomechanical Engineering,* 136(5), pp. 051008-051008-7.

Sanders, R., 1973. Torsional elasticity of human skin in vivo. *Pflügers Archiv - European Journal of Physiology,* Volume 342, pp. 255-60.

Silver, F., Freeman, J. & DeVore, D., 2001. Viscoelastic properties of human skin and processed dermis. *Skin Research and Technology,* Volume 7, pp. 18-23.

Sun, K. S., Siprashvili, Z. & Khavari, P. A., 2014. Advances in skin grafting and treatment of cutaneous wounds. *Science,* 346(6212), pp. 941-945.

Taylor, D. et al., 2012. The fracture toughness of soft tissues. *Journal of the Mechanical Behavior of Biomedical Materials,* Volume 6, pp. 139-47.

Wong, D. & Chang, H., 2009. Skin tissue engineering. s.l.:Harvard Stem Cell Institute.

Yoder, J. & Elliott, D., 2010. Nonlinear and anisotropic tensile properties of graft materials used in soft tissue applications. Clinical Biomechanics, 25(4), pp. 378-82.

# Chapter 3

# Effects of the conservation process on dermis mechanical properties

## 3.1 Preface

In the previous chapter, the mechanical properties of the decellularized dermis have been compared with a control tissue, assumed to be similar to the native one. However, the intact human skin called 'T0' used as a reference was not the freshly excised human dermis, but a dermis tissue which did not undergo any decellularization treatment despite having undergone the glycerolization process. This choice has been made taking into account two factors:

- since all the tested samples were preserved at 85% glycerol, also the control ones needed to be preserved in the same conditions, in order to prevent the introduction of any additional variability factor;
- the glycerol preservation method allows for an easier storage and transport.

The aim of the following study is therefore the comparison between freshly excised human dermis and glycerol preserved dermis, focusing on the effects of the conservation process on the mechanical properties of the tissue.

## 3.2 Introduction

Allografts preserved in 85% glycerol were introduced in 1984 by the Dutch National Skin Bank (relaunched as the Euro Skin Bank (ESB) in 1993) and to date the glycerol-preserved allograft (GPA) is in use in several European burn centres. This procedure, starting from the harvest from the donor, consists in a washing in 0.9 per cent saline solution containing penicillin and streptomyiin, followed by stirring in glycerol for two periods of several hours. Due to fluid exchange the final and storage concentration of glycerol in the GPA is 85 per cent. In this medium, the GPA can be stored at 4°C up to 2 years (Hermans, 1989). The glycerol preservation method was developed to make storage easier and cheaper than cryopreservation (the method of choice up to that time) while maintaining allograft effectiveness in the management of burns and other full thickness skin defects.

The object of this inquiry is whether the same conservation process is still suitable to a dermis allograft that, having the same structure, is addressed to an alternative clinical use. In fact, GPA common applications are related to burns and skin lesions, while the new substitute here analyzed is to be inserted under the skin in the abdominal or post oncological reconstructions, as a reinforcement patch for the overlying tissue. This clinical application is more demanding from the point of view of the allograft mechanical strength.

Trials were performed for decades to indicate the efficacy of GPA in terms of clinical outcomes. In 1987 Vloemans et al. have shown that there were no differences in the results between patients treated with cryopreseryed donor skin and GPA. Two years later Kreis et al. observed that when allograft skin preserved in 85 per cent glycerol is used as a temporary overlay for widely expanded autografts on primarily excised deep burn wounds, the rejection process is attenuated sufficiently enough to allow the outgrowth of the underlying autograft. In the same years Hoekstra demonstrated in tests using several bacterial strains that glycerol has slight antibacterial properties, therefore 85 per cent glycerol resulted to be a bacteriologically safe storage–medium (Hoekstra,

1987b). Glycerol treatment virucidal and antibacterial effects were also confirmed by other studies (Van Baare, et al., 1994; Basile, 1982). Great importance in literature is entrusted to the analysis of the structural integrity of post-treated dermis at a microscopic level. When compared at the light microscopical level to the untreated skin, the dermal part of the glycerol-treated skin didn't show shrunk, survived cells were mostly perivascularly located and any alteration was observed in the structure of the dermis of glycerol-treated skin (Richters, et al., 1996). McKay et al. also reported that the collagenous and elastic elements in the dermis were not affected by the glycerol treatment. However, the cells which had been treated with glycerol were dead. In fact, the current preservation protocol using glycerol provides a well-preserved but non-viable skin. Despite numerous studies on GPA structural integrity at the microscopic level, there is lack of information about GPA mechanical behavior at the macroscopic level. An analysis of the effects of this preservation method on the mechanical properties of ovine cardiac valve allografts was carried out by Aidulis et al., experiencing a significant reduction of the elastic modulus with respect to fresh control values and an increased extensibility, but any equivalent information can be found regarding GPA or glicerolized dermal allografts. Filling this shortage is the main objective of this study.

To study the structural integrity of untreated dermis and glycerol-preserved dermis, paired samples from the same donor were compared exploiting the experimental set-up and protocol optimized in the previous chapter.

It should be noted that the study of the influence of a specific treatment (such as the glycerolization) on the dermis mechanical properties is likely to run into a high level of uncertainty, especially when it is necessary to deal with the inter-subject variability. In fact the mechanical properties of dermis vary substantially not only from one anatomical site to another, but also in relation to age, sex, ethnicity, and many other factors. Surprisingly, despite the large volume of studies in the literature on skin biomechanics, few have examined age-related changes in the properties of human skin in vitro, so a direct comparison with the results

of this study is not feasible. In vivo studies suggest that ageing processes are associated with major structural changes in the dermal ECM, correlated with a loss in tissue compliance (Naylor, et al., 2011), and an increase in the Young's Modulus of the skin (Agache, et al., 1980; Alexander & Cook, 1976; Escoffier, et al., 1989; Grahame & Holt, 1969; Barel, et al., 1998; Sanders, 1973; Diridollou, et al., 2001). In this study four different donors were investigated, having different age and sex.

## 3.3 Materials and Methods

### 3.3.1 Specimens

Strips of dermis tissue, collected from the backs of human donors, were dissected along the cranio-caudal direction. Four different donors of either gender were considered, with ages ranging between 44 and the 72 years (Table 3.1).

*Table 3.1 Donors details*

| Donor | Gender | Age | Donor site |
|---|---|---|---|
| **707** | F | 44 | Back |
| **711** | M | 68 | Back |
| **713** | F | 72 | Back |
| **716** | M | 67 | Back |

Following the harvesting, samples were cut into two parts: the first portion (called 'FR' in the following) was dipped in sterile saline solution to be immediately tested, the other one ('T0' in the following) was placed in a medium composed of glycerol at a concentration of 50%, amikacin (1 mg/ml) and ampicillin (600 µg/ml) and then incubated for at least three hours at room temperature. The glycerol concentration was subsequently increased to 70% and then to 85%. The allografts were stirred gently for at least three hours at 33°C at each step. After glycerolisation, dermal grafts were sealed in labelled plastic boxes, which were stored at a temperature of 4°C for at least 2 weeks. Before testing, reticular dermis grafts were de-glycerolised by sequential washing in sterile 0.9% NaCl

solution at 37°C. The specimens were obtained by cutting out strips along the cranio-caudal (CC) and medio-lateral (ML) directions using the custom made die cutter described in the previous chapter.

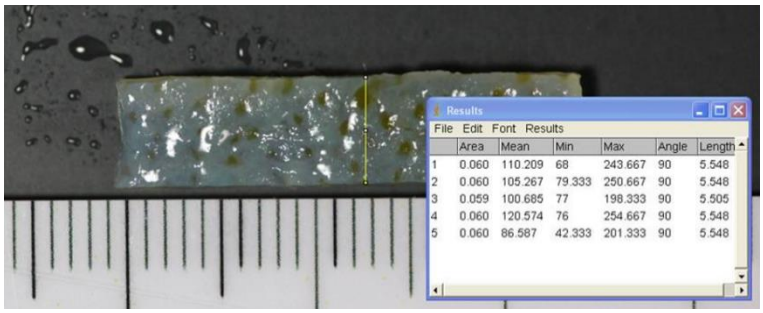


*Figure 3.1 Width misuration process for a glycerolized specimen (software ImageJ).*

The resulting specimen sizes were measured by means of photogrammetry (Figure 3.1) before mechanical testing, obtaining specimens with a 4.84±1.16-mm width, 2.25±0.50-mm thickness and 15.52±0.66-mm length (average ± std). Depending on the original strips size and shape a variable number of specimen was obtained for each combination of treatment (FR or T0), donor (707, 711, 713, 716) and cut orientation (CC or ML), for a total 75 specimens, detailed in Table 3.2.

*Table 3.2 Number of specimen for each combination of treatment (FR or T0), donor (707, 711, 713, 716) and cut orientation (CC or ML).*

| | | ML | CC |
|---|---|---|---|
| **707** | FR | 5 | 6 |
| | T0 | 7 | 8 |
| **711** | FR | 3 | 5 |
| | T0 | 4 | 5 |
| **713** | FR | 3 | 3 |
| | T0 | 3 | 4 |
| **716** | FR | 3 | 6 |
| | T0 | 4 | 6 |

### 3.3.2 Mechanical tests

Following the procedure detailed in the previous chapter, specimens were subjected to uniaxial tensile tests along both the cranio-caudal and medio-lateral directions to quantify the influence of the glycerolization treatment on the dermis tissue biomechanical behaviour. Prior to testing specimens size at rest was measured by means of a full-frame digital camera (Canon EOS 5D Mark II) with an autofocus lens for macro photography (Canon EF 100 mm f/2.8 Macro USM). The 21.0 MP images (5616x3744 pixels) obtained were post processed using the image analysis software ImageJ (National Institutes of Health, Bethesda, Maryland, U.S.). The width and the thickness of each specimen were assessed as an average of five different measurements, reaching a 0.01 mm/pixel measurement resolution (Figure 3.1).

Up to the instant preceding the tensile test, all specimens were kept hydrated in physiological solution. They were then clamped by titanium grips to the Bose Electroforce® 3200 testing machine. Rupture tensile tests were performed for all samples in displacement control at a strain rate of 0.032 $s^{-1}$ without executing any preconditioning cycles. The initial gap between the grips was 5 mm.

### 3.3.3 Data Elaboration

As concluded in the previous chapter, even though differences between engineering and true values can reach 84%, the engineering values remain useful to make comparisons, providing reliable indications with a simpler experimental set up and data processing. Here's why it has been chosen to report the results of rupture tests in terms of 'engineering' stress and strain.

The 'engineering curve' is obtained by ignoring the narrowing of the section during the elongation of the sample and referring always to the initial specimen length. The engineering stress $\sigma_e$ is therefore calculated by dividing the force F by the unloaded-cross sectional area $A_0$ of the

specimen while the engineering strain $\varepsilon_e$ is expressed as the change in length $\Delta L$ per unit of the original length $L_0$.

The engineering elastic modulus ($E_e$) has been calculated from the linear portion of the stress-strain curve (Nì Annaidh, et al., 2012a), which is the so-called 'linear region' where collagen chains are stretched (Fung, 1993; Özkaya, et al., 2012): curve data were locally derived with a moving average linear regression, and the constant trend of the derived curve was considered.

Three descriptive parameters were taken into account: the ultimate tensile strength ($UTS_e$), the ultimate deformation ($\varepsilon_{UTS,e}$), and the elastic modulus ($E_e$) (Figure 3.2).

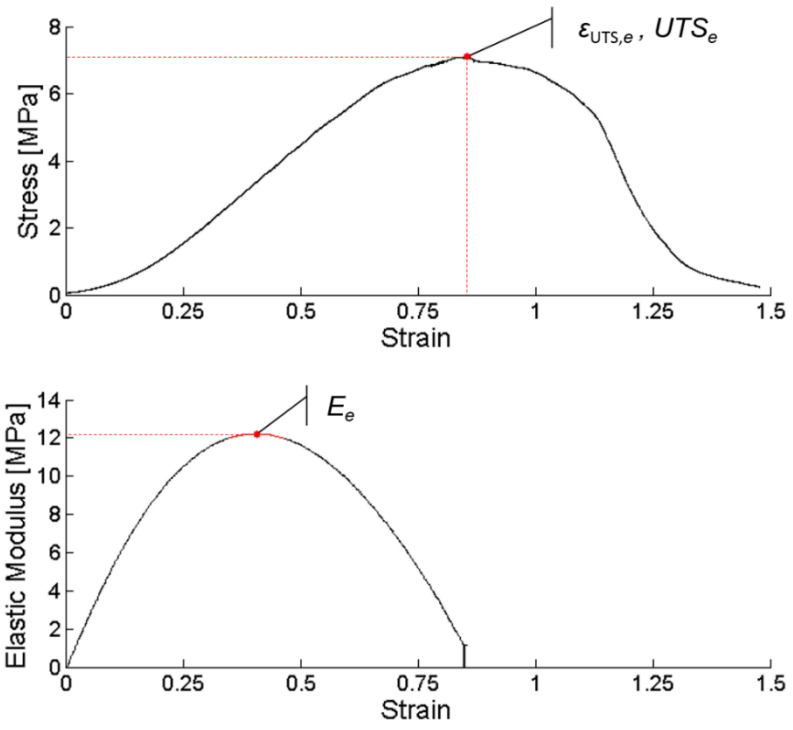


*Figure 3.2 (Up) Experimental stress strain curve, where the red point represents the ultimate strain/stress point; (Down) Moving average linear regression of the stress strain curve increasing portion. The red line point out the constant trend of the derived curve.*

### 3.3.4 Statistical analysis

The mechanical properties of the dermis were reported in relation to the testing direction (CC or ML), the donor (707, 711, 713, 716) and the treatment (called FR if the tissue has not been subjected to any treatment, or T0 if the tissue has undergone the glycerolization process). The donor factor was considered 'random', being the factor levels (the four donors) a random selection from a larger set of all the possible levels, while the treatment and testing direction were considered 'fixed'.

The statistical analysis of the experimental results was carried out using a multivariate analysis of variance (Matlab function 'anovan'), followed by a Tukey–Kramer post hoc test, after having tested the normality of the statistical distribution of all parameters by the Lilliefors test function. The Lilliefors test evaluates the null hypotheses $H_0$ that the data have been drawn from a normal distribution computing the Lilliefors test statistic $T$ as follows:

$$T = \max_x \left| \hat{F}(x) - G(x) \right|$$

*Equation 3.1*

were $\hat{F}(x)$ is the cumulative distribution function of a normal distribution with mean zero and standard deviation one and $G(x)$ is the empirical distribution function of the values of $Z_i$ computed using Equation 3.2.

$$Z_i = \frac{x_i - \bar{x}}{s}$$

*Equation 3.2*

with $\bar{x} = \frac{1}{n}\sum_{i=1}^{n} x_i$ and $s = \sqrt{\frac{1}{n-1}\sum_{i=1}^{n}(x_i - \bar{x})^2}$.

$H_0$ is rejected at the $\alpha$ significance level of $T$ exceeds the critical value for the test, tabulated as a function of the sample size and the chosen significance level. When data-sets of 4 samples were available,

the lillietest Matlab function was used to evaluate the normality of the distribution; when at most 3 replications were available, the null hypothesis was assumed to be true.

In the Tukey-Kramer method, the minimum significant difference (MSD) is calculated for each pair of means. MDS depends on the sample size in each group, the average variation within the groups, and the total number of groups. For a balanced design, all of the MSDs will be the same but for an unbalanced design, as in this work, pairs of groups with smaller sample sizes will have bigger MSDs. If the observed difference between a pair of means is greater than the MSD the pair of means is significantly different. Significance levels were set to $p < 0.05$ for all tests.

## 3.4 Results

Figures 3.3-3.5 show the average value of ultimate stress ($UTS_e$), ultimate strain ($\varepsilon_{UTS,e}$) and elastic modulus ($E_e$) with the relative standard deviations obtained from engineering formulation for different donors in both cut orientations. Numerical values (average ± SD) are listed in Tables 3.3-3.5. Dealing with ultimate stress and elastic modulus, glycerolized samples means increase of up to 191% and 212% respectively if compared to the freshly excised dermis. Only the 19% of the combinations exhibited a reduction of the evaluated parameters. The rise of the ultimate strain parameter seems to be having outcome only in 62% of cases, and reaching an increment of 50% at maximum.

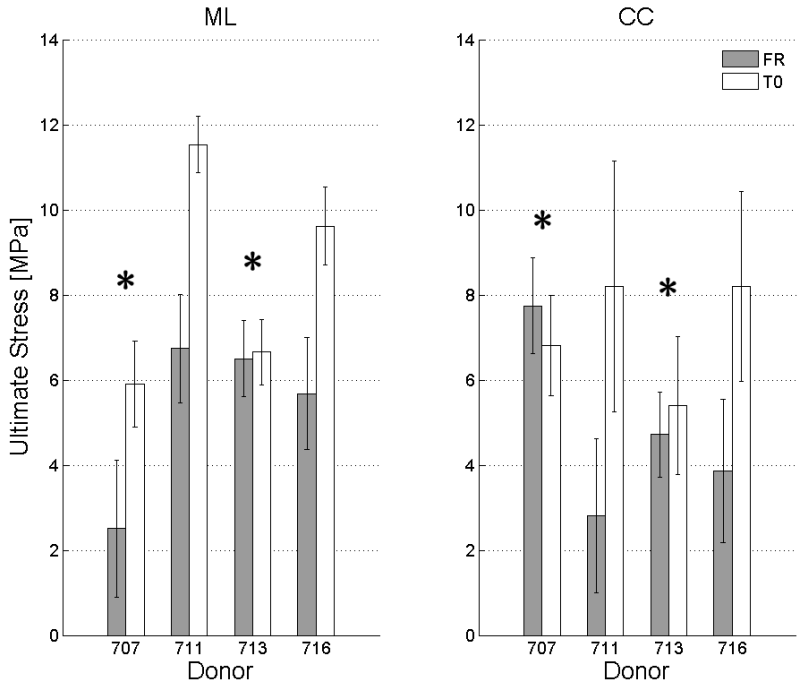


*Figure 3.3 UTS values obtained from engineering formulations for different donors. 'FR' and 'T0' pairs marked with an asterisk are not statistically different. Left side: results obtained along ML direction; right side: results obtained along CC direction.*

*Table 3.3 UTS values in [MPa] (average ± SD) for treated and untrated samples.*

| | **707** | **711** | **713** | **716** | **707** | **711** | **713** | **716** |
|---|---|---|---|---|---|---|---|---|
| **FR** | 2.51 ±1.62 | 6.74 ±1.28 | 6.50 ±0.89 | 5.68 ±1.32 | 7.75 ±1.12 | 2.81 ±1.82 | 4.72 ±0.99 | 3.87 ±1.68 |
| **T0** | 5.91 ±1.01 | 11.53 ±0.67 | 6.65 ±0.76 | 9.61 ±0.92 | 6,81 ±1.17 | 8.19 ±2.95 | 5.41 ±1.62 | 8.20 ±2.24 |

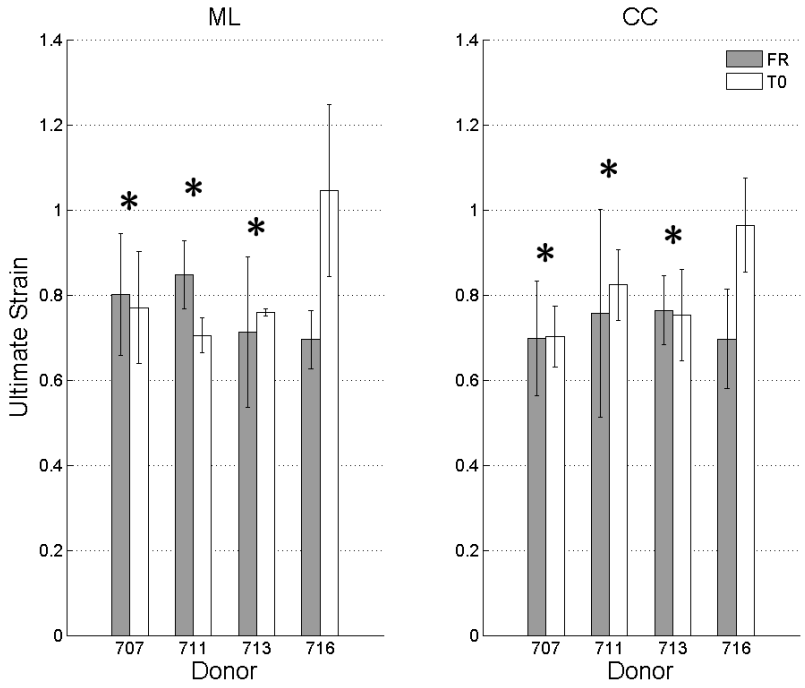


*Figure 3.4 Engineering ultimate strain corresponding to the ultimate stress for different donors. 'FR' and 'T0' pairs marked with an asterisk are not statistically different. Left side: results obtained along ML direction; right side: results obtained along CC direction*

*Table 3.4 Ultimate strain values (average ± SD) for treated and untrated samples.*

| | **707** | **711** | **713** | **716** | **707** | **711** | **713** | **716** |
|---|---|---|---|---|---|---|---|---|
| **FR** | 0.80 ±0.14 | 0.85 ±0.08 | 0.71 ±0.18 | 0.69 ±0.07 | 0.70 ±0.13 | 0.76 ±0.24 | 0.76 ±0.08 | 0.70 ±0.12 |
| **T0** | 0.77 ±0.13 | 0,70 ±0.04 | 0.76 ±0.01 | 1.04 ±0.20 | 0.70 ±0.07 | 0.82 ±0.08 | 0.75 ±0.11 | 0.96 ±0.11 |

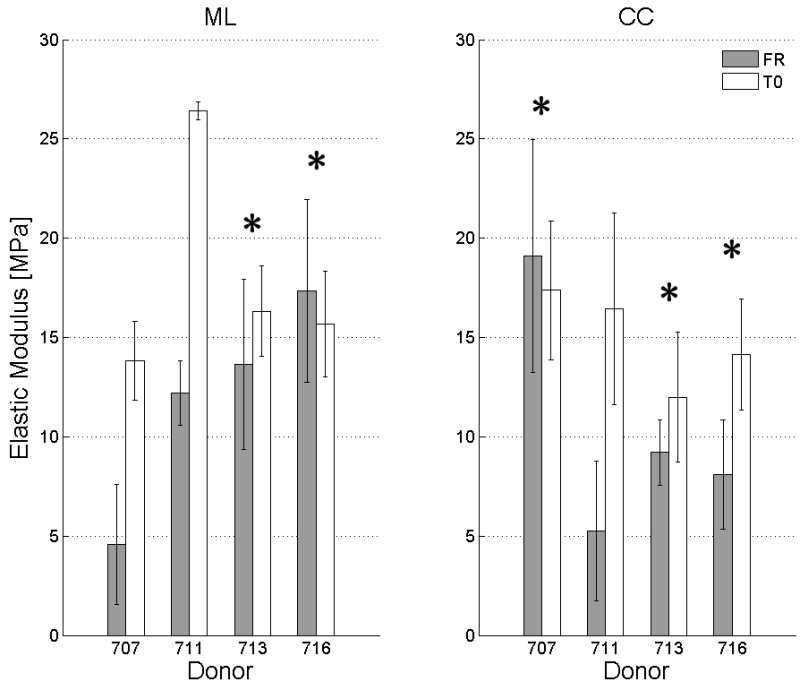


*Figure 3.5 Elastic modulus values for different donors. 'FR' and 'T0' pairs marked with an asterisk are not statistically different. Left side: results obtained along ML direction; right side: results obtained along CC direction*

*Table 3.5 Elastic modulus values in [MPa] (average ± SD) for treated and untrated samples.*

| | **707** | **711** | **713** | **716** | **707** | **711** | **713** | **716** |
|---|---|---|---|---|---|---|---|---|
| **FR** | 4.57 | 12.20 | 13.67 | 17.35 | 19.10 | 5.27 | 9.20 | 8.08 |
| | ±3.04 | ±1.63 | ±4.28 | ±4.59 | ±5.87 | ±3.52 | ±1.66 | ±2.76 |
| **T0** | 13.83 | 26.42 | 16.33 | 15.68 | 17.37 | 16.44 | 12.00 | 14.14 |
| | ±1.98 | ±0.45 | ±2.28 | ±2.67 | ±3.50 | ±4.83 | ±3.27 | ±2.81 |

The normality tests results – prerequisite for the subsequent variance analysis - are represented in Tables 3.6-3.7, which show the critical values referred to the sample size of the tested data-set and the 5% significance level, the Lilliefors test statistic $T$ and the output of the test. This latter returns 1 if it rejects the null hypothesis at the 5% significance level, and 0 if it cannot.

*Table 3.6 Results of normality tests (lillietest Matlab function) for Ultimate Stress, Ultimate Strain and Elastic Modulus parameters in the medio-lateral direction. The 'x' identifies the data sets containing only 3 replications.*

| | 707 | | 711 | | 713 | | 716 | |
|---|---|---|---|---|---|---|---|---|
| | FR | T0 | FR | T0 | FR | T0 | FR | T0 |
| **Ultimate Stress** | | | | | | | | |
| critical value | 0.343 | 0.304 | x | 0.375 | x | x | x | 0.375 |
| T | 0.292 | 0.178 | x | 0.289 | x | x | x | 0.326 |
| test output | 0 | 0 | x | 0 | x | x | x | 0 |
| **Ultimate Strain** | | | | | | | | |
| critical value | 0.343 | 0.304 | x | 0.375 | x | x | x | 0.375 |
| T | 0.163 | 0.127 | x | 0.164 | x | x | x | 0.342 |
| test output | 0 | 0 | x | 0 | x | x | x | 0 |
| **Elastic Modulus** | | | | | | | | |
| critical value | 0.343 | 0.304 | x | 0.375 | x | x | x | 0.375 |
| T | 0.291 | 0.181 | x | 0.234 | x | x | x | 0.235 |
| test output | 0 | 0 | x | 0 | x | x | x | 0 |

*Table 3.7 Results of normality tests (lillietest Matlab function) for Ultimate Stress, Ultimate Strain and Elastic Modulus parameters in the cranio-caudal direction. The 'x' identifies the data sets containing only 3 replications.*

| | 707 | | 711 | | 713 | | 716 | |
|---|---|---|---|---|---|---|---|---|
| | FR | T0 | FR | T0 | FR | T0 | FR | T0 |
| **Ultimate Stress** | | | | | | | | |
| critical value | 0.324 | 0.288 | 0.343 | 0.343 | x | 0.375 | 0.324 | 0.324 |
| T | 0.162 | 0.202 | 0.278 | 0.253 | x | 0.270 | 0.354 | 0.254 |
| test output | 0 | 0 | 0 | 0 | x | 0 | 1 | 0 |
| **Ultimate Strain** | | | | | | | | |
| critical value | 0.324 | 0.288 | 0.343 | 0.343 | x | 0.375 | 0.324 | 0.324 |
| T | 0.296 | 0.193 | 0.211 | 0.169 | x | 0.296 | 0.219 | 0.170 |
| test output | 0 | 0 | 0 | 0 | x | 0 | 0 | 0 |
| **Elastic Modulus** | | | | | | | | |
| critical value | 0.324 | 0.288 | 0.343 | 0.343 | x | 0.375 | 0.324 | 0.324 |
| T | 0.171 | 0.224 | 0.370 | 0.310 | x | 0.255 | 0.153 | 0.158 |
| test output | 0 | 0 | 1 | 0 | x | 0 | 0 | 0 |

In 11 of 16 experimental data sets 4 replications or more were available, and considering the three analyzed parameters as a whole the null hypothesis was accepted in the 94% of the cases.

Since sample properties are shown to be normally distributed, according to the Lilliefors test, the following variance analysis could be performed. The results of the analysis of variance are shown in (Table 3.8). Considering the treatment, the donor and the specimen orientation as singol factors, they are all not significant for the considered parameters. The donor is significant when its interactions with the treatment and orientation factors are considered, except for the ultimate strain parameter where the donor-orientation interaction becames not significant. Moreover, the specimen orientation-treatment interaction is not significant for all parameters.

Having rejected the null hypothesis that all the means are equal, a more detailed look to the data has been addressed, comparing different pairs of means through the Tukey-Kramer test. In Figure 3.3-3.5, pairs of means composed of 'T0' samples with their respective reference 'FR' are marked with an asterisk if they're not statistically different for the represented parameter. Dealing with the glycerolization effects on the native tissue, only 2 donors out of 4 (the female donors) appeared to have a not significantly different behaviour with reference to all the considered parameters. Regarding male donors the tissue properties along both directions appear significantly stiffer (higher UTS), with $\varepsilon_{UTS,e}$ and E not affected significantly respectively for 711 and 716 donor. As a whole the glycerolization process produces a stiffening of the tissue which is expressed in an increase of the ultimate stress and elastic modulus parameters with respect to the native tissue, even in the cases where this increase is statistically not significant.

*Table 3.8 Anova results for the ultimate stress, ultimate strain and elastic modulus. Boldface characters are used to highlight factors that are not significant ($p > 0.05$).*

| **Ultimate Stress** | | | | | |
|---|---|---|---|---|---|
| *Source* | *Sum Sq.* | *DOF* | *Mean Sq.* | *F* | *p* |
| Donor | 29.67 | 3 | 9.89 | 0.17 | **9.15E-01** |
| Orientation | 14.72 | 1 | 14.72 | 0.39 | **5.74E-01** |
| Treatment | 133.38 | 1 | 133.38 | 5.86 | **9.30E-02** |
| Donor*Orientation | 117.20 | 3 | 39.07 | 14.51 | 2.87E-07 |
| Donor*Treatment | 71.93 | 3 | 23.98 | 8.91 | 5.40E-05 |
| Orientation*Treatment | 6.43 | 1 | 6.43 | 2.39 | **1.27E-01** |
| Error | 166.88 | 62 | 2.69 | | |
| Total | 532.22 | 74 | | | |

| **Ultimate Strain** | | | | | |
|---|---|---|---|---|---|
| *Source* | *Sum Sq.* | *DOF* | *Mean Sq.* | *F* | *p* |
| Donor | 0.14 | 3 | 0.05 | 0.47 | **7.28E-01** |
| Orientation | 0.01 | 1 | 0.01 | 0.64 | **4.76E-01** |
| Treatment | 0.08 | 1 | 0.08 | 0.78 | **4.40E-01** |
| Donor*Orientation | 0.04 | 3 | 0.01 | 0.81 | **4.95E-01** |
| Donor*Treatment | 0.32 | 3 | 0.11 | 6.52 | 6.60E-04 |
| Orientation*Treatment | 0.00 | 1 | 0.00 | 0.24 | **6.25E-01** |
| Error | 1.02 | 62 | 0.02 | | |
| Total | 1.67 | 74 | | | |

| **Elastic Modulus** | | | | | |
|---|---|---|---|---|---|
| *Source* | *Sum Sq.* | *DOF* | *Mean Sq.* | *F* | *p* |
| Donor | 39.60 | 3 | 13.20 | 0.04 | **9.90E-01** |
| Orientation | 91.87 | 1 | 91.87 | 0.32 | **6.11E-01** |
| Treatment | 540.24 | 1 | 540.24 | 6.01 | **9.00E-02** |
| Donor*Orientation | 899.90 | 3 | 299.97 | 20.08 | 3.30E-09 |
| Donor*Treatment | 283.42 | 3 | 94.47 | 6.32 | 8.23E-04 |
| Orientation*Treatment | 31.51 | 1 | 31.51 | 2.11 | **1.51E-01** |
| Error | 926.38 | 62 | 14.94 | | |
| Total | 2777.79 | 74 | | | |

## 3.5 Discussion

Decellularized allograft made of cadaveric human dermis were originally used to improve the wound healing of deep burns being placed underneath expanded, thin autologous skin grafts, and at present this is one of the treatments of choice for closure of full-thickness skin loss. The Euro Skin Bank has turned into a center of excellence for the management of human dermis, thanks to the development of a glycerolization technique which allows an easy transport and storage, ensuring good clinical outcomes. Several clinical studies investigated the advantages of GPA clinical use and the effects of the glycerolization treatment on the structure of collagen and elastin. However only a few directed their attention on the macroscopic mechanical behaviour of GPA. The macroscopic mechanical response of a dermis allograft stored according to the standard glycerolization process has a clinical significance when the typical application is converted in a new clinical application whenever a high mechanical resistance is required, as in more recent applications for abdominal wall reconstruction.

This study results point out differences in the glycerolization effects depending on the native tissue. In fact, the donor-treatment interaction is significant for each parameter considered. The generalized increase of strength of the T0 samples appears to be more pronounced in samples derived from male donors, even though the donor factor isn't a significant factor for the elastic modulus parameter.

This results are in contrast with findings of Aidulis et al. who investigated the effects of preservation at 4°C in a high concentration of glycerol of ovine cardiac valve allografts. Aidulis' team noted a reduction of the elastic modulus of the tissue with respect to fresh control values, whereas the extensibility was increased, but in spite of this effects it was found a 20% greater collagen content in leaflets that had been glycerolize, even though the mechanism and the relevance of the increase in collagen content found no explanation (Aidulis, et al., 2002). A greater collagen content in glycerolized specimens could be an explanation of the stiffer behaviour observed in this study.

Interesting considerations on the age-related changes and sex-dependent behavior of the dermis can be deduced as well. Four different donors of either gender were considered in this study, with ages ranging between 44 and the 72 years. Grahame and Holt (1969) found that values for the elastic modulus for intact forearm skin in healthy adult female subjects was significantly higher than that obtained in males, and despite the different harvesting zone, Grahame's results are partially confirmed from this study, where female donors' samples reached higher value of ultimate stress and elastic modulus when the cranio-caudal direction was considered. The high anisotropy typical of biological tissues was here confirmed again.

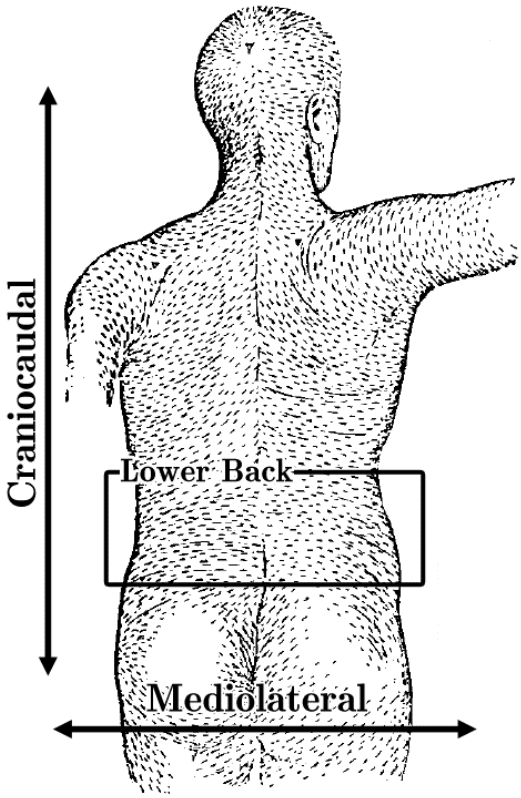


*Figure 3.6 Langer's lines distribution in the lower back (Langer, 1978)*

As expected (Figure 3.6), native dermis response was stiffer in the medio-lateral direction (along Langer's lines) than in the cranio-caudal

direction (across Langer lines), with the only exception of donor 707 (female, 44 years). This behavior is therefore accentuated in older donors, in agreement with the more parallel arrangement of skin collagen during senescence demonstrated by Marcos-Garcés et al.

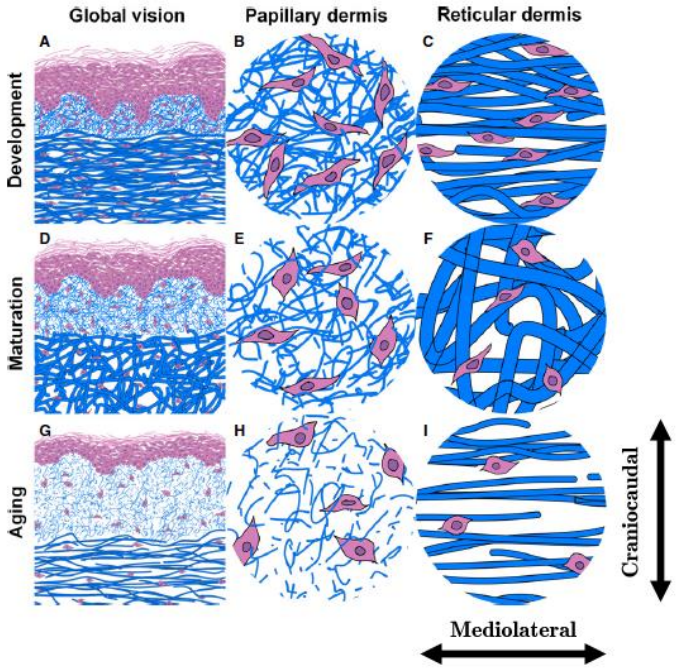


*Figure 3.7 Proposed evolutional model from the histopathological parameters throughout life (Marcos-Garcés, et al., 2014).*

Marcos-Garcés asserts that in the last stage of life collagen bundles lose density and thickness both in the papillary and reticular dermis, and, in this last location, the collagen is disposed in a parallel manner (Figure 3.7-I). The oriented collagen fibers produce an increase of the stiffness when the tissue is stressed parallel to the fibers axis (mediolateral direction in this work).

## 3.6 Conclusions

The objective of this work was to perform a biomechanical comparisons among freshly excised human dermis and glycerol preserved dermis. Dealing with this kind of analysis cannot exempt the author from facing

the inter-subject variability, main feature of biological tissues. In fact, the need to test a sufficient number of samples forced to harvest samples from different donors, which can't always be incorporated into a predefined design of experiment. The reduced number and the variability of the source is the main limitation of this work.

On the whole the influence of the glycerolization procedure on the mechanical properties of excised human dermis resulted to be statistically significant, causing a stiffening of the tissue, with higher ultimate stress and elastic modulus if compared with fresh dermis (FR). Despite this effects, the increase of the ultimate stress and elastic modulus parameters with respect to the native tissue was not considered a negative outcome due to the persistence of the deformability features. In fact the ultimate strain reduction, when present, is moderate.

It was also found agreement between this study's outcomes and existing studies in literature regarding donor's influence, with particular attention to age and sex dependent effects.

## 3.7 References

Agache, P., Monneur, C., Leveque, J. & De Rigal, J., 1980. Mechanical Properties and Young's Modulus of Human Skin in Vivo. Archives of Dermatological Research, Volume 269, pp. 221-232.

Aidulis, D. et al., 2002. Processing of ovine cardiac valve allografts: 1. Effects of preservation method on structure and mechanical properties. Cell and Tissue Banking, 3(2), pp. 79-89.

Alexander, H. & Cook, T., 1976. Variation with age in the mechanical properties of human skin in vivo. Bedstore Biomechanics, pp. 109-118.

Barel, A., Lambrecht, R. & Clarys, P., 1998. Mechanical function of the skin: state of the art. Current Problems in Dermatology, Volume 26, pp. 69-83.

Basile, A., 1982. A comparative study of glycerinized and lyophilized porcine skin in dressing for third-degree burns. Plastic and Reconstructive Surgery, Volume 69, pp. 969-972.

Diridollou, S., Vabrey, V., Bersony, M. & Vaillantz, L., 2001. Skin ageing: changes of physical properties of human skin in vivo. International Journal of Cosmetic Science, Volume 23, pp. 353-362.

Escoffier, C. et al., 1989. Age-related mechanical properties of human skin: an in vivo study. Journal of Investigative Dermatology, Volume 93, pp. 353-357.

Fung, Y.-C., 1993. Biomechanics: Mechanical properties of living tissues. New York: Springer-Verlag.

Grahame, R. & Holt, P., 1969. The influence of ageing on the in vivo elasticity of human skin. Gerontologica, Volume 15, pp. 121-139.

Hermans, M., 1989. Clinical experience with glycerol-preserved donor skin treatment in partial thickness burns. Burns, 15(1), pp. 57-59.

Hoekstra, M., 1987b. Glycerolization of human cadaver allograft donor skin. A study of the inhibition of growth of microorganism. Aachen, Hettich B., p. 53.

Kreis, R. et al., 1989. The use of non-viable glycerol-preserved cadaver skin combined with widely expanded autografts in the treatment of extensive third-degree burns. The Journal of Trauma and Acute Care Surgery, Jan, 29(1), pp. 51-4.

Langer, K., 1978. On the anatomy and physiology of the skin. I. The cleavability of the cutis. British Journal of Plastic Surgery, 31(1), pp. 3-8.

Marcos-Garcés, V. et al., 2014. Age-related dermal collagen changes during development, maturation and ageing – a morphometric and comparative study. Journal of Anatomy, Volume 225, pp. 98-108.

McKay, I. et al., 1994. Reconstruction of human skin from glycerol-preserved allodermis and cultured keratinocyte sheets. Burns, 20(S1), pp. S19-22.

Naylor, E., Watson, R. & Sherratt, M., 2011. Molecular aspects of skin ageing. Maturitas, April, Volume 69, pp. 249-256.

Nì Annaidh, A. et al., 2012a. Characterization of the anisotropic mechanicl properties of excised human skin. Journal of the Mechanical Behavior of Biomedical Materials, Volume 5, pp. 138-48.

Özkaya, N., Nordin , M., Goldsheyder, D. & Leger, D., 2012. Fundamentals of Biomechanics - Equilibrium, Motion, and Deformation. New York: Springer-Verlag.

Richters, C. D., Hoekstraz, M. J., van Baare, J. & Kamperdijk, E. W. A., 1996. Morphology of glycerol-preserved human cadaver skin. Burns, 22(2), pp. 113-116.

Sanders, R., 1973. Torsional elasticity of human skin in vivo. Pflügers Archiv - European Journal of Physiology, Aug, 342(3), pp. 255-60.

Van Baare, J., Buitenwerf, J. & Hoekstra, M., 1994. Virucidal effect of glycerol as used in donor skin preservation. Burns, Volume 20, pp. S77-S80.

Vloemans, A. F. P. M., Kreis , R. W. & Hoekstra, . M. J., 1987b. Treatment of scalds in children with glycerol preserved allograft skin. A comparable and retrospective survey. s.l., Hettich B., p. 69.

# Chapter 4

# Suture retention tests on HADM

## 4.1 Introduction

As mentioned in the previous chapter, acellular dermal matrix (ADM) applications are not limited to biological dressing on scalds, temporary coverage on excised burns and wound bed preparation. Indeed, it has be reported to be used clinically for applications which involve the high mechanical resistance prerequisite. An example is the repair of rotator cuff tears (Barber, et al., 2008; Burkhead , et al., 2007; Snyder & Bond, 2007; Wong, et al., 2010), during which the dermal matrix is typically used to provide biomechanical strength as well as support directed healing. In fact, the acellular dermal matrix has been successfully used as an augmentation grafts which can reinforce the tendon repair and gradually become incorporated into the repaired tissue. In this application, the allograft is secured to the humerus and the supraspinatus tendon using the sutures and suture anchors.

Other application is the Achilles tendon augmentation in neglected Achilles ruptures (Lee, 2007; Barber, et al., 2006). Here the acellular dermal matrix is used as an augmentation graft which facilitates the end-to-end anastomosis. The weakest point of this kind of repair is located between the suture and the tendon and, therefore, the main critical

property for a tendon augmentation graft is to possess an adequate suture retention strength to withstand the expected anatomic forces (Barber, et al., 2006).

In addition, human ADM is commonly used for breast reconstruction procedures (Nahabedian , 2009; Macadam & Lennox, 2012; Zienowicz & Karacaoglu, 2007), hernia repair (Mitchell & Cima, 2011) and in the treatment of chronic wounds (Randall, et al., 2008).

Hence, dependent on the intended use, the biomechanical response of the sutured allografts may be of clinical significance, especially in potentially load bearing applications (Moore, et al., 2015).

Usually suture retention tests are performed on biological and synthetic patches to see how closely they replicate native tissue mechanical properties and to determine the appropriate suture material and thickness based on the resulting behaviour of the sample. Concerning mechanically demanding applications, often the aim is not the comparison with an analogous native tissue but the assessment of load to failure strengths and modes of failure in order to confirm the applicability to a different body part. For example, the adoption of an acellular dermal matrix as an augmentation graft in rotator cuff or tendon repair.

A standard suture test protocol for allograft patches does not exists, and thus, in some studies, the testing protocols were adapted from the methods described within the ANSI/AAMI(ISO 7198:1998/2001/® 2004 "Cardiovascular implants – Tubular vascular prostheses" standard (Barber & Aziz-Jacobo, 2009; Adelman, et al., 2014; Bose Corporation, 2015). In accordance with the standard, specimens were sutured at a minimum distance from the specimens free end. Either suture threads or a stainless steel wire equivalent in diameter to the suture size were commonly used. The sutures were usually not tied, but wrapped around a specially designed suture-holding fixator or clamped to a standard testing machine grip. The tissue other end is always held firmly in a tissue clamp. A different test configuration was implemented by Obermiller and his team (Obermiller, et al., 2004). In this latter work a circular defect was repaired using a continuous suture and the resistance was tested using a ball burst compression cage. This much more complex set

up generates a uniform and physiological distribution of the stresses, but produces a data set difficult to interpret.

This work is focused on a qualitative investigation which has the purpose to determine whether the presence of sutures could affect the mechanical strength of the sutured tissue at physiological strains. For this reason, not only the most common test configuration was used, but additional configurations which investigate the behavior of sutured patches compared to the behavior of a reference intact specimen was implemented. Moreover, both quasi-static and impulsive solicitation were considered.

## 4.2 Materials and Methods

### 4.2.1 Specimens preparation

Strips of dermis tissue, collected from the backs or the thigh of human donors, were dissected along the cranio-caudal direction and decellullarized for five or six weeks in NaOH and DMEM mediums. Five different donors of either gender were considered, with ages ranging between 23 and the 68 years (Table 3.1). Three different characterizations were performed, and each involved a different specimen preparation.

*Table 4.1 Donors details*

| Donor | Gender | Age | Donor site | Test type |
|---|---|---|---|---|
| **711** | M | 68 | Back | I |
| **640** | F | 64 | Thigh | II |
| **647** | F | 68 | Back | II,III |
| **642** | M | 23 | Back | III |
| **651** | F | 52 | Back | II |

The first test type (I) consisted in the analysis of the influence of the presence of a suture through one end of the specimen. This characterization is similar to most of those present in the literature. After cutting the specimens with dimensions of approximately 10x30 mm, the suture thread was inserted into one free end, approximately 5-mm away from the three sides (Figure 4.1).

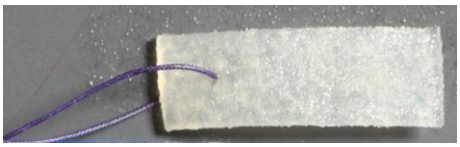

*Figure 4.1 Specimen preparation, test type I.*

This characterization involved a single donor (711) and two decellularization treatment (NaOH and DMEM) lasting both five and six weeks were considered. The cut orientation factor was also considered, obtaining a total of 14 specimens (Table 3.2).

*Table 4.2 Number of specimen for each combination of treatment (NaOH or DMEM), treatment duration (T5, T6) and cut orientation (CC or ML). Test type I.*

| | | ML | CC |
|---|---|---|---|
| **DMEM** | T5 | 2 | 2 |
| | T6 | 2 | 2 |
| **NaOH** | T5 | 2 | - |
| | T6 | 2 | 2 |

The second and the third test types (II, III) investigated the presence of one or two stitches between two pieces of dermis, and compares the sutured dermis behaviour with an undamaged control specimens of dermis. In the second analysis **static solicitations** were imposed, while in the third analysis the specimens were subjected to **impulsive stimuli**.

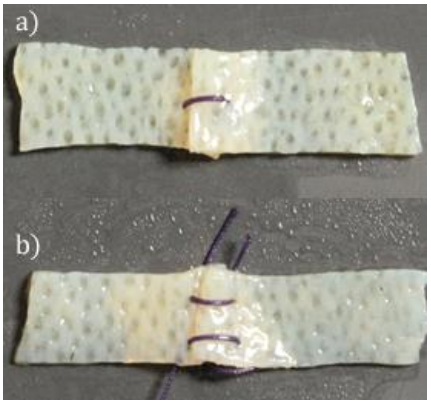


*Figure 4.2 Specimen preparation with a) one suture stitch and b) two suture stitches. Test type II and III.*

The sutured dermis was prepared cutting 10x40mm specimens in two half, and using one or two stitches to bring the parts together again (Figure 4.2). For each pair of sutured specimens, a 10x40mm intact specimen was prepared.

The second and the third characterizations considered multiple donors and the two decellularization treatments, but the absence of any indications regarding the cutting direction for these donors made it impossible to consider the cutting direction as a factor. A total of 12 specimens for the second characterization and 14 specimens for the third were obtained (Tables 4.3 and 4.4).

*Table 4.3 Number of specimen for each combination of donor (640, 647) and treatment (NaOH or DMEM). Test type II.*

| | | One stitch | Two stitches | Intact |
|---|---|---|---|---|
| **640** | DMEM T6 | 1 | 1 | 1 |
| | NaOH T6 | 1 | 1 | 1 |
| **647** | DMEM T6 | 1 | 1 | 1 |
| | NaOH T6 | 1 | 1 | 1 |

*Table 4.4 Number of specimen for each combination of donor (647, 642. 651) and treatment (NaOH or DMEM). Test type III.*

| | | One stitch | Two stitches | Intact |
|---|---|---|---|---|
| **647** | DMEM T6 | 1 | 1 | 1 |
| | NaOH T6 | 1 | 1 | 1 |
| **642** | NaOH T6 | 2 | - | 2 |
| **651** | NaOH T6 | 2 | - | 2 |

A Covidien suture thread was used (2-0 Polysorb™), which is a coated, braided synthetic absorbable suture composed of LACTOMER™, a glycolide/lactide copolymer which is a synthetic polyester composed of glycolide and lactide derived from glycolic and lactic acids (Covidien, 2016). A simple interrupted suture was chosen because, compared with running sutures, this suturing technique is easier to place and has a greater tensile strength. The disadvantage is the length of time required for the stitches placement.

Prior to testing, specimens size at rest was measured by means of a full-frame digital camera (Canon EOS 5D Mark II) with an autofocus lens for macro photography (Canon EF 100 mm f/2.8 Macro USM). The 21.0 MP images (5616x3744 pixels) obtained were post processed using ImageJ image analysis software (National Institutes of Health, Bethesda, Maryland, U.S.). The width and the thickness of each specimen were assessed as an average of five different measurements, reaching a 0.01 mm/pixel measurement resolution. Each specimen was then deglycerolised by sequential washing in sterile 0.9% NaCl solution at 37°C.

### 4.2.2 Mechanical Tests and Data Elaboration

All mechanical tests were performed with the Bose Electroforce® 3200 testing machine in displacement control mode. A full-frame digital camera was used to follow entirely each test, capturing images at a 0.33Hz frame rate. This choice is necessary for the post-processing and comparison of results. In fact, stress-strain curves cannot be directly compared,due to the stitches presence. For this reason it was chosen to exploit an image analysis (where possible), with different modalities depending on the test.

#### 4.2.2.1. Test type I

As previously described, test type I consisted in the analysis of the influence of a suture passing through one free end of the specimen, similarly to the standard suture retention tests. This implied the need to secure the suture thread to the upper crosshead of the testing machine. For this reason a special gripping has been specifically designed and implemented that would allow the thread locking while avoiding any breakages in the interlocking point.

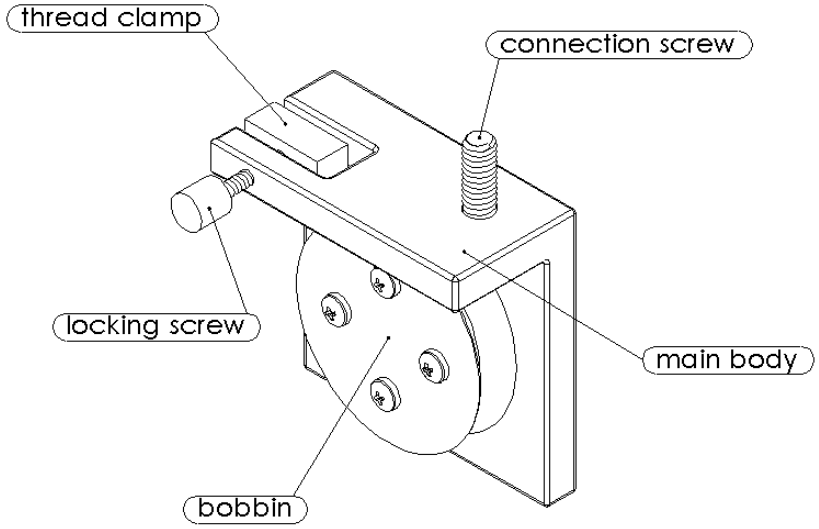


*Figure 4.3 Thread gripping design.*

The grip (Figure 4.3) consists in an aluminium main body to which a plastic material bobbin is fixed. The thread is coiled on the bobbin and blocked by the thread clamp, which is fastened to the main body through a locking screw. The whole grip is connected to the testing machine through a connection screw (UNF 10-32).

The specimen was thus constrained at the machine titanium grip in its lower part, so that the distance between the lower grip and the stitch insertion point was about 10 mm. The suture thread was clamped to the purpose-designed gripping apparatus superiorly (Figure 4.4a).

A 0.16 mm/s rate of displacement was then applied, reaching a 10-mm total displacement. The applied loads were acquired by the testing machine sensor.

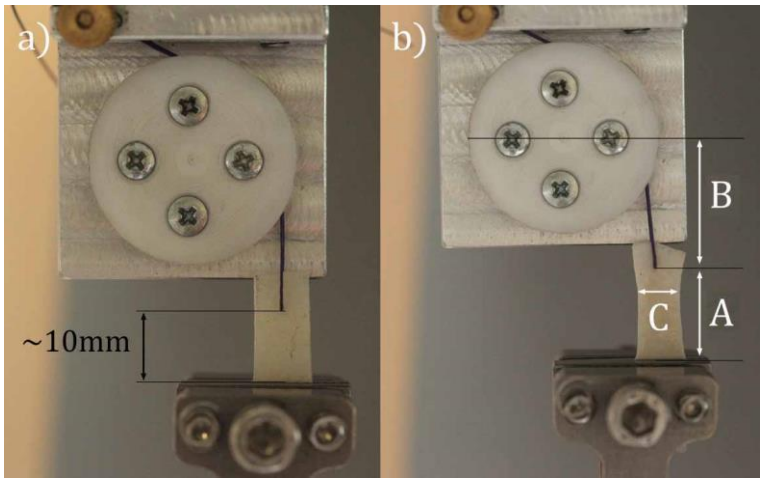


*Figure 4.4 a) Specimen positioning and b) measure labels.*

The analysis of the images captured during the test has allowed to distinguish the contribute of the dermis tissue and of the suture thread to the total displacement. In particular, the dermis elongation was labelled with the letter A, while the thread one was labelled with the letter B. The necking zone was also sized and called C (Figure 4.4b).

#### 4.2.2.2. Test type II

Test type II purpose was the investigation of the suture effects in relation to the number of stitches. The prepared specimens (Par. 4.2.1) were clamped to the testing machine through two titanium grips (Figure 4.5). Similarly to the previous case, a 0.16 mm/s rate of displacement was imposed, for a 10-mm total displacement.

The image analysis has involved a larger number of measures: all elongations of the dermis estimated between the grips and each stitch insertion point were measured, together with the elongation of each stitch. The associated labels are depicted in Figure 4.5. The total elongation (L) and the necking (S) were evaluated in the intact specimen case.

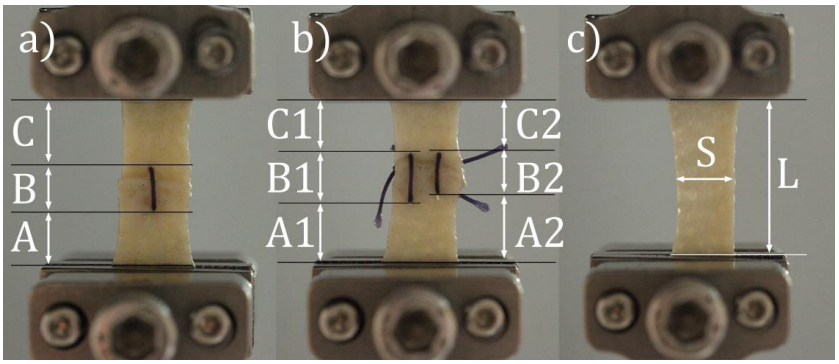


*Figure 4.5 a) One stitch, b) two stitches and c) intact specimens mounted into the testing machine titanium grips, with indications of the measures labels.*

#### 4.2.2.3. Test type III

Test type III required the application of impulsive stimuli. Two different analysis were performed.

- The first one considers a set of specimens similar to the one described in the previous paragraph, subjected to a triangular pulse. The slope of this pulse was setted to 200 mm/s (10 Hz) (Figure 4.6). The choice was made in order to mimic a cough lasting for 0.1 seconds (Smith, 2007).

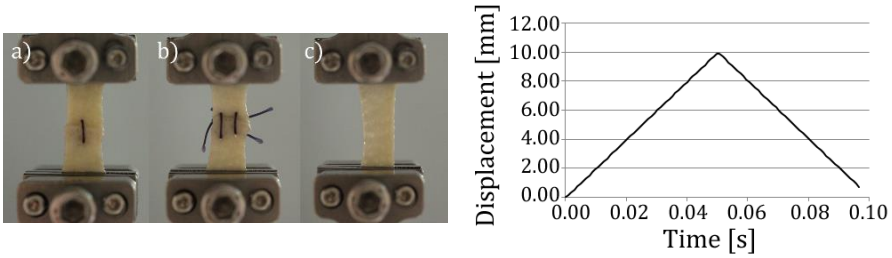


*Figure 4.6 10 Hz triangular pulse.*

- The second analysis pertained only specimens with one suture stitch and the intact dermis, used as a reference. In order to investigate the strain rate dependence, a new 20 Hz triangular pulse was added to the first one (Figure 4.7).

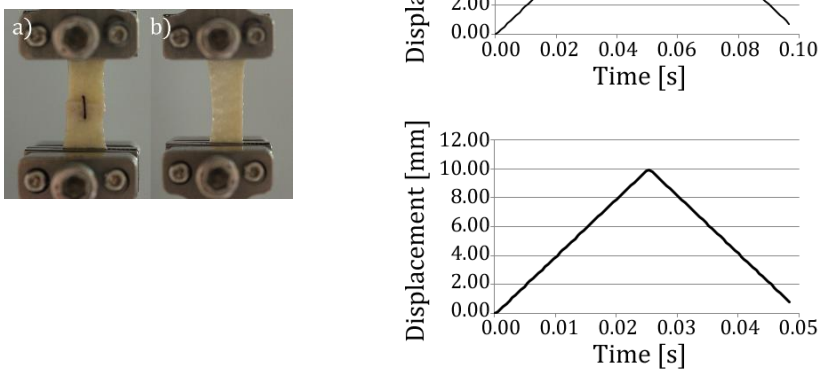


*Figure 4.7 10 Hz and 20 Hz triangular pulses.*

The high rates involved in the impulsive tests made it impossible an image analysis, which was therefore excluded.

## 4.3 Results and Discussion

### 4.3.1 Test type I

Figure 4.8 shows a representative result for the group of specimens treated with the DMEM medium for 6 weeks. For each mechanical test, four curves are reported: the load-time curve (black line) is the testing machine sensors output while the three dotted lines (in blue) are the graphical analysis outcome. It is recalled that A and B represents respectively the dermis and the thread elongations, while C is a measure of the specimen width in the necking zone.

Average results for each tested group are reported in Figure 4.9. Load-time curves show greater variability than displacement-time curves, which are substantially repeatable. The only exception is the B measure, which, it is recalled, is the length of the distance between the edge of the grip and the suture insertion point.

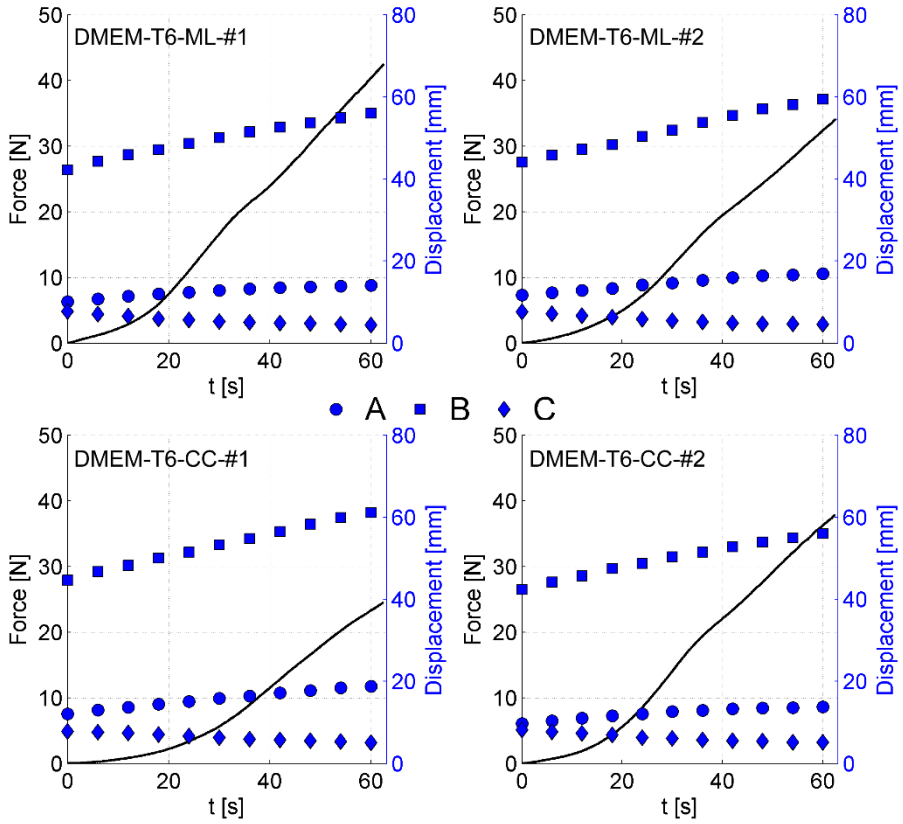


*Figure 4.8 Load-time (black line) and displacement-time (blue dots) curves for the four specimens belonging to the DMEM-T6 group.*

This discrepancy is due to the variable response of the biological tissue, in contrast to the linear and repeatable behaviour of the suture thread. The higher standard deviation of the A measure detected in the NaOH-T6-CC group of specimens is attributable to the different initial length of the thread. In fact, the magnitude of the standard deviation is constant for the whole duration of the test and it is also present at time zero.

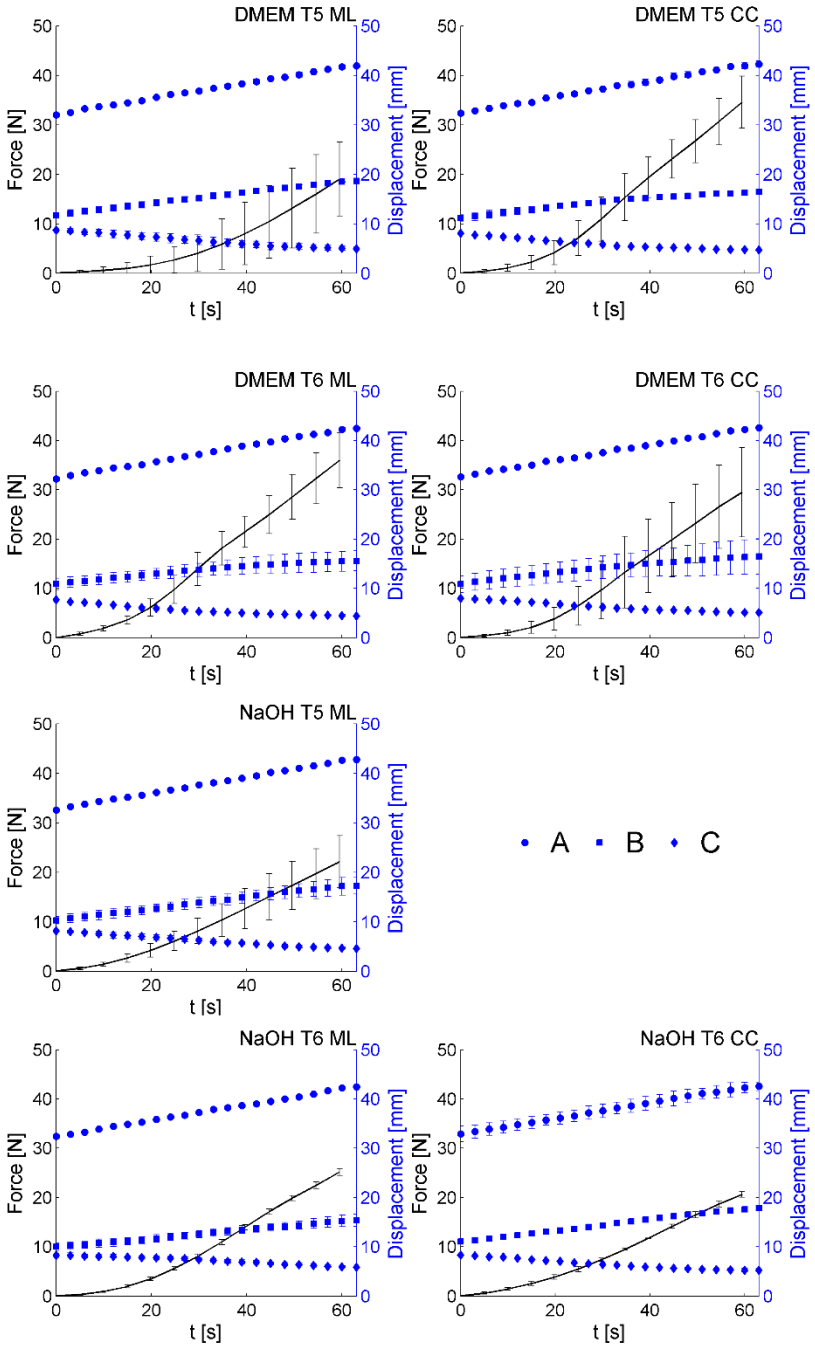


*Figure 4.9 Test type I results for each tested group: average and standard deviations are represented for both load-time (black lines) and displacement-time (blue dotted lines) curves.*

A deeper analysis of the forces extent can be done by plotting the trends of the force over the stretch ratio. The stretch ratio $\lambda$ is calculated using Equation 4.1:

$$\lambda = 1 + \frac{\Delta l}{l_0}$$

*Equation 4.1*

where the initial length $l_0$ is defined as the distance between the edge of the grip and the suture insertion point, and the linear change in length $\Delta l$ is the displacement of the testing machine upper crosshead.

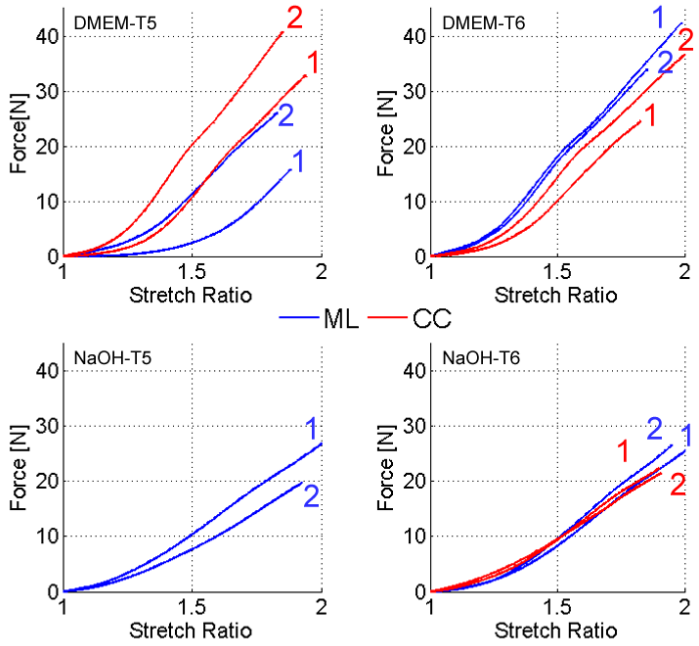


*Figure 4.10 Loading curve plotted over the stretch ratio for the 14 suture retention tests.*

Figure 4.10 shows the loading curves for the 14 suture retention tests. Cranio-caudal data for the NaOH-T5 group are missing, because of the lack of the material. The obtained curve differs from the typical J-shape curves of the biological material (shown in the Chapter 2). An inflection point is indeed visible in proximity of a 20N force. This behaviour is not observable in tests reaching a peak strength lower than 20N (e.g.

DMEM-T5-ML, specimen #1). This inflection point separates a low stretch zone with a behavior comparable to biological tissues one and a high stretch zone with a linear behavior. The slope of the stress-strain curve in the linear region (~200 MPa) falls inside the elastic modulus ranges of similar 2.0 absorbable sutures (Greenwald , et al., 1994). This peculiar trend can be found in a similar analysis performed on porcine pericardium (Bose Corporation, 2015).

*Table 4.5 Maximum load and cross-section values of all analysed samples. In each pair of specimen, higher cross-sections are related to higher loads.*

| | | | Specimen | Maximum load [N] | Cross-section [mm²] |
|---|---|---|---|---|---|
| DMEM | T5 | ML | 1 | 15.87 | 12.56 |
| | | | 2 | 25.96 | 15.46 |
| | | CC | 1 | 32.94 | 12.56 |
| | | | 2 | 40.80 | 14.87 |
| | T6 | ML | 1 | 42.47 | 11.80 |
| | | | 2 | 34.03 | 10.71 |
| | | CC | 1 | 24.52 | 11.67 |
| | | | 2 | 37.81 | 12.10 |
| NaOH | T5 | ML | 1 | 19.59 | 10.82 |
| | | | 2 | 27.49 | 11.10 |
| | T6 | ML | 1 | 26.50 | 12.14 |
| | | | 2 | 27.41 | 13.01 |
| | | CC | 1 | 22.31 | 11.39 |
| | | | 2 | 21.39 | 11.11 |

Higher or lower values reached in paired specimens of the same test is attributable to the different specimen cross-section. In fact, larger cross-sections are always related to higher force values, as shown in Table 4.5. This trend is confirmed by Adelman (2014) and Moore (2015) works, which highlights that the mean suture retention strength increases with increasing material thickness.

Considering the contribution in terms of deformation of the dermis tissue and the suture thread, it can be noted that the respective contribution are equivalent only when the load exceeds ~30 N (Table 4.6 - encircled specimens). When lower forces are reached, the dermis elongation is considerably greater than the thread one.

*Table 4.6 Dermis and thread maximum elongations of all analysed samples.*

| | | | Specimen | Maximum load [N] | Dermis elongation [mm] | Thread elongation [mm] |
|---|---|---|---|---|---|---|
| DMEM | T5 | ML | 1 | 15.87 | 7.19 | 2.67 |
| | | | 2 | 25.96 | 6.71 | 3.31 |
| | | CC | 1 | 32.94 | 5.92 | 4.32 |
| | | | 2 | 40.80 | 4.63 | 4.87 |
| | T6 | ML | 1 | 42.47 | 4.00 | 5.97 |
| | | | 2 | 34.03 | 5.31 | 5.10 |
| | | CC | 1 | 24.52 | 6.95 | 2.96 |
| | | | 2 | 37.81 | 4.29 | 5.62 |
| NaOH | T5 | ML | 1 | 19.59 | 7.63 | 2.74 |
| | | | 2 | 27.49 | 6.32 | 3.74 |
| | T6 | ML | 1 | 26.50 | 6.39 | 2.79 |
| | | | 2 | 27.41 | 7.20 | 2.99 |
| | | CC | 1 | 22.31 | 5.70 | 4.35 |
| | | | 2 | 21.39 | 5.06 | 4.96 |

It must be emphasized that up to now other suture investigations on Acellular Dermal matrixes have not take into account the specimens cutting directions, making no differences between CC and ML specimens and studying the only dependence on the thickness factor (Adelman, et al., 2014; Moore, et al., 2015).

### 4.3.2 Test type II

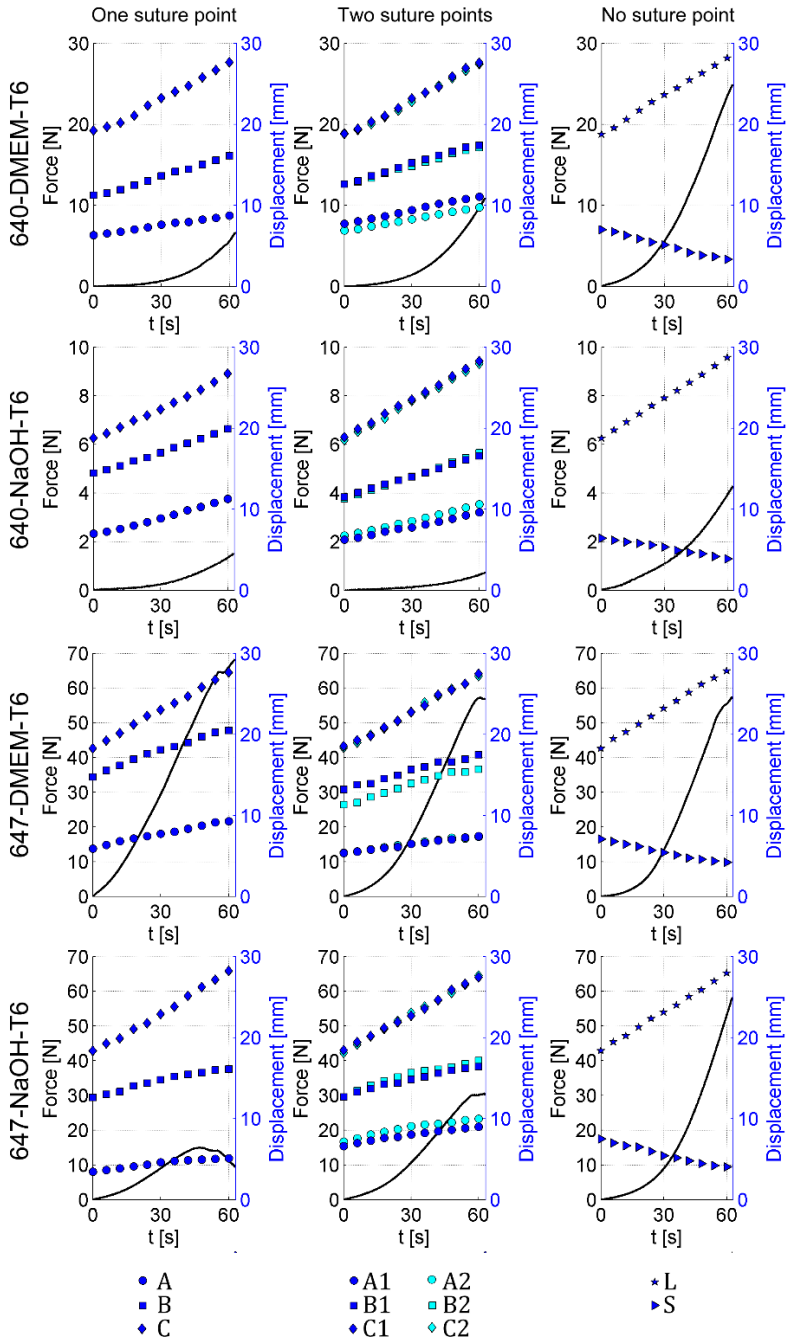


*Figure 4.11 Test type II results: force-time curves (black lines) and displacement-time curves (dotted lines).*

Figure 4.11 shows all results for the second characterization. Two different donors were considered in this analysis, but indications regarding the dermis patch orientation weren't available. Nevertheless, some general conclusions can be drawn.

Image analysis has witnessed the difficulty to suture repeatable stitches on a soft and wet tissue like dermis. In fact, in the "two suture points" case, the paired measure A1-A2 and B1-B2 (which, it is recalled, involve the suture insertion points) are not coincident.

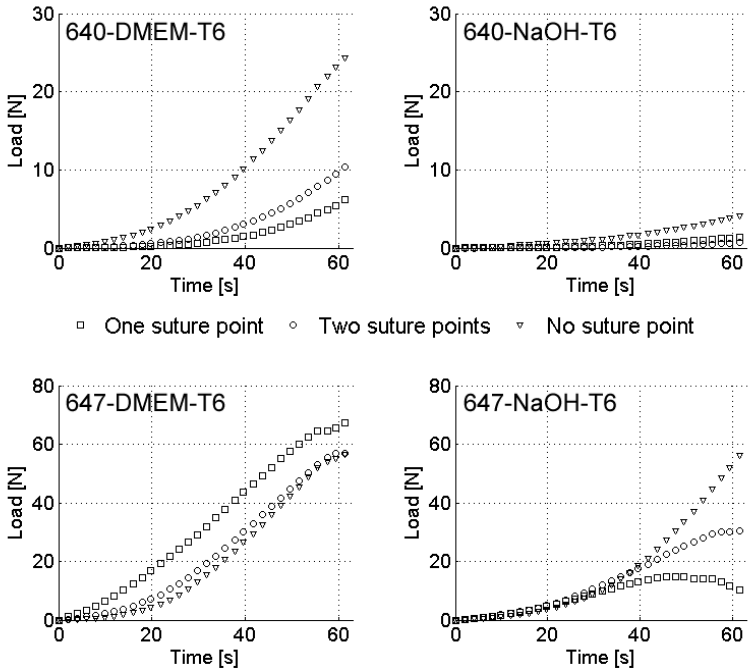


*Figure 4.12 Load-time trends for the test-type II.*

With reference to peak loads, the intact specimen mechanical response is always higher than the sutured dermis (Figure 4.12). An exception should be made for the 647-DMEM group of specimens. In this set of tests, the peak load magnitude reached by the sutured dermis is comparable to the intact dermis, and the dermis sutured with one single stitch has higher mechanical strength. As said, this is an exception, since the sutured dermis presents in any other case a lower mechanical resistance. Conversely, the presence of one or two stitches do not show

substantial differences. On average, the mechanical response of dermis treated by means of DMEM (either intact or sutured) is higher compared to the specimens decellularized using NaOH, although it must be remembered that the cutting direction was unknown for the donors here considered.

According to the author's knowledge, similar tests are not reported in the literature and a comparison is therefore not possible. Nevertheless in spite numerous sources of variability, it can be stated that the presence of sutures increases the patch deformability, thus lowering the forces. This behaviour turns out to be very beneficial in the immediate postoperative period, when the dermis allograft has not been incorporated and colonized by the host tissue yet and, therefore, the suture collaborates to withstand the imposed deformations.

### 4.3.3 Test type III

The last characterization consists in an investigation of the sutured and intact dermis mechanical response to an impulsive stimulus. The importance of this characterization lies in the possibility of impulsive events that may occur in the post-operative period. A pulse generated by a cough was taken as a representative example (Smith, 2007), although other events, such as a sneeze or a sudden effort, could possibly generate a similar solicitation.

A first set of specimen consisting of specimens with one or two stitches, coupled to an undamaged specimen, was subjected to a 10Hz triangular pulse.

*Table 4.7 Hysteresis loop areas.*

| | DMEM-T6 | NaOH-T6 |
|---|---|---|
| ■ | 0.122 J | 0.185 J |
| ● | 0.294 J | 0.045 J |
| ▼ | 0.366 J | 0.210 J |

The resulting load-displacement curves are depicted in Figure 4.13. The loading and unloading curves obtained do not follow the same path and the difference in the calculated area under the loading and unloading

curves gives an indication of the energy lost due to internal friction and damping in the material (Table 4.7).

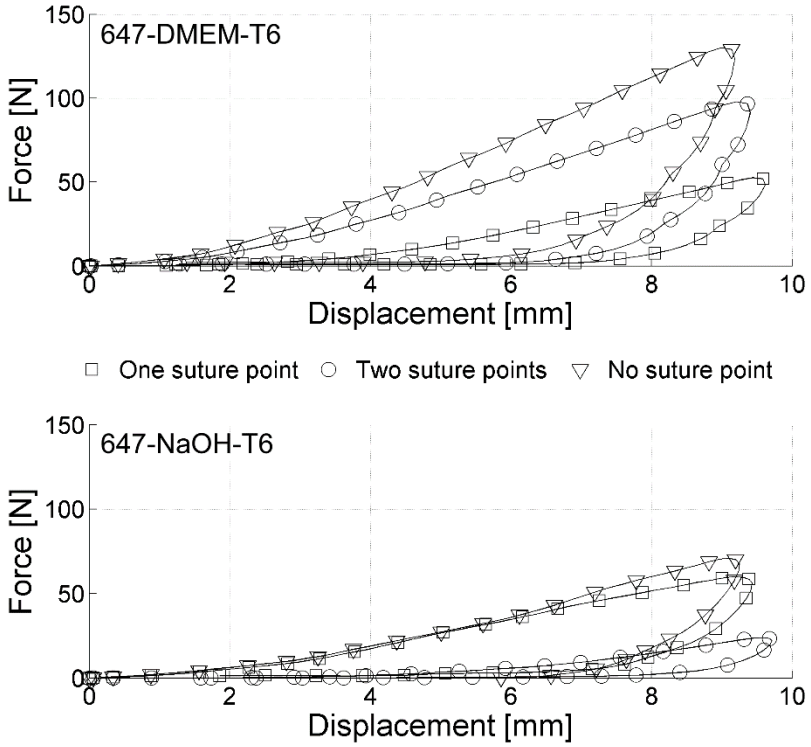


*Figure 4.13 Impulse response to a 10Hz triangular pulse (donor #647 - specimens treated with DMEM (top) and NaOH (bottom) for 6 weeks).*

Similarly to the quasi-static characterizations (Par. 4.3.2), the undamaged specimen always reaches higher forces on equal deformations. Also the hysteresis loop area (namely the loss energy) is higher than in the sutured dermis cases. Therefore, the presence of the suture thread cut down the viscoelastic behaviour of the dermis tissue, reducing, as a consequence, its ability to adsorb energy.

The second set of specimens comprises 8 tests performed on two donors exploiting two triangular pulse (10Hz and 20Hz). The material paucity has led to exclude the specimens with two stitches from this analysis. Moreover only the NaOH treatment was considered.

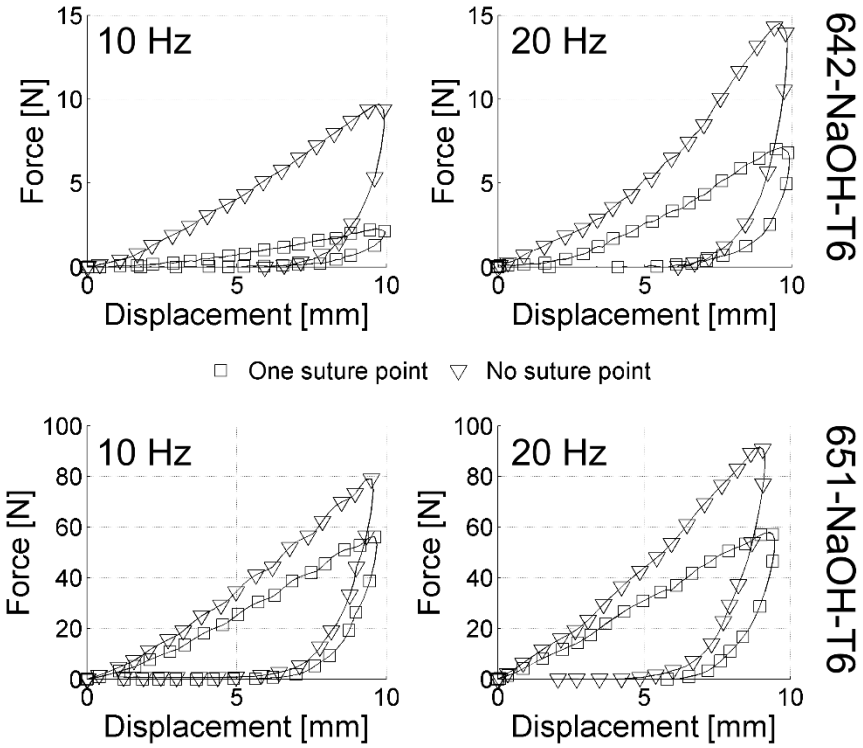


*Figure 4.14 Impulse response to a 10Hz (left) and a 20Hz (right) triangular pulse (donor #642 - specimens treated with NaOH (top) and donor #651 - specimens treated with NaOH (bottom) for 6 weeks).*

The resulting load-displacement curves are depicted in Figure 4.14, while the calculated hysteresis loop areas are listed in Table 4.8.

*Table 4.8 Hysteresis loop areas.*

| | 642-NaOH-T6 | | 651-NaOH-T6 | |
|---|---|---|---|---|
| | 10 Hz | 20 Hz | 10 Hz | 20 Hz |
| ■ | 0.007 J | 0.023 J | 0.200 J | 0.231 J |
| ▼ | 0.036 J | 0.049 J | 0.259 J | 0.298 J |

Both the maximum force values and the loss energies increases with increasing strain rate, which is in accordance with the documented strain-rate dependent behaviour of skin (Arumugam, et al., 1994; Shergold, et al., 2006; Ni Annaidh, et al., 2014). In any case, the energy

dissipated by sutured specimens is always lower compared to undamaged one, regardless of the strain rate.

## 4.4 Conclusions

This work was focused on a qualitative investigation aimed to determine whether the presence of sutures could affect the mechanical strength of the sutured tissue at physiological strains. Both for this reason and for the impossibility of obtaining sufficiently large displacements with the used testing machine, the rupture of the specimen was never reached. Nevertheless, characteristic curves of the sutured dermis behaviour were obtained and were compared with control intact specimens. This analysis showed an increase in the elasticity of the sutured specimens, which appears to have beneficial effects in the immediate post-operative period, when the dermis allograft has not yet been incorporated and colonized by the host tissue. Moreover, this response was observed both in quasi static and dynamic conditions. A new characterization procedure which couples results coming from both the testing machine and an image analysis was here implemented, in order to provide additional information beside the only "suture retention strength" value. This method could allow to isolate the suture material effect, deducing the contribution of the only tissue to the overall deformation.

This study results may be of clinical significance in potentially load bearing applications and in cases where the shortage of material requires joining allografts by sutures in order to obtain patches to cover large defects (Deeken, et al., 2012).

## 4.5 References


Adelman, D., Selber, J. & Butler, C., 2014. Bovine versus Porcine Acellular Dermal Matrix: A Comparison of Mechanical Properties. *Plastic and Reconstructive Surgery,* 2(5).

Arumugam, V., Naresh, M. & Sanjeevi, R., 1994. Effect of strain rate on fracture behaviour of skin. *Journal of Biosciences,* Volume 19, pp. 307-13.

Barber, F. & Aziz-Jacobo, J., 2009. Biomechanical Testing of Commercially Available Soft-Tissue Augmentation Materials. *Arthroscopy: The Journal of Arthroscopy and Related Surgery,* 25(11), pp. 1233-1239.

Barber, F., Herbert, M. & Boothby, . M., 2008. Ultimate tensile failure loads of a human dermal allograft rotator cuff augmentation. *Arthroscopy: The Journal of Arthroscopic and Related Surgery,* 24(1), pp. 20-24.

Barber, F., Herbert, M. & Coons, D., 2006. Tendon Augmentation Grafts: Biomechanical Failure Loads and Failure Patterns. *Arthroscopy: The Journal of Arthroscopic and Related Surgery,* 22(5), pp. 534-8.

Bose Corporation, 2015. *TA ElectroForce.* [Online] Available at: http://electroforce.tainstruments.com/electroforce/assets/pdf/appBriefs/appbrief˙PericardiumSutureRetention.pdf [Accessed 13 March 2016].

Burkhead , W., Schiffern, S. & Krishnan, S., 2007. Use of Graft Jacket as an Augmentation for Massive Rotator Cuff Tears. *Seminars in Arthroplasty,* 18(1), pp. 11-18.

Covidien, 2016. *Polisorb Suture.* [Online] Available at: http://www.covidien.com/imageServer.aspx?contentID=14357&contenttype=application/pdf [Accessed 7 March 2016].

Deeken, C. et al., 2012. Differentiation od biological scaffold materials through physicomechanical, thermal, and enzymatic degradation techniques. *Annals of Surgery,* Volume 255, pp. 595-604.

Greenwald , D., Shumway , S., Albear, P. & Gottlieb, L., 1994. Mechanical comparison of 10 suture materials before and after in vivo incubation. *Journal of Surgical Research,* 56(4), pp. 372-7.

Lee, D., 2007. Achilles Tendon Repair with Acellular Tissue Graft Augmentation in Neglected Ruptures. *The Journal of Foot and Ankle Surgery,* 46(6), pp. 451-455.

Macadam, S. & Lennox, P., 2012. Acellular dermal matrices: Use in reconstructive and aesthetic breast surgery. *The Canadian Journal of Plastic Surgery,* 20(2), pp. 75-89.

Mitchell, C. & Cima, R., 2011. A Novel Technique for the Repair of Urostomal Hernias Using Human Acellular Dermal Matrix. *Urology,* 77(3), pp. 746-750.

Moore, M. et al., 2015. Decellularization of human dermis using non-denaturing anionic detergent and endonuclease: a review. *Cell and Tissue Banking,* 16(2), pp. 249-259.

Nahabedian , M., 2009. AlloDerm Performance in the Setting of Prosthetic Breast Surgery, Infection, and Irradiation. *Plastic and Reconstructive Surgery,* 124(6), pp. 1743-53.

Ni Annaidh, A. et al., 2014. *Strain rate effects on the failure characteristics of excised human skin.* Montreal, Canada, 9th International Conference on the Mechanics of Time Dependent Materials.

Obermiller, F. et al., 2004. A comparison of suture retention strengths fo three biomaterials. *Medical Science Monitor,* 10(1), pp. 1-5.

Randall, K. et al., 2008. Use of an Acellular Regenerative Tissue Matrix in Combination with Vacuum-assisted Closure Therapy for Treatment of a Diabetic Foot Wound. *The Journal of Foot and Ankle Surgery,* 47(5), pp. 430-433.

Shergold, O., Fleck, N. & Radford, D., 2006. The uniaxial stress versus strain response of pig skin and silicone rubber at low and high strain rates. *International Journal of Impact Engineering,* Volume 32, p. 1384–1402.

Smith, J., 2007. Ambulatory methods for recording cough. *Pulmonary Pharmacology & Therapeutics,* Volume 20, pp. 313-318.

Snyder, S. & Bond, J., 2007. Technique for Arthroscopic Replacement of Severely Damaged Rotator Cuff Using "GraftJacket" Allograft. *Operative Techniques in Sports Medicine,* 15(2), pp. 86-94.

Wong, I., Burns, J. & Snyder, . S., 2010. Arthroscopic GraftJacket repair of rotator cuff tears. *Journal of Shoulder and Elbow Surgery,* 19(2S), pp. 104-9.

Zienowicz, R. & Karacaoglu, E., 2007. Implant Based Breast Reconstruction with Allograft. *Plastic and Reconstructive Surgery,* 120(2), pp. 373-381.

# Chapter 5

# Constitutive models of HADM: parameterization through 3D Finite Element Modelling coupled to uniaxial experimental tests

## 5.1 Introduction

As repeatedly highlighted in the previous chapters, dermis behavior is still not well understood and predicting its deformation through constitutive models has been always challenging.

To the authors' knowledge there's a paucity in literature regarding the constitutive material modelling of dermis, despite numerous studies have been performed on the skin modelling as a whole. The attempts to develop a computational model of skin started in the 70s with Danielson's work. He modelled the skin as an elastic membrane, transporting the existing knowledge on the behavior of stretchable thin membranes in the field of biological tissues (Danielson, 1973). The hyperelastic modelling of skin (rabbit skin) was introduced in 1976 (Tong & Fung, 1976). The absence of computer softwares and modelling tools in those years forced the approach used to describe the skin to mathematical equations. This choice, limited in computational complexity, slowed down the research of a computational model for the skin until the early 90s. With

innovations in computer science, engineering softwares has been developed and FE simulation of skin behaviour has become possible. In 2003 Hendriks and his team developed a numerical-experimental method to characterize the non-linear mechanical behaviour of human dermis subjected to suction tests (Hendriks, et al., 2003). A finite element model exhibiting extended Mooney material behaviour was used, finding a good agreement between computational and experimental outputs. Molinari et al. used the hyperelastic model implemented by Tong & Fung (1976) to simulate the biomechanical behaviour of the skin using data from a virtual surgery (Molinari, et al., 2005). Moreover, the Arruda-Boyce hyperelastic constitutive model was used to model the mechanical behavior of soft tissues subjected to indentation (Liu, et al., 2004). Also the mechanical properties of human skin in vivo were evaluated integrating experimental data and the Ogden hyperelastic model (Manan, et al., 2012; Evans & Holt, 2009).

The hyperelastic models found application in the description of different biological tissues like brain tissue (Miller & Chinzei, 2002) and face soft tissue (Chabanas, et al., 2004). This interesting last work proposed to simulate the morphological outcomes of maxillofacial surgery comparing different modelling options. The great strength of this study, however, is the validation procedure based on a comparison of the simulations with the post-operative CT scan. In fact, the assessment of the simulations quality is one of the most important issue in soft tissue modelling, but despite many models were proposed in the literature, few works present satisfying validation procedures.

In this chapter, four different models were implemented, and an evaluation procedure was carried out based on a quantitative comparison of the simulation results with parameters extracted from the experimental uniaxial tests.

### 5.1.1 The nonlinear analysis

In mechanics, it is often assumed that the displacements are small compared to the characteristic size of the structure and that the deformations are infinitesimal, so that the measure of the deformation can be

obtained as the symmetric part of the displacement gradient. The equilibrium equations are thus written directly on the undeformed configuration of the body. Furthermore, typically it is assumed that the relationship between the stress and the deformation is linear elastic. Under the above assumptions, the analysed problem will be considered linear. It follows that for this kind of problems, the implemented finite element method turns out to be a linear algebraic system. Sometimes, however, it is not possible to take as valid these linearity hypotheses with good approximation. In fact it may happen that the structure subjected to a solicitation becomes significantly deformed. In these cases it is not appropriate to consider the deformations as infinitesimal, and consequently it is not permissible to write the equilibrium equations on the undeformed configuration. It's then necessary to take into account the nonlinearity and to impose the equilibrium on the deformed configuration, which is not known a priori and constitutes an unknown variable of the structural problem. In this case the problem becomes non-linear and this nonlinearity is generally called **geometric nonlinearity**.

Another issue is that typically, materials exhibit a linear elastic behaviour in a limited range of stress and strains. Exceeded a certain deformation value, the material constitutive equation is not linear anymore. Even in this case, the structural equilibrium problem becomes nonlinear and this nonlinearity is generally called **material nonlinearity**.

Lastly, there is a final kind of non-linearity which is the **contact nonlinearity**. It takes into account changes in the boundary conditions of the structures involved in the analysis.

Dealing with biological tissues subjected to ex vivo uniaxial solicitation, the geometric and material nonlinearities are the main challenges to face. In fact, during the test the specimen undergoes very large deformations, and consequently the load-deformation curve becomes highly non-linear.

### 5.1.2 Hyperelasticity

The hyperelastic materials are a particular class of elastic materials which respond elastically when subjected to very large strains. Hence

they account both for nonlinear material behaviour and geometric nonlinearity (large shape changes). They find application in describing elastomers (vulcanized rubber and synthetic polymers) and some biological materials. This materials shows a microstructure of chain-line molecules, which confers an isotropic behaviour at small deformations and an anisotropic behaviour at larger deformation, as the molecule chains realign to the loading direction. Under an essentially monotonic loading condition, however, many of these materials can be approximated as isotropic. Nevertheless, some classes of hyperelastic materials cannot be modeled as isotropic, such as biomaterials. The typical volumetric behaviour of hyperelastic materials can be grouped into two classes: materials (such as polymers) which have small volumetric changes during deformation and these are incompressible or nearly-incompressible materials; materials (such as foams) which can experience large volumetric changes during deformation, and these are compressible materials.

The hyperelastic material constitutive models are derived from strain-energy potentials that are functions of the deformation invariants. An exception is the response function model which obtains the constitutive response functions directly from experimental data (Ansys Inc., 2013a). The strain-energy potential is expressed as a function of the strains invariants, which in turn can be expressed in function of the stretches. In any deformation state, there are relations which correlate the stretches along different directions.

As an example, let's consider the uniaxial case examined in this study. The invariants of the Cauchy-Green deformation tensor (Equation 5.1) are described by Equations 5.2.

$$[C] = \begin{bmatrix} \lambda_1^2 & 0 & 0 \\ 0 & \lambda_2^2 & 0 \\ 0 & 0 & \lambda_3^2 \end{bmatrix}$$

*Equation 5.1*

$$I_1 = \lambda_1^2 + \lambda_2^2 + \lambda_3^2$$
$$I_2 = \lambda_1^2\lambda_2^2 + \lambda_2^2\lambda_3^2 + \lambda_3^2\lambda_1^2$$
$$I_3 = \lambda_1^2\lambda_2^2\lambda_3^2$$

*Equations 5.2*

Assuming an incompressible behaviour of the material it will follow that the third invariant will always be equal to 1 (Equation 5.3):

$$\lambda_1^2\lambda_2^2\lambda_3^2 = 1$$

*Equation 5.3*

For a uniaxial strain state, the ratio of the stretches along the directions orthogonal to the test axis will be identical:

$$\lambda_1 = \textit{stretch along the test axis}$$

$$\lambda_2 = \lambda_3 = \textit{stretches in the two orthogonal directions}$$

$$\lambda_2\lambda_3 = \lambda_1^{-1}$$
$$\lambda_2 = \lambda_3 = \lambda_1^{-\frac{1}{2}}$$

*Equations 5.4*

Therefore, for a uniaxial tensile, the first and the second invariants will be:

$$I_1 = \lambda_1^2 + 2\lambda_1^{-1}$$
$$I_2 = 2\lambda_1 + \lambda_1^{-2}$$

*Equation 5.5*

These invariants and stretches definitions are the starting point for the discussion of the two hyper-elastic models used in this work: the Mooney-Rivlin model and the Ogden model.

#### 5.1.2.1. Mooney-Rivlin model

The form of the strain energy potential for the Mooney-Rivlin hyperelastic model is:

$$W = \sum_{i,j=0}^{N} C_{ij}(I_1 - 3)^i (I_2 - 3)^j + \sum_{i=1}^{N} \frac{1}{D_i}(J_{el} - 1)^{2i}$$

*Equation 5.6*

with $C_{00} = 0$ and $J_{el} = 1$ if the material is incompressible.

In a 5 constant model, $N = 2$ and the strain energy potential will be:

$$W = C_{10}(I_1 - 3) + C_{01}(I_2 - 3) + C_{20}(I_1 - 3)^2 + C_{11}(I_1 - 3)(I_2 - 3) + C_{02}(I_2 - 3)^2$$

*Equation 5.7*

Recalling the relationship between invariant and stretch for a case of uniaxial tension expressed in the previous paragraph (Equation 5.5), the engineering stress formulation will be:

$$\sigma_e = 2(\lambda - \lambda^{-2})\left(\frac{\partial W}{\partial I_1} + \frac{1}{\lambda}\frac{\partial W}{\partial I_2}\right)$$

*Equation 5.8*

where $\sigma_e$ = engineering stress, $W$ = strain energy, $\lambda$ = stretch parallel to $\sigma_e$ and $I_1, I_2$ = strain invariants.

Replacing the strain invariants (Equation 5.5) in the stress formulation relation (Equation 5.8) the final stress-stretch relation can be obtained:

$$\begin{aligned}\sigma_e &= 2(\lambda - \lambda^{-2})[C_{10} + 2C_{20}(I_1 - 3) + \lambda^{-1}C_{01} + 2\lambda^{-1}C_{02}(I_2 - 3) \\ &\quad + C_{11}(I_2 - 3 + \lambda^{-1}I_1 - 3\lambda^{-1})] \\ &= 2(\lambda - \lambda^{-2})[C_{10} + \lambda^{-1}C_{01} + 2C_{20}(\lambda^2 + 2\lambda^{-1} - 3) \\ &\quad + 2C_{02}(2\lambda + \lambda^{-2} - 3) + 3C_{11}(\lambda - 1 - \lambda^{-1} + \lambda^{-2})]\end{aligned}$$

*Equation 5.9*

The commercial FE software used for the analysis (Ansys Mechanical APDL 14.5) considers some stability verifications for the Mooney-Rivlin hyperelastic material.

A nonlinear material is stable if the secondary work required for an arbitrary change in the deformation is always positive:$\partial\sigma_{ij}\partial\varepsilon_{ij} > 0$, where $\partial\sigma_{ij}$ is the change in the Cauchy stress tensor corresponding to a change in the logarithmic strain $\partial\varepsilon_{ij}$ (Gorash, et al., 2015). Since the change in stress is related to the change in strain through the material stiffness tensor, checking for stability of a material can be more conveniently accomplished by checking for the positive definiteness of the material stiffness. The stability check is carried out through the check of the list of relations between the model constants shown in Table 5.1.

*Table 5.1 Stability condition for the hyperelastic Mooney-Rivlin model*

| | Stability condition |
|---|---|
| $C_{10} + C_{01}$ | $> 0$ |
| $C_{20}$ | $> 0$ |
| $C_{02}$ | $< 0$ |
| $C_{20} + C_{11} + C_{02}$ | $> 0$ |

#### 5.1.2.2. Ogden model

The strain-energy potential of the Ogden compressible foam model is based on the principal stretches of left-Cauchy strain tensor similarly to the Mooney-Rivlin model and has the form:

$$W = \sum_{i=1}^{N} \frac{\mu_i}{\alpha_i}\left(\lambda_1^{\alpha_i} + \lambda_2^{\alpha_i} + \lambda_3^{\alpha_i} - 3\right) + \sum_{k=1}^{N} \frac{1}{d_k}(J_{el} - 1)^{2k}$$

*Equation 5.10*

For an incompressible material, $J_{el} = 1$ and $I_3 = 1$, hence Equation 5.10 becomes:

$$W = \sum_{i=1}^{N} \frac{\mu_i}{\alpha_i} (\lambda_2^{\alpha_i} + \lambda_2^{\alpha_i} + \lambda_1^{-\alpha_i} \lambda_2^{\alpha_i} - 3)$$

*Equation 5.11*

Considering the uniaxial case:

$$W = \sum_{i=1}^{N} \frac{\mu_i}{\alpha_i} (\lambda^{\alpha_i} + \lambda^{-\frac{\alpha_i}{2}} + \lambda^{-\alpha_i} \lambda^{\frac{\alpha_i}{2}} - 3) = \sum_{i=1}^{N} \frac{\mu_i}{\alpha_i} (\lambda^{\alpha_i} + 2\lambda^{-\frac{\alpha_i}{2}} - 3)$$

*Equation 5.12*

Therefore, the final engineering stress-stretch relation will be:

$$\sigma_e = \frac{\partial W}{\partial \lambda} = \sum_{i=1}^{N} \mu_i \left( \lambda^{\alpha_i - 1} - \lambda^{-\frac{\alpha_i}{2} - 1} \right) = \sum_{i=1}^{N} \mu_i \left( \lambda^{\alpha_i - 1} - \lambda^{-\left(1 + \frac{\alpha_i}{2}\right)} \right)$$

*Equation 5.13*

The 4th order Odgen model used in this work is thus described by Equation 5.14.

$$\sigma_e = \mu_1 \left( \lambda^{\alpha_1 - 1} - \lambda^{-\left(1 + \frac{\alpha_1}{2}\right)} \right) + \mu_2 \left( \lambda^{\alpha_2 - 1} - \lambda^{-\left(1 + \frac{\alpha_2}{2}\right)} \right) + \mu_3 \left( \lambda^{\alpha_3 - 1} - \lambda^{-\left(1 + \frac{\alpha_3}{2}\right)} \right) + \mu_4 \left( \lambda^{\alpha_4 - 1} - \lambda^{-\left(1 + \frac{\alpha_4}{2}\right)} \right)$$

*Equation 5.14*

#### 5.1.2.3. Least squares fit analysis

As can be seen in Equation 5.8 the deviatoric stress is determined solely by the deformation and the derivatives of the elastic potential function. These derivatives are called the response functions and they can be determined directly from experimental data, bypassing the need to fit the potential function parameters to the experimental data. The experimental data consists of the measured deformation and stress so

that the only unknowns in the constitutive equations are the response functions. Ansys Reference Manual recommends that this test data should be taken from several modes of deformation over a wide range of strain values. In fact, it has been observed that to achieve stability, the material constants should be fit using test data in at least as many deformation states as will be experienced in the analysis. In this work, the considered stress-strain data came solely from uniaxial tests, but, being the deformation state re-created in the finite element model purely uniaxial, the parameter extraction was considered accurate.

The curve fitting process is based upon a regression analysis which uses the computational method called **least squares method**. The method used the minimization of the sum of squared error (SSE) between experimental and Cauchy predicted stress values. This sum of the squared error (error norm) is defined by:

$$Err = \sum_{i=1}^{n} w_i \left[\sigma_i^{exp} - \sigma_i^{eng}(c_j)\right]^2$$

*Equation 5.15*

where $Err$ is the least square residual error, $\sigma_i^{exp}$ are the experimental stress values, $\sigma_i^{eng}$ are the engineering stress values (function of the hyperelastic material constants), $n$ is the number of experimental data points and $w_i$ are the weights associated with different data point. If the error is normalized the same weight ($w_i = 1$) is associated to each data point. Equation 5.15 is minimised by setting the variation of $Err$ to $\partial Err^2 = 0$. This generate a system of equations which are used to extract the hyperelastic constants:

$$\begin{cases} \dfrac{\partial Err^2}{\partial c_1} = 0 \\ \dfrac{\partial Err^2}{\partial c_2} = 0 \\ \quad etc. \end{cases}$$

## 5.2 Materials and Methods

As previously mentioned, the Ansys Mechanical APDL software has been used for the finite element analysis. It comprises all recently developed hyperelastic models in its material library and it is also equipped with a curve fitting tool for the estimation of the material constants by inputting user's experimental data.

Four different finite element models were thus implemented for four experimental stress-strain uniaxial curves (extracted from the described in Chapter 2), in both compressible and incompressible conditions:

- Linear elastic model;
- Linear elastic model with geometric nonlinearity (from here on called 'Linear GNL');
- 5 parameters Mooney-Rivlin model;
- $4^{th}$ order Ogden model.

On the whole, 32 models were obtained, with few lacking data which will be detailed afterwards.

### 5.2.1 FE model optimization

A preliminary study was carried out to optimize the FE model for what concerns discretization and boundary conditions. The starting geometry was a 5x5x3-mm parallelepiped (Figure 5.1).

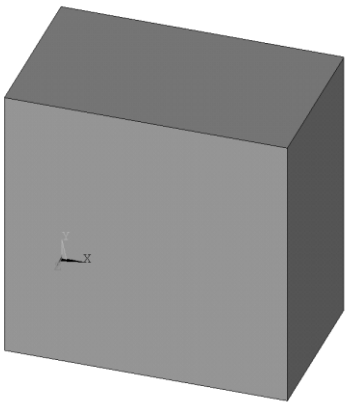

*Figure 5.1 Starting geometry.*

### Elements and Mesh

The element choice was guided by the material application and the tridimensional geometry. Ansys has two structural elements which supports hyperelasticy: solid185 and solid186. Both of them are 3D solid elements that exhibits quadratic displacement behaviour. They have three degrees of freedom per node: the translations along the x, y and z directions. The main difference in the node number: 8 nodes for the solid185 element (one node for each vertex) and 20 nodes for the solid186 element (one node for each line middle point) (Figure 5.2).

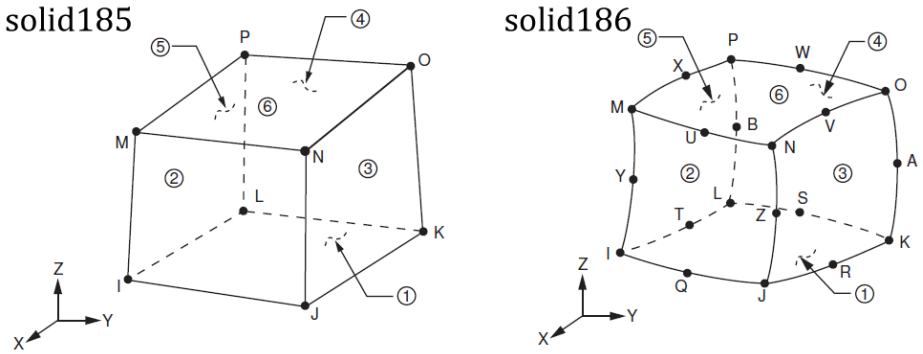


*Figure 5.2 Solid185 and Solid186 element configuration (Ansys Inc., 2013b).*

A sensitivity analysis was thus conducted in order to choose the type of element and to optimize the size of the mesh (Table 5.2). Four different element dimensions for the two element types were imposed, considering an external load (10 N) applied to the specimen upper surface. Both a linear material and a Mooney-Rivlin hyperelastic material were considered. The outputs considered were the upper surface displacement and the mean stress in the middle plane of the specimen (y = 2.5 mm). Despite the results to the linear model do not show substantial differences between the two elements, solid185 element does not appear suitable to obtain the convergence of the results for the hyperelastic model with the considered element edge length. Regarding the mesh size, the

goal is to seek a compromise between accuracy and computational times. Larger elements, and therefore a smaller number of elements which describe the behaviour of the entire geometry, not only reduce the results accuracy but also prejudice the simulation convergence at larger strains due to element distortions. Conversely very small elements greatly increase the computation time, and does not always help the simulation convergence.

*Table 5.2 Sensitivity analysis results for the linear elastic model and the Mooney-Rivlin hyperelastic model.*

| **Linear Elastic Model** | | | | |
|---|---|---|---|---|
| | solid186 | | solid185 | |
| Element Edge Length | Displacement [mm] | Mean stress [MPa] | Displacement [mm] | Mean stress [MPa] |
| 1 mm | 0.812 | 0.610 | 0.834 | 0.611 |
| 0.5 mm | 0.821 | 0.620 | 0.815 | 0.632 |
| 0.25 mm | 0.821 | 0.634 | 0.822 | 0.621 |
| 0.2 mm | 0.821 | 0.629 | 0.826 | 0.625 |
| **Mooney-Rivlin Hyperelastic Model (5 parameters)** | | | | |
| | solid186 | | solid185 | |
| Element Edge Length | Displacement [mm] | Mean stress [MPa] | Displacement [mm] | Mean stress [MPa] |
| 1 mm | 1.530 | 1.787 | 1.477 | 1.960 |
| 0.5 mm | 1.530 | 1.795 | 1.515 | 1.800 |
| 0.25 mm | 1.530 | 1.787 | 1.526 | 1.790 |
| 0.2 mm | 1.529 | 1.785 | 1.530 | 1.788 |

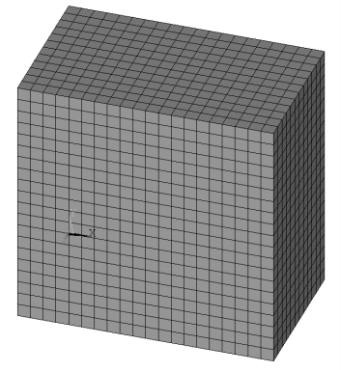

*Figure 5.3 Solid186 mesh (0.25 mm element edge length).*

After due consideration, the chosen element was the solid186 with an element edge length of 0.25mm (Figure 5.3). Under these conditions, for a 5x5x3 mm model, 21945 nodes and 4800 elements were obtained.

### Boundary conditions: constraints

In order to simulate the conditions of a uniaxial test, all the degrees of freedom of the lower surface of the model were totally constrained. The upper surface was left free to move only in the vertical direction, thus constraints in the horizontal plane were imposed.

The imposition of the vertical movement was done through the application of a constant force to a master node to which were connected the nodes belonging to the upper surface (slave nodes). This procedure can be carried out in Ansys using two different commands, which are not interchangeable. For the linear models Ansys provides the CERIG command, while nonlinear models require the use of the MPC184 command (Ansys Inc., 2013c). Wanting to carry out a comparative analysis of linear and nonlinear models, boundary conditions should be identical. That's why the behaviour of the two commands was investigated.

The CERIG command defines a rigid region (the upper surface in this case) by automatically generating constraint equations to relate nodes in the region, and connect them to a geometric location. The restriction of this command is having six degrees of freedom per node (six rigid body motions in the global Cartesian space). If the elements used doesn't satisfy this hypothesis (like in the solid186 case) a mass point having six degree of freedom can be build. This latter will be used as the master node (Figure 5.4a).

The MPC184 command comprises a general class of multipoint constraint element that apply kinematic constraints between nodes. This elements are divided into "constraint elements" (e.g. rigid link) and "joint element" (e.g. revolute), and they all have six degree of freedom. For our purpose a simple rigid links is enough, and this modality can be selected by choosing KEYOPT(1)=0. For this configuration an external node, centered with respect to the upper surface, should be define. This node will be used as the master node, to which all the slave nodes will be connected individually. In this way, the force applied to the master will be transmitted to all other nodes (Figure 5.4b).

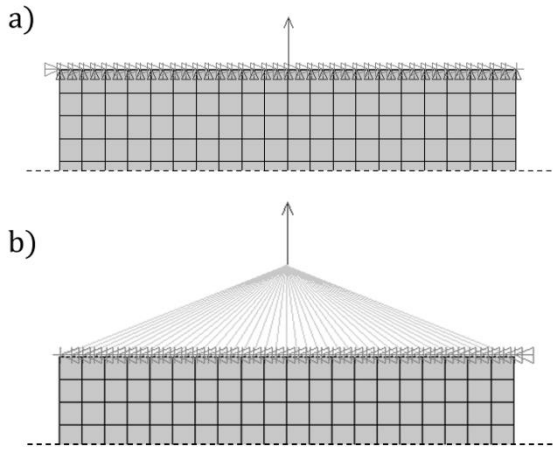


*Figure 5.4 Upper surface constraint imposed using a) the CERIG command and b) the MPC184 command.*

The MPC184 command is unusable in the linear case, in fact it doesn't accept the NLGEOM,OFF command. Conversely, the CERIG command seems not to give problems in the nonlinear case, since the simulation reaches convergence. Despite this, a warning message is displayed: *"Constraint equations may not be valid for elements that undergo large deflections."*

A comparison between the two commands for a nonlinear case (Mooney-Rivlin hyperelastic method) was performed anyway. Comparing the results obtained with the CERIG command in the nonlinear cases with the corresponding results obtained with the MPC184, there are no difference either in terms of displacement or in terms of stress distributions, as can be appreciated considering Figure 5.5. However, it is preferable to use each approach for the specific situation it was implemented on. Thus, the CERIG command was used only for the linear case.

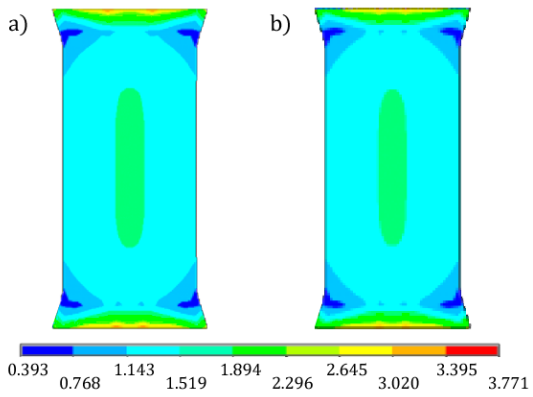


*Figure 5.5 σy [MPa] distributions in the a) CERIG and b) MPC184 case for a Mooney-Rivlin model.*

### Boundary conditions: loads

The magnitude of the load applied to the master node has been determined according to the experimental curves (Figure 5.6) and the convergence issues, mainly generated by the elastic model with geometric nonlinearities.

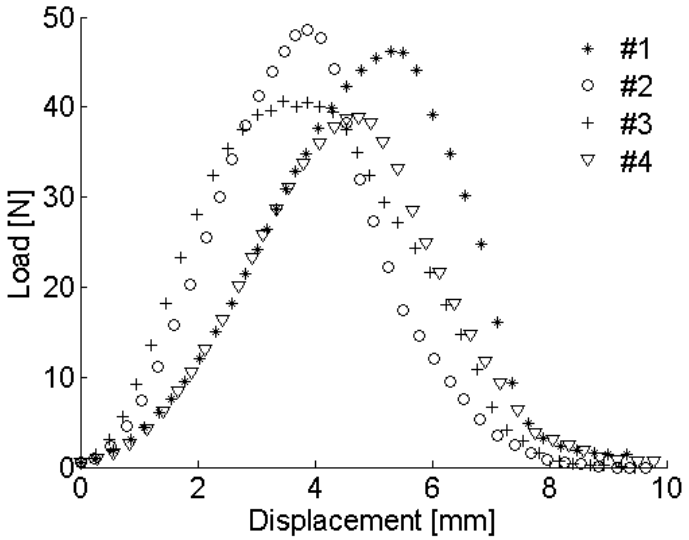


*Figure 5.6 Experimental load-displacement curves.*

A realignment of the forces was carried out and the displacement was set equal to zero when a 0.25N force was recorded. Considering a new zero in the displacement axis implied the update of the initial geometry, due to the changed initial conditions in terms of specimens length and cross-section, which were extrapolated from the synchronized images captured throughout the tensile tests. A 10N load was then chosen and applied to each model (Figure 5.7).

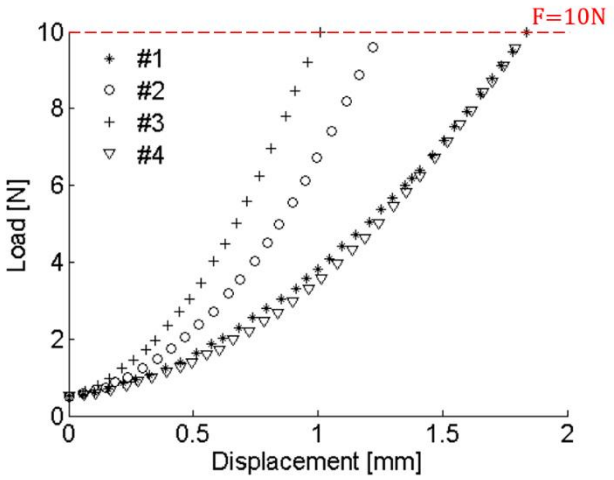


*Figure 5.7 Experimental load-displacement curves cutted to the maximum load considered.*

### 5.2.2 Material Properties

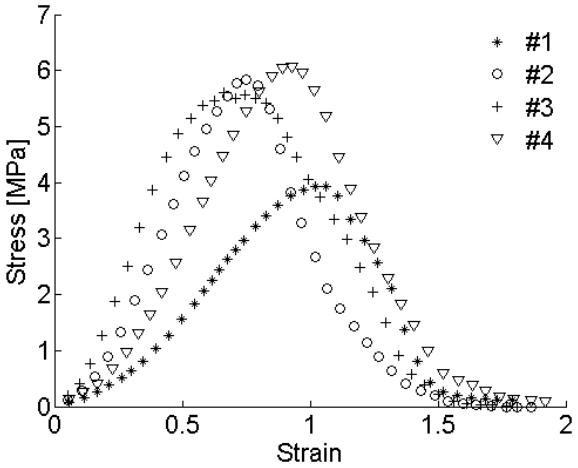


*Figure 5.8 Experimental engineering stress-strain curves.*

The material definition for all the implemented models came from the engineering stress-strain curves (Figure 5.8).

### Linear elastic model and linear elastic model with geometric nonlinearity

Linear elastic models require two input values for the material definition: the Young modulus and the Poisson's ratio. These values were calculated in correspondence of a 10N force, through linear regression (Figure 5.9). As previously mentioned, both compressible and incompressible models were implemented. In the linear case the incompressibility is realised through imposing 0.5 Poisson's ratio. Ansys maximum accepted value for the Poisson's ratio is $0.49\overline{9}$, thus 0.499 value was setted.

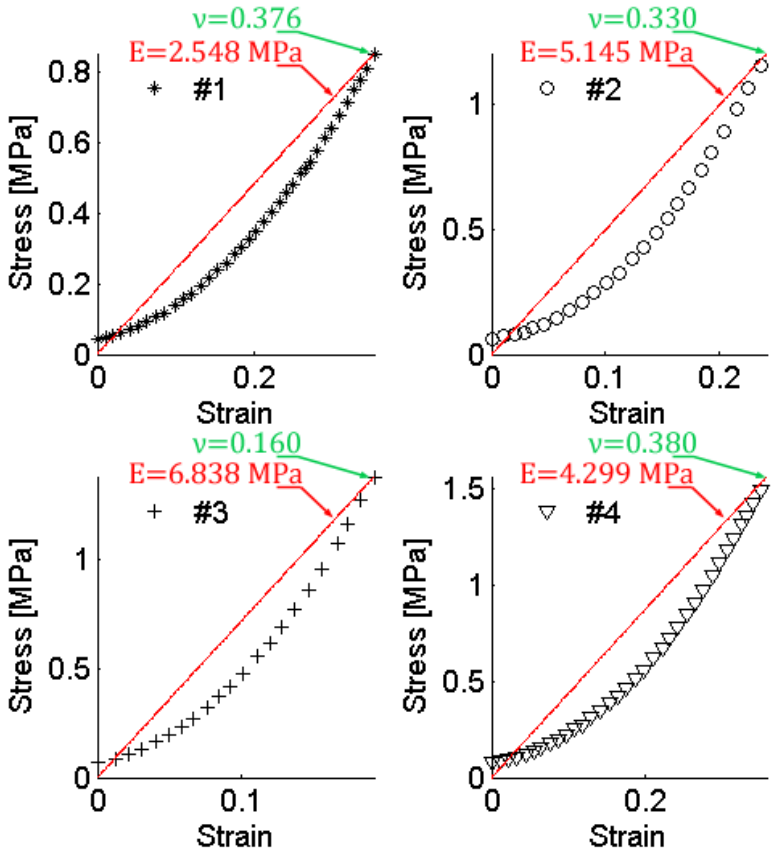


*Figure 5.9 Linear material parameters for the four experimental curves cutted at 10N (compressible case).*

### Mooney-Rivlin model

The Mooney-Rivlin parameters were obtained through the Ansys curve fitting tool as explained in Par. 5.1.2.3. A 5 parameters model was considered since it satisfactory fitted the experimental data (Figure 5.10). Also in this case a distinction must be made between the compressible and thr incompressible case. In the incompressible model only five material constant are required $(\mathtt{C01}, \mathtt{C10}, \mathtt{C11}, \mathtt{C02}, \mathtt{C20})$, while the incompressibility parameter $d$ is set to zero. Therefore in this case the engineering stress-strain curve is sufficient to describe the material. Without the assumption of complete material incompressibility, an additional volumetric test would be necessary. This test (Pressure-Volume-Temperature test – PVT test) characterizes the compressibility and volumetric expansion of the material by measuring the change in volume of the test sample due to a change in pressure (or temperature). The resultant volumetric strain-hydrostatic stress curve slope is the bulk modulus (hydrostatic stress = - bulk modulus * volumetric strain). The Mooney-Rivlin model have a single incompressibility constant $d$ in the volumetric term of the strain-energy potential. If a straight line is fit through the PVT test data, the incompressibility parameter $d$ can be calculated from the following relationship to the bulk modulus $K$:

$$d = \frac{2}{K}$$

*Equation 5.16*

where

$$K = \frac{E}{2(1-2\nu)}$$

*Equation 5.17*

Not being available the volumetric strain - hydrostatic stress curve, $d$ was estimated through the Poisson's ratio used for the linear compressible model.

### Ogden model

The eight parameters needed to describe the incompressible 4th order Ogden model was evaluated from the engineering stress-strain curve through the fitting process previously described (Figure 5.10).

For the compressible model implementation a higher order fit was desired for the incompressibility parameterd. This implies the use of the volumetric strain - hydrostatic stress curve, to perform a further curve fitting. In fact, for a 4th order Ogden model, the volumetric component will contain four incompressibility terms: $d_1, d_2, d_3$ and $d_4$.

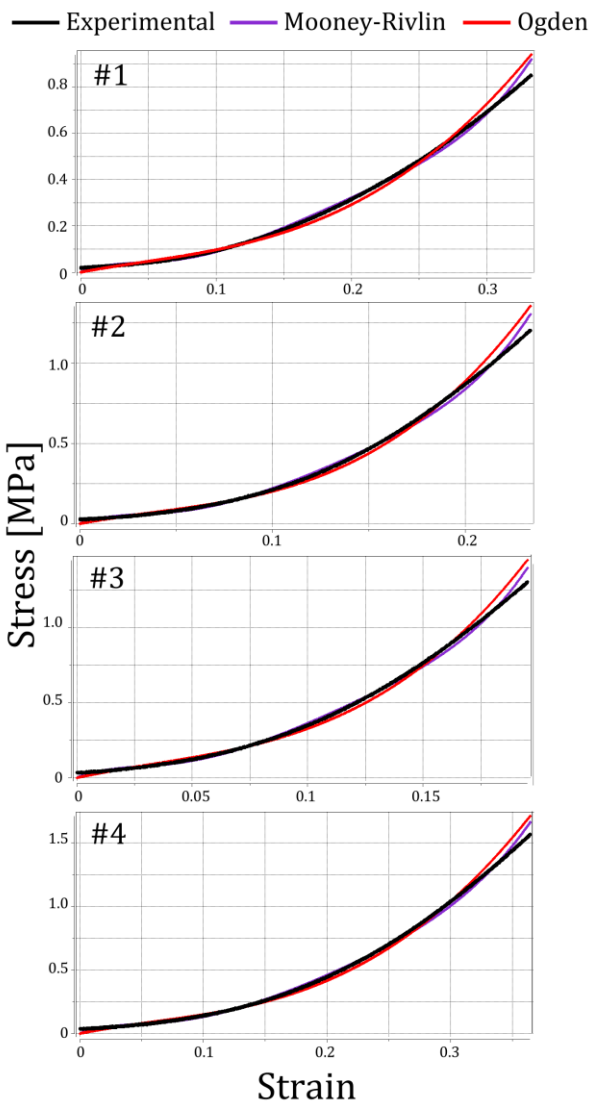


*Figure 5.10 Curve fitting results for all stress-strain curves considered (incompressible case).*

A one term approximation wasn't feasible in this case, hence the compressible Ogden model was excluded from the analysis. Tables 5.3-5.6 summarize the models parameters for the four experimental curves. Initial geometry, mesh entities and materials parameters are listed, together with the experimental curve used.

*Table 5.3 Models details of specimen #1.*

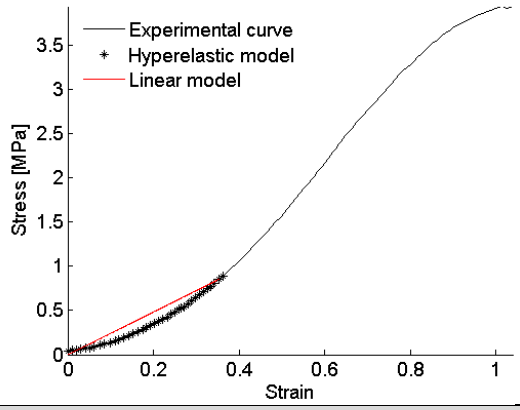


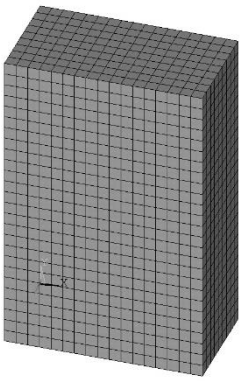

| | | | | | | |
|---|---|---|---|---|---|---|
| **Geometry** | | | | | | |
| Thickness | 2.219 [mm] | | | | | |
| Width | 4.093 [mm] | | | | | |
| Length | 6.447 [mm] | | | | | |
| **Mesh** | | | | | | |
| #nodes | 18504 | | | | | |
| #elements | 3978 | | | | | |
| **Materials properties** | | | | | | |
| *Linear elastic/Linear GNL* | | | | | | |
| Compressible | E=2.548 [MPa] | | | ν=0.376 | | |
| Incompressible | E=2.548 [MPa] | | | ν=0.499 | | |
| *Mooney-Rivlin model* | | | | | | |
| | *C10* | *C01* | *C20* | *C11* | *C02* | *d* |
| Compressible | -9.217 | 9.610 | 141.657 | -361.598 | 238.867 | 0.584 |
| Incompressible | -9.217 | 9.610 | 141.657 | -361.598 | 238.867 | 0 |
| *Ogden model* | | | | | | |
| Incompressible | *μ1* | *α1* | *μ2* | *α2* | | |
| | -63.128 | 1.760 | -61.449 | 1.755 | | |
| | *μ3* | *α3* | *μ4* | *α4* | | |
| | 47.352 | 2.630 | 199.010 | 0.478 | | |

*Table 5.4 Models details of specimen #2.*

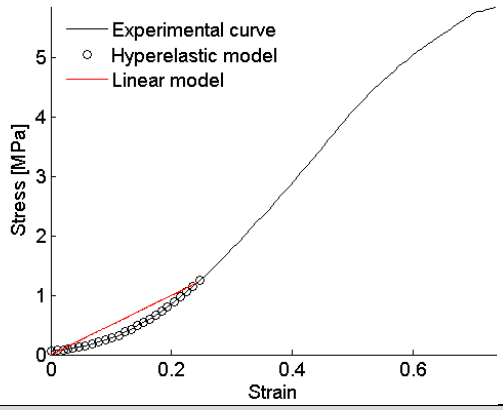


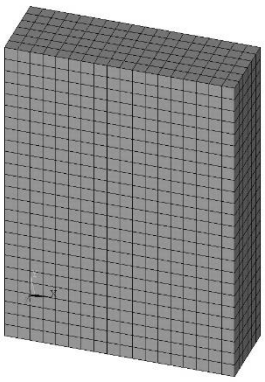

| | | | | | | |
|---|---|---|---|---|---|---|
| **Geometry** | | | | | | |
| Thickness | 1.477 [mm] | | | | | |
| Width | 4.434 [mm] | | | | | |
| Length | 6.242 [mm] | | | | | |
| **Mesh** | | | | | | |
| #nodes | 13023 | | | | | |
| #elements | 2700 | | | | | |
| **Materials properties** | | | | | | |
| *Linear elastic/Linear GNL* | | | | | | |
| Compressible | E=5.145 [MPa] | | | ν=0.330 | | |
| Incompressible | E=5.145 [MPa] | | | ν=0.499 | | |
| *Mooney-Rivlin model* | | | | | | |
| | *C10* | *C01* | *C20* | *C11* | *C02* | *d* |
| Compressible | -21.265 | 21.978 | 847.920 | -2030.700 | 1240.00 | 0.396 |
| Incompressible | -21.265 | 21.978 | 847.920 | -2030.700 | 1240.00 | 0 |
| *Ogden model* | | | | | | |
| Incompressible | *μ1* | *α1* | *μ2* | *α2* | | |
| | -173.710 | 2.002 | -173.000 | 2.003 | | |
| | *μ3* | *α3* | *μ4* | *α4* | | |
| | 130.540 | 3.005 | 560.120 | 0.542 | | |

*Table 5.5 Models details of specimen #3.*

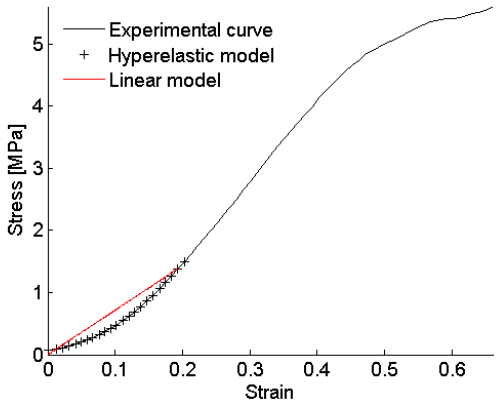


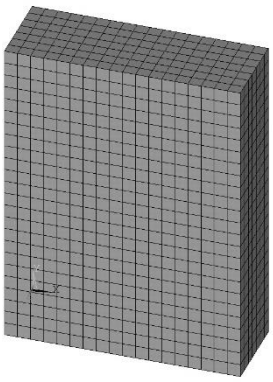

| **Geometry** | | | | | | |
|---|---|---|---|---|---|---|
| Thickness | 1.514 [mm] | | | | | |
| Width | 4.269 [mm] | | | | | |
| Length | 5.758 [mm] | | | | | |
| **Mesh** | | | | | | |
| #nodes | 14373 | | | | | |
| #elements | 3024 | | | | | |
| **Materials properties** | | | | | | |
| *Linear elastic/Linear GNL* | | | | | | |
| Compressible | E=6.838 [MPa] | | | ν=0.160 | | |
| Incompressible | E=6.838 [MPa] | | | ν=0.499 | | |
| *Mooney-Rivlin model* | | | | | | |
| | *C10* | *C01* | *C20* | *C11* | *C02* | *d* |
| Compressible | -32.908 | 33.908 | 1978.700 | -4648.000 | 2770.500 | 0.597 |
| Incompressible | -32.908 | 33.908 | 1978.700 | -4648.000 | 2770.500 | 0 |
| *Ogden model* | | | | | | |
| Incompressible | *μ1* | *α1* | *μ2* | *α2* | | |
| | -72738 | 0.884 | -15658 | 2.0741 | | |
| | *μ3* | *α3* | *μ4* | *α4* | | |
| | 46124 | 1.610 | 109730 | 0.2057 | | |

*Table 5.6 Models details of specimen #4.*

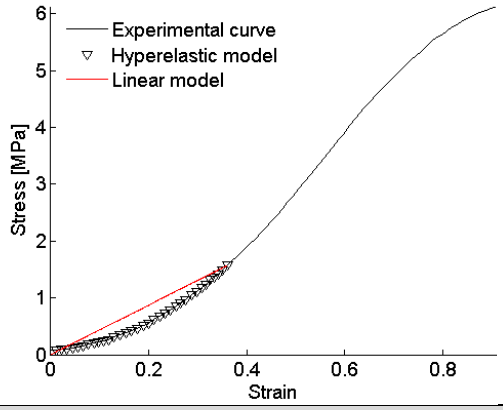


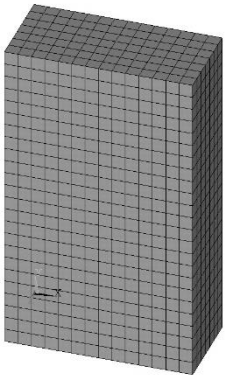

| | | | | | | |
|---|---|---|---|---|---|---|
| **Geometry** | | | | | | |
| Thickness | 1.608 [mm] | | | | | |
| Width | 3.407 [mm] | | | | | |
| Length | 5.884 [mm] | | | | | |
| **Mesh** | | | | | | |
| #nodes | 11305 | | | | | |
| #elements | 2352 | | | | | |
| **Materials properties** | | | | | | |
| *Linear elastic/Linear GNL* | | | | | | |
| Compressible | E=4.299 [MPa] | | | ν=0.380 | | |
| Incompressible | E=4.299 [MPa] | | | ν=0.499 | | |
| *Mooney-Rivlin model* | | | | | | |
| | *C10* | *C01* | *C20* | *C11* | *C02* | *d* |
| Compressible | -11.350 | 11.941 | 122.500 | -317.730 | 215.800 | 0.335 |
| Incompressible | -11.350 | 11.941 | 122.500 | -317.730 | 215.800 | 0 |
| *Ogden model* | | | | | | |
| Incompressible | *μ1* | *α1* | *μ2* | *α2* | | |
| | -36075 | 0.740 | -7639.100 | 1.722 | | |
| | *μ3* | *α3* | *μ4* | *α4* | | |
| | 22643 | 1.341 | 54986 | 0.173 | | |

### 5.2.3 Data Elaboration

The outputs of the simulations were analyzed and compared with experimental data through three parameters: the upper surface displacement (elongation), the necking area and the mean stress along the vertical direction evaluated in the specimen middle section.

The upper surface displacement was the imposed condition for the experimental tests (see Chapter 2), while in the finite element analysis is an output consequence of the application of the load.

The necking area was extracted from the specimen transversal middle plane. In particular, the nodes of the perimeter were exported from Ansys and a numerical integration was performed in the Matlab environment. Results were compared with the experimental area measured through photogrammetry set up. It's recalled that the images from two orthogonal directions were captured during the experimental tests, with a frame rate of 0.33 Hz (Par. 2.3.2). Width and thickness of the specimen were then evaluated and, approximating the section to a rectangle, the area over time curve was obtained.

The mean stress $\sigma_y$ is the ratio between the load and the cross-section (i.e. the necking area). It was evaluate from the experimental data considering the true curves (Par. 2.3.4).

## 5.3 Results and Discussion

The general output of the finite element analysis are displacements and stress information for a deformed geometry. In the current study, displacements (in terms of deformed shape) and stresses were used to determine the best model through a comparison with the deformed shapes and the global stresses resulting from the experimental tests.

The outputs parameters of all the simulations are represented specimen by specimen in the following paragraphs. It was decided to represent data separately for each specimen, because of their high variability, both in terms of size and characteristic curves.

In the following histograms three groups of bars, relative to the three considered parameters, contain the information of the four models, which should be compared with the experimental results depicted in white. It can be noted in some cases the absence of results regarding the linear GNL (linear elastic with geometric nonlinearity) model. This is due to the impossibility of producing a converged solution when analyzing a linear material model which involves large deformation in a nonlinear system of equations. In fact, the geometric nonlinearity produced an excessive elements distortion: it can be noted a general trend to achieve greater elongations (and consequently lower necking areas) for linear models which enable large deformations. Less distortions were found in the hyperelastic models, which didn't have troubles to converge under any circumstances. Obviously, the convergence of the linear model is granted.

Regarding the linear GNL models, specimen #1 only bore 82.4% of the applied force (8.24 N) in the incompressible case, and 95.5% (9.55 N) in the compressible case. Specimen #4 linear GNL models obtained convergence only for 79.5% of the applied force (7.95 N) in the incompressible case, but succeeded to converge in the compressible case, though reaching high elongations, and therefore high element distortions.

It is recalled that the compressible Ogden model was excluded from consideration (Par. 5.2.2).

### 5.3.1 Specimen #1

Incompressible models

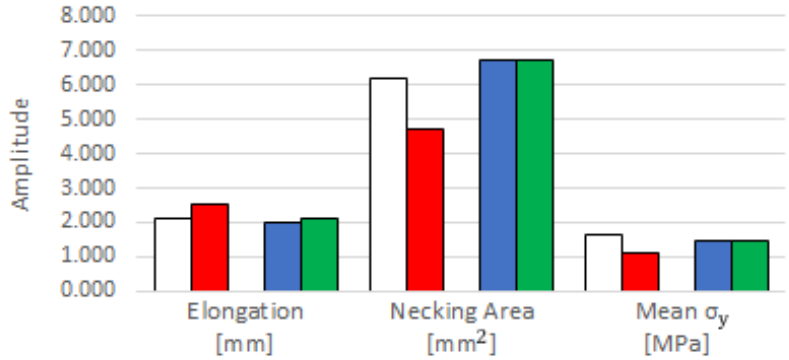


| | Elongation [mm] | Necking Area [mm²] | Mean $\sigma_y$ [MPa] |
|---|---|---|---|
| Experimental | 2.143 | 6.160 | 1.623 |
| Linear | 2.521 | 4.709 | 1.086 |
| Linear GNL | | | |
| Mooney-Rivlin | 2.005 | 6.724 | 1.447 |
| Ogden | 2.106 | 6.701 | 1.473 |

Compressible models

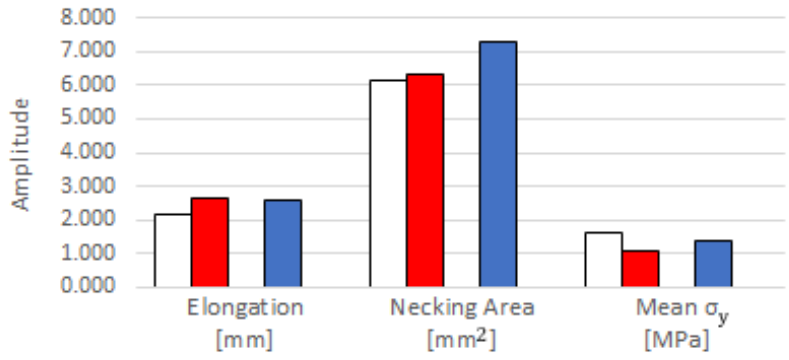


| | Elongation [mm] | Necking Area [mm²] | Mean $\sigma_y$ [MPa] |
|---|---|---|---|
| Experimental | 2.143 | 6.160 | 1.623 |
| Linear | 2.653 | 6.342 | 1.087 |
| Linear GNL | | | |
| Mooney-Rivlin | 2.605 | 7.288 | 1.368 |

*Figure 5.11 Specimen #1 parameter results for incompressible (top) and compressible (bottom) models.*

### 5.3.2 Specimen #2

Incompressible models

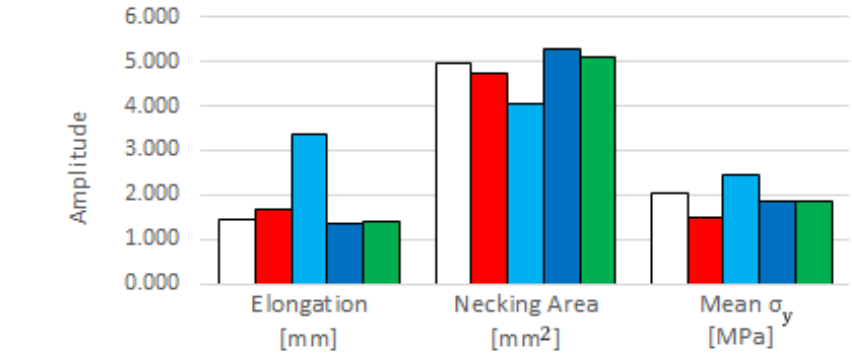


| | Elongation [mm] | Necking Area [mm²] | Mean $\sigma_y$ [MPa] |
|---|---|---|---|
| Experimental | 1.460 | 4.947 | 2.021 |
| Linear | 1.688 | 4.749 | 1.502 |
| Linear GNL | 3.362 | 4.056 | 2.467 |
| Mooney-Rivlin | 1.370 | 5.262 | 1.845 |
| Ogden | 1.413 | 5.091 | 1.876 |

Compressible models

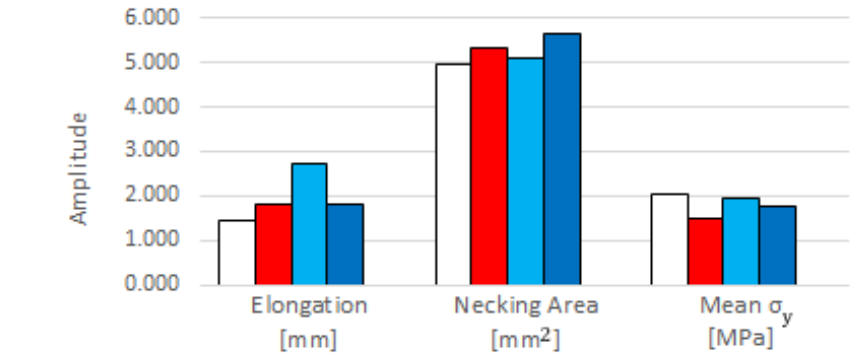


| | Elongation [mm] | Necking Area [mm²] | Mean $\sigma_y$ [MPa] |
|---|---|---|---|
| Experimental | 1.460 | 4.947 | 2.021 |
| Linear | 1.788 | 5.322 | 1.508 |
| Linear GNL | 2.717 | 5.091 | 1.954 |
| Mooney-Rivlin | 1.812 | 5.653 | 1.765 |

*Figure 5.12 Specimen #2 parameter results for incompressible (top) and compressible (bottom) models.*

### 5.3.3 Specimen #3

Incompressible models

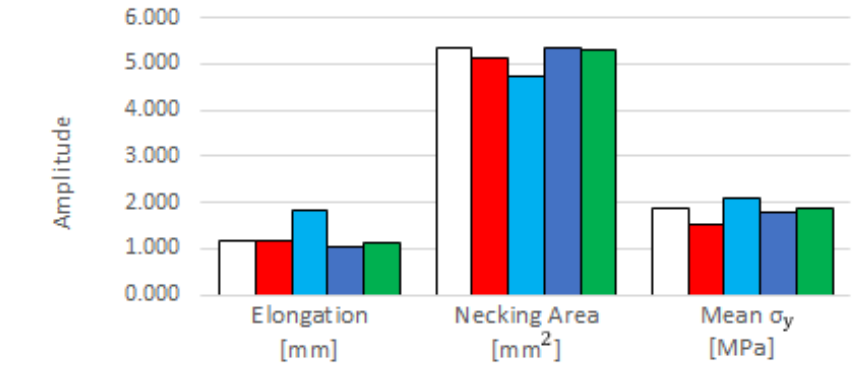


| | Elongation [mm] | Necking Area [mm²] | Mean $\sigma_y$ [MPa] |
|---|---|---|---|
| Experimental | 1.159 | 5.365 | 1.864 |
| Linear | 1.180 | 5.130 | 1.515 |
| Linear GNL | 1.834 | 4.751 | 2.096 |
| Mooney-Rivlin | 1.034 | 5.369 | 1.778 |
| Ogden | 1.137 | 5.296 | 1.857 |

Compressible models

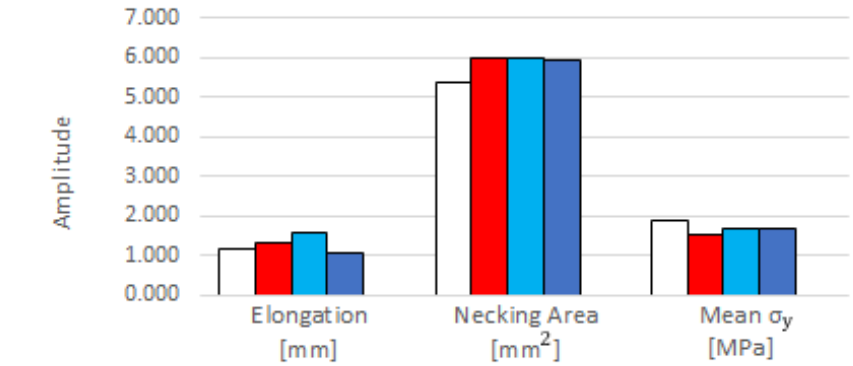


| | Elongation [mm] | Necking Area [mm²] | Mean $\sigma_y$ [MPa] |
|---|---|---|---|
| Experimental | 1.159 | 5.365 | 1.864 |
| Linear | 1.292 | 6.001 | 1.535 |
| Linear GNL | 1.565 | 5.977 | 1.665 |
| Mooney-Rivlin | 1.034 | 5.938 | 1.680 |

*Figure 5.13 Specimen #3 parameter results for incompressible (top) and compressible (bottom) models.*

### 5.3.4 Specimen #4

Incompressible models

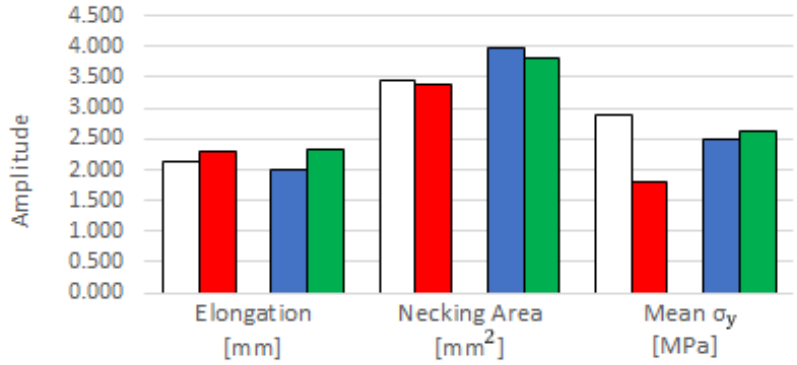


| | Elongation [mm] | Necking Area [mm²] | Mean $\sigma_y$ [MPa] |
|---|---|---|---|
| Experimental | 2.145 | 3.461 | 2.889 |
| Linear | 2.291 | 3.386 | 1.808 |
| Linear GNL | | | |
| Mooney-Rivlin | 1.999 | 3.982 | 2.478 |
| Ogden | 2.328 | 3.801 | 2.619 |

Compressible models

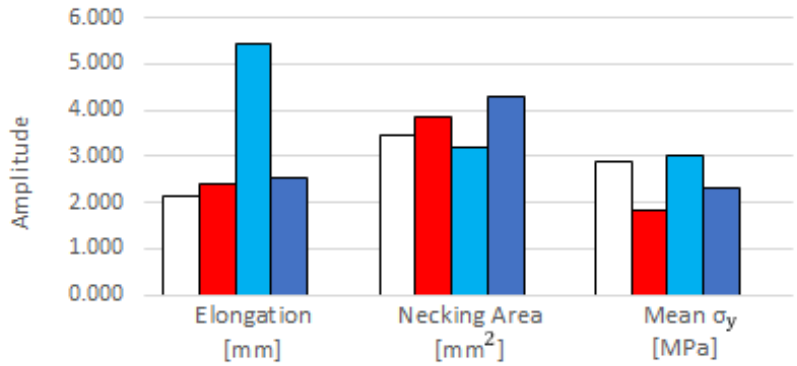


| | Elongation [mm] | Necking Area [mm²] | Mean $\sigma_y$ [MPa] |
|---|---|---|---|
| Experimental | 2.145 | 3.461 | 2.889 |
| Linear | 2.393 | 3.840 | 1.809 |
| Linear GNL | 5.425 | 3.211 | 3.018 |
| Mooney-Rivlin | 2.519 | 4.305 | 2.320 |

*Figure 5.14 Specimen #4 parameter results for incompressible (top) and compressible (bottom) models.*

Besides numerical values, further considerations can be extracted from the analysis of obtained deformed shapes. The deformed shape of the incompressible and the compressible models are represented in the following by:

- the projection of the deformed shape of the four models in the frontal plane, with the indication of the initial undeformed geometry (black square) (Figure 5.15 left);
- the necking area perimeters extracted from the models middle plane, with the indication of the initial undeformed cross-section (black square) (Figure 5.15 right).

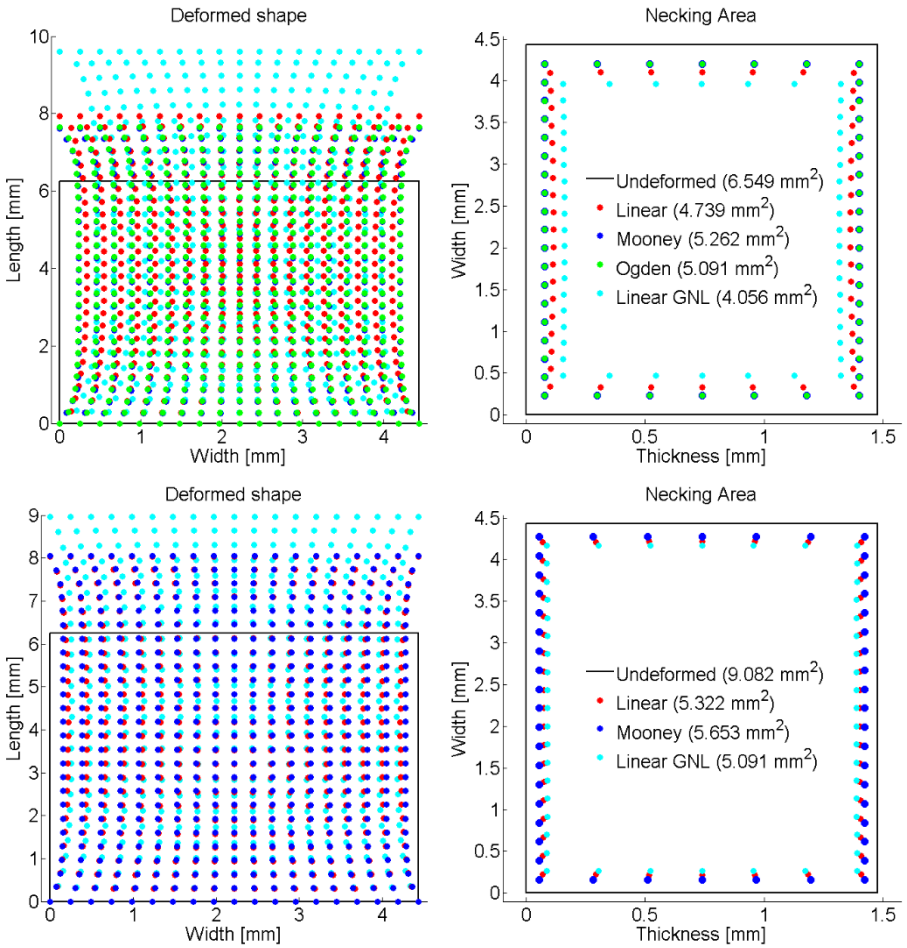


*Figure 5.15 Deformed shapes and necking areas for the four models in the incompressible (top) and compressible (bottom) cases. Results are referred to specimen #2.*

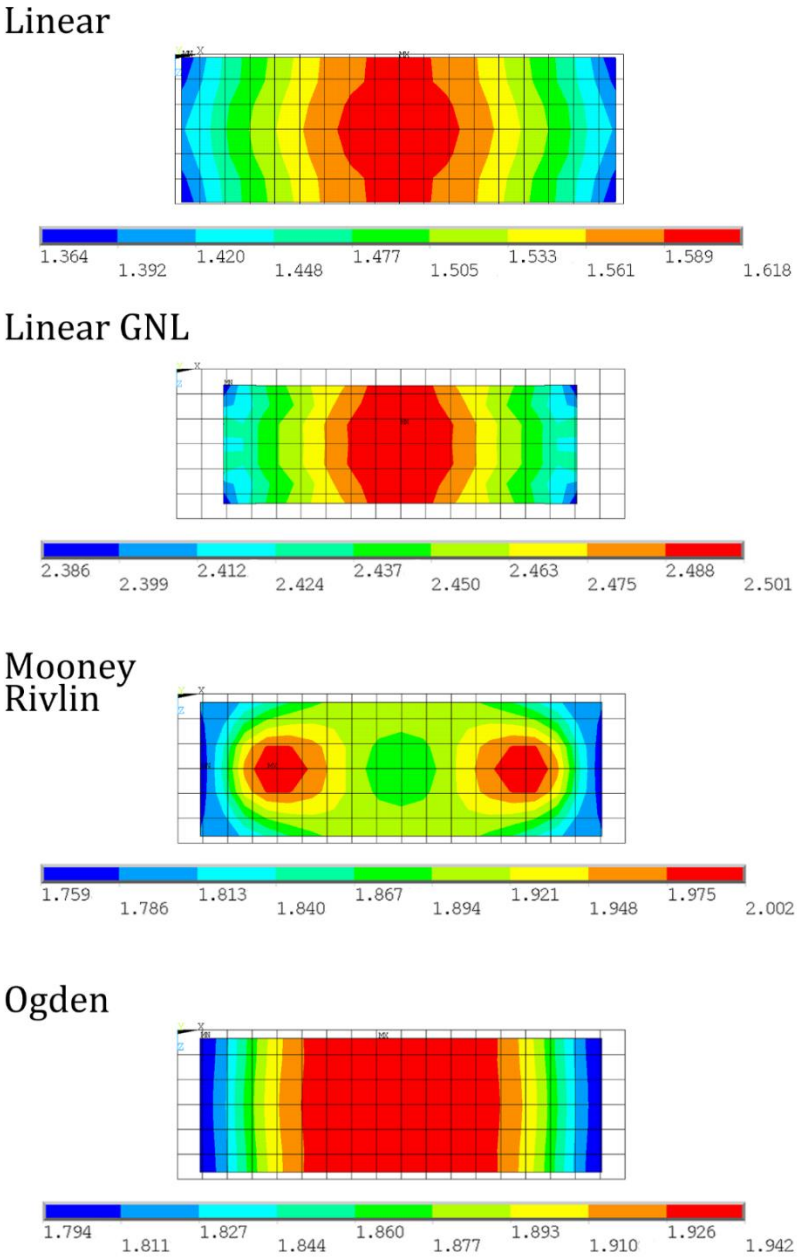


*Figure 5.16 Specimen #2, incompressible models: stress distribution along the y direction in the necking area [MPa]. The gridded area represents the undeformed mesh.*

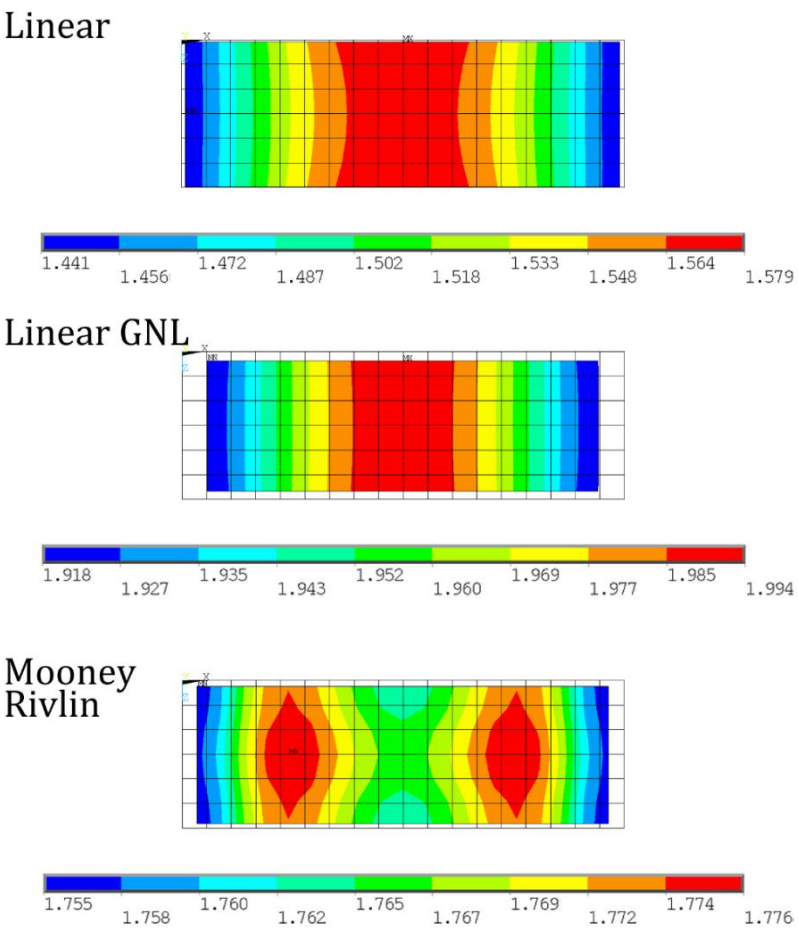


*Figure 5.17 Specimen #2, compressible models: stress distribution along the y direction in the necking area [MPa]. The gridded area represents the undeformed mesh.*

Figures 5.16 and 5.17 show the $\sigma_y$ distributions in the necking area. Quantitatively speaking, all nonlinear models reach higher stress values than the linear elastic model. This is due to the stress calculation method in the linear elastic model. In fact, it uses the undeformed cross-section, being its main hypothesis the presence of only small deformations. This assumption leads to the underestimation of the average value of stress, which occurs systematically in all linear models results (Figures 5.11-5.14). On the contrary, the linear GNL model always overestimate the average stress value. This happens due to the large deformations in terms of elongation, and consequently in terms of necking, which take place in

these types of models. The two hyperelastic models reach similar stress mean values in correspondence of the necking area. However, the stress distributions in the core of the specimen are totally different: the Ogden model shows a large volume of the model having a quite constant stress value, while the Mooney-Rivlin model shows a characteristic distribution constituted by two symmetrical regions with higher stress values, surrounded by lower values of stress that extend to the very core of the specimen.

Figures 5.11, 5.12 and 5.13 shows the specimen #2 results. The latter was taken as an example, since it produced a converged solution for all models. To simplify the discussion, the results concerning the other three specimens are represented in the Supplementary Material section (Par. 5.6).

Considering all the results as a whole, a comparison can be made considering the percentage errors committed by each model with respect to the experimental test, showed in Figures 5.18 and 5.19. The linear elastic models have relatively low errors, but this result falls within the expectations. In fact, the linear material was built exactly on the stress-strain point corresponding to the imposed boundary condition (F=10N). So it is obvious to fall into an acceptable result in terms of the parameters related to the deformations outputs. As mentioned, however, an underestimation of the stress values is obtained, and it should be remembered that this linear models would lead to higher errors imposing different boundary conditions (being equal the material parameters). The linear GNL model, which enable large deformations, causes an overestimation of the elongation parameter, which ranges between the 35÷153% of the experimental value. Lower percentage errors are committed in the compressible case, and this is the reason why the compressible linear GNL models produce more easily a converged solution then the incompressible ones.

Finally, the hyperelastic models shows lower errors with respect to the experimental results, except for the Mooney-Rivlin compressible

model. The simplifying assumptions made for the definition of the compressibility is therefore deleterious to the model, and it is thus preferable the choice of an incompressible model.

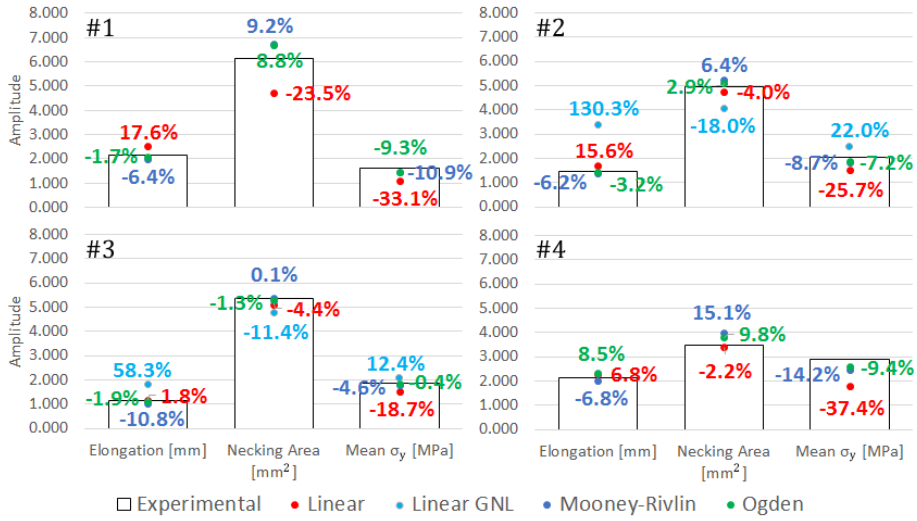


*Figure 5.18 Percentage errors committed by each incompressible model with respect to the experimental results.*

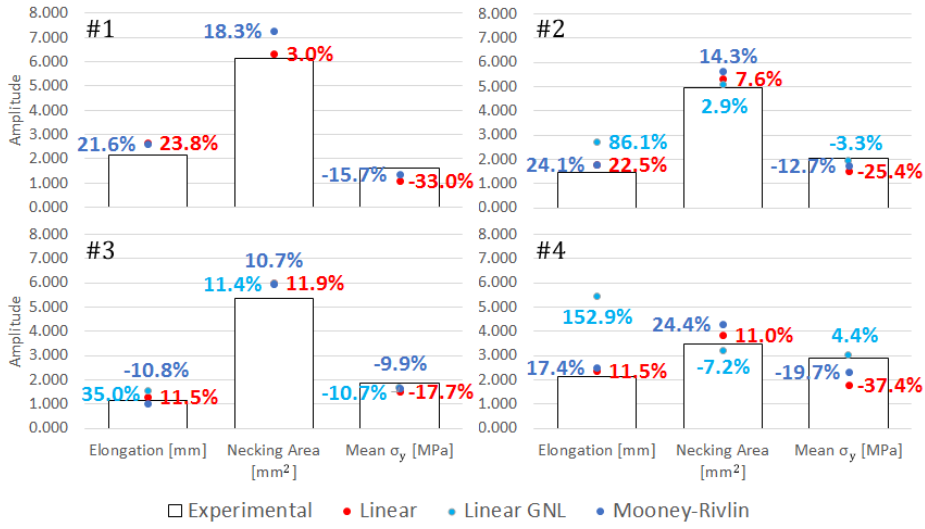


*Figure 5.19 Percentage errors committed by each compressible model with respect to the experimental results.*

Table 5.7 lists the average percentage errors for each model. It is clear that despite the linear GNL model shows lower average percentage

errors for two parameters out of three (necking area and the mean $\sigma_y$), the high overestimation of the third parameter makes the model not suitable to the description of the uniaxial solicitation of a biological specimen. Conversely, the Ogden incompressible model showed on average behaviour close to the experimental reality.

*Table 5.7 Average percentage errors in relation to the experimental results for each incompressible (I.) and compressible (C.) model.*

| | Linear Elastic | | Linear Elastic GNL | | Mooney-Rivlin | | Ogden |
|---|---|---|---|---|---|---|---|
| | I. | C. | I. | C. | I. | C. | I. |
| Elongation | 10.47% | 17.33% | 94.27% | 91.35% | 7.545% | 18.46% | 3.84% |
| Necking Area | 8.57% | 8.34% | 14.72% | 7.18% | 7.67% | 16.92% | 6.17% |
| Mean $\sigma_y$ | 28.74% | 28.37% | 17.23% | 6.15% | 9.62% | 14.48% | 6.55% |

The final point of interest regards the comparison between the global and the local deformation of the specimen. In fact, in a uniaxial experimental test it is usually considered a global behavior through a stress-strain curve evaluated from the global displacement of the upper crosshead of the testing machine (namely, the upper surface of the specimen) and the load recorded by the testing machine sensors. This is the typical procedure for the isotropic materials in which, with a good approximation, the overall behavior can be correlated to the local one. Anyway, it is not always applicable in cases where the material is highly anisotropic. That's why the identification of the regions in which the local and global deformations coincide is of great interest. Considering specimen #2 as a representative example, Table 5.8 lists the global deformations evaluated from the initial and final specimen lengths of both the experimental data and the finite element models.

*Table 5.8 Global deformations calculated from the initial and final specimen length (I. = incompressible models; C.= compressible models).*

| | Experimental | Linear Elastic | Linear Elastic GNL | Mooney-Rivlin | Ogden |
|---|---|---|---|---|---|
| I. | 23.4 % | 27.0% | 53.9% | 22.0% | 22.6% |
| C. | | 28.6% | 43.5% | 29.0% | - |

Analysing the local εy distributions in the hyperelastic incompressible models (Figure 5.20), a large volume of the specimen core has a deformation comparable to the global one (23.4%). Each other model has only small areas near the constraint points with deformations in the range 0.2-0.25, while in the core region higher strain values are reached.

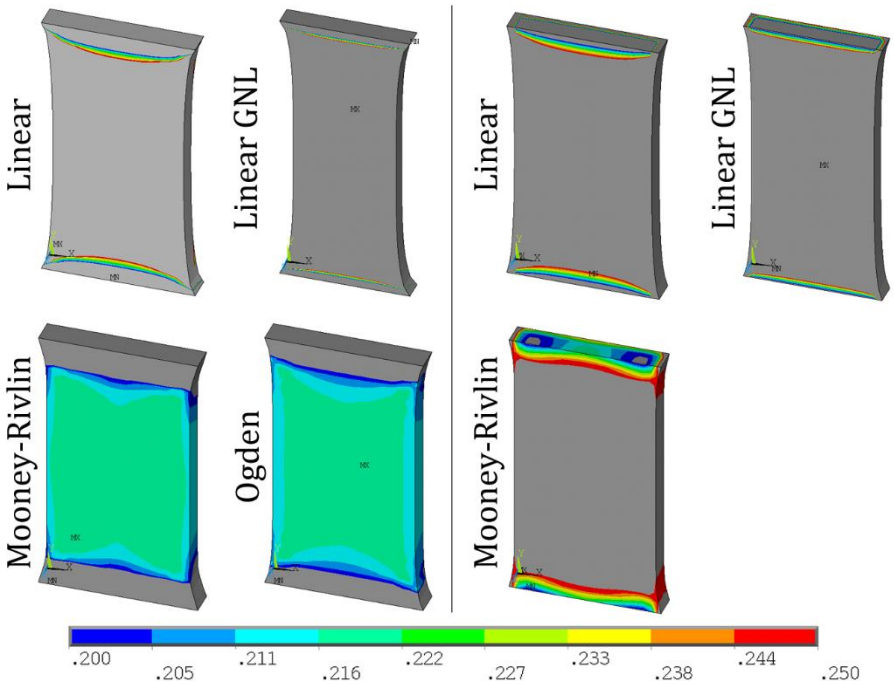


*Figure 5.20 Specimen #2: εy distribution in the range comprised between 20-25% for the incompressible (left) and compressible (right) models. All images represent a longitudinal section of the model.*

These results shows once again the more realistic behaviours of the incompressible hyperelastic models.

## 5.4 Conclusions

This work has exploited four uniaxial experimental data set to systematically implement and validate linear and nonlinear finite element models. The objective was not only to determine models parameters, but more importantly, to investigate the effects of different nonlinearities on three output parameters obtainable from experimental tests (deformation and global stress). It was found that the results obtained from

the hyperelastic models well represent the experimental situation, and in particular the incompressible Odgen model shows less than 7% percentage variations for all the considered parameters. It was then confirmed the inadequacy of the linear models to describe the behaviour of a biological material like dermis. In fact, either with a linear elastic model or with a linear model which enable the geometric nonlinearities, an acceptable solution can be found only calibrating the material parameters (elastic modulus and Poisson's ratio) on the applied load. Besides, the linear GNL model generates high distortions of the elements, which compromise the convergence of the simulation.

Despite the Ogden hyperelastic model resulted adequate to the description of a dermis specimen subjected to a uniaxial stress, it is based on an isotropic assumption which is in contrast with the biological materials high anisotropy. Thus, although the description of a specific state of stress could be appropriate, this will not be true with more complex stress configurations.

Nevertheless, the incompressible Ogden model is suitable for the description of the dermis behaviour when the isotropic assumption holds, such as in small deformation conditions.

## 5.5 References


Ansys Inc., 2013a. *ANSYS Mechanical APDL Theory Reference.* Canonsburg, PA: ANSYS, Inc..

Ansys Inc., 2013b. *ANSYS Mechanical APDL Element Reference.* Canonsburg, PA: s.n.

Ansys Inc., 2013c. *ANSYS Mechanical APDL Advanced Analysis Guide.* Canonsburg, PA: Ansys Inc..

Chabanas, M. et al., 2004. Comparison of linear and non-linear soft tissue models with post-operative CT scan in maxillofacial surgery. In: *Medical Simulation.* Cambridge: Springer Berlin Heidelberg, pp. 19-27.

Danielson, D., 1973. Human Skin as an Elastic Membrane. *Journal of Biomechanics,* Volume 6, pp. 539-546.

Evans, S. & Holt, C., 2009. Measuring the mechanical properties of human skin in vivo using digital image correlation and finite element modelling. *Journal of Strain Analysis for Engineering Design,* 44(5), pp. 337-345.

Gorash, Y., Comlekci, T. & Hamilton, R., 2015. *CAE-based application for identification and verification of hyperelastic parameters.* s.l., Journal of Materials: Design and Applications. .

Hendriks, F. et al., 2003. A numerical-experimental method to characterize the non-linear mechanical behaviour of human skin. *Skin Research and Technology,* 9(3), pp. 274-283.

Liu, Y., Kerdok, A. & Howe, R., 2004. *A Nonlinear Finite Element Model of Soft Tissue Indentation.* Cambridge, Springer-Verlag.

Manan, N. et al., 2012. *Determining Hyperelastic Parameters of Human Skin Using 2D Finite Element Modelling and Simulation.* Kuala Lumpur, IEEE.

Miller, K. & Chinzei, K., 2002. Mechanical properties of brain tissue in tension. *Journal of Biomechanics,* 35(4), pp. 483-490.

Molinari, E. et al., 2005. Simulation of the Biomechanical Behavior of the Skin in Virtual Surgical Applications by Finite Element Method. *IEEE Transactions on Biomedical Engineering,* Volume 52, pp. 1514-1521.

Tong, P. & Fung, Y., 1976. The stress-strain relationship for the skin.. *Journal of Biomechanics,* 9(10), pp. 649-657.

## 5.6 Supplementary Material

Incompressible models

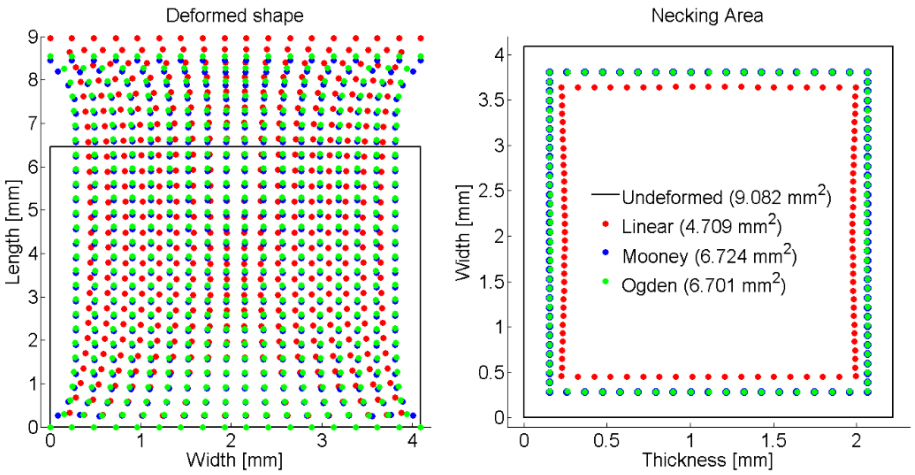


*Figure 5.21 Deformed shape of the incompressible models for the specimen #1.*

Compressible models

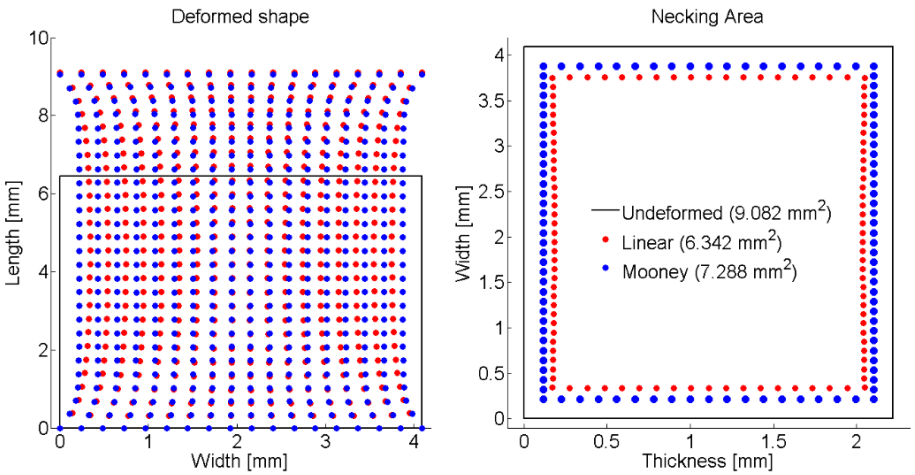


*Figure 5.22 Deformed shape of the compressible models for the specimen #1.*

Incompressible models

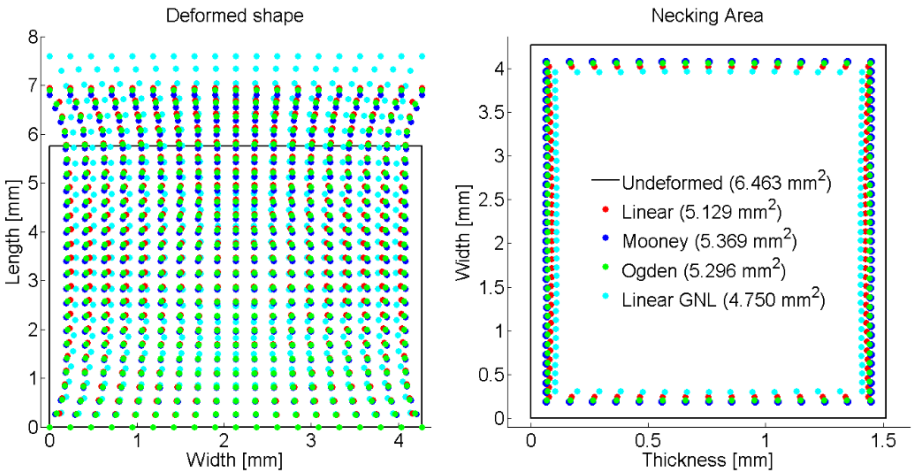


*Figure 5.23 Deformed shape of the incompressible models for the specimen #3.*

Compressible models

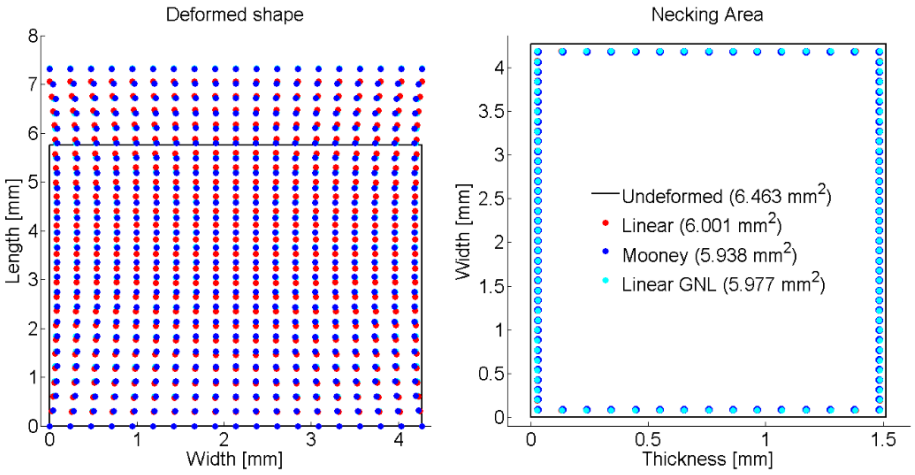


*Figure 5.24 Deformed shape of the compressible models for the specimen #3.*

Incompressible models

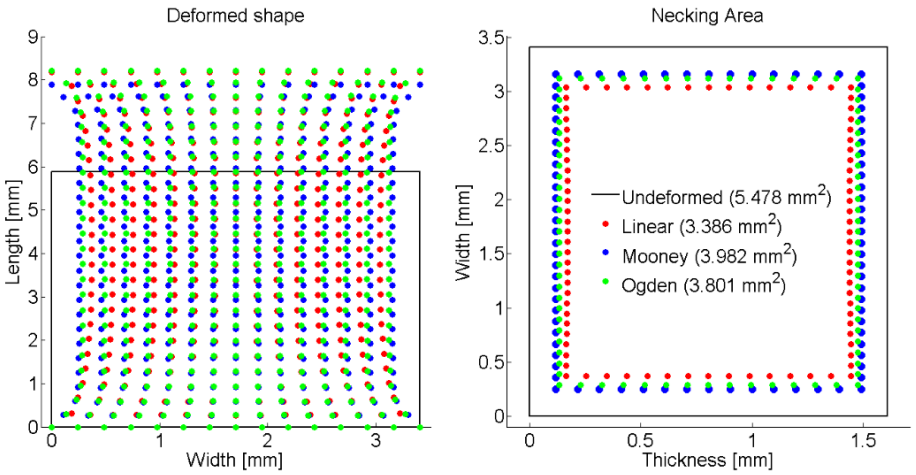


*Figure 5.25 Deformed shape of the incompressible models for the specimen #4.*

Compressible models

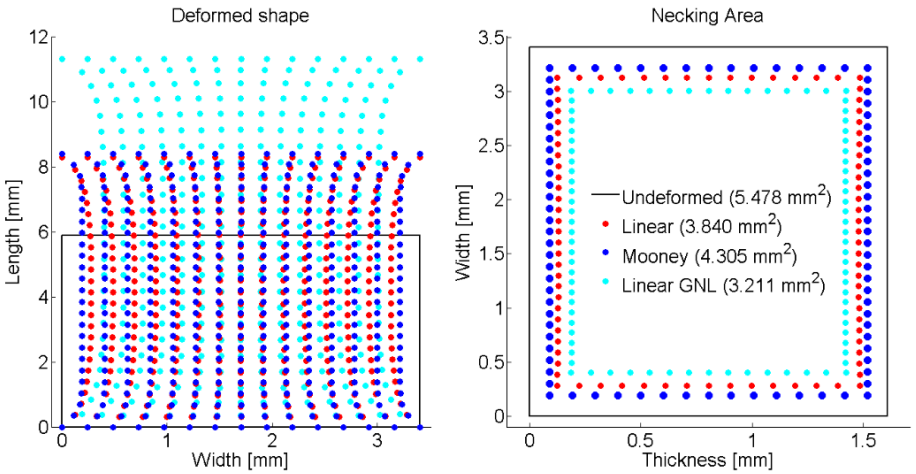


*Figure 5.26 Deformed shape of the compressible models for the specimen #4.*

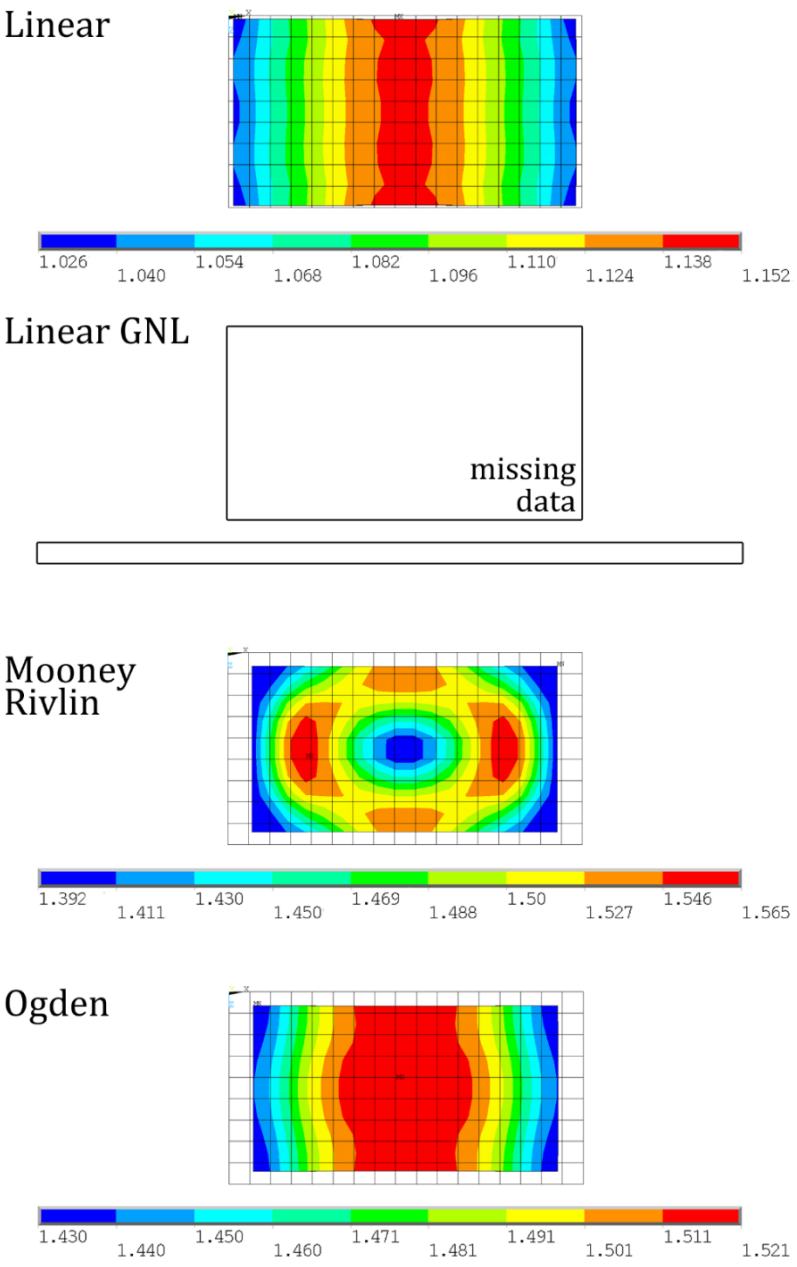


*Figure 5.27 Specimen #1, incompressible models: stress distribution along the y direction in the necking area [MPa]. The gridded area represents the undeformed mesh.*

Compressible models

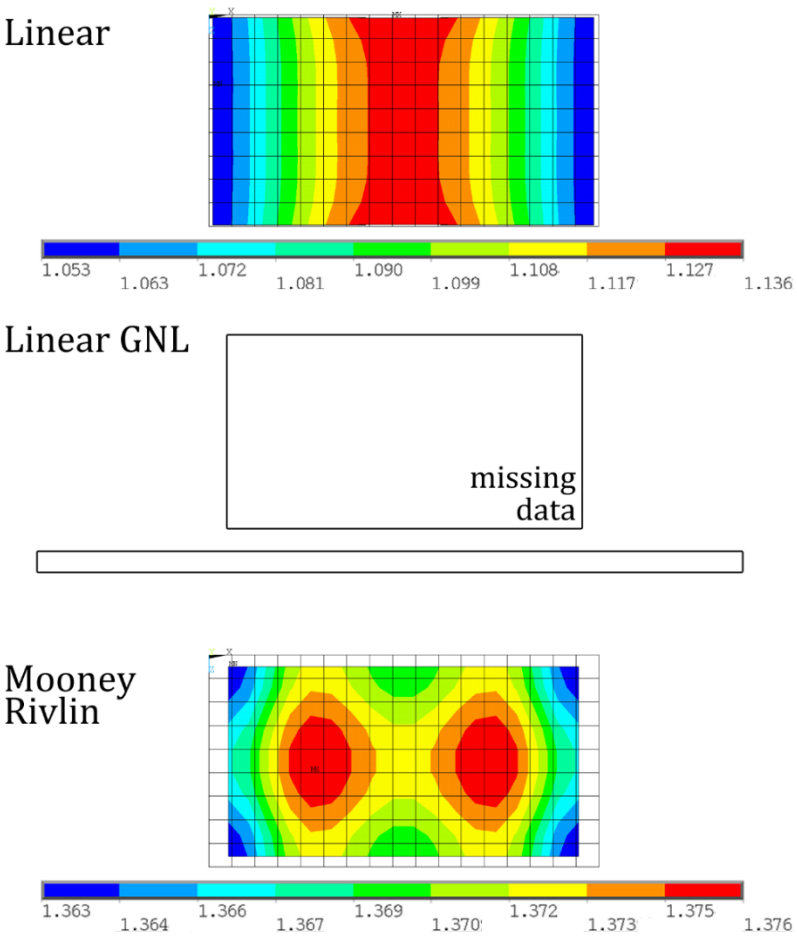


*Figure 5.28 Specimen #1, compressible models: stress distribution along the y direction in the necking area [MPa]. The gridded area represents the undeformed mesh.*

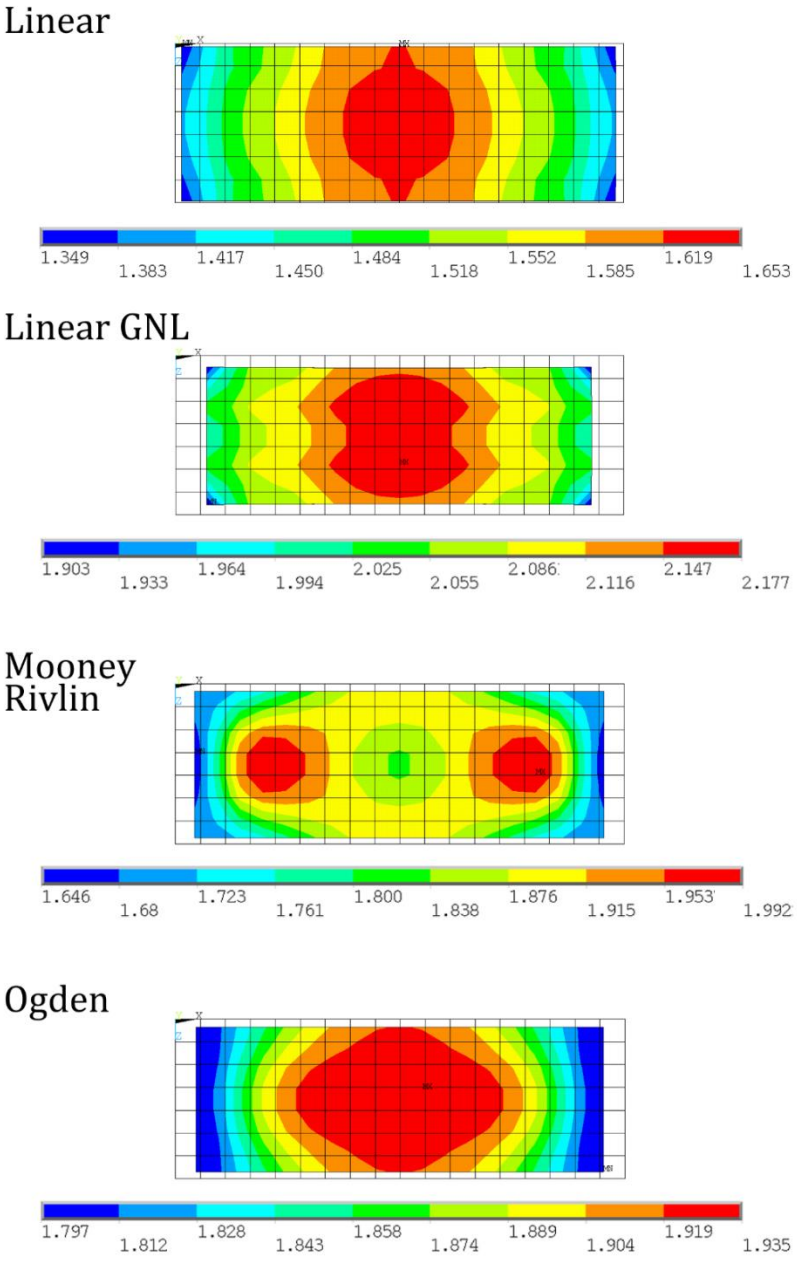


*Figure 5.29 Specimen #3, incompressible models: stress distribution along the y direction in the necking area [MPa]. The gridded area represents the undeformed mesh.*

Compressible models

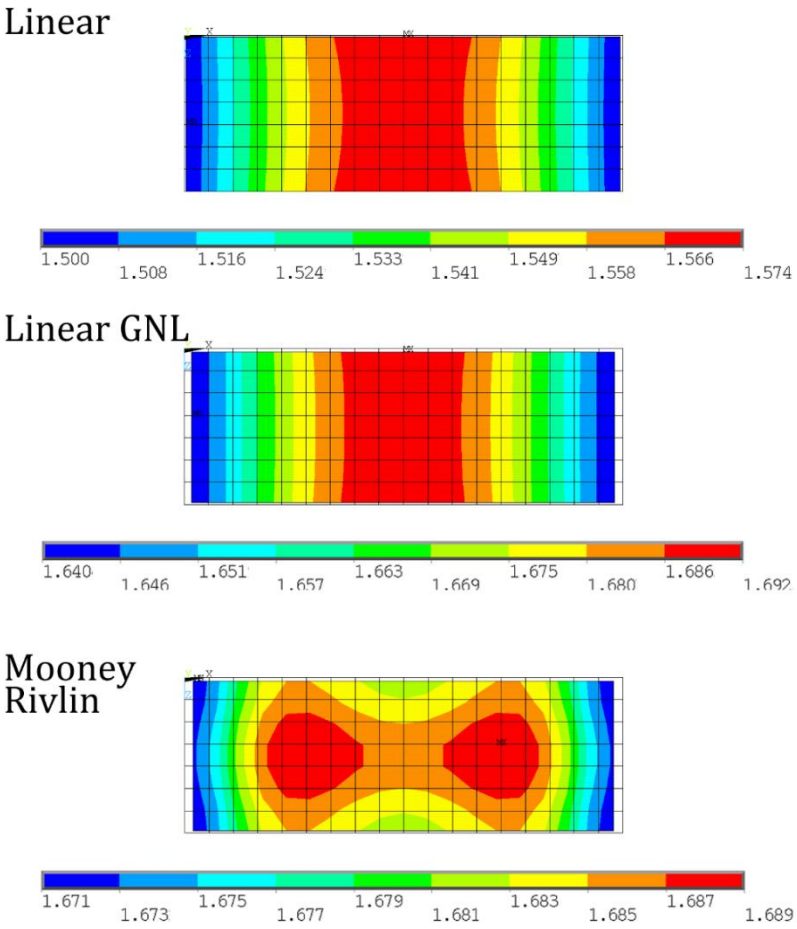


*Figure 5.30 Specimen #3, compressible models: stress distribution along the y direction in the necking area [MPa]. The gridded area represents the undeformed mesh.*

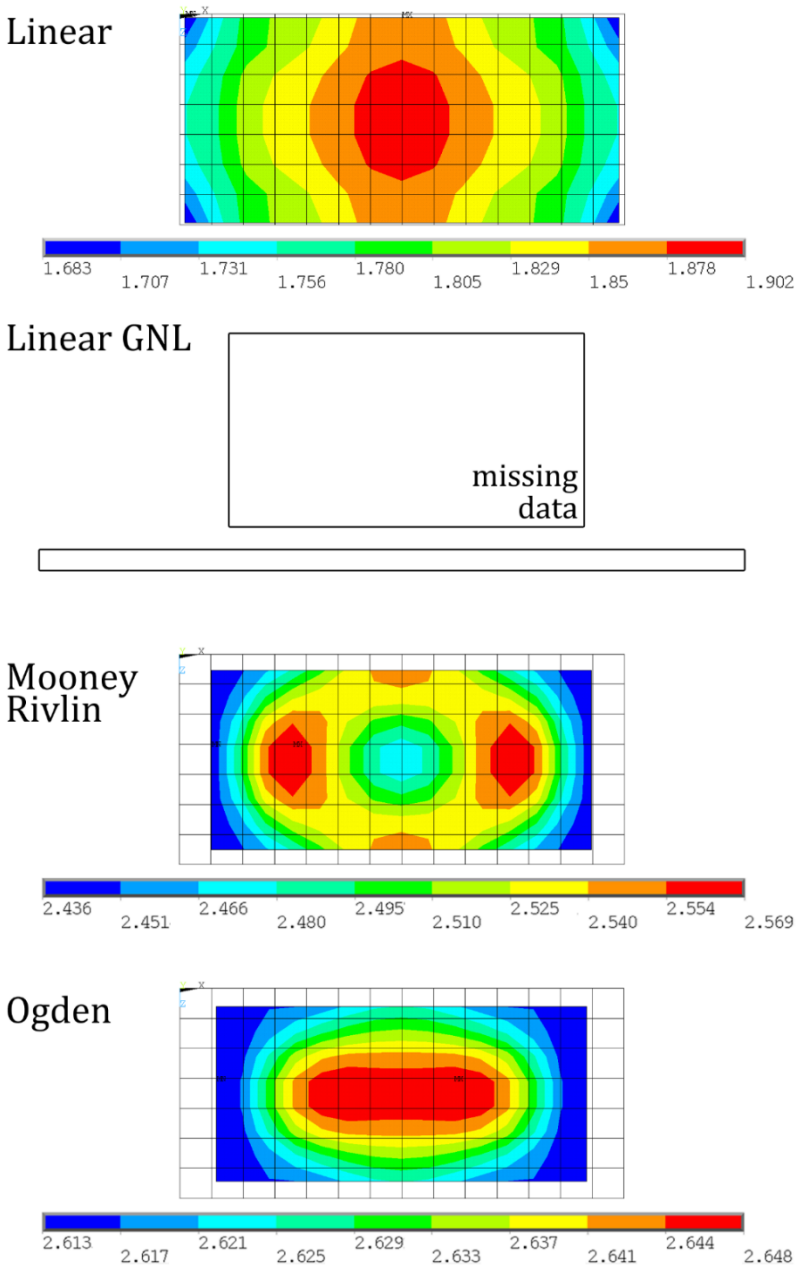


*Figure 5.31 Specimen #4, incompressible models: stress distribution along the y direction in the necking area [MPa]. The gridded area represents the undeformed mesh.*

Compressible models

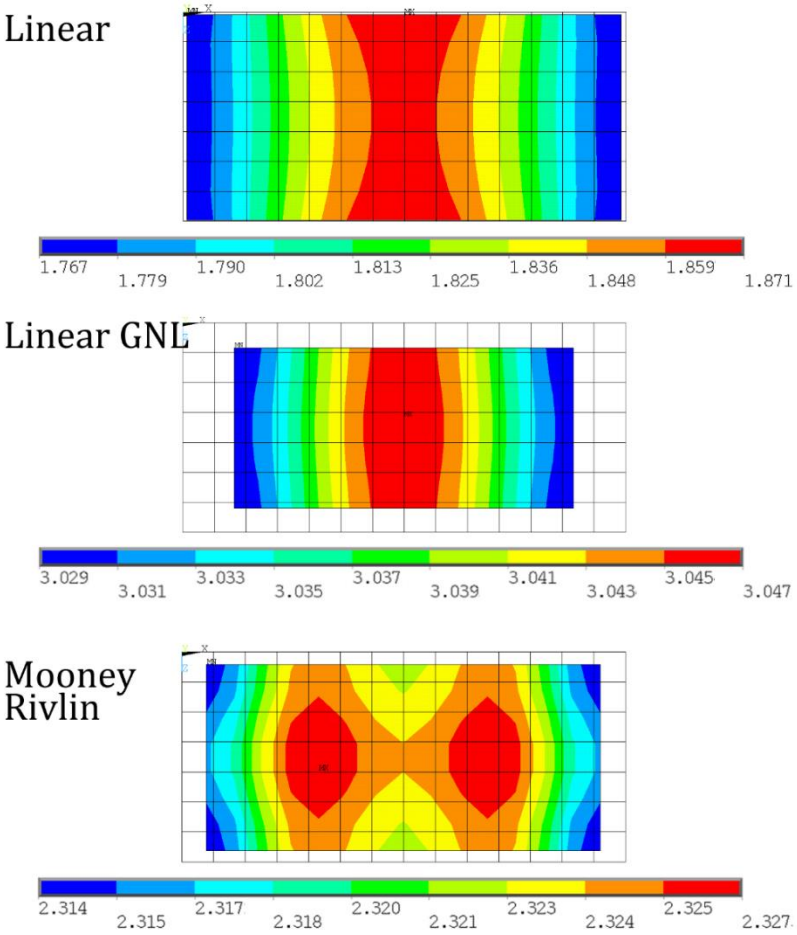


*Figure 5.32 Specimen #4, compressible models: stress distribution along the y direction in the necking area [MPa]. The gridded area represents the undeformed mesh.*

# Chapter 6

# Design of a equibiaxial fixture for biological tissues characterization

## 6.1 A review of planar biaxial tensile test systems for soft tissues

In the literature several examples of biaxial systems or uniaxial tensile machine conversion systems can be found, and generally this devices can be classified into two large families:

- multiple actuation systems;
- single actuation systems.

Any device made by the same number of actuators and load cells fall within the first family, and in this cases the two loading directions can operate independently. The main quality of this devices is the ability to reproduce precisely a wide range of stress states, at the cost of a high economic investment.

A single actuation biaxial fixture for a uniaxial tensile machine is extremely advantageous from the economic point of view, being the cost of implementation definitely lower with respect to the first family of devices. Moreover the possibility to exploit the same testing machine both for uniaxial and biaxial characterizations enhances the machine on which the fixture is housed.

### 6.1.1 Multiple actuation systems

Both commercial devices and custom made solutions can be classified in the multiple actuation systems family. Many commercial apparatuses for the biaxial characterization of materials are available in the market, although not all of them can be adapted to the characterization of soft tissues. In fact oversized frames and limitation on the lowest measurable load make unusable commercial solutions implemented by Instron® or MTS®, as well as custom made devices such as those described by Makinde (1992) and Smits (2006). Table 6.1 lists the multiple actuation systems available for soft tissues characterization.

*Table 6.1 Multiple actuation systems for soft tissues characterization*

| | |
|---|---|
| Zwuik/Roell<br><br>The mediX0.1 biaxial testing machine is designed for mechanical testing of natural and artificial tissues.<br>Maximum test load: 100 N<br>Strain control: laser extensometer (laserX-tens)<br>Attachment systems: hook-and-suture | 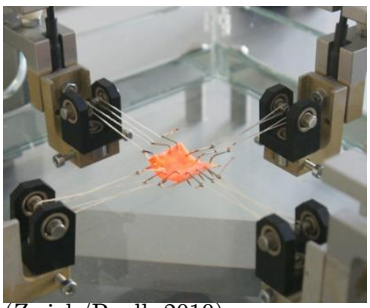 <br>(Zwick/Roell, 2010) |
| CellScale Biomaterials Testing<br><br>The BioTester is a test instrument designed to characterize soft tissues and biomaterials.<br>Maximum test load: 23 N<br>Strain control: high resolution CCD camera to collect time synchronized images for post test analysis<br>Attachment systems: hook-and-suture or grip based |  <br>(CellScale, 2013) |

### TA ElectroForce

The ElectroForce planar biaxial TestBench instrument is designed for soft tissue characterization. It consists of two linear motors and two reaction brackets mounted on a horizontal baseplate with two load cells, one for each axis of loading.

Maximum test load: 200 N

Strain control: with Digital Video Extensometer (DVE)

Attachment systems: hook and clamp tensile grips

(Electroforce, 2014)

### TESTRESOURCES

574LE2 Biomechanics and Tissue Tester is a configurable electrodynamic test system featuring four independent modular dynamic servo actuators.

Maximum test load: 250 N

Strain control: E-VID digital video extensometer camera

Attachment systems: hook and clamp tensile grips

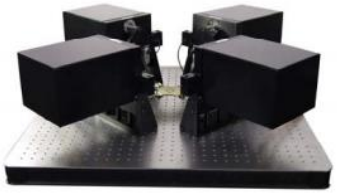

(TESTRESOURCES, 2016)

### Grashow et al (2006)

Biaxial testing rig made by four screw-driven linear actuators and two load cells.

Maximum test load: 2.45 N

Strain control: marker deformations measured optically

Attachment systems: two loops of 000 nylon suture to each side of the specimen

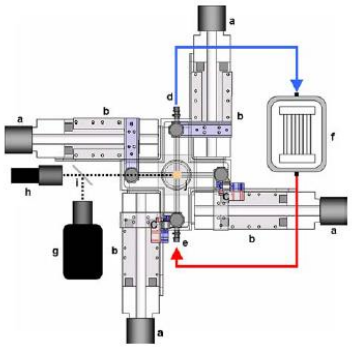

(Grashow, et al., 2006)

Johlitz & Diebels (2011)

The biaxial testing device contains four step engines which are arranged in a cruciform manner; the force measurement is realised by two force sensors.

Maximum test load: 100 N

Strain control: deformation of the measuring field is mapped with a camera Marlin F-131B

Attachment systems: clamp tensile grips

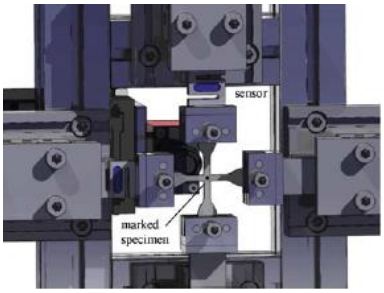


(Johlitz & Diebels, 2011)

Skulborstad (2013)

The biaxial testing apparatus consists of four Parker 402XE linear motion guides, each with 220 mm Travel.

Maximum test load: -

Strain control: Polarized Image Correlation

Attachment systems: suture loops

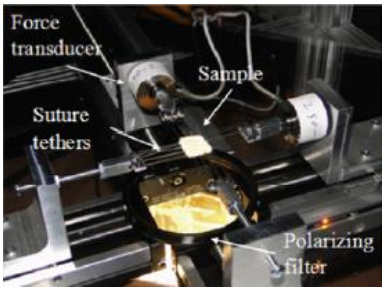


(Skulborstad , et al., 2015)

Zemànek et al (2009)

The testing rig consists of a bedplate carrying two orthogonal ball screws, equipped with force gauges, two servo motors and four carriages ensuring symmetric biaxial deformation of the specimen.

Maximum test load: -

Strain control: CCD camera

Attachment systems: clips

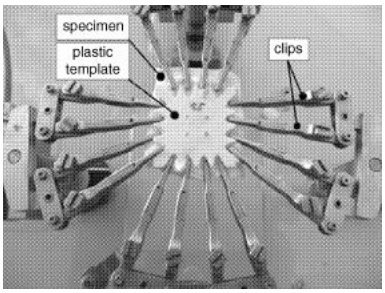


(Zemánek, et al., 2009)

### 6.1.2 Single actuation systems

In an attempt to reduce the cost associated with building multiple actuation test machines, attachments have been designed for existing machines such as tensile and compression testers for the purpose of biaxial testing. The most common biaxial test setup is that of converting a standard tensile machine. In Table 6.2 is presented a list of the existing mechanisms capable of converting a uniaxial movement into a biaxial motion. Dealing with conversion mechanisms, although in most cases they were implemented for the characterization of metal sheets, polymers

or fabrics, it would be easy to adjust them for the use in soft tissues characterization field.

*Table 6.2 Single actuation systems for soft tissues characterization*

| | |
|---|---|
| Duncan et al (1999)<br><br>The test fixture consists of pivoted scissor arms that resolve the machine crosshead movement into extension of the test specimen at ± 45° to the axis of the test machine. The total force measured on the pull rod of the test machine can be resolved into biaxial components through a geometrical correction factor.<br>Maximum test load: -<br>Strain control: video extensometry<br>Attachment systems: screwed clamps |  <br>(Duncan, 1999) |
| Prendergast et al (2003)<br><br>The biaxial rig was designed so that it could be used on a standard uniaxial Instron 1011 testing machine. It is equipped with one loed cell. High-strength fishing line was used for the cable network.<br>Maximum test load: -<br>Strain control: Digital camera image acquisition<br>Attachment systems: Crocodile clips, hooks | 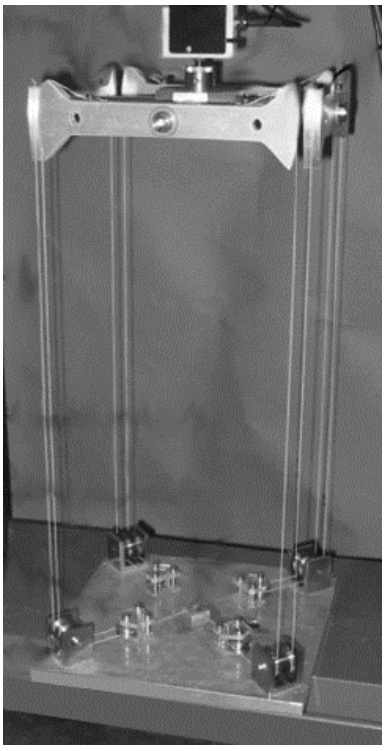 <br>(Lally , et al., 2004) |

Bathnagar (2007)

The mechanism is adapted on a uniaxial tension machine Instron 4302 and is capable of producing either equibiaxial or non-equibiaxial tension. The geometry is so designed that various stress ratios can be applied using a single set-up. The specimen is instrumented with rosette strain gages in order to measure the load in the horizontal direction.

Maximum test load: -

Strain control: Strain gages

Attachment systems: clamp tensile grips

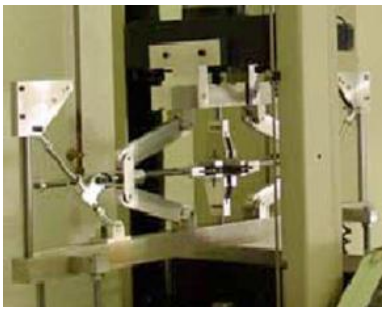

(Brieu, et al., 2007)

Cavallaro et al (2004)

Biaxial loading begins by moving the crosshead of the test machine in a downward vertical motion so that the machine applies a vertical load to the fixture. Doing so creates an equal extension along both two horizontal directions, resulting in biaxial tensile loads.

Maximum test load: -

Strain control: Strain gauges

Attachment systems: clamp tensile grips

(Cavallaro, et al., 2004)

## 6.2 Device requirements

Biaxial testing devices have to be much more elaborate then uniaxial ones because of the need to meet additional requirements, and the experimental problems increase being the test subject a biological tissue.

Being the cost competitiveness one of the main goals of this project, the adopted solution was conceived as an accessory to the uniaxial tensile machine, in order to take advantage of the machine own actuation and data acquisition systems, integrating the device with the missing sensors. Moreover the device has been entirely realized through rapid prototyping

methods (3D Printing) thus greatly reducing the cost of materials and machining. The used 3D printer is a Stratasys uPrint SE Plus (Stratasys Inc., Edina, Minnesota, United States) and its main specifications are listed in the following table.

*Table 6.3 uPrint SE Plus Product Specifications*

| | |
|---|---|
| **Model material** | ABS |
| **Support material** | SR-30 soluble |
| **Build size** | 203 x 203 x 152 mm |
| **Layer thickness** | .254 mm or .330 mm |

The biaxial device main requisite is the ability to control two loading directions which must be able to expand freely. In the single actuation systems this expansion along two orthogonal axes is obtained by exploiting a conversion mechanism from a uniaxial motion.

Biaxial experiments on soft biological tissues are generally problematic, presenting additional challenges unique to biological tissues. Just a few of the experimental problems include (Sacks, 2001):

- small specimen sizes;
- difficulty in gripping (without doing damage) and in specimen positioning;
- structural and compositional heterogeneity;
- difficulty in assuring constant forces along specimen edges;
- large specimen-to-specimen variability.

Ensuring a firm specimen gripping without damaging the tissue is mandatory and challenging because of the above mentioned small specimen size, texture and humidity conditions. That's why in literature various solutions where adopted. In all of them the specimen is mounted in the device in trampoline-like fashion although the grasping mechanism vary from one author from another. The preponderant solutions make use of thin threads (suture material) (Waldman & Lee, 2002; Skulborstad , et al., 2015; Grashow, et al., 2006), clips (Zemánek, et al., 2009; Prendergast, et al., 2003) and hooks (Lally , et al., 2004; Kahlon, et al., 2015). The device here presented is inclusive of accessories for the

simple and repeatable positioning of biological specimens by means of 12 hook evenly distributed on the four sides of the specimen (see 6.3.3).

*Table 6.4 Biaxial fixture requisites*

| Requirements | Description |
|---|---|
| Low cost | The choice of implementing a biaxial fixture for a uniaxial testing machine reduces significantly the realization costs, as well as the adoption of rapid prototyping method for the realization of the components. |
| Loading directions | Two loading directions (which must be able to expand freely) need to be controlled. |
| Specimen gripping /positioning | Ensuring a firm specimen gripping without damaging the tissue is mandatory. It's also necessary to ensure a simple and repeatable positioning of the specimen in order to guarantee the homogeneity of deformations. |
| Uniform stress-strain state | A region of uniform stress-strain state must be ensure so that the data analysis can be performed simply. This target region must be small and located away from the outer edges to avoid the effects of the gripping mechanism. |
| Optical measure of strain | Strain measure should be performed avoiding any mechanical interference with the specimen (tracking the position of markers mounted in the specimen upper surface). |
| Signals recording | Load signals from two orthogonal directions should be recorded, thus avoiding the indirect evaluation of stress. |

A non-contact strain measurement is fundamental to avoid any mechanical interference with the specimen. Hence, the device configuration must ensure the visibility of the specimen during the whole test in order to allow an optical measure of strains tracking the position of markers mounted in the upper specimen surface. This implies the use of an imaging device able to generate a synchronized image acquisition. The substantial anisotropy of soft biological tissues make it necessary to record not only a local distribution of strains on the specimen surface, but also load responses from the two orthogonal directions, without going through any indirect evaluation of forces and stresses.

Finally, a region of uniform stress-strain state must be ensure so that the data analysis can be performed simply. This target region must be small and located away from the outer edges to avoid the effects of the gripping mechanism.

An exhaustive list of all the requirements for the biaxial fixture is catalogued in Table 6.4.

## 6.3 Architectural design of the system

### 6.3.1 Interfacing with the existing framework

In order to meet the first requirement of a low cost device, a single actuation system was chosen, hence the biaxial fixture has been integrated in an existent framework. The selected uniaxial tensile machine (Bose Electroforce® 3200) is represented in Figure 6.1.

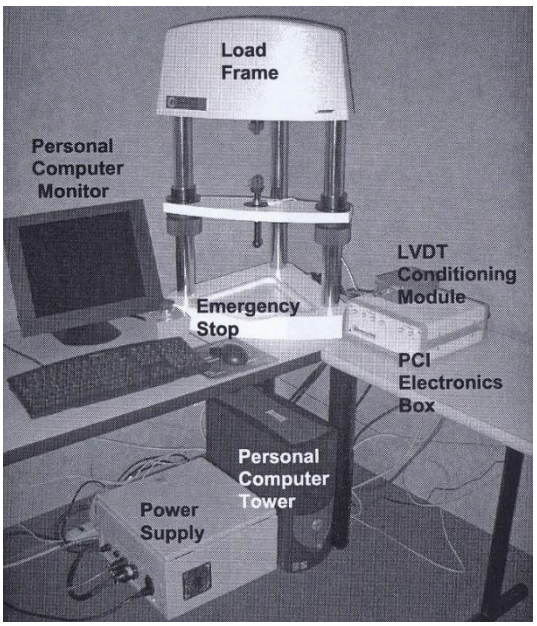


*Figure 6.1 Bose Electroforce® 3200 test instruments set-up*

#### 6.3.1.1. Electromagnetic linear actuator

The Bose Electroforce® 3200 is fitted with an electromagnetic linear actuator illustrated in Figure 6.2b. It consists of two sections of fixed coils wrapped in a core (also known as a stator) and a Neodymium Iron Boron (NdFeB) magnet that is able to move up and down, as shown in Figure 6.2a. The current that passes through the coils of the stator gen-

erates and modulates a magnetic flux that interacts with the flux generated by the magnet, causing the magnet to react with a force, depending on the polarity of the coil flux. Hence, the stator can be considered as an electromagnet producing a north and south pole as a function of current. When the current is applied the appropriate poles of the magnet are either attracted or repelled producing a force directly proportional to the current in the coils.

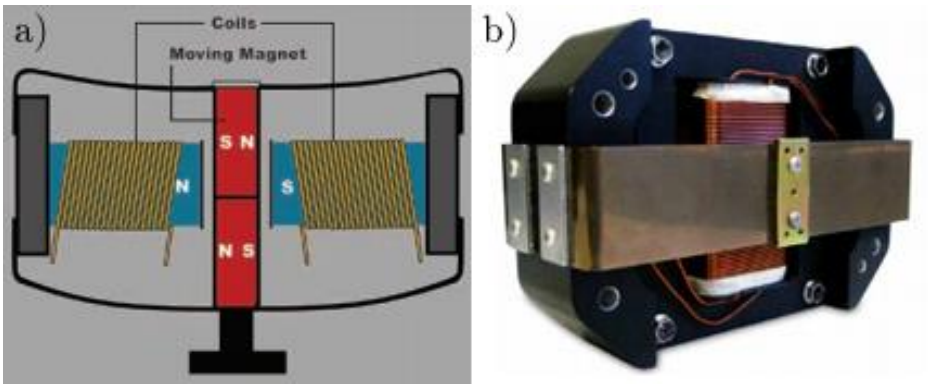


*Figure 6.2 a) Scheme of moving magnet motor; b) flexure assembly of moving magnet motor. (Electroforce, 2014)*

#### 6.3.1.2. Displacement transducer

The displacement transducer is a *Schaevitz MHR 250 LVDT*. A linear variable differential transformer (LVDT), shown schematically in Figure 6.3b, is made up of a single primary coil and two secondary coils. Both primary and secondary coils are wrapped around a hollow, non-magnetic bobbin, and the core slides inside the bobbin. An oscillating excitation voltage is applied to the primary coil. The current flowing through the primary coil creates an alternating magnetic field, which induces alternating voltages in the two secondary coils. The core, made of a ferromagnetic material, tends to concentrate the magnetic field in its vicinity, and as a result, if it is closer to one of the secondary coils, the voltage in that coil will be higher. The two coils are connected electrically and consequently as shown in Figure 6.3, hence the two voltages oppose each other. If the core is centered between the two secondary

coils, the voltage in the two secondary coils is equal, therefore the net output voltage will be zero (or at a minimum). If the core is not centered, there will be a net output voltage. The output, being an AC rms voltage, is always positive and gives no obvious information about the direction in which the core has been displaced from the centered position. This is a problem that can be solved with appropriate signal conditioners. The transducer is connected to the input channels of the PCI by means of the LVDT conditioner module, designed to interface with the six-wire LVDT (Figure 6.3a).

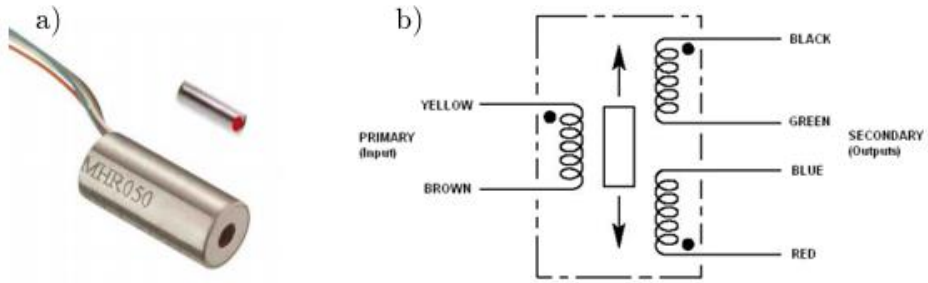


*Figure 6.3 a) Schaevitz MHR 250 LVDT; b) LVDT scheme. (MEAS, 2015)*

#### 6.3.1.3. Force transducers

The Bose Electroforce® 3200 features as its force transducer a *Honeywell Sensotec Sensors Model 31 Mid* (Figure 6.4). Here are listed the main technical characteristics of the load cell:

- maximal force: 225 N (50 lb);
- accuracy: ±0.25% F.S.;
- non linearity/hysteresis: ±0.15% F.S.;
- repeatability: ±0.10% F.S.;
- operating temperature: -65°F to 250°F;
- temperature effect, Zero: 0.015% F.S./°F;
- strain gage units: 350 Ω (stainless steel);
- case material: stainless steel;
- weight: 21-250 g.

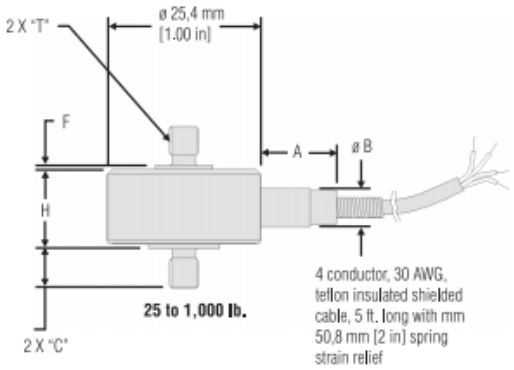


*Figure 6.4 Sensotec Model 31 load cell (Honeywell, 2004).*

The load cell is a transducer that is used to indirectly convert a force into an electrical signal. The force being sensed deforms a strain gauge. This deformation is measured as an electrical signal, because the strain changes the effective electrical resistance of the wire. A load cell usually consists of four strain gauges in a Wheatstone bridge configuration. The electrical signal output is typically on the order of a few millivolts and requires amplification by an instrumentation amplifier before being used. The output of the transducer is connected to the PCI Series Controls thanks to four outputs as showed in the wiring diagram (Figure 6.5).

The conversion of the existing system in a biaxial testing set-up required the integration of an additional force transducer. Most of the existing single actuation solutions planned to deduce the force/stress response orthogonally to the loading direction by means of geometrical relationships (Duncan, 1999; Lally , et al., 2004) or by indirect estimate from strains data (Brieu, et al., 2007). However this procedure does not appear suitable to the analysis of highly anisotropic materials such as biological tissues. Accordingly, the system has been equipped with a force transducer analogous to the pre-existing one and arranged in a direction orthogonal to the loading axis (see 6.3.3).

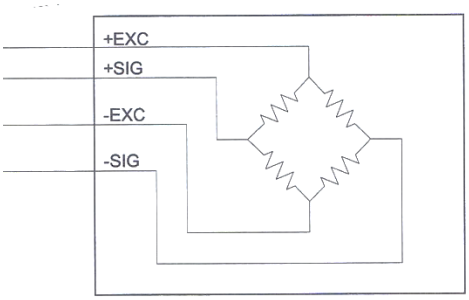


*Figure 6.5 Wiring diagram of the load cell.*

In order to integrate the new transducer with the existing framework, it was mandatory to interface with the PCI signal input conditioner, which is designed to interconnect with a wide variety of sensors. The connectors used for the input channels are 15-pin High-Density (HD-22) D-Subminiature Plugs (Figure 6.6).


*Figure 6.6 AMP plug, terminals, shroud and jackscrews.*

The following table is a summary of the inputs for the PCI signal conditioner.

*Table 6.5 Signal input connector pinouts*

| Pin | Designation | Description |
|---|---|---|
| 1 | +SIG | Positive input to the differential amplifier |
| 2 | -SIG | Negative input to the differential amplifier |
| 3 | ACOM | Analog common |
| 4 | +EXC | Positive excitation voltage |
| 5 | -EXC | Negative excitation voltage |

| | | |
|---|---|---|
| 6 | +15V | Positive 15V regulated power supply voltage |
| 7 | OFFSET | Differential amplifier offset input |
| 8 | -15V | Negative 15V regulated power supply voltage |
| 9 | 2.5V | 2.5 Volt Reference signal |
| 10 | 5V | 5 Volt Reference signal |
| 11 | GAIN | One terminal of the gain setting resistor |
| 12 | GAIN | One terminal of the gain setting resistor |
| 13 | SHLD | Chassis ground |
| 14 | REF IN | Excitation voltage reference input |
| 15 | 10V | 10 Volt Reference signal |

The first two pins are the input to the first stage differential amplifier. The signals can have a range up to ±10V, depending on the amplifier gain setting. Pins 4 and 5 are the positive and negative precision regulated bridge excitation signals. These pins may be programmed to supply different excitation voltages (2.5V, 5V or 10V) and they drive strain gauge type sensors. The excitation voltage is programmed connecting the REF IN pin to the desired precision reference voltages (pins 9, 10 or 15). When one of them is connected to REF IN, the voltage is buffered and appears on +EXC and –EXC.

The calibration of the sensor is obtained by means of a calibration resistor connected across the two gain pins (11 and 12). These pins programs the voltage gain of the differential amplifier. The value of the resistor may be determined by using the following equation:

$$Rg = \frac{6000\Omega}{GAIN - 1}$$

*Equation 6.1*

The gain may be derived from the sensitivity of the sensor as follows:

$$GAIN = \frac{9.43}{S \cdot E \cdot R \cdot 0.001}$$

*Equation 6.2*

Where:

- S = Sensor sensitivity in mV/V
- E = Excitation voltage

- R = Ratio of Transducer full scale to WinTest full scale

The R values allows the choice of a convenient WinTest full scale value (for example 225N WinTest full scale for 50lbs. transducer full scale). The value of Rg is chosen to provide a gain factor of 1.06 which allows the use of the full transducer range even for a small tare (offset) value (Bose Corporation, 2005).

Considering the Honeywell Sensotec Sensors Model 31 Mid load cell added to the experimental set-up, calibration data are listed in Table 6.6.

*Table 6.6 Load cell calibration resistor*

| | |
|---|---|
| S [mV/V]= | 2.3593 |
| E [V] = | 10 |
| R = | 1 |
| GAIN = | 399.69 |
| Rg [- ] = | 15.05 (1% tolerance resistor) |

The realized pinouts configuration is depicted in Figure 6.7.

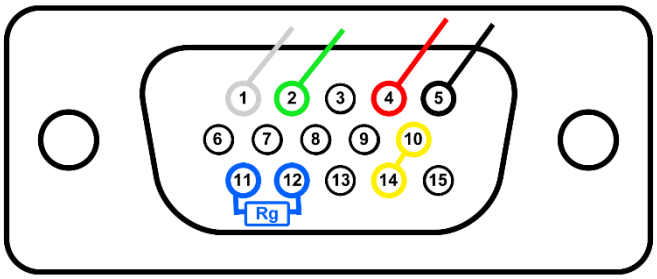


*Figure 6.7 Pinout configuration. Wiring codes: grey - (+) output; green - (-) output; red - (+) excitation; black - (-) excitation.*

The architecture of the entire framework, comprising the original structure and the additional transducer, is represented in Figure 6.8.

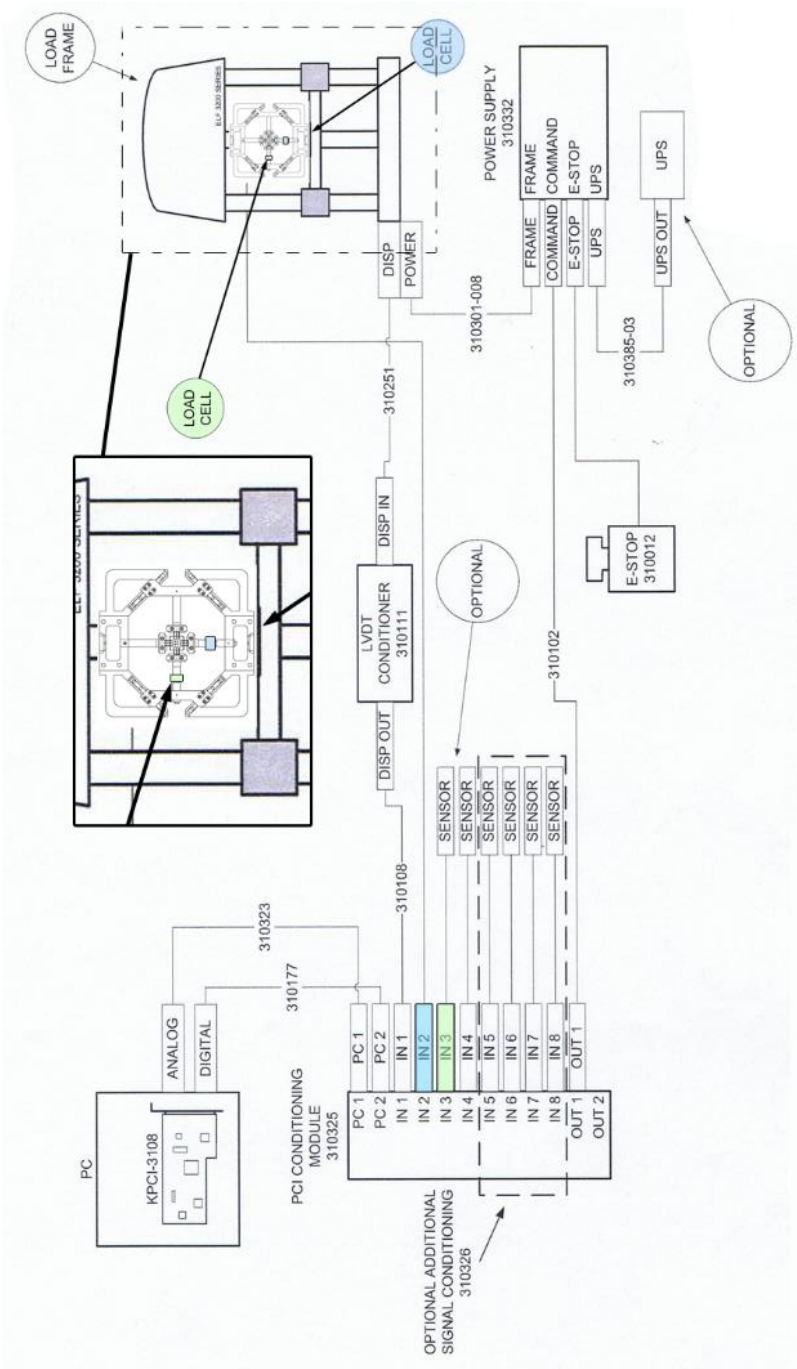


*Figure 6.8 Architecture of the biaxial testing framework*

### 6.3.2 The conversion mechanism

The biaxial conversion frame is depicted in Figure 6.9. It has a symmetrical configuration with respect to both the vertical and horizontal axes.

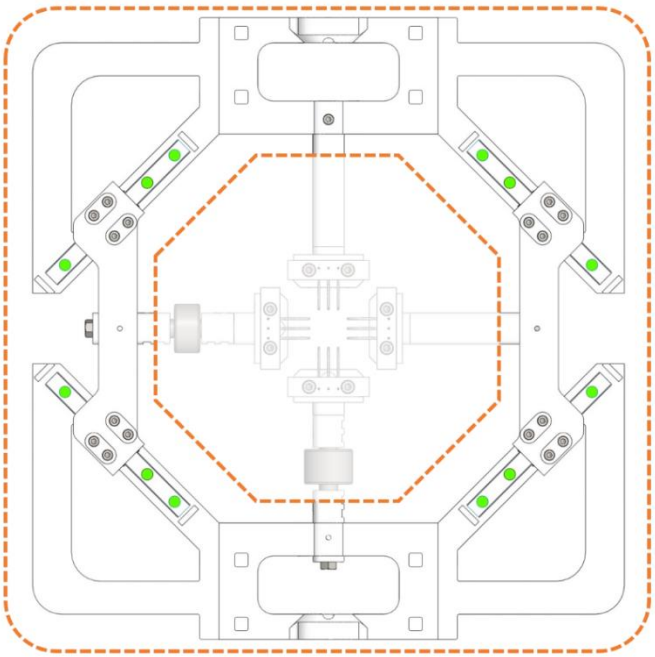

*Figure 6.9 Biaxial conversion frame*

The conversion frame was designed dimensionally compatible with the Bose Electroforce® 3200 available test space, detailed in Table 6.7. Its overall dimensions in the starting position are 320.40 mm of height, 305.42 mm of width and 48.58 mm of thickness.

*Table 6.7 Bose Electroforce® 3200 frame dimensions*

| Parameter | Bose Electroforce® 3200 |
|---|---|
| Range of displacement | 12.5 mm |
| Test space | |
| Vertical test space | 0-450 mm |
| Load cell to back column | 305 mm |

It is composed by two identical crossheads (Figure 6.10), fit to bind the device to the testing machine. The lower crosshead is fixed on the bottom of the tensile machine by means of four AISI 316L M3 screws, while the upper half is fixed on the moving crosshead of the machine through the same fastening method.

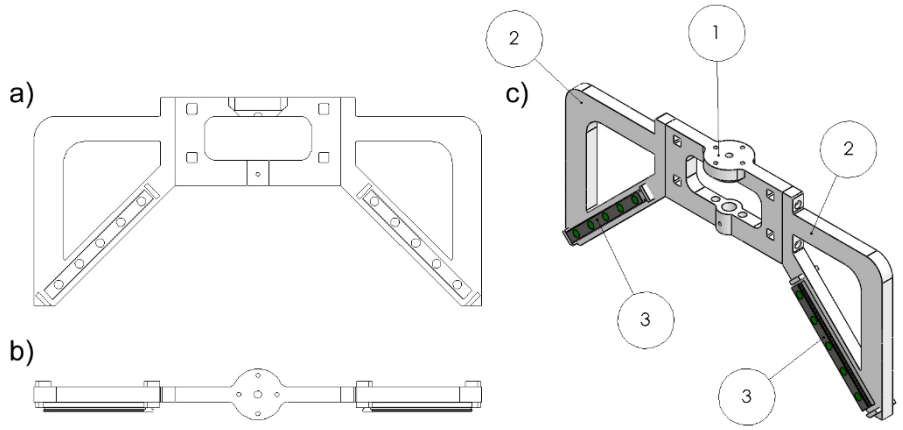


*Figure 6.10 Crosshead sub-assembly composed by 1) Connector, 2) Lateral extensions, 3) Linear guideway rails: a) front b) top and c) isometric view.*

The choice to take advantage of rapid prototyping techniques forced the device design, being the 3D printing machining binding in terms of maximum size of the component, undercuts and cavities. That's why the majority of the components have been designed as multi-part assemblies, devising when needed alternative couplings between parts.

For instance, the joint between the connector and the lateral extensions (Figure 6.11) required the presence of two AISI 316L M3 screws on each side. The four holes in the connector lateral faces have demanded the addition of supplementary perpendicular openings (1) for the removal of the support material from the lateral holes (2).

A couple of linear guideway rails are assembled with the two lateral extensions by means of two AISI 316L M3 screws (Figure 6.10). Two blocks upstream and below the rails were considered to prevent the slipping of the linear guideway blocks over the rail limits.

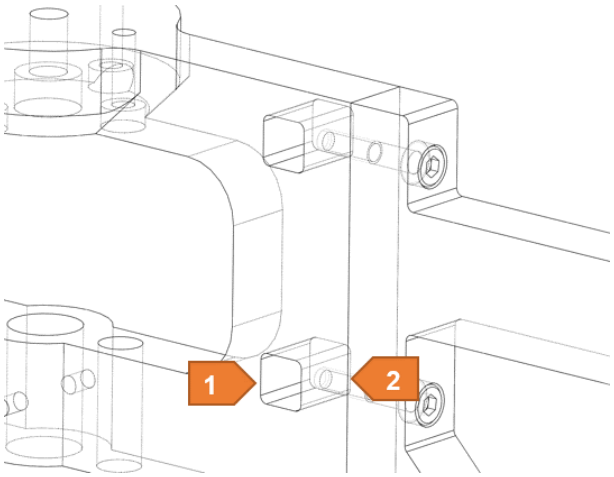


*Figure 6.11 Design solution: connector-lateral extension coupling*

Two identical links (Figure 6.12) act as a connection between the upper and lower crossheads, due to the presence of four linear guideways. Two linear guideway blocks are secured to each link with four AISI 316L M3 screws. The relative angles between each linear guideway rail and their associated link are equal to 45°.

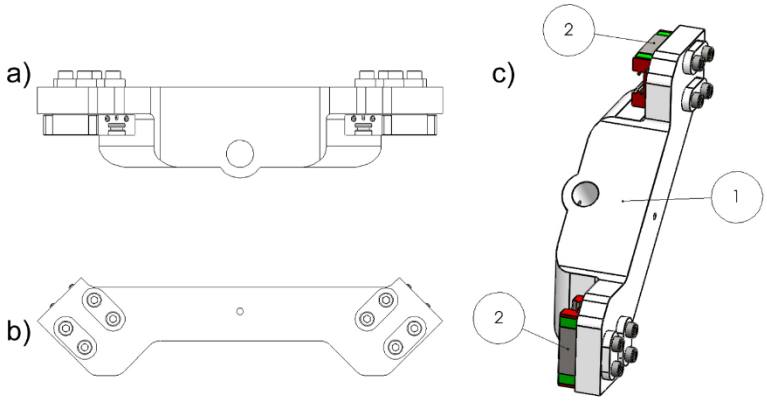


*Figure 6.12 Link sub-assembly composed by 1) Link, 2) Linear guideway blocks: a) longitudinal b) top and c) isometric view.*

Commercial Hiwin® MGN series linear guideways were selected. They are entirely made from stainless steel and they own 2-row recirculation ball bearing guide. Their internal structure is depicted in Figure 6.13.

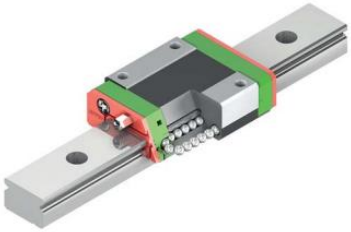

*Figure 6.13 Structure of the MNG series Hiwin linear guideway*

*The details and features of the selected model are listed in Table 6.8 and* Table 6.9.

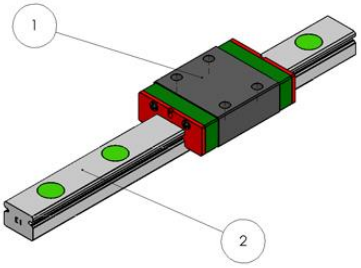


*Table 6.8 MGN block features (Hiwin®). Variables are depicted in Figure 6.14.*

| ① MGN09-C-Z1-C-M | | | | | | | | | | | | | |
|---|---|---|---|---|---|---|---|---|---|---|---|---|---|
| Installation dimensions [mm] | | | Dimensions of the block [mm] | | | | | | | | | Load Ratings [N] | | Weight [kg] |
| H | $H_1$ | N | W | B | $B_1$ | C | L1 | L | $G_n$ | Mxl | $H_2$ | $C_{dyn}$ | $C_0$ | |
| 10 | 2 | 5.5 | 20 | 15 | 2.5 | 10 | 18.9 | 28.9 | ∅1.4 | M3x3 | 1.8 | 1860 | 2550 | 0.02 |

| Dynamic Moment [Nm] | | | Static Moment [Nm] | | |
|---|---|---|---|---|---|
| Mx | My | Mz | Mx | My | Mz |
| 8 | 5 | 5 | 11.76 | 7.35 | 7.35 |

*Table 6.9 MNG rail features (Hiwin®). Variables are depicted in Figure 6.14.*

| ② MGNR09-R100-C-M | | | | | | | | |
|---|---|---|---|---|---|---|---|---|
| Assembly screw for rail [mm] | Dimensions of rail [mm] | | | | | | Length [mm] | Weigth [kg] |
| | $W_R$ | $H_R$ | D | h | d | P | | |
| M3x8 | 9 | 6.5 | 6.0 | 3.5 | 3.5 | 20.0 | 100 | 0.038 |

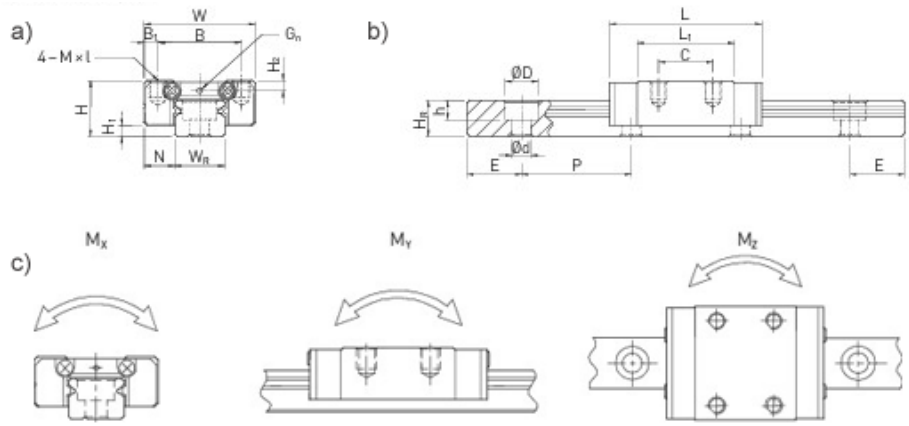


*Figure 6.14 Linear guideway sub-assembly: a) cross and b) lateral view; c) moments configuration.*

By construction, when the moving crosshead of the tensile machine is displaced, the higher crosshead of the conversion device moves accordingly; whereas, the lower crosshead secured to the base of the tensile machine remains motionless, identically to any uniaxial testing. The connective links, which in turn are attached to the upper and lower crossheads of the conversion device through the four linear guideways, are forced by the vertical displacement to move along the perpendicular direction. Thus, the ideal horizontal line which connects the links midpoint remains on the median of the segment formed by the vertical grips. In this fashion, when the moving crosshead goes up, the upper crosshead moves with a velocity "v" whereas the lower crosshead remains motionless. Concurrently, the lateral links move up with a velocity of "v/2" and

simultaneously shift in the horizontal axis with a velocity of "v" in opposite directions, thus obtaining an equibiaxial tension (Figure 6.15).

Considering the Bose Electroforce® 3200 available stroke (12.5 mm, Table 6.7), the maximum displacement of the upper crosshead engenders an identical 12.5-mm-stroke in the horizontal direction.

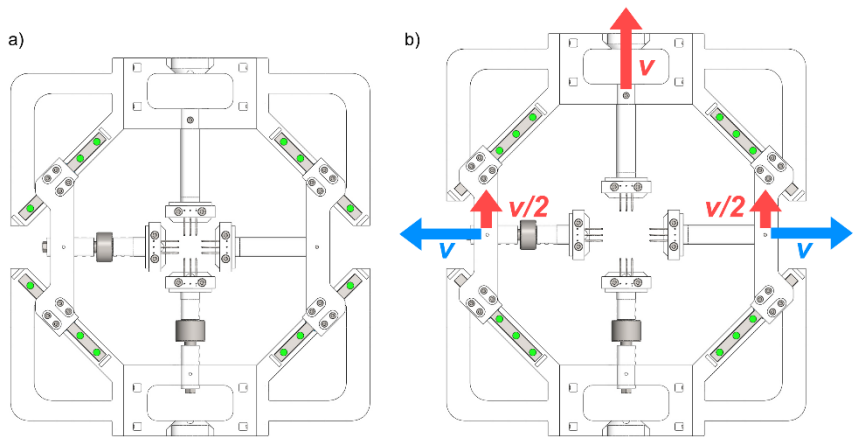


*Figure 6.15 Biaxial device in a) close and b) open configuration. Red arrows represent vertical velocities whereas blue arrows represent horizontal velocities.*

### 6.3.3 The gripping apparatus

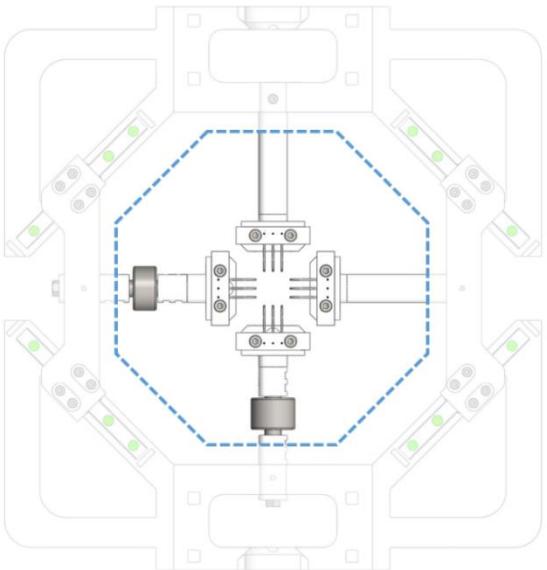

*Figure 6.16 Biaxial gripping apparatus*

The gripping apparatus is composed by two couples of homologous arms. Each couple contains a sensorized arm, equipped with a load cell, and a contralateral arm and is arranged along one of the loading direction. The not sensorized arms are secured respectively to the upper crosshead and to the right link through an AISI 316L M3 screw. The sensorized arms, due to the presence of the load cells, needed an articulate design that would allow the grip fastening in the correct position and a reversible connection with the load cell.

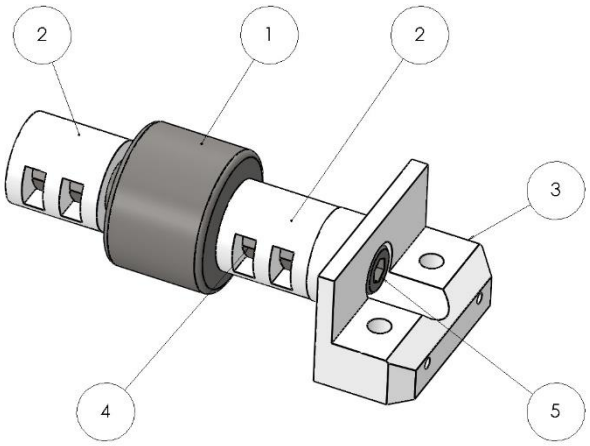


*Figure 6.17 Lower gripping arm sub-assembly composed by 1) Load cell, 2) Load cell adapter, 3) Gripping terminal, 4) M5 Nuts and 5) securing M5 screw.*

Taking as example the lower gripping arm depicted in Figure 6.17, it can be noted the need of two load cell adapters to ensure the fastening of the load cell both with the lower crosshead and the gripping terminal. To avert the attachment of the load cell thread directly to a threaded hole in the printed material, four AISI 316L M5 nuts were stucked in two housings placed on the lateral wall of each load cell adapted. This ploy, not only allows for an easily reversible connection with the load cell, but also permit a secure and 'in place' coupling with the gripping terminal. Regarding the crosshead joint, a stopper fixed with an AISI 316L M5 screw to the load cell adapter provides a secure placement (Figure 6.18).

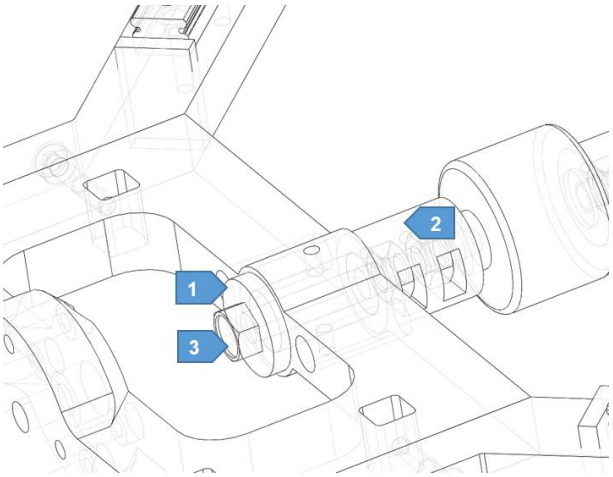


*Figure 6.18 Design solution: connector-load cell adaptor coupling; 1) stopper; 2) load cell adapter; 3) M5x25 screw.*

The four gripping arms with their gripping terminals make up the housings for the actual grasping devices: the hooks holders. These latters are removable sub-assemblies which can be easily secured to the gripping terminals by means of two AISI 316L M4 screws each (Figure 6.19). The removal of the four hooks holders is mandatory to enable a facilitated positioning of the specimen, as will be explained later.

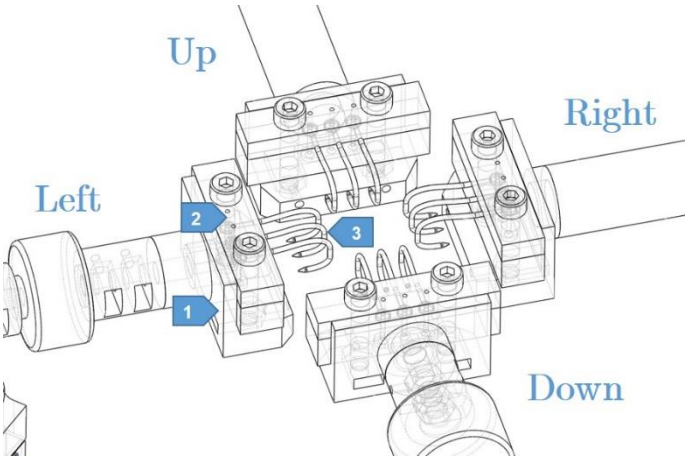


*Figure 6.19 Magnification of the gripping zone: 1) Gripping terminal; 2) Hooks holder; 3) Hooks.*

The hooks holder comprises two mated sub-unities which houses the hooks ends in specific slots. All the hooks degrees of freedom are then

blocked by three nails which are inserted through both the sub-unities and the 1-mm-hole located at the terminal part of the hooks (Figure 6.20).

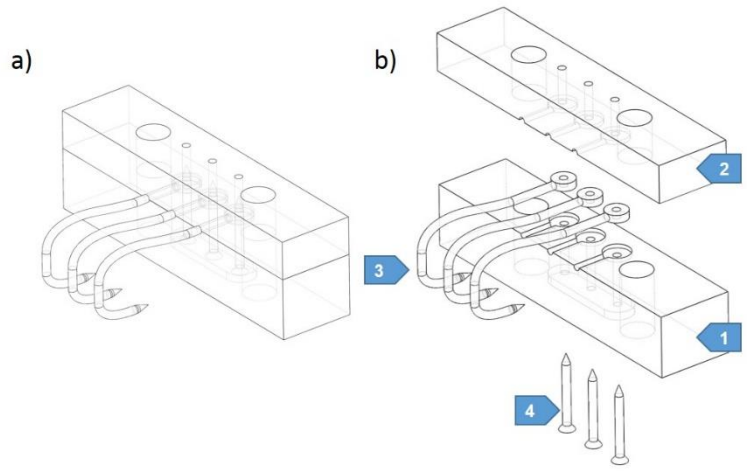


*Figure 6.20 Hooks holder sub-assembly composed by 1) Lower hook holder, 2) Upper hook holder, 3) Hooks and 4) Blocking nails: a) isometric and b) exploded view.*

To simplify the description, the drawings of all parts and assemblies of the equibiaxial conversion device can be found in Appendix A.

## 6.4 Specimen mounting procedure

The handling of a biological sample which by its nature appears flabby and slippery is always laborious. This complications are magnified when a fine positioning is required, as needed in the case of biaxial characterization. Especially when performed by hooks and wires, the quality of the specimen gripping affects the homogeneity of the stress and strain field, since an uneven positioning of the load application points generates unbalanced boundary conditions which would lead to a reversal of the assumption of equibiaxiality. That's why a positioning method was devised, assisted by dedicated accessories. In this paragraph it will be presented a detailed description of the method, including the hooks insertion, the markers placement and the mounting of the specimen within the conversion mechanism.

As a first step the square tissue specimen is placed on a 3D printed ABS base (Figure 6.21-B). This base (Figure 6.21-A) was designed to act both as a hooks guide and as a tissue platform.

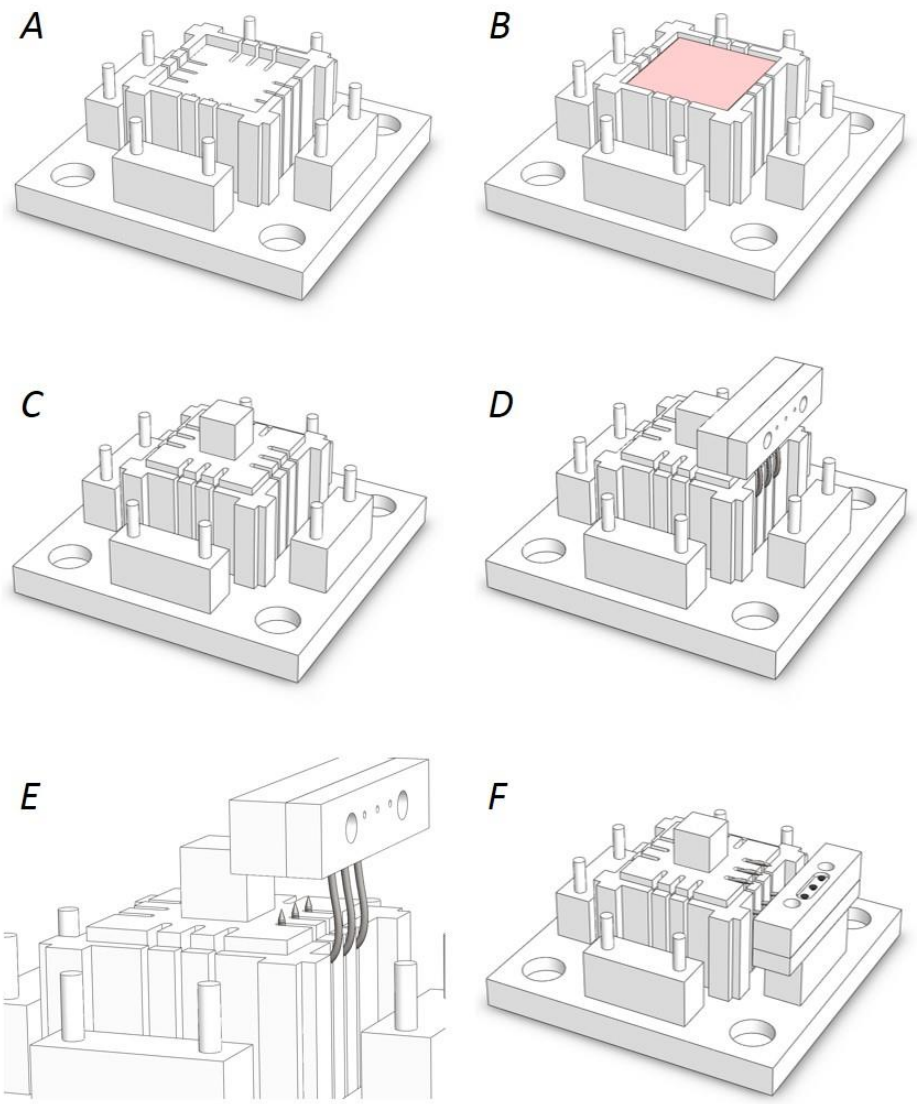


*Figure 6.21 The specimen mounting procedure. Part I.*

Its dimensions allow to accommodate a 30x30-mm–specimen, even if a scaled version would be easily obtainable. The base has, on the four sides, 12 slits for the passage of the hooks and a cover to keep the tissue in place during the punching operation. To ensure the passing of the hooks, the cover has the same amount of corresponding slits (Figure 6.21-C). Three at a time, with the help of the hook holder, the hooks are passed along the slits exposing their sharp tip to the tissue (Figure 6.21-D,E). After the hooks insertion, the hook holder is placed on the underlying support to avoid accidental solicitations to the tissue (Figure 6.21-F, Figure 6.22-G). Removing the cover, the correct insertion of hooks can be checked (Figure 6.22-H). The following step is the transfer of the specimen-hooks holders ensemble from the base to a carrier, which will allow for both the placement of the markers and the transfer of the specimen into the conversion frame. Therefore, a carrier complementary to the base is dovetailed on the latter, and four locks are rotated until the four hook holders are bound to the carrier (Figure 6.23-I,J,K).

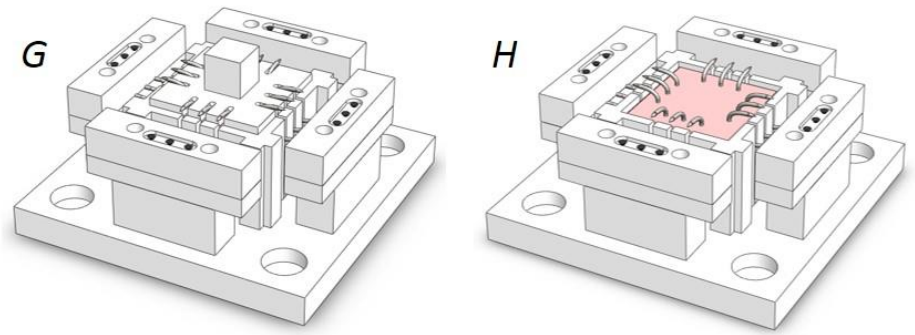


*Figure 6.22 The specimen mounting procedure. Part II.*

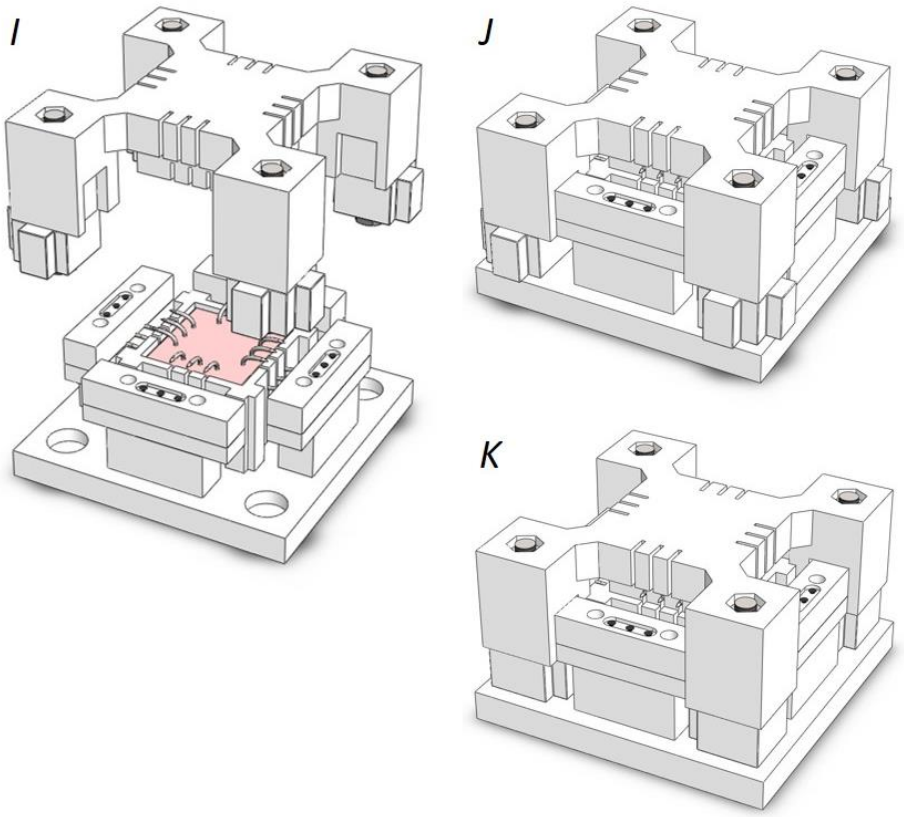


*Figure 6.23 The specimen mounting procedure. Part III.*

Removed the base, the specimen-hooks holders ensemble is ready to be marked and fitted in the device (Figure 6.24-L). To favour an equi-spaced positioning of the markers, a dots guide provided with 16 circular holes can be placed on the specimen. It acts as a mask for the drawing of sixteen points (Figure 6.24-M,N,O,P). An alcohol base waterproof black marker can be used to draw dots on the wet soft surface of the tissue.

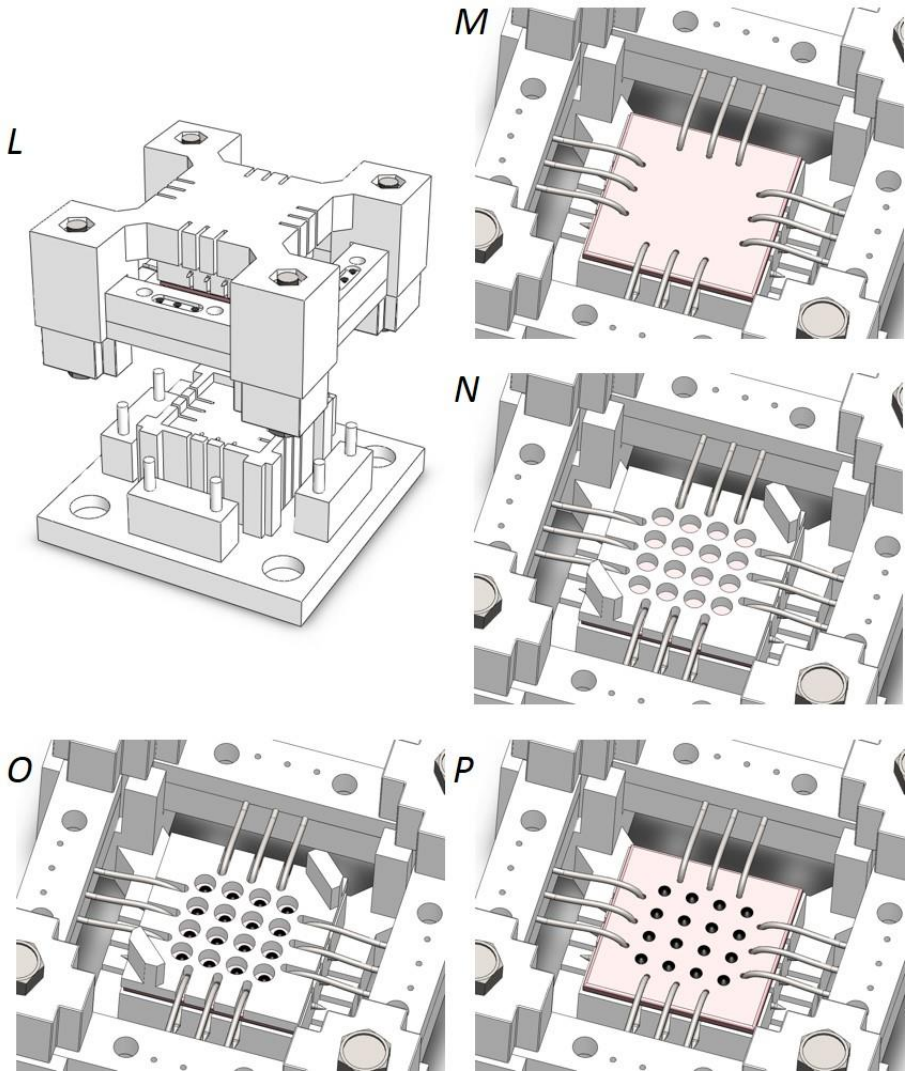


*Figure 6.24 The specimen mounting procedure. Part IV.*

Finally, the carrier is transferred into the conversion frame (Figure 6.25-Q) securing the four hooks holders on the gripping terminals (Figure 6.25-R) through eight AISI 316L M4 screws (Figure 6.25-S). The carrier locks are then rotated (Figure 6.25-T) to release the carrier from the conversion frame and to remove it from the hooks holders, leaving the specimen carefully positioned into the device (Figure 6.25-U,V).

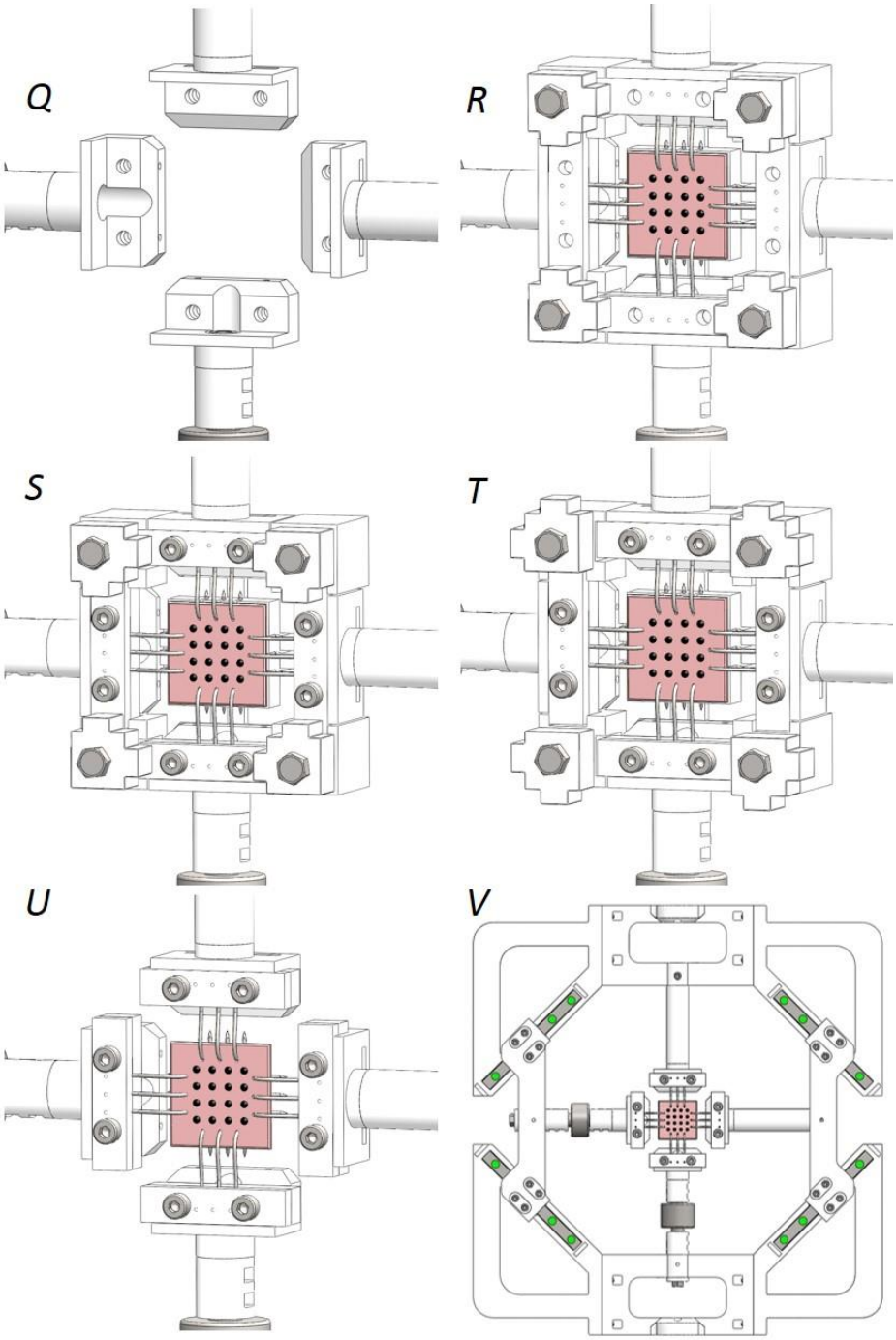


*Figure 6.25 The specimen mounting procedure. Part V.*

## 6.5 Device validation

### 6.5.1 Verification of the grips motion with unbalanced loads

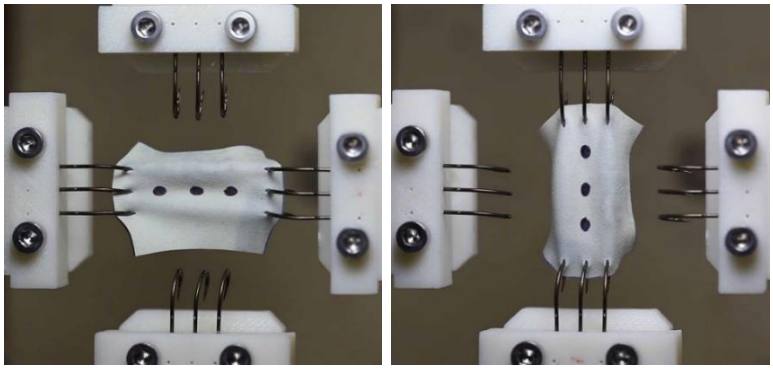

*Figure 6.26 Testing configuration with specimen mounted in two orthogonal directions.*

The first assessment covered the verification of the grips motion in two orthogonal loading conditions, which mimic an unbalanced load state (Figure 6.26). Specifically, a rubber sample was mounted within the biaxial fixture first in a horizontal configuration leaving free the vertical hooks. Secondly, the sample was rotated 90 degrees and the test was repeated. A constant 0.16 mm/s displacement rate was maintained for a total displacement of 10 mm.

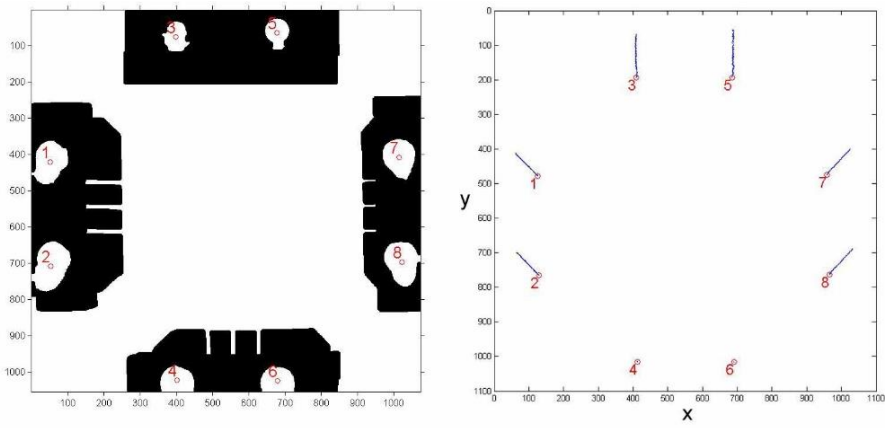


*Figure 6.27 Screws segmentation and movement tracking.*

The video recordings of both tests were processed and the eight holding screws (which maintain the hooks holders bound to the device) were segmented so as to follow their centroids during the test time (Figure 6.27).

For both sets of images, the horizontal strain was then calculated between the mean position of points 1 and 2 and the mean position of points 7 and 8 during time. Similarly, from the remaining points the strain in the vertical direction was evaluated. The resulting strain-time curves are represented in Figure 6.28.

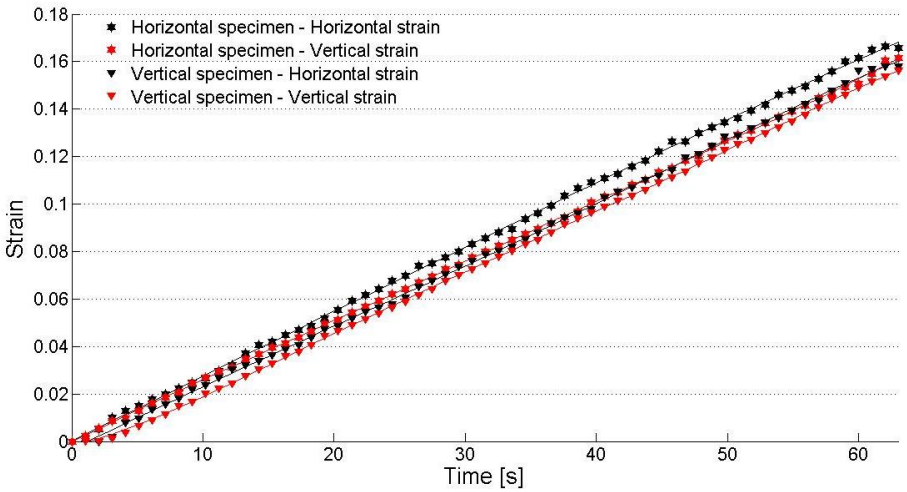


*Figure 6.28 Strain-Time curves resulting from the screws tracking in the two testing configurations.*

A linear regression was performed for the four displacement-time curves obtained from the two tests, obtaining the curve slope, namely the displacement rate of the four grips in unbalanced load conditions. The resultant slopes are listed in Table 6.10.

*Table 6.10 Linear regression results (displacement rate) for the displacement-time curves*

| | Horizontal specimen | Vertical specimen |
|---|---|---|
| Horizontal velocity | 0.166 mm/s | 0.161 mm/s |
| Vertical velocity | 0.157 mm/s | 0.162 mm/s |
| Mean velocity | 0.162 mm/s | 0.162 mm/s |

Therefore the mean percentage error with respect to the nominal speed is about 1%.

### 6.5.2 Verification of the equibiaxial strain distribution

Isotropic specimen case.

It has been previously mentioned (Par. 6.2) the need to measure strains avoiding any mechanical interference with the specimen. For this reason the device conceivement has planned to ensure optimum visibility of the specimen during the test. A Canon EOS 5D Mark II digital camera with an autofocus lens for macro photography (Canon EF 100 mm f/2.8 Macro USM) and a camera stand was used for the recording of each test. Therefore images were captured and post processed using a purpose-build Matlab GUI (2012a, The MathWorks, Inc., Natick, Massachusetts, United States).

The resulting videos (dimensions: 1920x1088; frame rate: 25 FPS) were then post-processed for the extraction of all the frames. These frames constitute the main inputs for the strains identification.

For validation purpose, it was chosen to detect strains by tracking the position of markers drawn in the upper surface of an isotropic rubber specimen, but also a random pattern of speckles was created to perform digital image correlation (DIC).

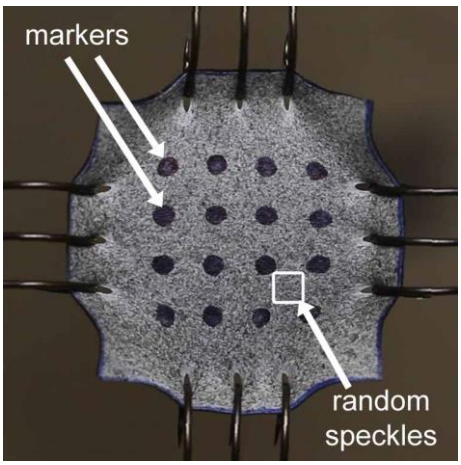


*Figure 6.29 Isotropic rubber specimen prepared with markers and random speckles.*

#### 6.5.2.1. Optical tracking of markers

All the optical tracking procedure was performed in the Matlab environment, and all steps were then embedded in a graphical user interface (GUI).

First of all, the frames extracted from the video were analysed so as to identify the first frame, and subsequently one frame per second was selected. The first frame selection is made through the identification of a change in the location on at least one of the markers drawn on the specimen. The image extraction frequency, setted to 1 Hz, was considered appropriate to the displacement rate imposed to the specimen (0.16 mm/s).

Each image was then processed following the steps listed below:

- **Color conversion**: the RGB image is converted to grayscale by eliminating the hue and saturation information while retaining the luminance (Figure 6.30).

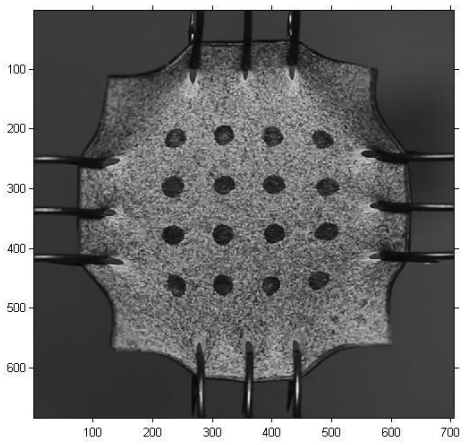


*Figure 6.30 RGB to grayscale conversion*

- **Binary conversion**: converts the grayscale image to binary by thresholding. The output binary image has values of 1 (white) for all pixels in the input image with luminance greater than a predefined level and 0 (black) for all other pixels (Figure 6.31).

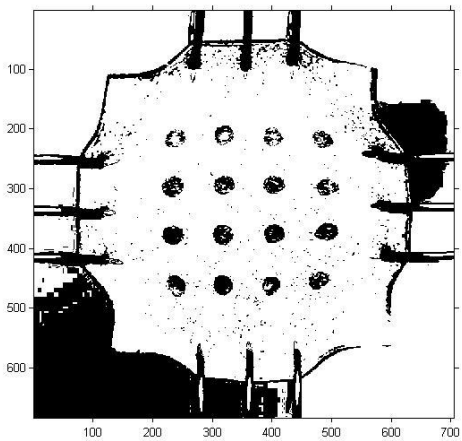


*Figure 6.31 Binary conversion. Threshold value setted to 0.2.*

- **Complement of the image**: in the complement of the binary image, black becomes white and white becomes black (Figure 6.32).

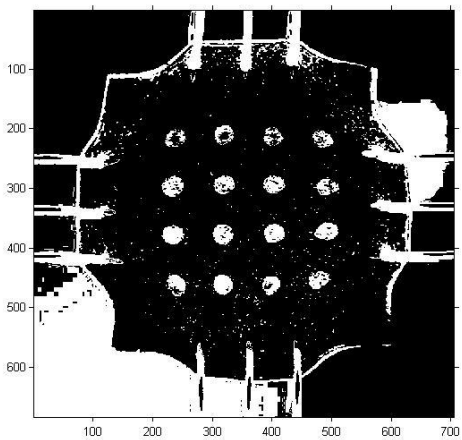


*Figure 6.32 Complement of the binary image.*

- **Noise cleaning**: removal from the binary image of all connected components (objects) that have fewer than a define number of pixels (Figure 6.33).

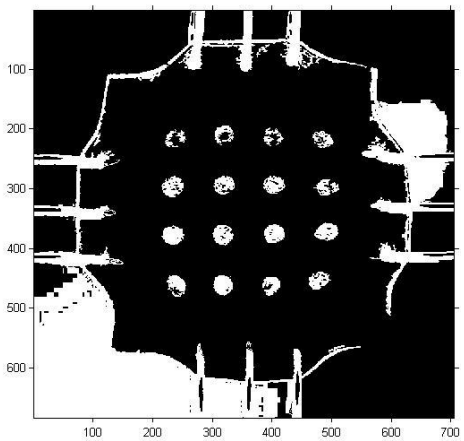


*Figure 6.33 Noise removal from the binary image. Objects composed of fewer than 100 pixel were removed.*

- **Morphological closing**: morphological closing of the binary image with a flat disk-shaped structuring element with a specified radius.

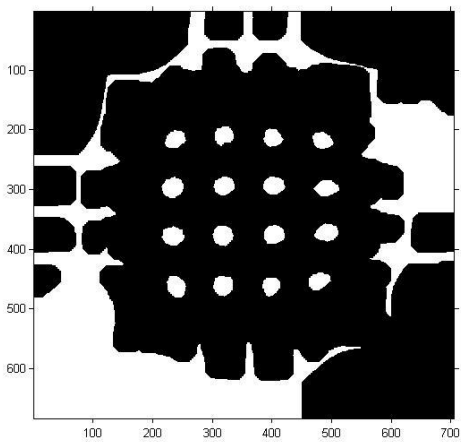


*Figure 6.34 Morphological closing. Radius = 20 pixels.*

- **Boundaries tracing**: detection of the exterior boundary of objects contained in the binary image (Figure 6.35).

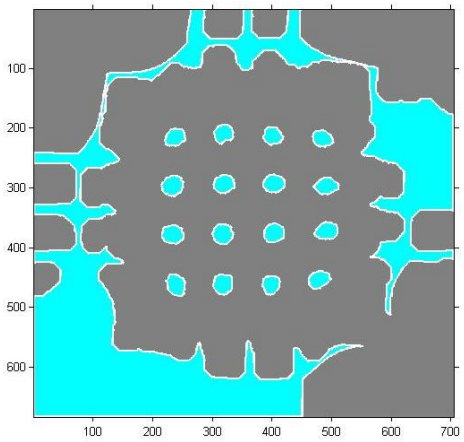


*Figure 6.35 Objects boundaries detection.*

- **Roundness recognition**: after the estimate of each object's area and perimeter a simple index indicating the roundness of the objects was computed (Figure 6.36). This index is equal to one only for a circle and it is less than one for any other shape. The discrimination process is controlled by setting an appropriate threshold.

$$index = \frac{4\pi \cdot Area}{Perimeter^2}$$

*Equation 6.3*

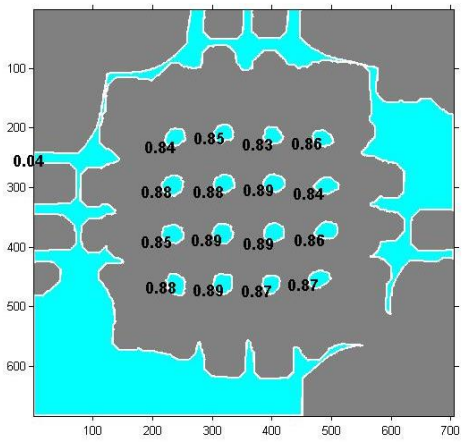


*Figure 6.36 Roundness recognition. Threshold value = 0.80.*

- **Centroids sorting**: the centroids of each identified object (index > 0.80) are sorted in order to assign the same label to every marker on each processed image (Figure 6.37).

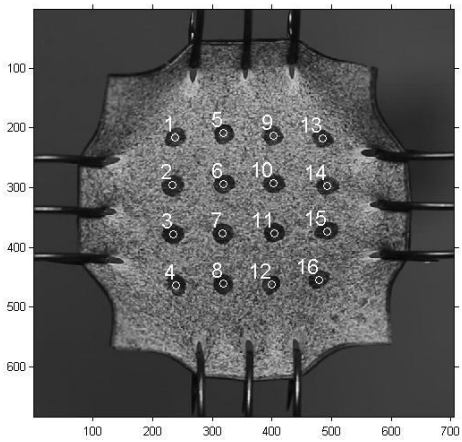


*Figure 6.37 Centroids sorting from 1 to 16.*

Using this procedure, the markers position during the entire test was followed and a graph of the local displacement was realized (Figure 6.38), showing the markers initial location (in red) and their movement over time (in blue).

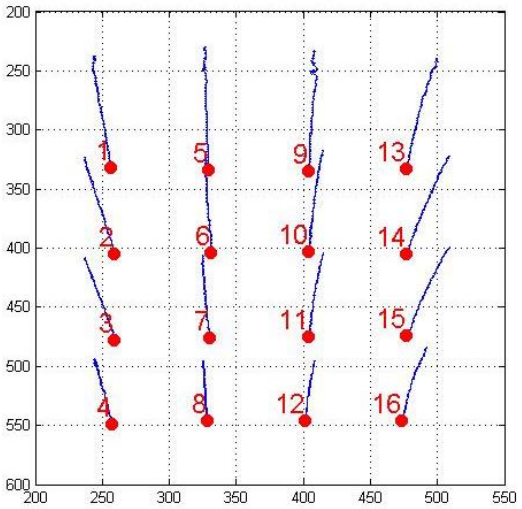


*Figure 6.38 Markers displacement over time (blue lines) and marker initial location (red dots).*

#### 6.5.2.2. Finite element modelling

The output of the previous images post processing is the main input of a finite element model having the purpose to analyze the behavior of the isotropic specimen tested by means of the biaxial conversion device.

The analysis was performed using the software Mechanical APDL 14.5 (Ansys Inc., Canonsburg, Pennsylvania, U.S.). The choice was driven by the possibility to set up the simulation by means of textual code in APDL language, which can be generated using a purpose-written Matlab code.

**Geometry**

The model geometry was created starting from keypoints associated with the centroids coming from the first frame. Keypoints from 1 to 16 are the 16 sorted markers centroids; keypoints from 17 to 28 are the centroids related to the hooks insertion points, which were segmented following the same procedure used for the markers; keypoints 29 to 31 are the four vertex of the square specimen (Figure 6.39).

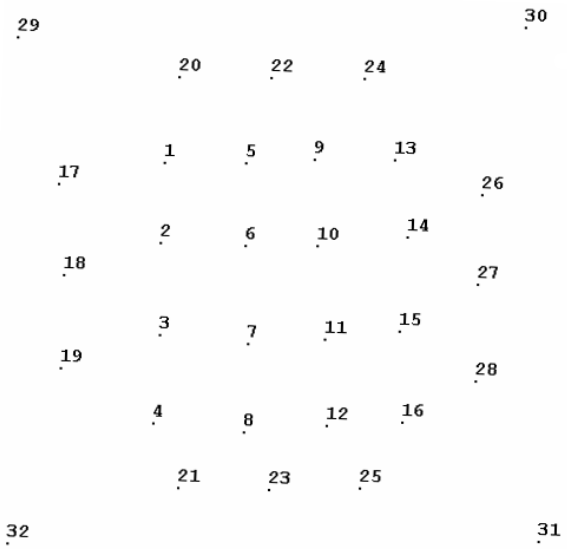


*Figure 6.39 Geometric model: keypoints definition.*

Lines between points was then constructed, to delimit the areas constituting the model (Figure 6.40). This type of geometry reconstruction is necessary to ensure that on each point of interest (keypoint) coexists a mesh node.

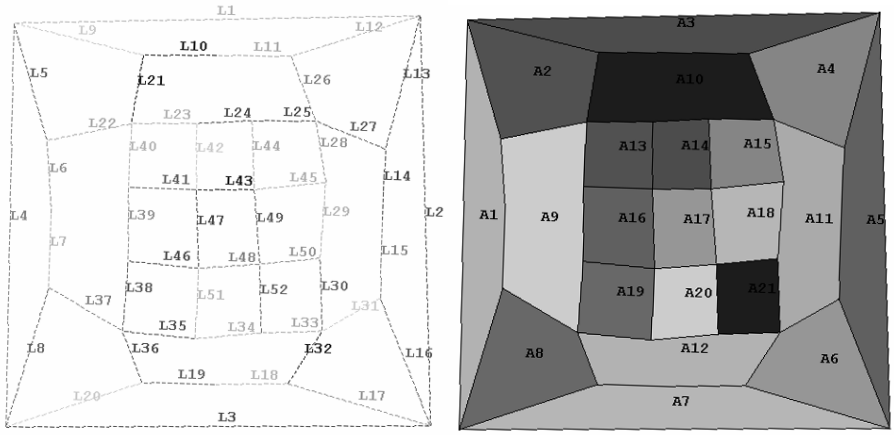


*Figure 6.40 Geometric model: lines and areas definition.*

**Material**

The stress-strain curve concerning the test was computed starting from the loads recordings and the horizontal and vertical strains measured in the central region of the specimen, delimited by the markers #6, #7, #10 and #11.

In particular, the nominal stress and strain obtained by the biaxial tensile test in the two orthogonal directions are defined by the following equations:

$$\sigma_V(t) = \frac{F_V(t)}{L_V(t) \cdot s(t)}$$

*Equation 6.4*

$$\sigma_H(t) = \frac{F_H(t)}{L_H(t) \cdot s(t)}$$

*Equation 6.5*

$$\varepsilon_V(t) = mean\left(\frac{l'_{x,u}(t) - l_{x,u}}{l_{x,u}}; \frac{l'_{x,d}(t) - l_{x,d}}{l_{x,d}}\right)$$

*Equation 6.6*

$$\varepsilon_H(t) = mean\left(\frac{l'_{y,l}(t) - l_{y,l}}{l_{y,l}}; \frac{l'_{y,r}(t) - l_{y,r}}{l_{y,r}}\right)$$

*Equation 6.7*

where

- $L_V(t)$ and $L_H(t)$ are the mean distances between the hooks insertion points in the vertical and in the horizontal direction respectively;
- $F_V(t)$ and $F_H(t)$ are the vertical and horizontal load cells outputs;
- $s(t)$ is the specimen thickness over time, evaluated knowing the $L_V$ and $L_H$ arrays and assuming an isochoric condition.

All parameters meanings are depicted in Figure 6.41.

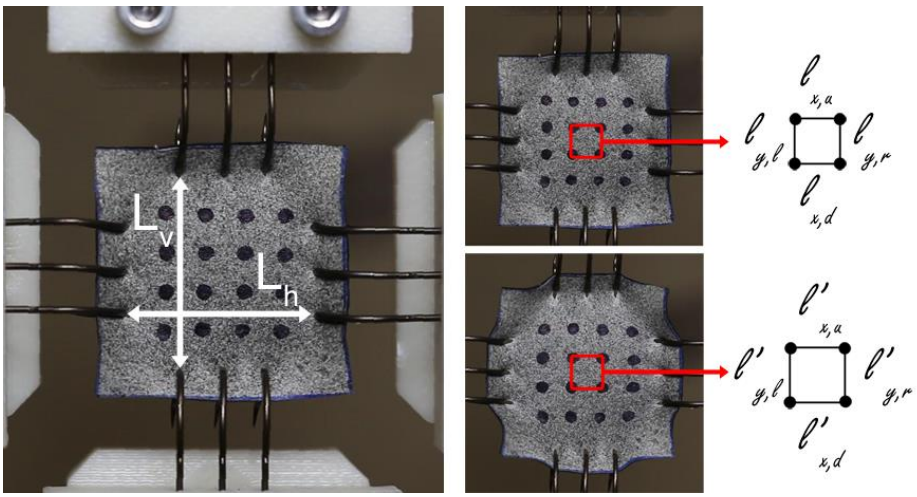


*Figure 6.41 Parameters extraction for stress and strain evaluation.*

The resulting stress-strain curves and the mean stress-strain curve that mediates the behaviour of the material in the central area of the specimen are plotted in Figure 6.42.

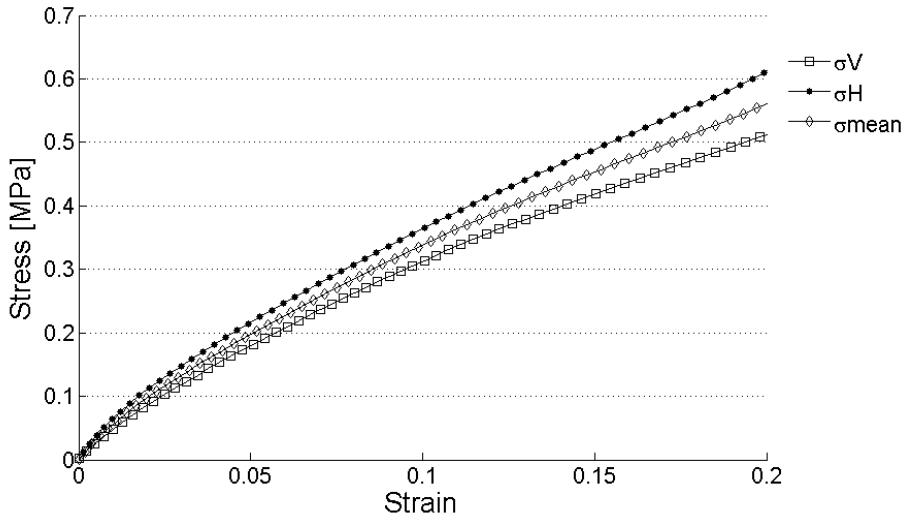


*Figure 6.42 Stress-strain curves evaluated in the central region of the specimen.*

The mean equibiaxial stress-strain curve was then fitted with two hyperelastic constitutive models in the Ansys curve fitting toolbox. Details regarding the models formulation and the curve fitting procedure were discussed at length in Chapter 5. In particular, a Mooney-Rivlin 5 parameters model and an Ogden 4 parameters model were used. The fitting results are listed in Table 6.11.

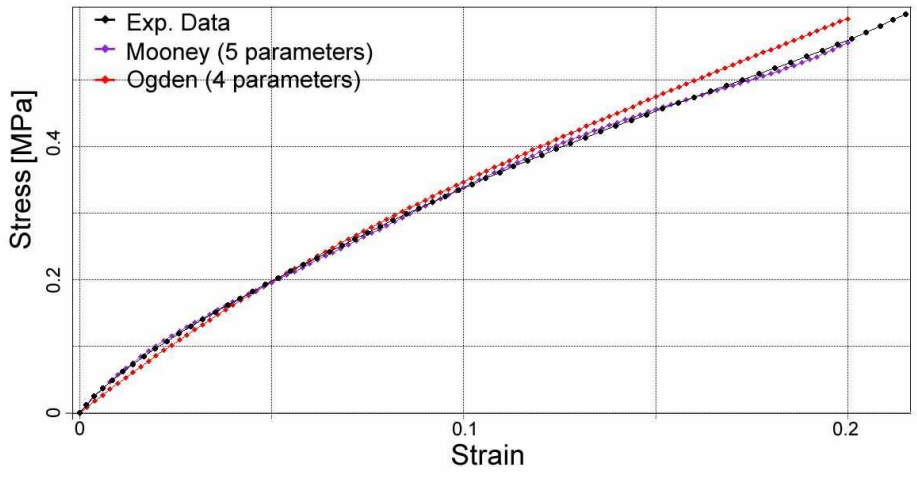


*Figure 6.43 Curve fitting plot in a strain range equal to the ROI strains.*

*Table 6.11 Curve fitting results for the Mooney-Rivlin and the Ogden constitutive models.*

| Mooney-Rivlin (5 parameters) | | Ogden (4 parameters) | |
|---|---|---|---|
| *Parameter name* | *Parameter value* | *Parameter name* | *Parameter value* |
| C10 | 4.3346 | $\mu_1$ | 0.0891 |
| C01 | -3.7796 | $\alpha_1$ | 4.3266 |
| C20 | 30.8465 | $\mu_2$ | 0.0891 |
| C11 | -39.8447 | $\alpha_2$ | 4.3266 |
| C02 | 14.0592 | $\mu_3$ | 0.0891 |
| d | 0 | $\alpha_3$ | 4.3266 |
| | | $\mu_4$ | 0.0891 |
| | | $\alpha_4$ | 4.3266 |
| | | $d_1$ | 0 |
| | | $d_2$ | 0 |
| | | $d_3$ | 0 |
| | | $d_4$ | 0 |

From Figure 6.43 a better fit can be noted for the Mooney-Rivlin model within a strain range compatible to the strains present in the central area of the specimen.

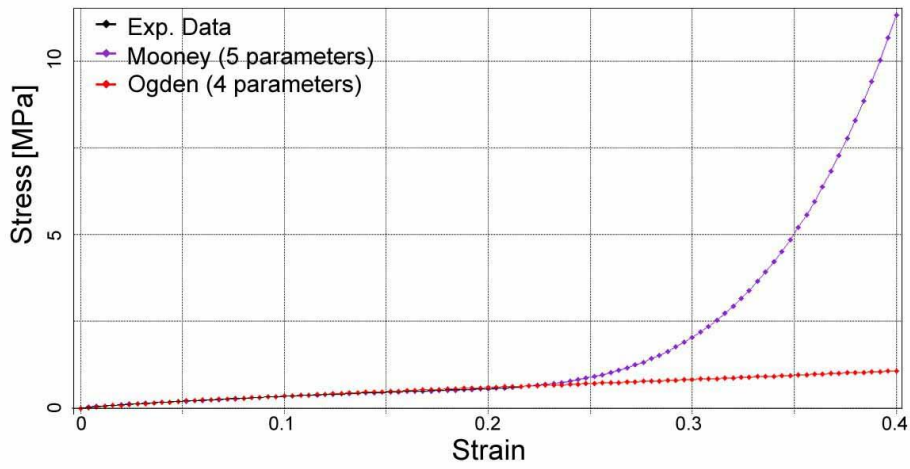


*Figure 6.44 Curve fitting plot in a strain range equivalent to the test global strain.*

Despite this, for higher strains the curve diverges (Figure 6.44), making the behaviour description unreliable in areas with high deformation (close to the gripping points).

For its more conservative behaviour the selected constituent model was the Ogden model.

**Mesh**

The model discretization was realized using a high order planar element (Figure 6.45). Plane183 has quadratic displacement behaviour and is defined by 8 nodes having two degrees of freedom at each node: translations in the nodal x and y directions. This element has hyperelasticity capabilities, thus it is suitable for the application of interest (Ansys Inc., 2013).

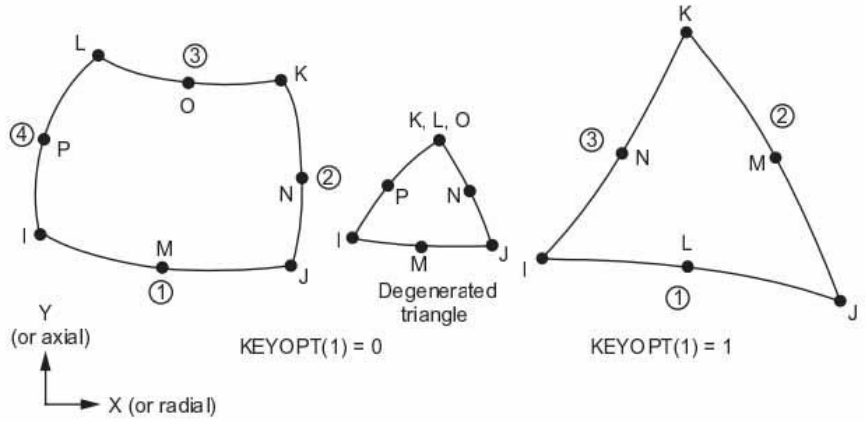


*Figure 6.45 Plane183 geometry (Ansys Inc., 2013).*

The element dimensions were setted according to the required output detail and the computational time needed for the solving process, obtaining a 15120 nodes and 4963 elements mesh (

Figure 6.46). Forcing the presence of the nodes on the keypoints causes an irregular discretization of the model. Nevertheless, Plane183 elements are well suited to modelling irregular meshes.

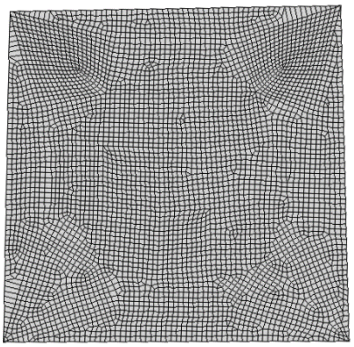

*Figure 6.46 Model discretization: Plane183 mesh.*

### Boundary Conditions

As previously mentioned, the imposed boundary conditions were the 28 time-displacement curves representing markers and hooks motions during the experimental test. They were applied to the 28 nodes associated with the respective 28 geometrical keypoints.

Therefore, for each node were considered two 63x2 tables containing in the first column the time array (from 0 to 63 seconds) and in the second column the nodal translation in the x (or y) direction. An exception was made for the keypoints #21, #23 and #25, which identify the insertion points of the lower hooks. Being the latter substantially motionless, fixed constraints in both directions were considered (Figure 6.47a). A further constraint condition was then considered, excluding the markers displacements and leaving the hooks constraints unchanged (Figure 6.47b).

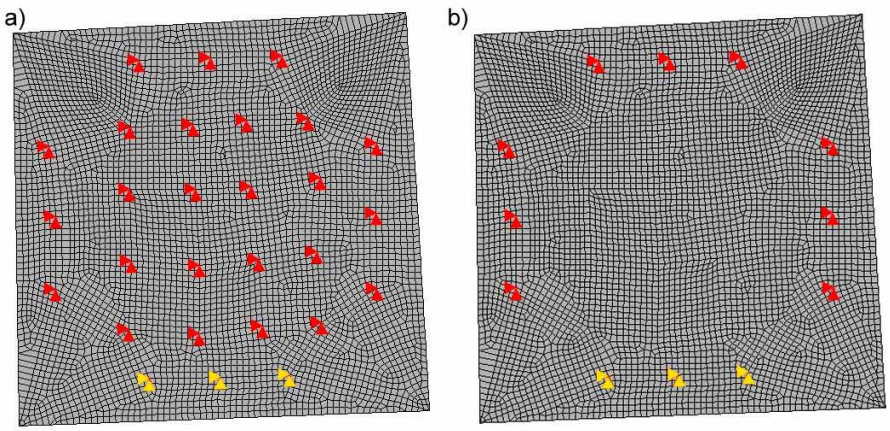


*Figure 6.47 Boundary conditions. a) Complete constraints configuration; b) Constraints configuration comprising only the hooks insertion points. In yellow are represented the fixed constraints.*

Figure 6.48 and Figure 6.49 show the strain distributions resulting from the two finite element analysis, considering, in the first case, the simultaneous presence of both markers and hook insertion points. The second simulation excludes the markers influence, imposing only the hooks movement during the test. The time instant represented coincides with the last instant of the experimental test (t = 63 s).

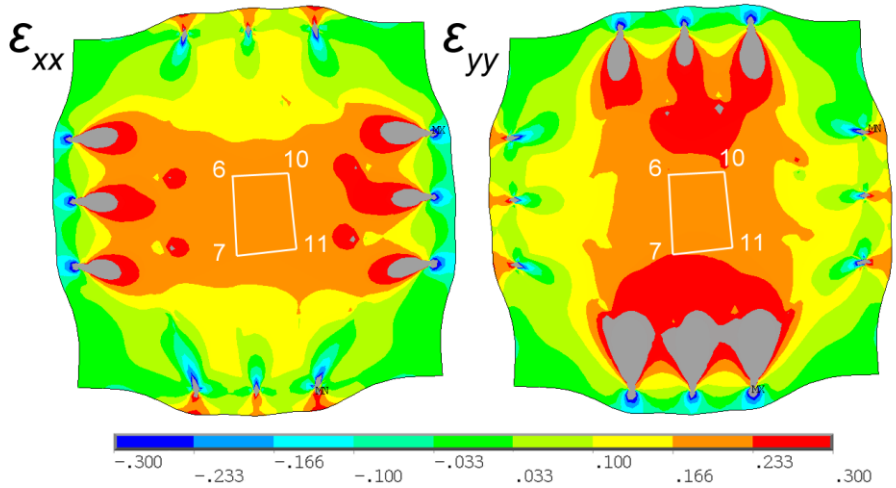


*Figure 6.48 Strain distributions along x and y directions with boundary conditions given by the markers and the hooks insertion points.*

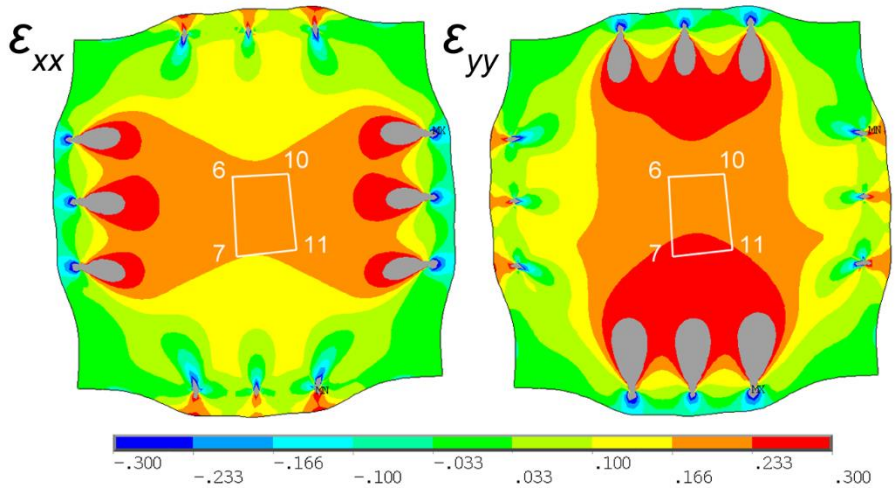


*Figure 6.49 Strain distributions along x and y directions with boundary conditions given only by the hooks insertion points.*

The region bordered in white represents the region of interest enclosed by markers #6, #7, #10 and #11. Even though the markers presence induces an irregular strain distribution in the vicinity of the displacements application points, in both analysis the ROI exhibits strains in the x and the y directions in the range (0.20±0.04).

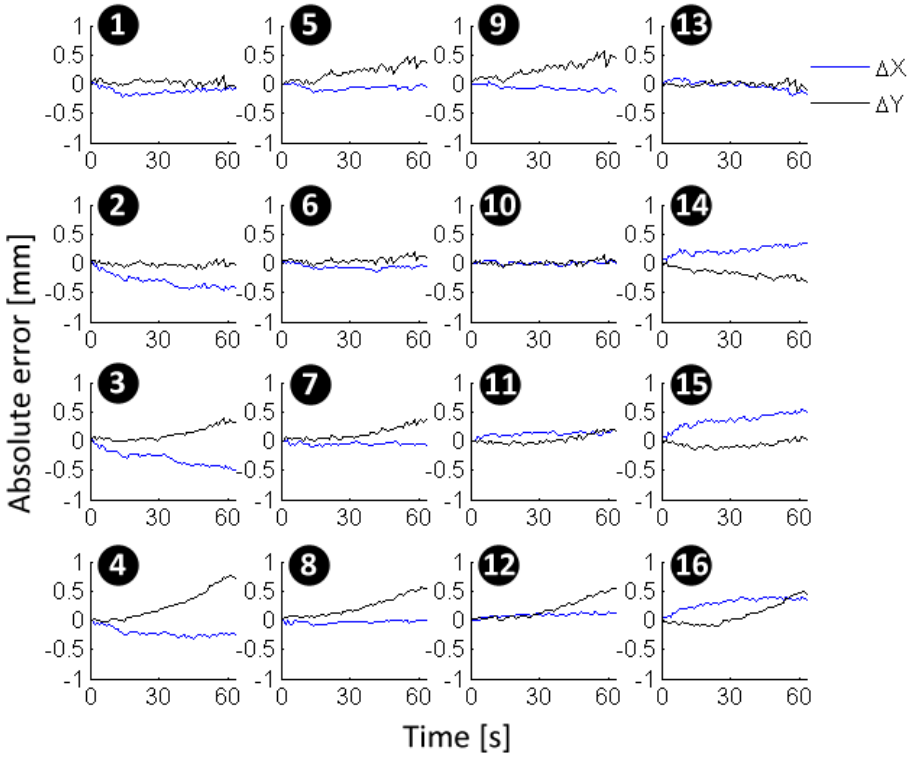


*Figure 6.50 Absolute error vs. time for the 16 nodes corresponding to the 16 markers. Blue lines represents the error along the x direction with respect to the experimental displacement. Black lines represents the error along the y direction with respect to the experimental displacement.*

Considering in detail the nodal displacements at the markers for the two simulations, major discrepancies emerge in correspondence of the side markers with respect to the central region. Figure 6.50 shows the absolute error along the x (blue) and y (black) direction produced by the second simulation (which, it is recalled, does not consider the movement of the markers as a boundary condition) with respect to the first

simulation (namely, with respect to the experimental markers displacements). The absolute error increases with increasing time, and therefore with increasing global deformation of the specimen. Moreover, the error increases as the distance from the ROI grows. In fact, those regions appears out of range with respect to the material description range. However, the absolute error is negligible in the specimen ROI, confirming the adequacy of the constitutive model and, therefore, the equibiaxial strain distribution inside the ROI.

#### 6.5.2.3. Digital Image Correlation

The same experimental test was used to perform a local strain analysis, through a Matlab-based Digital Image Correlation (DIC) code, implemented at the University of Illinois in 2013 (Jones, 2013).

Digital Image Correlation is a noncontacting optical method for strain measurement that has been widely applied in scientific research. It analyze and compare digital images acquired from the surface of a substrate equipped with a random pattern of speckles. Digital images acquired during the specimen deformation document the "speckle" distribution and can be represented by the greyscale intensity distribution. This intensity distribution describes the surface point by point, associating to each point an intensity value. With the progression of the specimen deformation, each point of the undeformed image (the reference image 'r') is assumed to exist at a new location in the deformed image ('d'). Therefore, the in-plane surface displacement can be evaluated by finding the position of the intensity distribution that most closely resembles the original distribution (Zhang & Arola, 2004).

Jones Matlab code efficaciously performs this process correlating a subset of pixels around each control point in the deformed image with a larger subset (generally twice as big) around the corresponding control point in the reference image. It computes the normalized cross-correlation coefficient C for a range of theoretical displacements $(u', v')$ according to Equation 6.8:

$$C(u',v') = \frac{\sum_{x',y'}\left[\left(r(x',y') - \overline{r_{u',v'}}\right)\left(d(x'-u',y'-v') - \bar{d}\right)\right]}{\left\{\sum_{x',y'}\left[\left(r(x',y') - \overline{r_{u',v'}}\right)^2\right]\sum_{x',y'}\left[\left(d(x'-u',y'-v') - \bar{d}\right)^2\right]\right\}^{\frac{1}{2}}}$$

*Equation 6.8*

The actual displacement $(u, v)$ for a control point is the theoretical displacement $(u', v')$ corresponding to the maximum correlation coefficient. Strains are then calculated by interpolation displacement using finite element shape functions (Jones, 2013).

In the following paragraphs the steps taken to run the correlation will be described in detail. The procedure was performed tracing the scheme described by Jones (2013).

- **Color conversion**: all images were converted to black and white, as required by the code.
- **Correlation parameters settings**: dealing with large deformations, one essential parameter was the choice of using the preceding image as a reference image (while the first image is usually picked for small deformations analysis). A ROI was then defined (Figure 6.51), with a consequent grid of control points (20 pixels of spacing between points)

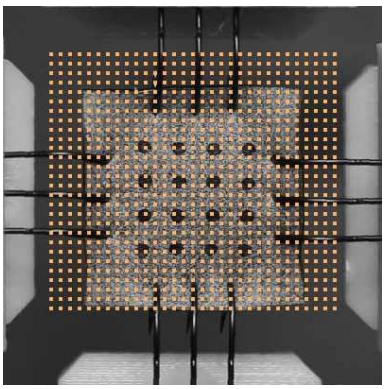

*Figure 6.51 ROI and grid of control points definition.*

- **Deletion of poorly correlated data:** the existence of portion of the ROI not presenting a good correlation isn't uncommon, as shown in Figure 6.52a. The reason can be the presence of a poor speckle pattern, as in the image background. Here's why the code allows for the deleting of the poorly correlated data, in order to obtain a smaller ROI with good data (Figure 6.52b).

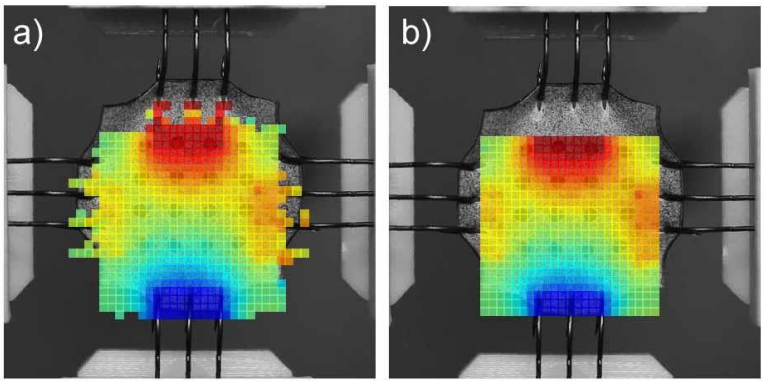


*Figure 6.52 a) Before and b) after the deletion of poorly correlated data.*

- **Displacements smoothing and strains calculation:** prior to calculating strains, the displacements were smoothed using a Gaussian kernel with 15 control points. Strains were then calculated by interpolating displacements using finite elements shape functions. In particular, a 9-nodes quadratic finite element interpolation scheme was used.

Figures 6.53, 6.54 and 6.55 shows the digital image correlation results, in terms of strain distribution along the x and y directions, and Von Mises equivalent strain distribution. Three different time instants are highlighted: initial, final and an intermediate instant.

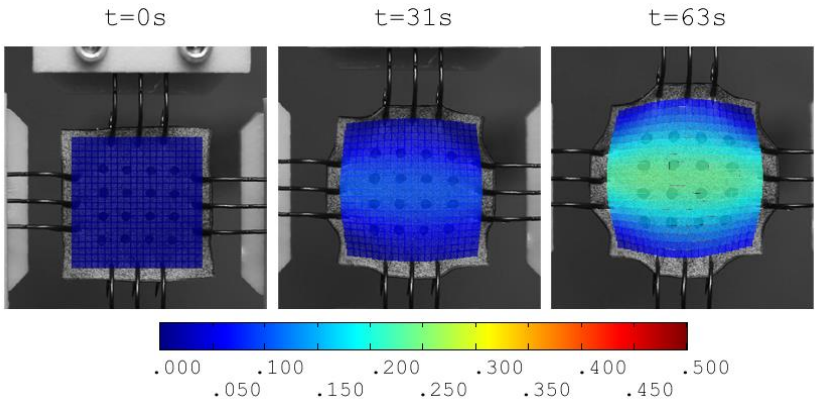


*Figure 6.53 Strain distribution along the x direction in the initial (t=0s), intermediate (t=31s) and final instant (t=63s).*

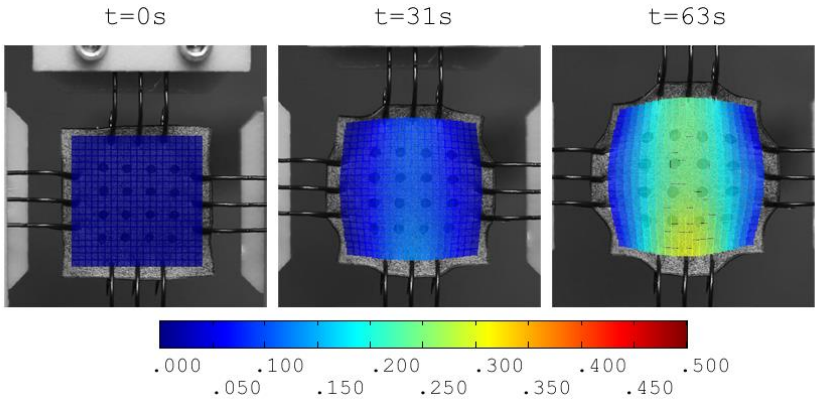


*Figure 6.54 Strain distribution along the y direction in the initial (t=0s), intermediate (t=31s) and final instant (t=63s).*

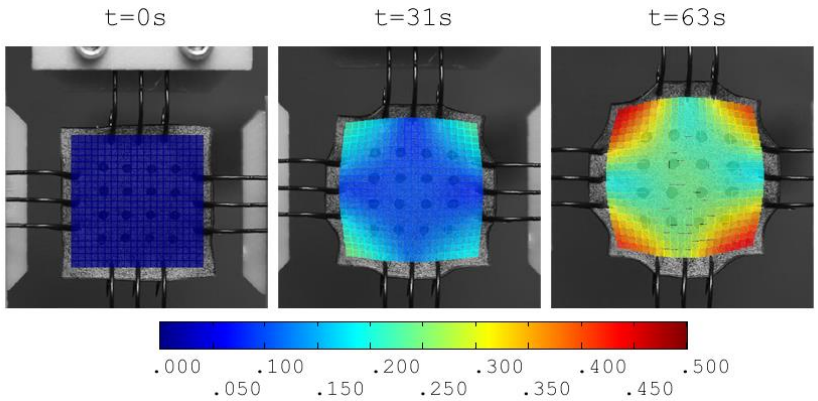


*Figure 6.55 Equivalent Von Mises Strain distribution in the initial (t=0s), intermediate (t=31s) and final instant (t=63s).*

The equibiaxiality of the strain distribution is here again confirmed by the similar behaviour along the two orthogonal directions. From Figure 6.55 an unexpected distribution at the corners of the specimen can be noted, which is expressed in higher values of deformation. This is induced by the out of plane movement of the not-constrained corners. This would not happen with the use of a cruciform specimen, considered as a standard shape for biaxial material characterizations. Despite this, the device was designed for the gripping of biological tissues notoriously difficult to handle and cut into complex shapes. The square shape is the most frequently adopted solution for the biaxial characterization of biological tissues (Skulborstad , et al., 2015; Prendergast, et al., 2003; Zemánek, et al., 2009; Lally , et al., 2004).

It should be noted that either from the finite element analysis or from the correlation procedure, gripping effects at high strains emerge due to the lower constraint. They're more visible in the vertical strain distributions, and they produce a non-symmetrical distribution with respect to the horizontal axis of the test. The cause is attributable to the absence of a motionless point in the center of gravity of the specimens. In fact, the device considers as a fixed constraint the lower gripping zone, which implies the motion of the specimen middle point.

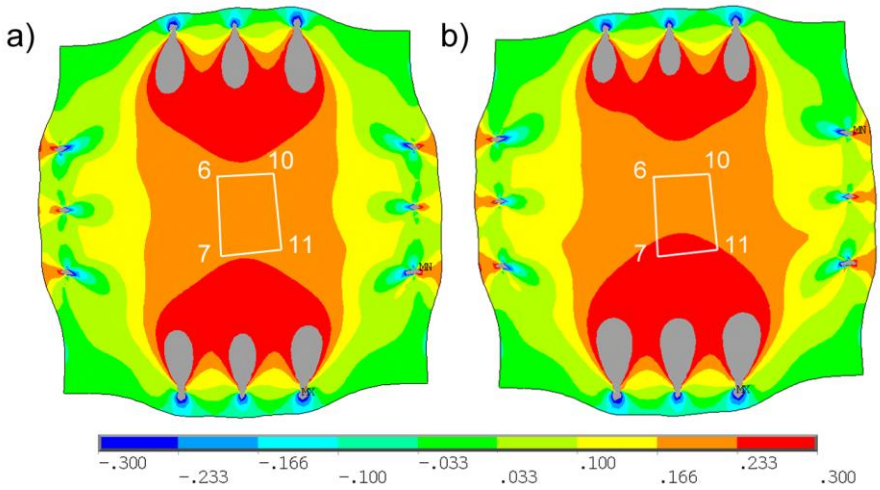


*Figure 6.56 Comparison between finite element models characterized by a) motionless specimen middle point and b) motionless lower hooks insertion points. Strain distribution along the y direction ($\varepsilon_{yy}$).*

Figure 6.56 compares strain distributions along the y direction obtained in the previous subchapter (b) with the result obtained modifying the hooks boundary conditions so that the fixed constraint is transferred in the middle point of the specimen (a). The symmetrical $\varepsilon_{yy}$ distribution is evident in the latter case.

### 6.5.3 Verification of the equibiaxial strain distribution

Anisotropic specimen case.

#### 6.5.3.1. Digital Image Correlation

Similarly to the isotropic case, a preliminary test on the anisotropic tissue, object of study, was carried out. A square human dermis specimen was prepared and the visible surface was equipped with a 4x4 matrix of markers and a random pattern of speckles. Obtaining the random speckles was challenging due to the wet surface of the sample. 12 additional markers were positioned on the hooks, so as to verify the correct displacement of the grips (Figure 6.1).

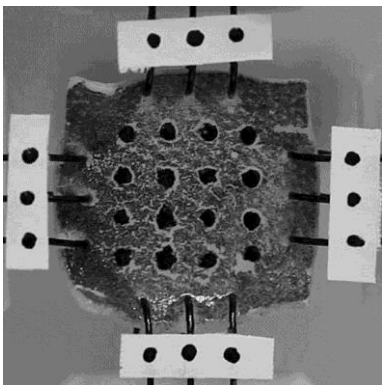

*Figure 6.57 Dermis specimen positioned into the biaxial device.*

Firstly, the markers were tracked along the entire test and the strain-time (Figure 6.58) and stress-strain (Figure 6.59) curves were evaluated. The procedure to obtain the strain curves depicted in Figure 6.58 will be detailed in the following paragraph (Par. 6.5.4). It is clearly evident from the test anisotropy of the results: the stress-strain outcomes in the

two orthogonal directions are highly different, and in particular the behaviour is stiffer along the horizontal direction, which leads to assume the presence of a preferred fibres orientation along this axis.

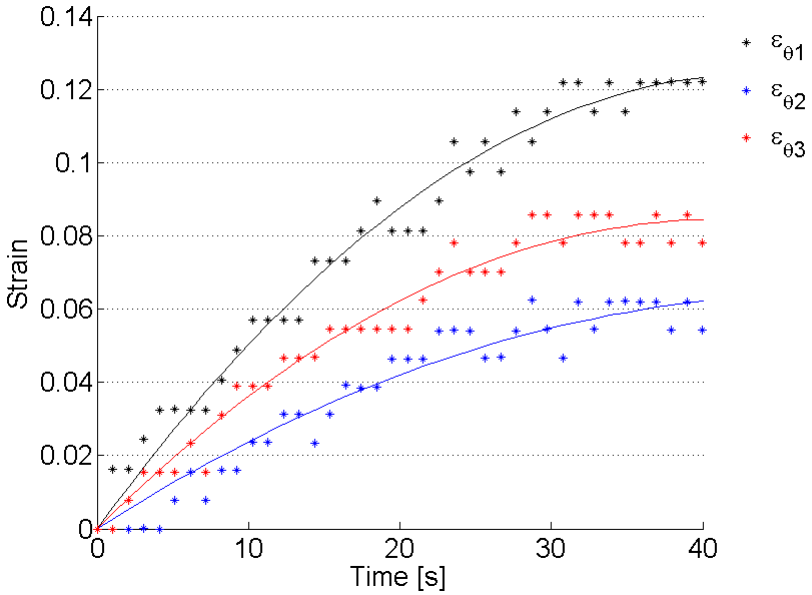


*Figure 6.58 Strain vs time curves in the central region of the specimen.*

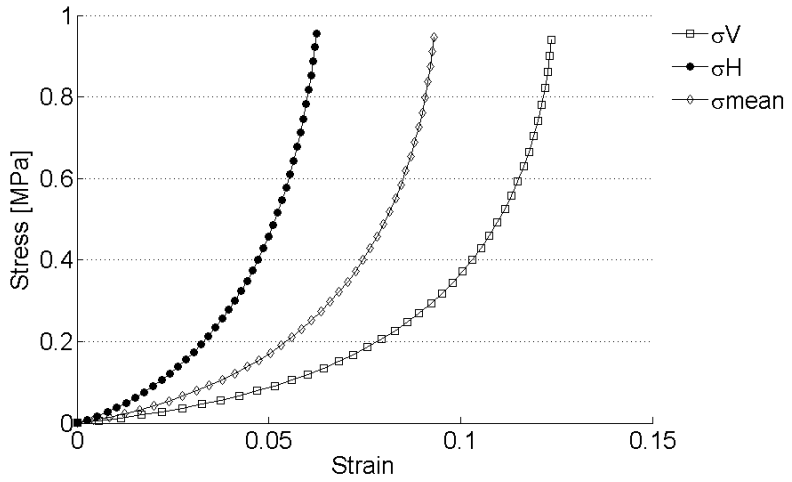


*Figure 6.59 Stress-strain curves evaluated in the central region of the specimen.*

The DIC procedure previously explained was then followed to correlate the frames captured during the test. Again, Figures 6.60, 6.61 and 6.62 shows the digital image correlation results, in terms of strain distribution along the x and y directions, and Von Mises equivalent strain distribution. Three different time instants are highlighted: initial, final and an intermediate instant. The material anisotropy is hereagain confirmed by the not homogeneous strain distribution. Higher strain values are reached in the $\varepsilon_y$ distribution, in accordance with the stress-strain results. When t=40s (namely, at the final instant of the test) the central region of the specimen reaches strains values equal to 0.06 along the x axis and 0.12 along the y axis (Figure 6.59). This is confirmed by the $\varepsilon_x$ and $\varepsilon_y$ distributions in the target region.

Made this considerations, it appear obvious that even though the designed biaxial fixture is able to provide an equibiaxial deformation state, the resultant local strain distribution of a not isotropic specimen is not necessarily uniform. The main cause of this particular behavior is the rearrangement of the collagen fibers along a preferential loading direction, and it follows that a mean stress-strain curve, such as the one depicted in Figure 6.59, shouldn't be used to describe a presumed isotropic behavior of the material in the target region of the specimen.

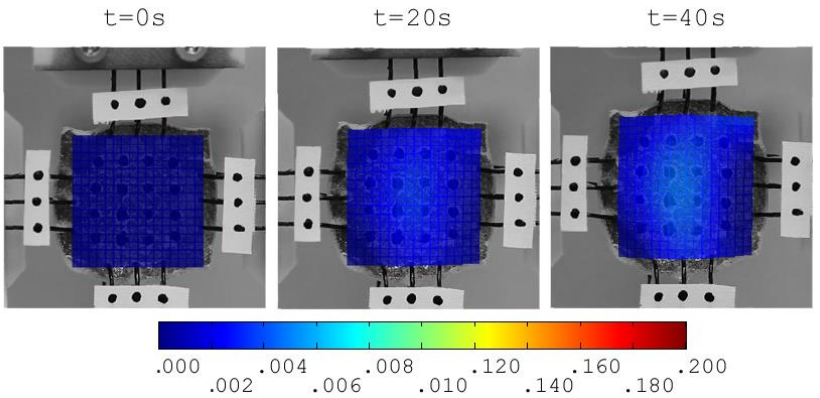


*Figure 6.60 Strain distribution along the x direction in the initial (t=0s), intermediate (t=20s) and final instant (t=40s).*

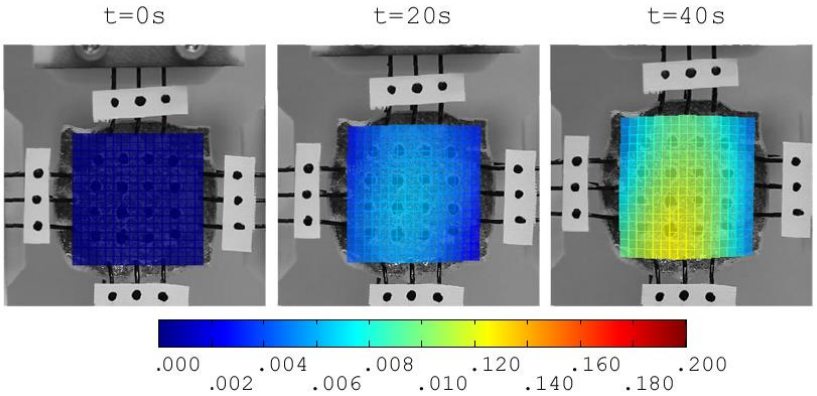


*Figure 6.61 Strain distribution along the y direction in the initial (t=0s), intermediate (t=20s) and final instant (t=40s).*

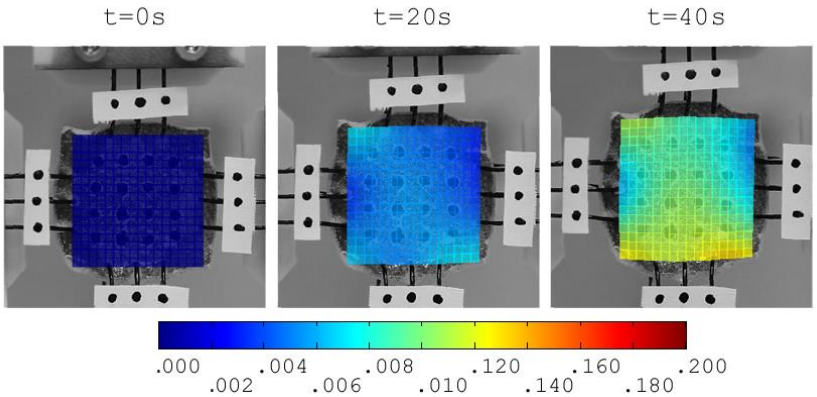


*Figure 6.62 Equivalent Von Mises Strain distribution in the initial (t=0s), intermediate (t=20s) and final instant (t=40s).*

### 6.5.4 Verification of the shear strain extent

The final assessment regarding the device equibiaxiality in the central region of the specimen is addressed to the verification of the absence of shear strain. This is obtained exploiting the rosette gage theory.

The rosette gage theory is based on the assumption that a single strain gage is capable only of measuring the extensional strain in the direction that the gage is oriented. Therefore, the shear strain evaluation isn't feasible unless a rosette of strain gages is mounted on the specimen surface.

The two-dimensional state of strain on a surface is defined by three independent quantities which can be taken as either: (a) $\varepsilon_x$, $\varepsilon_y$, and $\gamma_{xy}$, or (b) $\varepsilon_1$, $\varepsilon_2$, and $\theta$, where case (a) refers to strain components with respect to an arbitrary xy axis system, and case (b) refers to the principal strains and their directions. This situation implies that it should be possible to determine these 3 independent quantities when three independent strain measurements on a surface point can be made. The most obvious approach is to place three strain gages in a "rosette", properly oriented and located as close as possible to the point of interest.

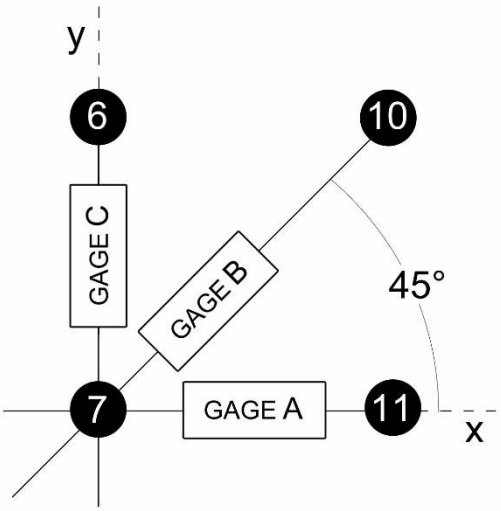


*Figure 6.63 Rectangular strain gage rosettes built between markers #6, #7, #10 and #11.*

Accordingly, a rectangular strain gage rosette was considered inside the central region of the specimen (Figure 6.63). The strains measured respectively between markers #7-#11, #7-#10 and #7-#6 provide the measurements $\varepsilon_{\theta_1}$, $\varepsilon_{\theta_2}$ and $\varepsilon_{\theta_3}$, ideally generated by as many strain gages placed on the lines connecting the markers.

For the rectangular rosette the strains along the x and y directions and the shear strain are described by the following equations (Wheeler & Ganji, 2009):

$$\varepsilon_x = \varepsilon_{\theta 1} \quad \varepsilon_y = \varepsilon_{\theta 3} \quad \varepsilon_{xy} = 2\varepsilon_{\theta 2} - (\varepsilon_{\theta 1} + \varepsilon_{\theta 3})$$

*Equation 6.9*

Figure 6.64 shows the strain-time curves evaluated in the specimen central region in the three previously described directions and shear strain-time curve determined exploiting the rectangular rosette theory. For the entire test the shear strain turns out to be almost zero, confirming the equi-biaxiality in the region of interest of the specimen.

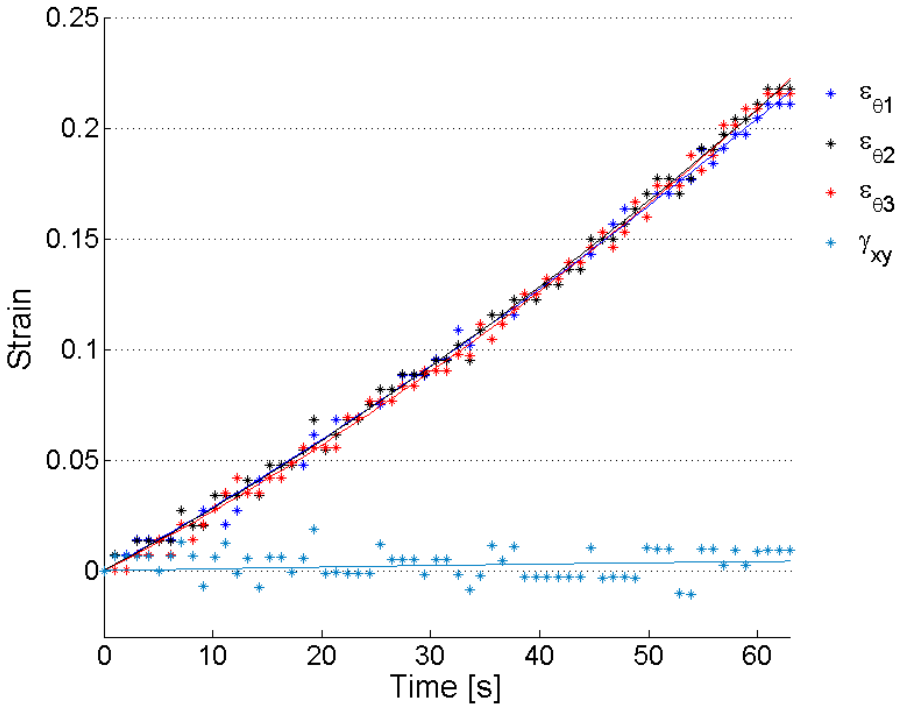


*Figure 6.64 Strain vs time curves in the central region of the specimen.*

## 6.6 Conclusions

This chapter deals with the development of a new low cost biaxial conversion mechanism for a uniaxial testing machine. This mechanism was realized through rapid prototyping method considerably reducing

the implementation costs and simplifying the design phase, assisted by the immediate printing and testing of the components. The printed material appears suitable for the testing of soft materials which, while reaching high deformations, do not generate forces such as to deform the device structure. Furthermore, the conversion device is suitable for the characterization of anisotropic materials, not being affected by any condition of unbalanced load.

All device requirements were reached and validated through the experimental testing of an isotropic rubber specimen. In particular, the optical measure of strains was performed, followed by the consequent evaluation of the uniformity of the strain distribution in a small central region of the specimen, located far from the gripping zone. The local strain distribution was extrapolated using different assessment procedures: the finite element method, the DIC method and the rosette gage theory. All the proofs have led to the same conclusion of equibiaxiality, even though an alteration of the strain distribution at high deformations caused by the lower fixed constraint was highlighted.

The experimental test have shown how the material description, used for the implementation of an Ogden constitutive model, accurately characterizes the material behavior in the strain range covered by the experimental test. Therefore the conversion mechanism appears to be very useful according to the results it provides for the implementation and verification of constitutive models.

In conclusion, the biaxial fixture here presented enables to carry out an equibiaxial tensile test at a very low cost and can be virtually adapted to any existing uniaxial tensile testing machine.

## 6.7 References


Ansys Inc., 2013. *ANSYS Mechanical APDL Element Reference.* Canonsburg, PA: s.n.

Bose Corporation, E. S., 2005. *ElectroForce 3200 Series Reference Manual.* Minnetonka: Bose Corporation.

Brieu, M., Diani, J. & Bhatnagar, N., 2007. A New Biaxial Tension Test Fixture for Uniaxial Testing Machine - A Validation for Hyperelastic Behavior of Rubber-like Materials. *Journal of Testing and Evaluation,* 35(4).

Cavallaro, P., Sadegh, A., Quigley, C. & Johnson, A., 2004. *Effects of Coupled Biaxial Tension and Shear Stresses on Decrimping in Pressurized Woven Fabrics,* s.l.: NUWC-NPT Technical Report 11,571.

CellScale, 2013. *BioTester.* [Online] Available at: http://cellscale.com/products/biotester/ [Accessed 28 January 2016].

Duncan, B., 1999. *Test methods for determining hyperelastic properties of flexible adhesives.,* s.l.: NPL Report CMMT(MN)054.

Bose ElectroForce, 2014. *ElectroForce® Linear Motion Systems.* [Online] Available at: http://electroforce.tainstruments.com/-electroforce/assets/pdf/Products/LinearMotionSystems.pdf [Accessed 8 Febbraio 2016].

Electroforce, T., 2014. *ElectroForce Planar Biaxial TestBench Instrument (2 Motor).* [Online] Available at: http://electroforce.-tainstruments.com/electroforce/en˙us/web/planar˙biaxial˙2˙motor/page.html [Accessed 28 January 2016].

Grashow, J., Yoganathan, A. & Sacks, M., 2006. Biaxial stress-stretch behavior of the mitral valve anterior leaflet at physiologic strain rates. *Annals of Biomedical Engineering,* 34(2), pp. 315-25.

Honeywell, 2004. *Honeywell sensing & control.* [Online] Available at: https://measurementsensors.honeywell.com/Product-Documents/Load/Model˙31˙Datasheet.pdf [Accessed 8 Febbraio 2016].

Johlitz, M. & Diebels, S., 2011. Characterization of a polymer using biaxial tension tests. Part I: Hyperelasticity. *Archive of Applied Mechanics,* 81(10), pp. 1333-1349.

Jones, E., 2013. *Documentation for Matlab-base DIC code.* Illinois: Copyright (c) 2013, Elizabeth Jones.

Kahlon, A., Hurtig, M. & Gordon, K., 2015. Regional and depth variability of porcine meniscal mechanical properties through biaxial testing. *The Journal of the Mechanical Behavior of Biomedical Materials,* Volume 41, pp. 108-14.

Lally , C., Reid, A. & Prendergast, P., 2004. Elastic behavior of porcine coronary artery tissue under uniaxial and equibiaxial tension. *Annals of Biomedical Engineering,* 32(10), pp. 1355-64.

MEAS, 2015. *Measurement specialities.* [Online] Available at: http://www.meas-spec.com/downloads/MHR˙Series.pdf [Accessed 8 Febbraio 2016].

Prendergast, P., Lally, C., Daly, S. & Reid, A., 2003. Analysis of Prolapse in Cardiovascular Stents: A Constitutive Equation for Vascular Tissue and Finite-Element Modelling. *Journal of Biomechanical Engineering,* 125(5), pp. 692-9.

Sacks, M., 2001. Biaxial Mechanical Evaluation of Planar Biological Materials. *Journal of Elasticity,* Volume 61, pp. 199-246.

Skulborstad , A., Swartz, S. & Goulbourne, N., 2015. Biaxial mechanical characterization of bat wing skin. *Bioinspiration & Biomimetics,* 10(3).

TESTRESOURCES, 2016. *574 Family Planar Biaxial Electrodynamic Fatigue Test Machines.* [Online] Available at: http://www.testresources.net/test-machines/574-family [Accessed 28 January 2016].

Waldman, S. & Lee, J., 2002. Boundary conditions during biaxial testing of planar connective tissues. Part 1: Dynamic Behavior. *Journal of Materials Science: Materials in Medicine,* 13(10), pp. 933-8.

Wheeler, A. & Ganji, A., 2009. *Introduction to Engineering Experimentation.* 3rd ed. s.l.:Prentice Hall.

Zemánek, M., Burša, J. & Děták, M., 2009. Biaxial Tension Tests with Soft Tissues of Arterial Wall. *Engineering Mechanics,* 16(1), pp. 3-11.

Zhang, D. & Arola, D., 2004. Applications of digital image correlation to biological tissues. *Journal of Biomedical Optics,* 9(4), pp. 691-9.

Zwick/Roell, 2010. *Zwick/Roell - Biaxial Test on Artificial Tissues.* [Online] Available at: http://www.zwick.co.uk/en/applications/-medical-industry/biomaterials/biaxial-teston-artificial-tissues.html [Accessed 28 January 2016].

# Chapter 7

# Equibiaxial mechanical characterization of HADM

## 7.1 Introduction

As a consequence of its oriented fibrous structure, dermis always exhibit a pronounced mechanical anisotropy, which has been largely discussed in the previous chapters, because of its wide occurrence when dealing with a uniaxial characterization. Planar biaxial testing allows for a two-dimensional stress-state that can be used to fully characterize the dermis properties.

In the previous chapter the main experimental problems involved in carrying out biaxial tests on biological specimens were highlighted. Recalling the main ones, care is needed when dealing with the effects of different gripping techniques, the large specimen-to-specimen variability and the homogeneity of deformation within the specimen. Moreover, being paramount the optical measure of strains avoiding any mechanical interference, also the marker positioning on a wet substrate is challenging. The strain optical measure is generally performed in a central target region which must be sufficient small and located away from the outer edges to avoid the gripping effects. In this central region the stress-strain field is considered homogenous (Sacks, 2001). This assumption is based on the Saint-Venant's principle which states that the stress distribution

may be assumed to be independent of the actual mode of load application, except in the immediate vicinity of where the load is applied (Waldman & Lee, 2002). Nevertheless, the effects of load applications may be very different, depending on the gripping method: by clamp or by suture. The suture case can possibly generate a discontinuous load transfer, also dependent on the number and on the vicinity of the suture points. On the contrary, the clamping method would generate a continuous load transfer at the expense of a stiffening of the tissue and of a greater chance of slipping during the test. Certain is that the placement of an allograft in vivo during a reconstructive surgery takes place via suture, and therefore the application of the load in the immediate postoperative period will be punctual. Another element to consider is the need to obtain a cruciform specimen for the clamp gripping method, which not only is more difficult to realize, but also causes the waste of a material already difficult to source.

The first investigators to develop (Lanir & Fung, 1974a) and utilize (Lanir & Fung, 1974b) planar biaxial testing for soft biological tissues were Lanir and Fung. They investigated the mechanical properties of rabbit skin demonstrating the nonlinear and orthotropic stress-strain response of the skin and the dependence of the latter on the specimen anatomic orientation. Moreover, they developed the most broadly used constitutive model for the biaxial response of skin (Tong & Fung, 1976).

The biaxial characterization of soft tissues involved then extensively the cardiac and artery tissues, with the aim of implement constitutive models useful to carry out preclinical tests of intravascular devices (Lally , et al., 2004; Grashow, et al., 2006; Prendergast, et al., 2003; Zemánek, et al., 2009; Billiar & Sacks, 2000), and the porcine meniscal (Kahlon, et al., 2015). In many cases, the research outcome are models parameters obtained through the fitting of a mean curve (Lally , et al., 2004; Prendergast, et al., 2003). The assumption is that although the anisotropy of the tissue is obvious and confirmed by the biaxial tests, the response of the tissue along two orthogonal axes has no significant difference at physiological loadings. This may not be true when it comes to

the skin, which can reach high strains both in vivo and in vitro. It appears then remarkable the lack of papers on the biaxial properties of human dermis. The aim of this work is to fill this gap presenting equibiaxial experimental curves of decellularized human dermis.

## 7.2 Materials and Methods

### 7.2.1 Biaxial mechanical tests

Large strips of dermis tissue, collected from the backs of human donors, were dissected along the cranio-caudal direction. They were then decellularized using an incubation in DMEM medium for 5 weeks. The treatment type and its duration were setted according to the uniaxial characterization results (see Chapter 2). Intact not decellularized human reticular dermis coming from the same donors was used as a control. The specimens were obtained by cutting out 30x30 mm squares using a custom made die cutter. A maximum of four specimens from each strip was obtained, except for the not-treated strip (T0) coming from donor 726. The total number of specimens is summarized in Table 7.1.

*Table 7.1 Number of specimens tested for each group. T0 stands for the not-treated specimens, while T5 indicate the decellularized specimens.*

| Donor | T0 | T5 |
|---|---|---|
| 718 | 4 | 4 |
| 726 | 2 | 4 |
| 728 | 4 | 4 |

The cutting orientation with respect to the sampling direction has been indicated by means of stitches sewed at the northwest vertex of the square. One stitch represented the first specimen, two stitches the second one, and so on (Figure 7.1). The sewed stitches have been positioned so as to avoid interferences with the gripping of the specimen. This numbering is needed in order preserve the original orientation and location during the measurement and washing procedures.

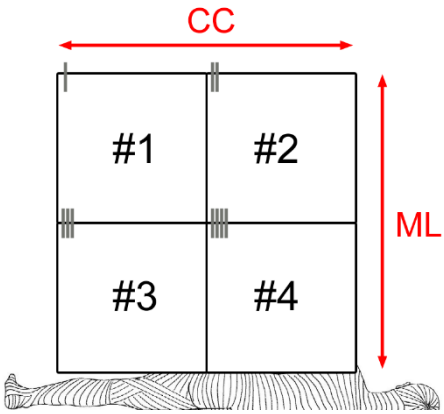


*Figure 7.1 Specimens cutting and orientation with respect to the body. CC: cranio-caudal direction; ML: medio-lateral direction.*

Before use, the dermis grafts were washed to remove all of the glycerol, dipping them sequentially in three different beakers filled with abundant saline solution 0.9% at +37°C for more than three minutes each. The specimens thickness was then obtained by means of photogrammetry as an average of five measures: 2.43±0.46-mm thickness (average ± std).

Following the mounting procedure described in the previous chapter, three hooks was inserted on each side of the sample, at a 5-mm distance from the edges. The spacing between the hooks was 5 mm. A 4x4 matrix of markers was then dawn on the visible surface with an alcohol-based permanent black ink and afterwards the specimen was carefully positioned into the biaxial testing device (Figure 7.2). The test speed was setted to 0.16mm/s and the test was stopped at the achievement of a 10-mm displacement on each axis.

A full-frame digital camera (Canon EOS 5D Mark II) with an autofocus lens for macro photography (Canon EF 100 mm f/2.8 Macro USM) was used to capture images of the specimen during the test with a frame rate setted to 1 Hz.

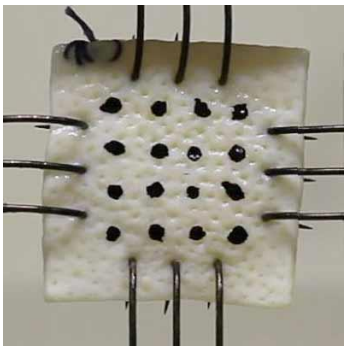

*Figure 7.2 Specimen positioning into the biaxial device.*

### 7.2.2 Data Elaboration

The loads were acquired by the two load cells positioned along the two loading directions, while the marker deformations were measured optically using the photogrammetry set-up.

The true stress was then calculated by dividing the load cell readings by the cross-sectional area of the specimen, which was taken as the product of the gauge length in the two orthogonal directions and the thickness of the specimen over time. The gauge lengths were evaluated through the ImageJ image analysis software as an average of three measures of the distance between the hooks, orthogonally to the loading direction (Equations 6.4 – 6.5). The strain of the tissue along the two loading directions was then determined from the distance increase between the central markers of the specimen in the horizontal and vertical directions (Equations 6.6 – 6.7).

From the experimental data obtained, the slope of the toe region was evaluated from 0 to a 10% of strain, and results from each specimen were compare with the surrounding specimens, searching for a preferential fibers orientation in the whole dermis strip.

## 7.3 Results and Discussion

A representative set of results of the biaxial tensile testing can be found in Figure 7.3 (all results can be found in Par. 7.6). It shows the stress-strain curves of four specimens cutted from the same dermis strip.

The graphs position reflects the specimens original position represented in Figure 7.1. In some cases the testing wasn't completed with success due to human errors during the experiment, resulting in a lack of data for medio-lateral direction of the not-treated specimens coming from donor 726.

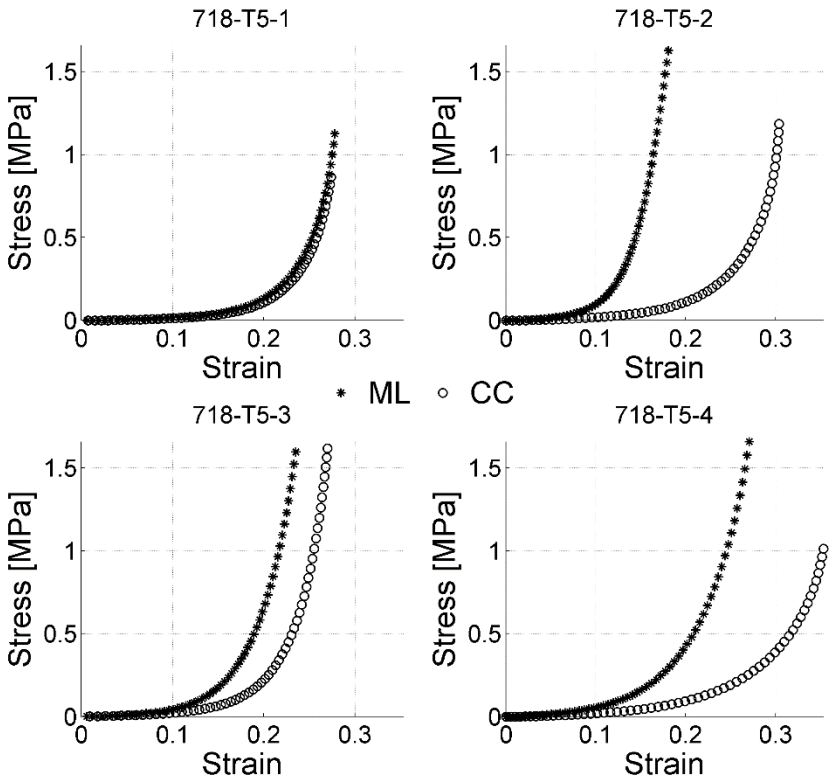


*Figure 7.3 A representative stress-strain set of curves (decellularized specimens from donor 718). The disposition of the plots reflects the positioning of the specimens of Figure 7.1.*

Results underline the anisotropic behaviour of dermis, since the mechanical response in one direction appears, most of the times, stiffer that the one in the orthogonal direction. In particular, the overall result for the biaxial data in the medio-lateral direction was higher than the cranio-caudal direction. This can be explained by the predominance of collagen fibres aligned along the medio-lateral direction in the dermis tissue taken from the lower back, which is in accordance with Langer findings

(Langer, 1978) and later works, already mentioned in Chapter 2, and listed in Table 7.2.

*Table 7.2 Mechanical properties of skin in literature. "Parallel to the Langer Line orientation" is equivalent to the medio-lateral direction in the lower back zone.*

| Author | Skin Location (Langer Line Orientation) | Elastic Modulus (MPa) |
|---|---|---|
| (Nì Annaidh, et al., 2012a) | Bottom Back (Parallel) | 73.81 ± 19.41 |
| | Bottom Back (Perpendicular) | 37.66 ± 36.41 |
| (Yoder & Elliott, 2010) | Alloderm (Parallel) | 221.48 ± 141.20 |
| | Alloderm (Perpendicular) | 11.21 ± 3.53 |

Similar findings were described by Lanir & Fung (1974b) ragarding the rabbit skin. They found a stiffer behaviour of the tissue along the body width (medio-lateral direction) then along the body length, when biaxially solicitated. As showed through DIC methods in the previous chapter, the high anisotropy causes a not homogeneus strain distribution along the specimen, also affecting its central ROI, in which the characteristic curve of the material is evaluated. Previous studies reported results regarding the percentage of the area which can be considered characterized by an uniform strain distribution. For instance, Humphrey et al. (1987) reported an uniform strain distribution within the central 4% ot the specimen area, while Billiar & Sacks (2000) found an uniformity of strains in the central 25% of the specimen area, but specifying that an homogeneous isotropic material loaded at four discrete locations per side was tested. For an anisotropic tissue the stress-strain distribution would be less uniform, thus a smaller percentage should be considered, even though direct experimental evidence is needed. Nevertheless, Oomens et al. (1993) claims that an homogeneous strains cannot be obtained because of the inhomogeneous materials properties and the challenging (sometimes impossible) manufacturing of sample. Anyhow, in this work about the 5% of the gauge area (from hooks to hooks) was considered for the stress-strain curves extraction.

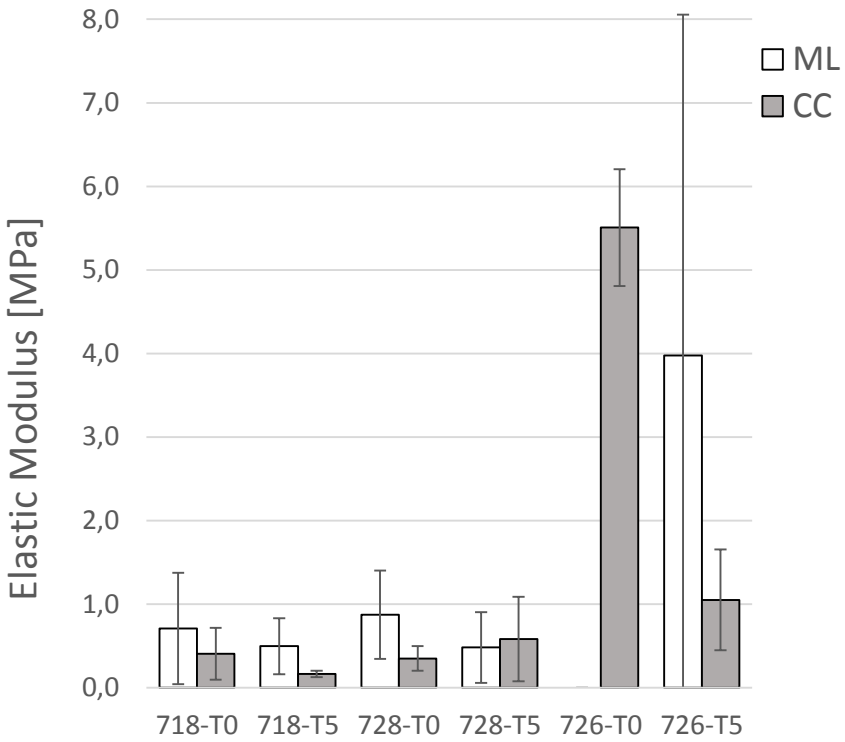


*Figure 7.4 Biaxial elastic modulus for the medio-lateral and the cranio-caudal directions. Values are the average values ± the standard deviation of the mean.*

The slope of the toe region in a physiological range of strains (0-10%) was evaluated from each experimental curve (Manschot & Brakkee, 1986). Results are represented in Figure 7.4 and in Table 7.3.

*Table 7.3 Biaxial elastic modulus value for the medio-lateral and the cranio-caudal directions (average ± SD).*

| | | Elastic Modulus [MPa] (average ± SD) | |
|---|---|---|---|
| | | T0 | T5 |
| 718 | ML | 0.708 ± 0.688 | 0.496 ± 0.335 |
| | CC | 0.406 ± 0.309 | 0.163 ± 0.038 |
| 728 | ML | 0.872 ± 0.530 | 0.481 ± 0.424 |
| | CC | 0.349 ± 0.148 | 0.582 ± 0.507 |
| 726 | ML | - | 3.976 ± 4.079 |
| | CC | 5.506 ± 0.699 | 1.049 ± 0.603 |

The higher stiffness of the tissue in the medio-lateral direction (along Langer lines) is here confirmed, with standard deviations relatively limited. Only exception the donor 726 which shows in general higher average values of elastic modulus, and in the decellularized tissues in particular shows high standard deviations along the medio-lateral direction (3.976 ± 4.079 MPa). The mean elastic modulus for the medio-lateral direction resulted from 43% to 74% higher than the cranio-caudal one, with the exception of the decellularized tissue coming from donor 728 which shows a cranio-caudal elastic modulus 20% higher than the medio-lateral one.

Comparing the paired native and decellularized groups of specimens, the reduction of the mechanical properties of the treated dermis with respect to the native tissue is hereagain confirmed for all donors, and considering both directions. Therefore, the missing medio-lateral results for donor 726 let envisage that a mean elastic modulus higher then 5.5 MPa would be obtained.

Surgical procedures begin and end with incisions, and the incisions planning is a mandatory step when a good outcome is desired in terms of scars and tension distribution in the scar proximity (Waldorf, et al., 2002). The incision planning is intimately related to the Langer's lines orientation, because incisions made parallel to Langer's lines may heal better and produce less scarring than incisions made across Langer's lines (Physiology, 2015). This consideration can also be shifted in cases which do not directly involve aesthetics, such as soft tissues reconstructive surgeries, were a biological graft is needed. When placed in a body part where the substitute will bear a physiological and anisotropic distribution of stress, the orientation of the graft should be consistent with the surrounding tissue. Therefore not only the stiffer direction of the host tissue should be known, but also the substitute one and, ideally, an equi-biaxial test performed on a small square specimen excerpts from the graft could provide this indication.

## 7.4 Conclusions

The biaxial mechanical behaviour of untreated and decellularized dermis was measured exploiting the purpose-made biaxial fixture described in the previous chapter. Stress-strain curves were evaluated from the loads acquired by two load cells positioned along two orthogonal axis and the optical measure of the deformations of four markers located in the central area of the specimen. Comparisons among the native and decellularized tissues demonstrated again the loss of mechanical strength caused by the decellularization treatment. Moreover the specimens resulted, on average, less extensible in the medio-lateral direction (namely, along the Langer lines) then in the cranio-caudal direction, confirming the correlation of dermis mechanical response with collagen fibres orientation with respect to the loading direction.

## 7.5 References

Billiar, K. & Sacks, M., 2000. Biaxial Mechanical Properties of the Natural and Glutaraldehyde Treated Aortic Valve Cusp - Part I: Experimental Results. *Journal of Biomechanical Engineering,* Volume 122, pp. 23-30.

Grashow, J., Yoganathan, A. & Sacks, M., 2006. Biaixal stress-stretch behavior of the mitral valve anterior leaflet at physiologic strain rates. *Annals of Biomedical Engineering,* 34(2), pp. 315-25.

Humphrey , J., Vawter, D. & Vito, R., 1987. Quantification of strains in biaxially tested soft tissues. *Journal of Biomechanics,* 20(1), pp. 59-65.

Kahlon, A., Hurtig, M. & Gordon, K., 2015. Regional and depth variability of porcine meniscal mechanical properties through biaxial testing. *Journal of Mechanical Behaviour of Biomedical Materials,* Volume 41, pp. 108-114.

Lally , C., Reid, A. & Prendergast, P., 2004. Elastic behavior of porcine coronary artery tissue under uniaxial and equibiaxial tension. *Annals of Biomedical Engineering,* 32(10), pp. 1355-64.

Langer, K., 1978. On the anatomy and physiology of the skin. I. The cleavability of the cutis. *British Journal of Plastic Surgery,* 31(1), pp. 3-8.

Lanir, Y. & Fung, Y., 1974a. Two-dimensional mechanical properties of rabbit skin—I. Experimental system. *Journal of Biomechanics,* 7(1), pp. 29-34.

Lanir, Y. & Fung, Y., 1974b. Two-dimensional mechanical properties of rabbit skin—II. Experimental results. *Journal of Biomechanics,* 7(2), pp. 171-182.

Manschot, J. & Brakkee, A., 1986. The Measurement and Modelling of the Mechanical Properties of Human Skin in vivo -- I. The Measurement. *Journal of Biomechanics,* 19(7), pp. 511-515.

Nì Annaidh, A. et al., 2012a. Characterization of the anisotropic mechanical properties of excised human skin.. *Journal of the Mechanical Behavior of Biomedical Materials,* Volume 5, pp. 138-48.

Oomens, C., Ratingen, M., Jannsen, J. & Hendriks, M., 1993. A Numerical-Experimental Method for a Mechanical Characterization of Biological Materials. *Journal of Biomechanics,* 26(4/5), pp. 617-621.

Physiology, B. A. a., 2015. *Lines of Cleavage and Surgery.* [Online] Available at: https://www.boundless.com/physiology/textbooks/-boundless-anatomy-and-physiology-textbook/the-integumentary-system-5/skin-diseases-disorders-injury-and-clinical-cases-69/lines-of-cleavage-and-surgery-424-184/ [Accessed 20 March 2016].

Prendergast, P., Lally, C., Daly, S. & Reid, A., 2003. Analysis of Prolapse in Cardiovascular Stents: A Constitutive Equation for Vascular Tissue and Finite-Element Modelling. *Journal of Biomechanical Engineering,* 125(5), pp. 692-9.

Sacks, M., 2001. Biaxial Mechanical Evaluation of Planar Biological Materials. *Journal of Elasticity,* Volume 61, pp. 199-246.

Tong, P. & Fung, Y., 1976. The stress strain relationship for the skin. *Journal of Biomechanics,* 9(10), pp. 649-657.

Waldman, S. & Lee, J., 2002. Boundary conditions during biaxial testing of planar connective tissues. Part 1: Dynamic Behavior. *Journal of Materials Science: Materials in Medicine,* Volume 13, pp. 933-938.

Waldorf, J., Perdikis, G. & Terkonda, S., 2002. Planning Incisions. *Operative Techniques in General Surgery,* 4(5), pp. 199-206.

Yoder, J. & Elliott, D., 2010. Nonlinear and anisotropic tensile properties of graft materials used in soft tissue applications. *Clinical Biomechanics,* 25(4), pp. 378-82.

Zemánek, M., Burša, J. & Děták, M., 2009. Biaxial Tension Tests with Soft Tissues of Arterial Wall. *Engineering Mechanics,* 16(1), pp. 3-11.

## 7.6 Supplementary Material

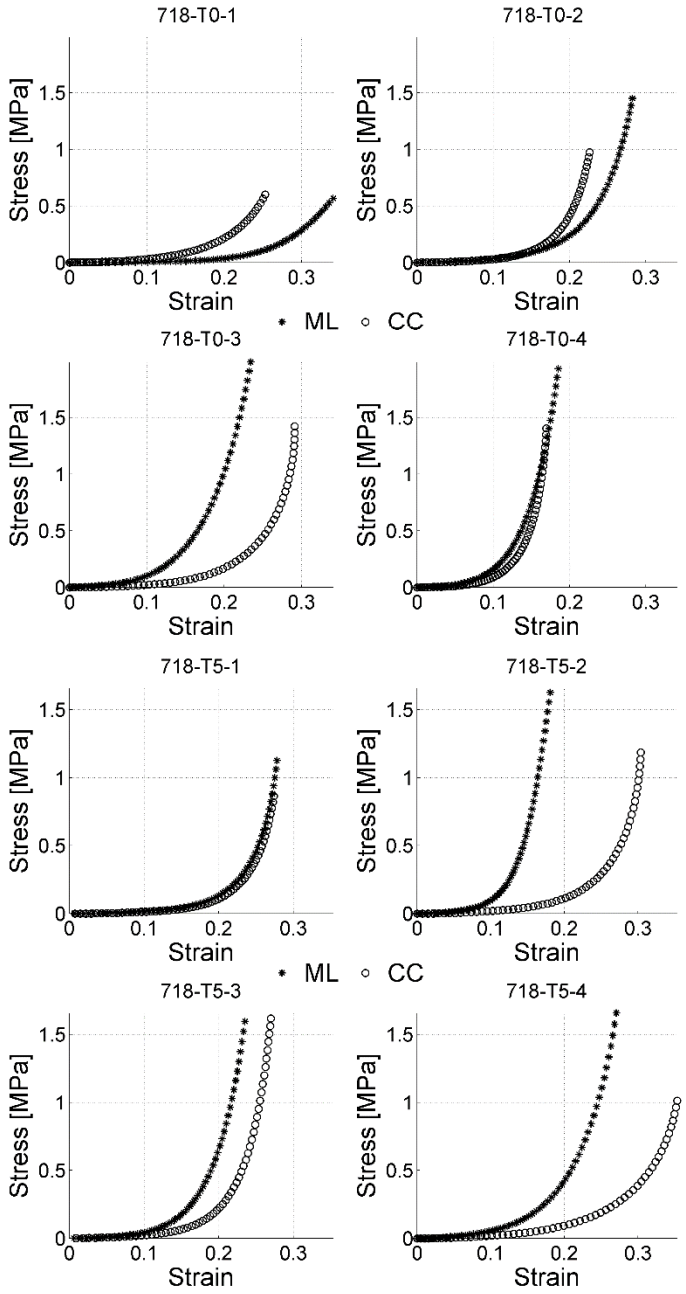


*Figure 7.5 Stress-strain curves for donor 718.*

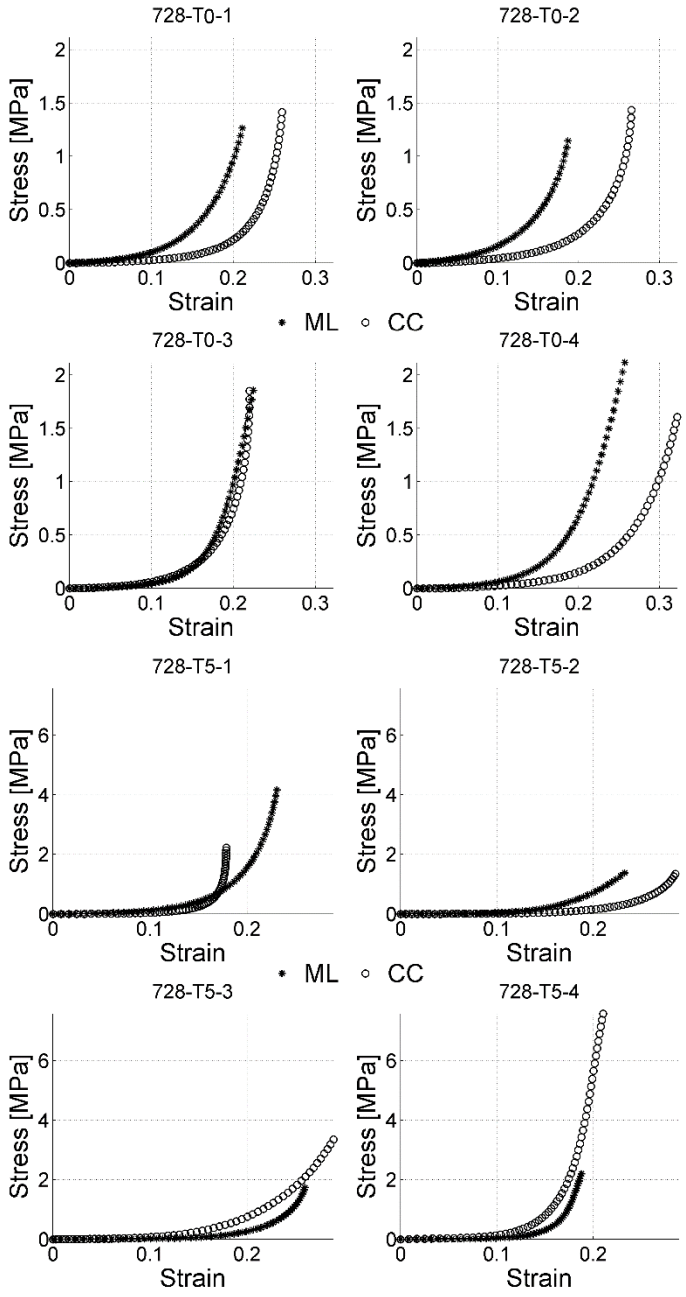


*Figure 7.6 Stress-strain curves for donor 728.*

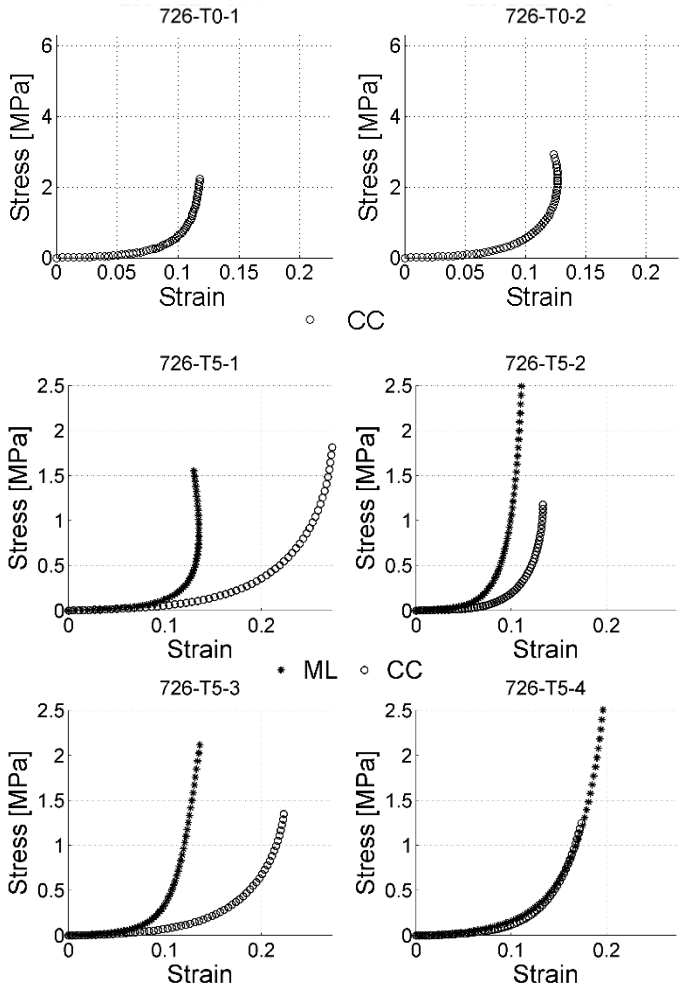


*Figure 7.7 Stress-strain curves for donor 726.*

# Chapter 8

# Conclusions

## 8.1 Major findings

This study presents at first a series of experiments aimed at the engineering and validation of an acellular dermal matrix produced starting from the excised human reticular dermis. The HADM object of study is directed at clinical applications which implicate demanding mechanical properties. Here's why the effects of the chemical treatments involved in the preparation of an acellular dermal matrix (decellularization and conservation processes) on the structural integrity of the native ECM represents an extremely important point.

Therefore, the effectiveness of a new decellularization treatment was assessed by means of a comparison with the mechanical behaviour of a HADM resulting from a standard decellularization in NaOH medium. The alternative methodology developed by the research unit of the Skin Bank (AOU Città della Salute e della Scienza) consists of keeping the tissue in DMEM (Dulbecco's modified Eagle medium) for a long period of time while being subjected to mechanical tilting. It was demonstrated that this process generates a dermal substitute which exhibited mechanical properties similar to the native tissue ones and better handling, greater flexibility and lower needle penetration resistance, when compared with the NaOH outcome.

Efforts have been made to identify the more correct stress-strain formulation for the extraction of faithful mechanical parameters, while maintaining a simple uniaxial experimental set-up. The comparison among mechanical properties measured from engineering, simplified true or true curves has demonstrated that ultimate tensile strength, deformation and maximum elastic modulus can be heavily underestimated considering engineering and simplified true curves. More realistic values obtained from true curves are therefore recommended when setting up dermis computational models, while engineering and true curves values remain useful for comparative analyses.

The effects of a standard conservation process were then investigated, comparing the freshly excised human dermis with the glycerol preserved dermis. The influence of the glycerolization procedure on the mechanical properties of excised human dermis resulted to be statistically significant, causing the stiffening of the tissue despite the maintenance of the ultimate deformability features of the native tissue. This is considered a positive outcome because of the clinical applications, demanding in terms of the strength required, in which the HADM will be employ. In this context, a correlation with age and sex of the donors was found, confirming the age-related changes and sex-dependent behavior of the dermis.

As a closure of the first stage of optimization of the new dermal substitute, a further study was performed, investigating the response of the tissue subjected to suture. In fact, dependent on the intended use, the biomechanical response of the sutured allografts may be of clinical significance, especially in potentially load bearing applications and in cases where the shortage of material obliges to obtain patches for large defects suturing allografts of smaller dimensions. Characteristic curves of the sutured dermis behaviour were thus obtained and compared with intact specimens used as a reference. This analysis showed an increase in the elasticity of the sutured specimens, which appears to have beneficial effects in the immediate post-operative period, when the dermis allograft has not yet been incorporated and colonized by the host tissue. A new characterization procedure which couples results coming from

both the testing machine and image analysis was here implemented, in order to provide additional information other than the only "suture retention strength" value. This method could allow to isolate the contribute given by the suture material, deducing the specific contribution of the tissue to the overall deformation. Finally, a dynamic characterization was performed, whose clinical relevance lies in the possibility of impulsive events that may occur in the post-operative period (e.g. coughs, sneezes or a sudden efforts).

The experimental data obtained from the uniaxial characterization were employed in an investigation of the effects of different nonlinearities (geometric and material nonlinearity) on three output parameters obtainable from experimental tests (deformation and global stress). Decellularized dermis behaviour was thus described by four linear and nonlinear hyperelastic models inputting the engineering stress-strain curves and validating the results through parameters extracted from the true formulation. The results obtained from the hyperelastic models well represented the experimental situation, and in particular the incompressible Odgen model showed less than 7% percentage variations for all considered parameters. Despite the Ogden hyperelastic model resulted adequate to the description of a dermis specimen subjected to a uniaxial solicitation, it is based on an isotropic assumption which is in contrast with the biological materials high anisotropy. Thus, the incompressible Ogden model seemed suitable for the description of the dermis behaviour when the isotropic assumption can be considered true, such as in small deformation conditions.

The uniaxial tensile testing is an effective and relatively simple method to obtain comparison parameters, useful as reference in the optimization processes. The required experimental set-up is present in almost all mechanical laboratories, therefore the cost of these tests is very low. However, a more complex biaxial (at least) set-up would be required to fully characterize the properties of a highly anisotropic tissue like the human dermis, and the high costs of these test benches often prevents this type of analysis. Here's why a new low cost biaxial conversion mechanism for a uniaxial testing machine was designed and realized in this

work. This mechanism was realized through rapid prototyping, considerably reducing the implementation costs and facilitating the design phase, assisted by the immediate printing and testing of the components. The performance of this device requirement was validated through experimental testing and computational analysis: the equibiaxial motion was so tested on a square specimen gripped through twelve hooks, and the uniform strain distribution in a central ROI of an isotropic rubber sample was evaluated by means of an optical measure of the strains. Therefore, this biaxial fixture has been proved to allow carrying out an equibiaxial tensile test on decellularized human dermis, at very low cost. From the equibiaxial characterization, stress-strain curves along the two loading axis were evaluated and the tested specimens resulted on average less extensible in the medio-lateral direction (namely, along the Langer lines) then in the cranio-caudal direction, confirming the correlation of dermis mechanical response with collagen fibres disposition with respect to the loading direction. The corroboration of this behaviour, known in surgical practice and already demonstrated considering the skin as a whole, represents an extremely interesting point in the clinical application. As a matter of fact, when placed in a body part where the substitute will bear a physiological and anisotropic distribution of stresses, the orientation of the HADM should be consistent with the surrounding tissue, thus it should be kept track of the orientation of the starting dermis in order to optimize the graft mechanical function.

## 8.2 Future works

The analysis here performed has made it possible to carry out a comprehensive description of the HADM optimized in collaboration with the Skin Bank (AOU Città della Salute e della Scienza). This substitute is today in the animal testing stage, and in the short term the clinical trials phase will begin. Therefore further experimental investigations will be needed, focusing primarily on the suture issue. The sutured dermis im-

pulsive response is indeed of great interest for surgeons, since the stability of the repair in the immediate postoperative period is an essential requirement for a successful surgery outcome.

The preliminary equibiaxial results here presented represent the starting point for an anisotropic constitutive modelling of the dermis substitute, which would allow for the improvement of the efficacy of the medical implants through the development of improved computer simulation tools. Although the isotropic Odgen constitutive model resulted feasible for the description of the tissue subjected to minor solicitations, the nonlinear configuration of the stresses in the immediate post operatory period would need a more reliable material model.

A deeper investigation in this direction will be helped by ongoing tests which aim to couple equibiaxial results with nanoindentation tests, in order to match the anisotropic behaviour of the tissue at the micro and the macro scale.

# Appendix A

## Equibiaxial conversion device

parts and assemblies drawings

In the following, the main parts and assemblies of the equibiaxial conversion device described in Chapter 6 are depicted. Tables listing all the constitutive parts of the assemblies are also present in the technical drawings. All the components were 3D printed in ABS. The only exceptions were the linear guidways (Hiwin®) and the twelve hooks.

| | Object | Quantity |
|---|---|---|
| 1 | Linear Guideway Block | 4 |
| 2 | Connector | 2 |
| 3 | Lateral Extension | 4 |
| 4 | Linear Guideway Rail | 4 |
| 5 | B18.3.1M - 3 x 0.5 x 16 Hex SHCS -- 16NHX | 8 |
| 6 | Link | 2 |
| 7 | Load Cell Adapter | 4 |
| 8 | Vertical Load Cell | 1 |
| 9 | Bottom Terminal | 1 |
| 10 | B18.2.4.2M - Hex nut, Style 2, M5 x 0.8 --D-N | 4 |
| 11 | B18.3.1M - 5 x 0.8 x 12 Hex SHCS -- 12NHX | 1 |
| 12 | Left Terminal | 1 |
| 13 | Horizontal Load Cell | 1 |
| 14 | Right Rod | 1 |
| 15 | Upper/Right Terminal | 2 |
| 16 | Upper Rod | 1 |
| 17 | Stopper for Gripping Arm - Bottom | 1 |
| 18 | Stopper for Gripping Arm - Left | 1 |
| 19 | Hook | 12 |
| 20 | Lower Hooks Holder | 4 |
| 21 | Upper Hooks Holder | 4 |
| 22 | Nail | 12 |
| 23 | B18.3.1M - 3 x 0.5 x 16 Hex SHCS -- 16NHX | 18 |
| 24 | B18.6.7M - M5 x 0.8 x 25 Indented HHMS --25C | 1 |
| 25 | B18.6.7M - M5 x 0.8 x 30 Indented HHMS --30C | 1 |
| 26 | B18.3.1M - 4 x 0.7 x 20 Hex SHCS -- 20NHX | 8 |

*Figure A.1 Equibiaxial conversion device assembly. The table lists all the constitutive parts.*

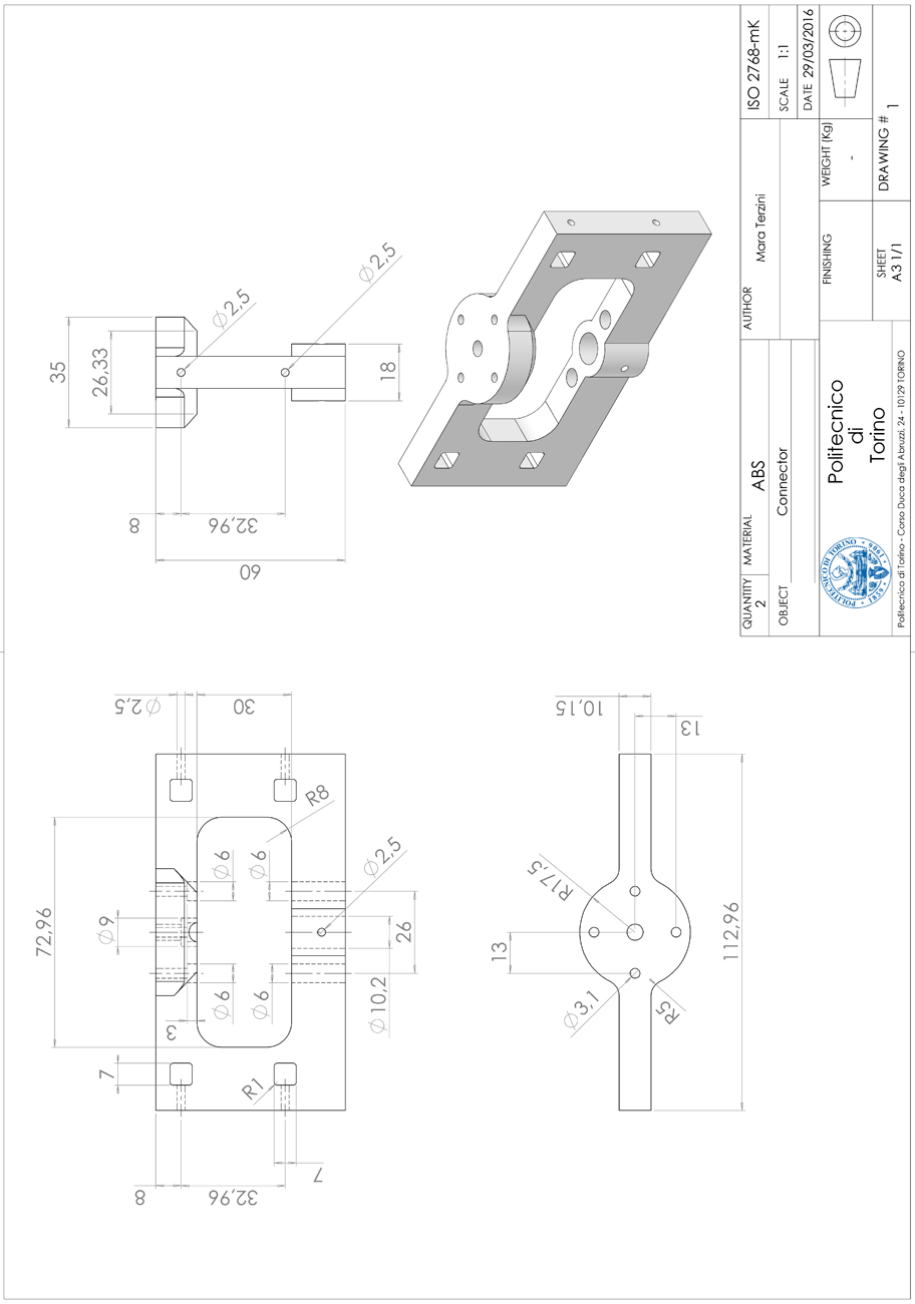


*Figure A.2 Connector drawing. The connector is included both in the upper and in the lower crossheads.*

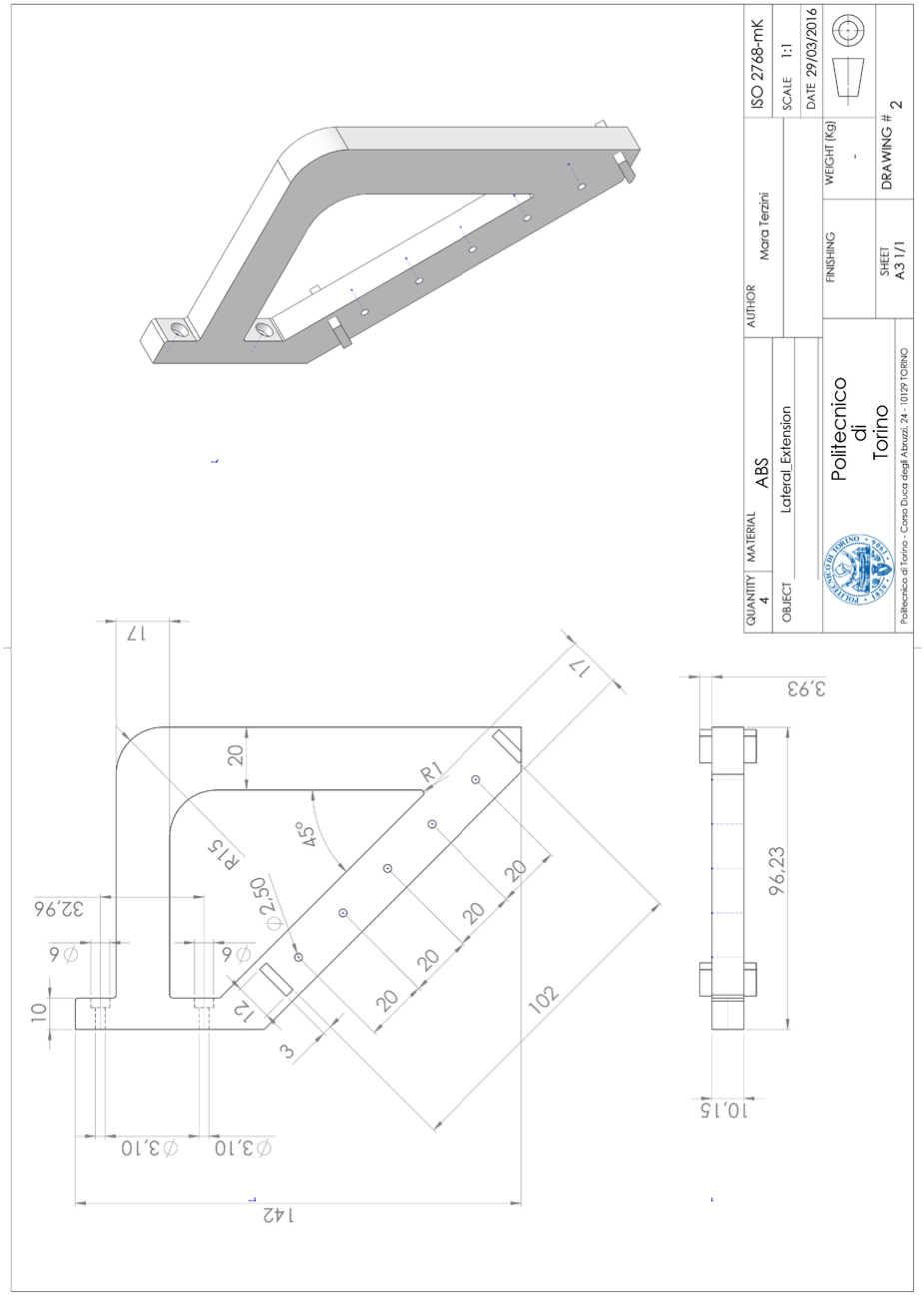


*Figure A.3 Lateral Extension drawing. The lateral extensions are included both in the upper and in the lower crossheads.*

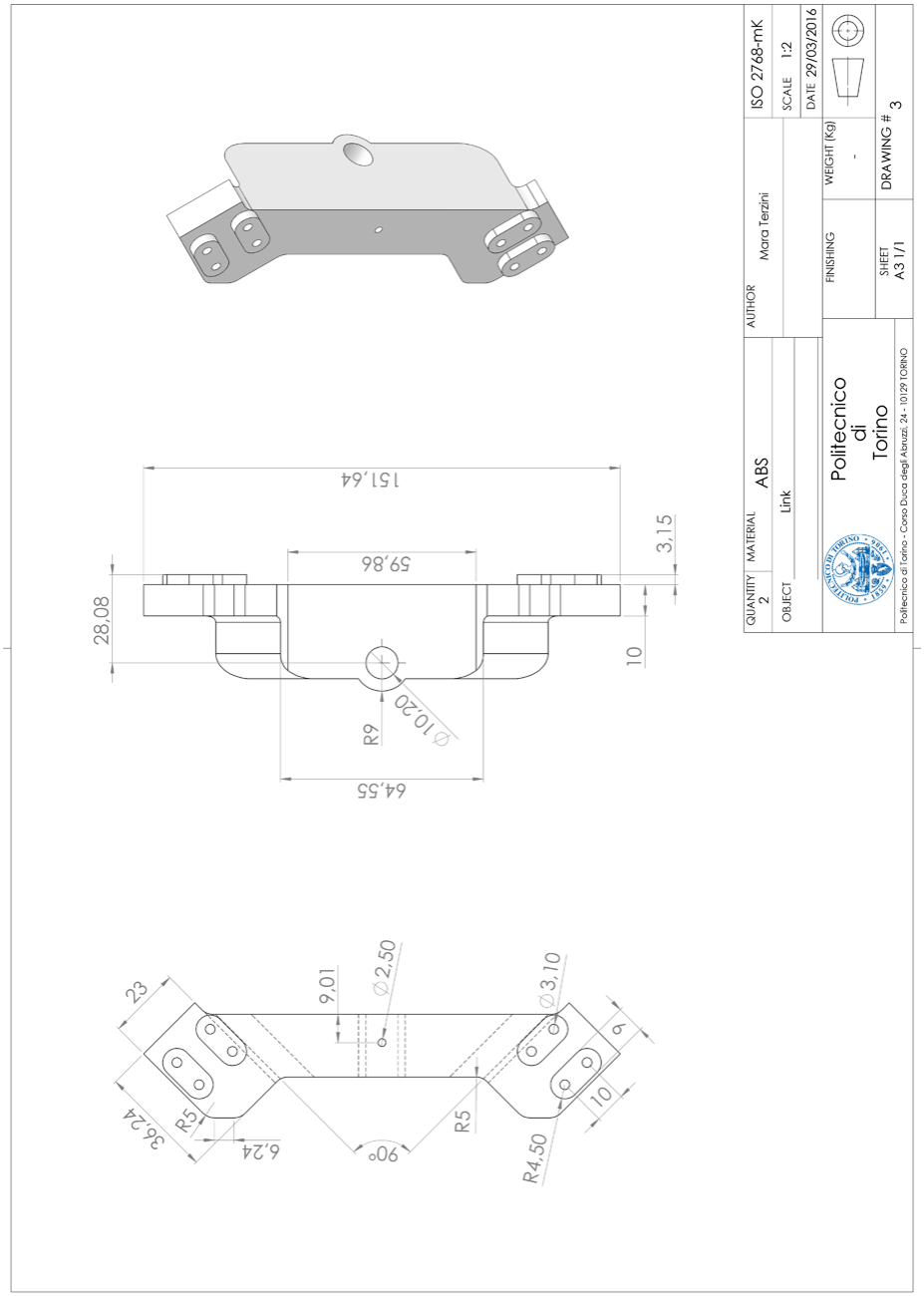


*Figure A.4 Link drawing. Two links connect the upper and lower crossheads through the four linear guideways.*

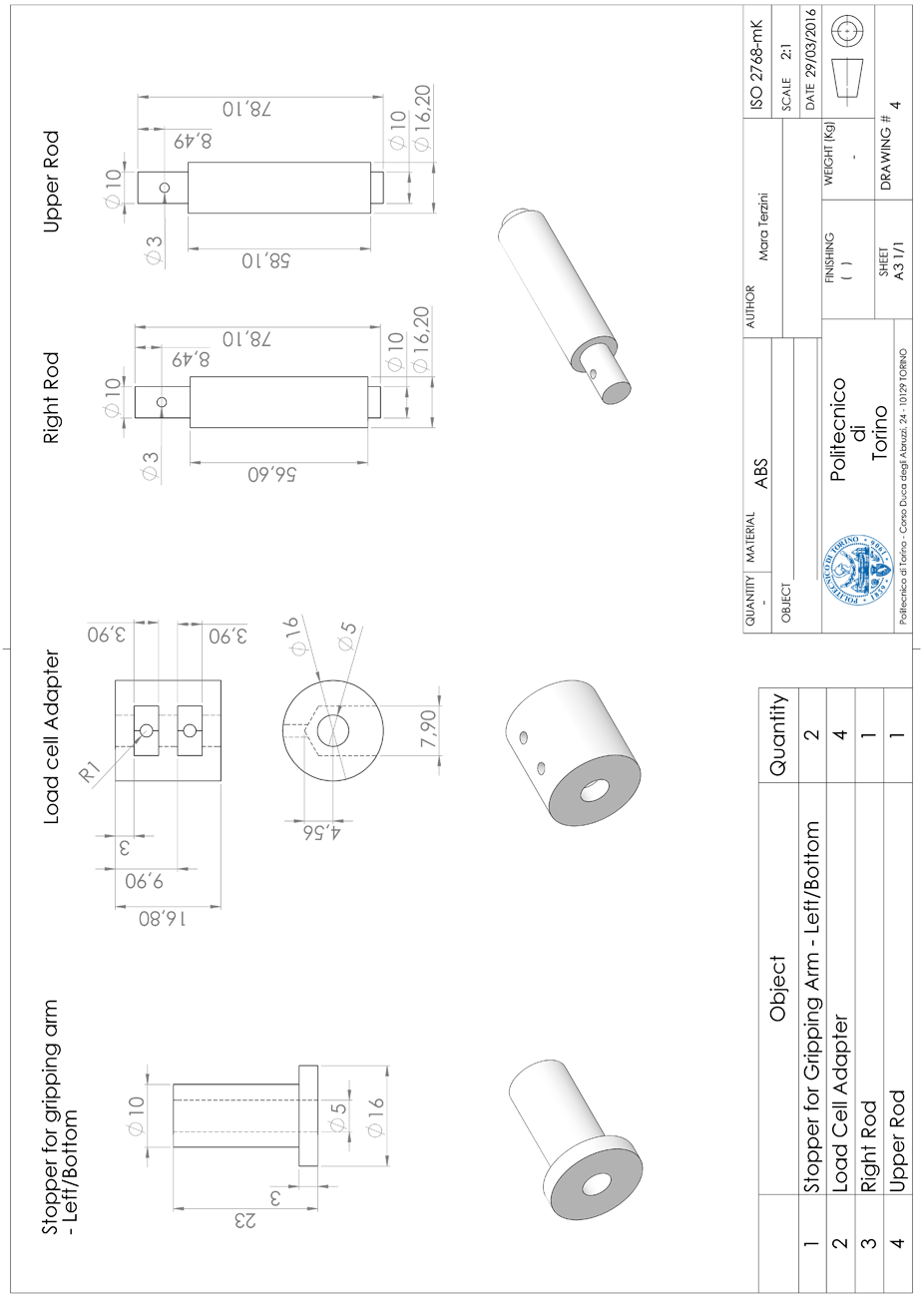


*Figure A.5 Drawing describing the left and the bottom stoppers for the gripping arms, the load cell adapter and the right and upper rods.*

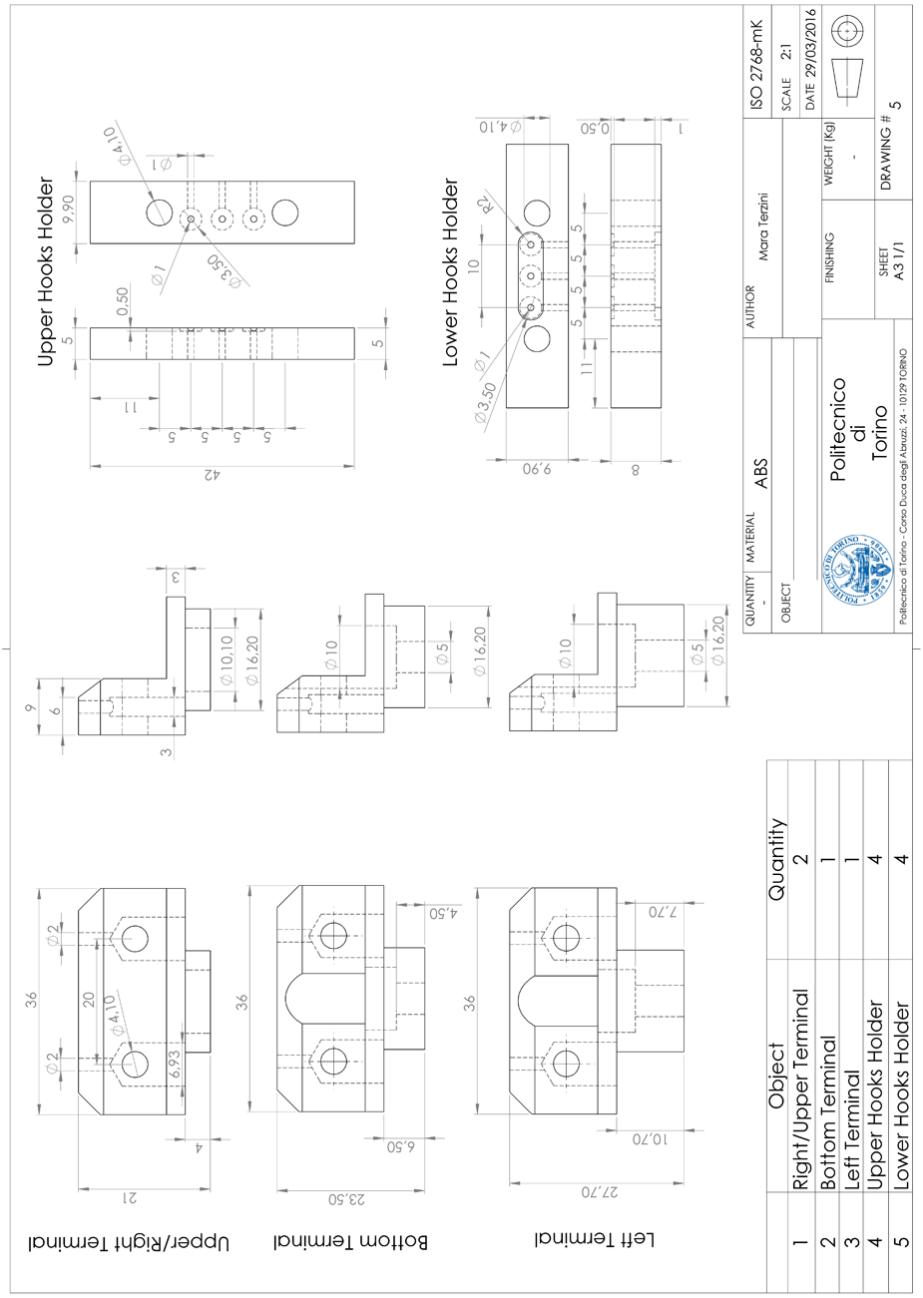


*Figure A.6 Drawing describing the four grippin terminals and the upper and lower hooks holder.*

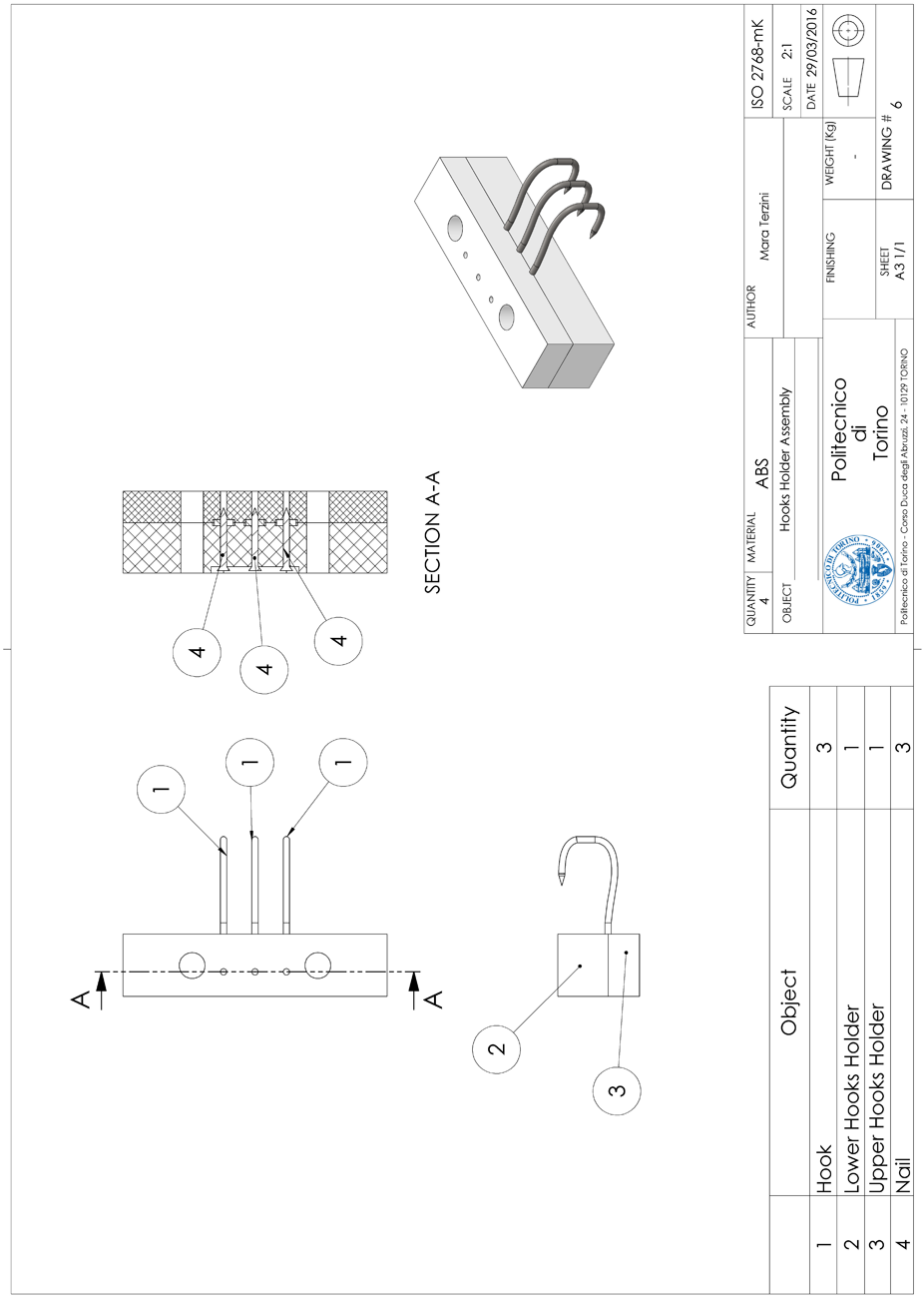


*Figure A.7 Hooks holder assembly.*

## Acknowledgements

I would like to express my gratitude to my supervisor, Prof. Alberto Audenino, whose competence was a striking addition to my doctoral experience. I appreciate his vast knowledge in many areas, which from time to time have made me "green with envy ". I would like to thank Prof. Elisabetta Zanetti, who patiently corrected my writings and presentations, taking time out from her busy schedule. Special thanks goes to Prof. Cristina Bignardi for providing me many opportunities to address a multitude of topics in the biomechanics field.

I thank my fellows, Seffo&Seffino, for the philosophical debates, for the outbursts and for the fun we have had in the last three years: I retain a lovely memory of our Neapolitan experience. I also thank my officemates for the laughs and for the pleasant and fun work environment you've created, enriching the experience of these years.

I would also like to thank my parents for their boundless love and sympathetic ear. You are always there for me.

Thanks to Luci, who inspires me, makes me laugh and brightens up my days.